Design and Optimisation of a Superparamagnetic Nanoparticle based on Ferritin

Towards Probing and Manipulating Cellular Functions

Inaugural-Dissertation

zur Erlangung des Doktorgrades
der Mathematisch-Naturwissenschaftlichen Fakultät
der Heinrich-Heine-Universität Düsseldorf

vorgelegt von

Andreas Neusch
aus Sigmaringen

Düsseldorf, November 2024

aus dem Institut für Experimentelle Medizinische Physik
der Heinrich-Heine-Universität Düsseldorf

Gedruckt mit der Genehmigung der
Mathematisch-Naturwissenschaftlichen Fakultät der
Heinrich-Heine-Universität Düsseldorf

Berichterstatter:

1. Prof. Dr. Cornelia Monzel
   Experimentelle Medizinische Physik
   Heinrich-Heine-Universität Düsseldorf

2. Prof. Dr. Philip Kollmannsberger
   Biomedizinische Physik
   Heinrich-Heine-Universität Düsseldorf

Tag der mündlichen Prüfung:
16. Januar 2025

Diese Arbeit ist für dich, Mama!

Eidesstattliche Versicherung

Ich versichere an Eides statt, dass die Dissertation von mir selbständig und ohne unzulässige fremde Hilfe unter Beachtung der ,,Grundsätze zur Sicherung guter wissenschaftlicher Praxis an der Heinrich-Heine-Universität Düsseldorf" erstellt worden ist.

Andreas Neusch	Datum

Abstract

Cellular signalling has been the source of a multitude of unanswered questions regarding its activation, underlying mechanisms, and role in disease outbreak and development. However, these questions can only be answered with reliable and precise methods to control the related signalling pathways. With this intention, various techniques have been developed during the past decades to manipulate and control selected pathways through external stimuli. One promising technique in this repertoire is magnetogenetics, which utilises magnetic nanoparticles (MNP) and external magnetic fields to remotely activate, redistribute, or heat selected components of signalling pathways.

This work used and developed a semisynthetic MNP platform based on the human iron storage protein ferritin, commonly referred to as Magnetoferritin (MFt). MFt consists of two distinct compartments: a protein nanocage and a synthetic, magnetic iron oxide core. It was shown in the past that the performance of the magnetic core during magnetogenetic actuation was unsatisfactory due to weak responses. Also, while being an effective shield against environmental conditions, the protein shell's functionality and targeting capabilities are limited. Thus, both of MFt's components were engineered in this work to maximise the overall effectiveness of the MNP.

On the one hand, the magnetic properties of the core were enhanced by introducing 7 % of cobalt to the iron oxide core with the goal of increasing the magnetic anisotropy. Even at these comparatively low doping levels, the core's magnetic properties increased drastically – namely, its blocking temperature, coercivity, and, most notably, heat dissipation via magnetic hyperthermia in an alternating magnetic field. The adjustments of these properties led to a fivefold increase in effective heat dissipation compared to undoped MFt. While cobalt doping of MFt increased its heat dissipation significantly, similar MNPs with larger magnetic cores exhibited enhanced response and thermal effectiveness under identical conditions. Hence,

doping of MFt's core qualifies the nanoagent as a mild heat mediator. However, its heating capabilities are limited.

On the other hand, the protein shell of MFt was genetically modified to be both fluorescent and specifically targetable to selected proteins. This selectivity was achieved by fusing a minimal binding domain of Protein A from *Staphylococcus aureus* to the surface of MFt. Protein A is capable of coupling to the constant part of antibodies. Hence, decorating MFt with an antibody of choice was achieved easily. Thus, the functionalised MFt could bind to the antibody's original target. With this approach, it was possible to bind the death receptor CD95, induce cluster formation, and subsequently apoptosis.

The modifications applied to the components of the nanoagent MFt in this work enhanced its performance and applicability in cellular contexts while maintaining high biocompatibility, owing to the passivating character of MFt's protein cage. Even in the presence of cobalt in MFt's core, biocompatibility was high, and usability in cell experiments was not impeded. Compared to synthetic iron oxide MNPs with a dextran shell, MFt was more readily taken up by cells. Also, the mobility of MFt in the cytosol was significantly higher during magnetic redistribution for up to 5 h after incubation.

Conclusively, MFt's increased heat dissipation, its biocompatibility, as well as the possibility to target any protein via antibody-mediated coupling make it a potent MNP for the investigation of signalling pathways in the context of magnetogenetics.

Contents

Chapter I

Introduction

I.1 Outline of this Dissertation

Cells are the most astonishing multi-taskers on Earth. They breathe, digest, talk to their neighbours, and replicate – sometimes all at the same time. The need to handle all of this simultaneously forced life to develop precise pathways, sophisticated structures, and intricate iterative cycles in order to stay on top of *everything* constantly. The management of this herculean task is fulfilled to a large extent by intra- and intercellular signalling pathways that evolved to react to incoming molecules as well as physical factors.

However, with that immense amount of tasks bombarding a single cell in shortest time frames, it cannot be excluded that, occasionally, errors occur. While some errors are negligible, others can lead to malfunctions and potentially serious disease.[1]

To this day, knowledge about many pathways is limited. The reasons for this lack of knowledge are multifaceted. While observing samples on a cellular level is possible with basic light microscopy, known for hundreds of years,[2] signalling pathways take place on a subcellular level. Therefore, shining light on these pathways becomes much more complicated.

First, the signalling components – such as proteins, hormones, or other molecules – are much smaller than the resolution limit of common light microscopes. Hence, techniques need to be applied to overcome conventional limits of detection. Second, cellular molecules are in a dynamic state, constantly changing local concentrations, conformations, and activation states. In order to observe signalling pathways and their key participants, it is, therefore, crucial to first manage to control them.

Over the past decades, diverse techniques have been developed that allow for not only observation of molecules on a subcellular level but also seizing control over their activation states, spatial distribution, and temporal dynamics. One groundbreaking invention in this regard was the development of *optogenetics*. Here, light-sensitive ion channels from retinal cells were expressed in neuronal cells to make them susceptible to light stimuli.[3] With this strategy, it was now possible to remotely activate selected signalling pathways in the blink of an eye using a light stimulus. The interplay of optogenetics and the widely established *fluorescence microscopy* was a dream come true for many life scientists – it was now possible to dig into exactly those questions that have remained unanswered for a long time: How is cellular signalling triggered? What are the thresholds for activation of certain pathways? Is it possible to manipulate pathways to prevent malfunction and disease?
Unfortunately, optogenetics came with various downsides. The low penetration depth of visible light in biological tissue rendered *in vivo* measurements of deep tissue impossible. Although this was overcome by implanting optical fibres into *e.g.* the brain of animals,[4] experiments became cumbersome, highly invasive, expensive, and ethically questionable. Furthermore, photodamage after the prolonged exposition, off-target stimulation, and side effects caused by the equipment – such as heating or infections – could impair experimental results. Lastly, genetic modifications of target organisms were required to express light-sensitive receptors in the cells of interest.

The quest to find ways to overcome these limitations led to the development of *magnetogenetics*. Here, magnetic fields are used to trigger cellular signalling instead of light stimuli. In contrast to light, magnetic fields can penetrate deep into tissue without the invasive and risky implantation of (light) delivery systems. Also, biological tissue is less susceptible to magnetic fields – side effects are therefore strongly reduced. Furthermore, it is possible to generate much larger magnetic fields and stimulate whole areas or even organisms using magnetogenetics. Lastly, magnetogenetic techniques could be used therapeutically since actuation can be achieved without genetic modifications to the target organism. Instead, to allow magnetogenetics to unfold its potential, *magnetic nanoparticles* (MNP) are an elemental component as a mediator between the applied magnetic field and the research target. Various efforts have been made in the past decade to design advanced MNPs

and tailor their properties exactly to experimental needs.
In this work, the human iron storage protein *ferritin* is used as a template for magnetogenetical applications. For this purpose, ferritin is engineered and filled with a magnetic core, which resulted in the semisynthetic magnetic nanoagent *Magnetoferritin*. This dissertation will present and discuss results that were obtained in the course of this journey.

In the beginning, Chapter II will introduce basic concepts related to this work. Section II.1 summarises the varieties of magnetism, with special regard to the magnetism of nanoscopic materials. In Section II.2, cellular signalling in general and pathways related to this work will be addressed. Finally, Section II.3 connects the ideas of biotechnology, nanotechnology, and magnetism that gave rise to magnetogenetics. Additionally, particular attention is given to ferritin and Magnetoferritin as the main protagonists of this story.
The main part is split into two sections, containing two manuscripts each. First, Chapter III discusses the creation, customisation, and physical and biological characterisation of the ferritin nanoagent. *Publication I* implements previously established methods for fabrication of *Magnetoferritin* and compares its performance to fully synthetic nanoparticles. To extend the applicability of the ferritin nanoagent, *Publication II* presents a hybrid, multifunctional ferritin. This construct can be used to target cancer-related membrane receptors specifically, induce the formation of receptor clusters, and, hence, even induce cellular reactions such as apoptosis.
Next, Chapter IV deals with the characterisation, modification, and actuation of the magnetic core of ferritin. In *Publication III*, a setup for heating magnetic nanoparticles via *alternating magnetic fields* is presented, successfully established, and tested on several MNPs. This setup is applied in *Publication IV* – here, Magnetoferritin's iron oxide core is doped with transition metals to customise its magnetic properties. Besides thorough characterisation of the affected magnetic properties, Magnetoferritin's heating capabilities are assessed using the setup built for *Publication III*.
Ultimately, Chapter V will summarise all results concerning magnetogenetics. The significance of the designed ferritin nanoagent will be discussed, as well as its potential for magnetogenetic applications.

I.2 Scientific Output

I.2.1 Articles

My main research project dealt with the development of a versatile magnetic nanoparticle for probing and investigating cellular signalling. Furthermore, I utilised and developed analytical techniques for nanoparticle characterisation in the course of my work. Based on this matter, three peer-reviewed journal articles and one manuscript were published that are enclosed in this dissertation in Chapter III and IV.

Article *Magnetic Nanoprobes for Spatio-Mechanical Manipulation in Single Cells*
Iuliia P. Novoselova* , Andreas Neusch*, Julia-Sarita Brand, Marius Otten, Mohammad Reza Safari, Nina Bartels, Matthias Karg, Michael Farle, Ulf Wiedwald, and Cornelia Monzel
* These authors contributed equally.
Nanomaterials (2021) | Volume 11 | Issue 9
https://doi.org/10.3390/nano11092267

Article *An efficient magnetothermal actuation setup for fast heating/cooling cycles or long-term induction heating of different magnetic nanoparticle classes*
Daniel A. Kuckla, Julia-Sarita Brand, Bastian Czech, Amirarsalan Asharion, Jan V. Jüttner, Iuliia P. Novoselova, Andreas Neusch, Philipp Hagemann, Mathias Getzlaff, and Cornelia Monzel
Journal of Physics D: Applied Physics (2023) | Volume 56 | Issue 50
https://doi.org/10.1088/1361-6463/acfb8f

Article *Semisynthetic Ferritin-based Nanoparticles with High Magnetic Anisotropy for Spatial Magnetic Manipulation and Inductive Heating*
Andreas Neusch, Ulf Wiedwald, Iuliia P. Novoselova, Daniel A. Kuckla, Nikolaos Tetos, Sarah Sadik, Philipp Hagemann, Michael Farle, and Cornelia Monzel
Nanoscale (2024) | Volume 16 | Issue 32
https://doi.org/10.1039/d4nr01652a

Manuscript *Semisynthetic Ferritin Nanocages for Flexible, Site-specific Targeting, Cluster-formation and Activation of Membrane Receptors*
Andreas Neusch, Christina Siepe, Liesa Zitzke, Alexandra C. Fux, and Cornelia Monzel
bioRxiv (2024) | Preprint (not peer-reviewed)
https://doi.org/10.1101/2024.11.01.621585

Furthermore, I was able to contribute techniques and methodology I learned during my main work to the following publications:

Article *Mobile and Immobile Obstacles in Supported Lipid Bilayer Systems and Their Effect on Lipid Mobility*
Luisa Coen, Daniel A. Kuckla, Andreas Neusch, and Cornelia Monzel
Colloids Interfaces (2024) | Volume 8 | Issue 54
https://doi.org/10.3390/colloids8050054
Here, I supervised and supported production of fluorescent proteins and determination of their molecular brightness.

Article *Heterogeneity of Lipopolysaccharide as Source of Variability in Bioassays and LPS-Binding Proteins as Remedy*
Alexandra C. Fux, Cristiane Casonato Melo, Sara Michelini, Benjamin J. Swartzwelter, Andreas Neusch, Paola Italiani, and Martin Himly
International Journal of Molecular Sciences (2023) | Volume 24 | Issue 9
https://doi.org/10.3390/ijms24098395
For this publication, I contributed to the creation of figures and proof-reading.

I.2.2 Presentations

Apart from the aforementioned articles and manuscripts, my work was presented and shared with the public on the following occasions:

Poster WEH Foundation | *Nanobiotechnology for Cell Interfaces*
March 2021 | virtual
Andreas Neusch, Julia-Sarita Brand, Marius Otten, Daniel A. Kuckla, Iuliia P. Novoselova, Matthias Karg, and Cornelia Monzel
Magnetic Manipulation Strategies Towards Cell Signaling Studies

Poster German Physical Society | *Annual Meeting*
September 2021 | virtual
Andreas Neusch, Iuliia P. Novoselova, Julia-Sarita Brand, Marius Otten, Matthias Karg, Michael Farle, Ulf Wiedwald, and Cornelia Monzel
Bio-inspired Magnetic Nanoprobes for Subcellular Manipulation Studies in Single Cells

Talk German Physical Society | *Annual Meeting*
September 2022 | Regensburg, Germany
Andreas Neusch, Iuliia P, Novoselova, Nikolaos Tetos, Michael Farle, Ulf Wiedwald, and Cornelia Monzel
A Semisynthetic Superparamagnetic Nanoprobe for Protein Targeting and Manipulation

Talk German Physical Society | *Annual Meeting*
March 2023 | Dresden, Germany
Andreas Neusch, Iuliia P. Novoselova, Liesa Zitzke, Sarah Sadik, Michael Farle, Ulf Wiedwald, and Cornelia Monzel
Bio-inspired Magnetic Nanoprobes For Subcellular Manipulation Studies in Single Cells

Poster European Chemical Society | *Chemistry Congress*
July 2024 | Dublin, Ireland
Andreas Neusch, Ulf Wiedwald, Daniel A. Kuckla, and Cornelia Monzel
Semisynthetic Ferritin-based Nanoparticles with High Magnetic Anisotropy for Spatial Magnetic Manipulation and Inductive Heating

Chapter II

Fundamentals

II.1 Magnetism

II.1.1 History of Magnetism

For thousands of years, magnetism has attracted humanity. Ever since the first discovery of then called *lodestones*, its strange, almost magical power fascinated anyone who got his hands on something magnetic. The curiosity's name originated in ancient Greece. The first mentions of the term *magnet* date back to the 5^{th} century B.C. Onomacritus was the first to mention *mágnēs líthos*, stones from Magnesia, a town in today's Turkey. Apparently, the Greeks discovered one of Earth's many natural deposits of lodestone there. Although interesting, no practical use could be made of magnetism and magnetic stones. This changed around 1000 A.C. when Chinese seafarers were the first to harness the powers of magnetism by designing the first compass – one of many revolutionary applications to come.[5]
However, at this time, the phenomena behind magnetism were still hardly understood, and it would take hundreds of years until this knowledge would be brought to light. Around 1800, Denis Poisson introduced the idea of *magnetic fields*, equivalent to electric fields. However, magnetic charges only appear in pairs of opposite polarity. Starting from 1820, Hans Christian Ørsted, André-Marie Ampère, Michael Faraday, and Pierre-Simon Laplace steadily established the connection between magnetism and electricity, which culminated in the formulation of Maxwell's equations in 1864. From then on, the coexistence and dependence of electric and magnetic fields were commonly accepted, and the term *electromagnetism* was established.

The connection between electrons and magnetism that was established in the 19$^{\text{th}}$ century was fundamental for further progress. With this knowledge, it became possible to use electrical currents to create magnetic fields and precisely control their properties. This crucial step was achieved by the invention of electromagnets, which opened up new technological applications, such as *magnetic resonance imaging* (MRI), mass spectrometry, or – in combination with superconducting materials at ultra-low temperatures – the generation of magnetic fields of extreme strength for levitation, particle accelerators, or fusion reactors.[5,6]
Nowadays, magnetism plays a major role in our society. Vital technologies such as fridge magnets and bag clasps would not be part of our life. The same applies to electric cars, TVs, computers, and electricity in general. All of this would not have been possible without humankind's advancements – that all started with someone's curiosity towards these strange stones that attract metal.

II.1.2 Fundamentals of Magnetism

The link between electrical currents and magnetism was a fundamental step towards a broader understanding of magnetic behaviour in matter. Based on this, electrons were a major suspect for further investigations of the magnetic force. In fact, magnetism is caused by the motion of electrons around their own axis and around their atomic nucleus.[7] These two types of motion can be translated into a *spin magnetic dipole moment* (μ_{s}) and an *orbital magnetic dipole moment* (μ_{orb}). While μ_s is an intrinsic property of the electron and can either be positive or negative, μ_{orb} can be influenced by factors in the surroundings of the electron and atom.[8] Combining μ_s and μ_{orb} of all electrons of an atom and all atoms of a material gives rise to the magnetic moment $\vec{m}$ of this material and determines the type of magnetic behaviour, the material will have.[6]
Empirically, it was discovered that atoms with unpaired electrons in their electron shell exhibit a magnetic moment. This holds true for 79 of the 103 stable chemical elements as long they are in their isolated atomic state. However, once those atoms form inter-atomic bonds, only a handful retain an effective magnetic moment. Among them are oxygen, iron, cobalt, and some rare metals.[9]

Excursion 1: H-M Diagrams

For visualisation of magnetic behaviour of any material *H-M curves* are commonly used, recorded via *vibrating sample magnetometers* (VSM) or *superconducting quantum interference devices* (SQUID).

Figure II.1.1 depicts the acquisition of an *H-M* curve for an undefined exemplary material. The measurement is performed at a constant temperature since results are highly temperature-dependent. Here, absolute values of H and M are used instead of vectorial fields to provide a clearer view of the magnetisation response. The curve records changes in M while the material is exposed to a sweeping external magnetic field H (see Figure II.1.1 B). (1) Initially, the material is unmagnetised. (2) The external field is switched on and steadily increases in one direction; M follows. At a preset maximal strength, H will decrease again. (3) After reducing H to 0, the material is demagnetised, and H is reversed. (4) The field increases in the opposite direction, magnetising the material accordingly as internal magnetic dipoles realign. The cycle completes by decreasing and switching off H to return to (1).

The shape of the *H-M* curve enables the determination of a material's magnetic behaviour. Care must be taken with the unit of M – some applications use the magnetic moment (unit: $\mathrm{A\,m^2}$), while others normalise M to the material's mass or iron content (unit: $\mathrm{A\,m^2\,g^{-1}}$).

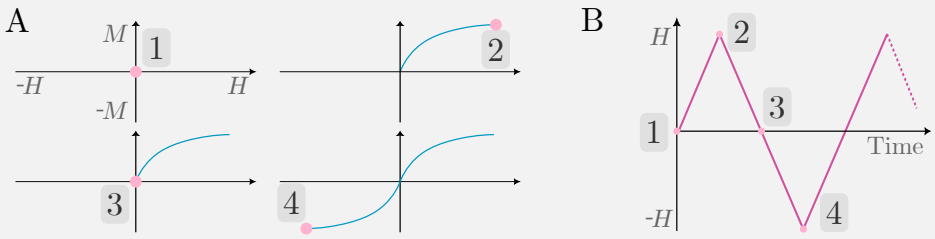

Figure II.1.1: Schematic recording of an *H-M* curve. (A) Curves of an exemplary material. The four graphs are snapshots of several points during the measurement. Numbers correspond to those in B. (B) Sweeping of the external magnetic field H during the measurement.

As implied, magnetic materials interact with their environment via magnetic fields, which are comparable to electric fields. However, there is one major difference – while there are electric monopoles creating electric fields, there are only magnetic dipoles.

Generally, there are two distinct types of magnetic fields: $\vec{H}$ and $\vec{B}$ fields. $\vec{B}$ fields are the manifestation of 'everyday magnetism' since they describe the *magnetic flux density* around both permanently magnetised materials and current-carrying conductors. On the other hand, the *magnetic field strength* $\vec{H}$ is independent of material properties and describes magnetic fields from external sources such as electric currents. The units used to describe magnetic fields have changed frequently over the last years, but now, $\vec{H}$ fields are usually quantified in $\mathrm{A\,m^{-1}}$, while Tesla (T) is used for $\vec{B}$ fields.
If a material with magnetic properties is subjected to an external magnetic field $\vec{H}$, its internal magnetic moments will align with the external field and give rise to the $\vec{B}$ field:

$$\vec{B} = \mu_0(\vec{H} + \vec{M}), \tag{II.1.1}$$

with the permeability of the vacuum μ_0 (equals to $\approx 4\pi\cdot\, 10^{-7}\,\mathrm{N\,A^{-2}}$) and the magnetisation of the material $\vec{M}$.[10,11] The magnetisation is the net magnetic dipole moment in a volume V.[12] Hence, it is correlated to the alignment of single magnetic dipole moments within the material.
The interplay of internal magnetisation and external magnetic fields defines whether a material is 'magnetic' or not (see also Excursion 1). These interactions condense in another important magnetic characteristic: the dimensionless *magnetic susceptibility* χ. It is a quantity for how strongly a magnetic material will adjust its magnetisation $\vec{M}$ to the externally applied magnetic field $\vec{H}$.[10] Generally, magnetisation $\vec{M}$, susceptibility χ and external field $\vec{H}$ are connected via

$$\vec{M} = \chi\vec{H}. \tag{II.1.2}$$

Depending on the characteristics of a magnetic material, it can be categorised into three groups: dia-, para-, and ordered magnetism. These characterisations will be described in Section II.1.2.1 and II.1.2.2.

II.1.2.1 Dia- and Paramagnetism

Diamagnetism In a *diamagnetic* material, the magnetic dipole moments μ_s and μ_orb are balancing each other out, leading to a net magnetisation of 0 – the material

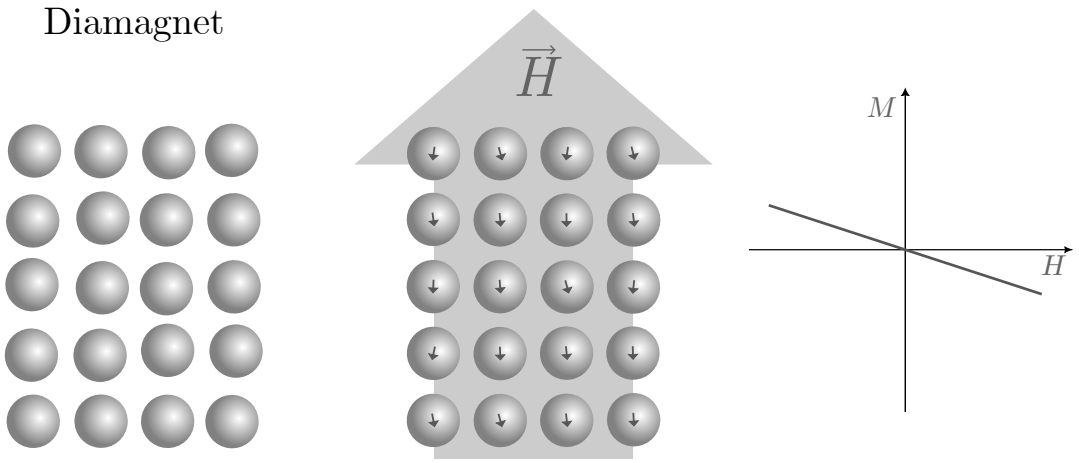

Figure II.1.2: Schematic depiction of a diamagnetic material in the absence and presence of an external magnetic field $\vec{H}$. The net magnetisation of the material opposes the external field, repelling the material. The H-M curve shows that the net magnetisation of the material opposes the H field and is relatively weak. This holds true for weak magnetic fields.

therefore is 'non-magnetic'. However, if an external magnetic field of decent strength is applied to the diamagnet, changes in the orbital motion of the electrons can occur.[5,7] This induces weak fields that are opposing the external $\vec{H}$ field. Hence, the diamagnet is pushed out of the field (see Figure II.1.2). The susceptibility χ (as introduced in Equation II.1.2) is in the order of -10^{-6}.[10]
A majority of everyday materials is diamagnetic. They consist only of non-magnetic atoms, and the induced fields are very weak in comparison to the other forms of magnetism. The magnetisation of a diamagnet will always be opposing the external field that is applied (see also Figure II.1.2).

Paramagnetism Similar to a diamagnet, *paramagnetic* materials have a net magnetisation of 0. However, due to unpaired electrons in the material, it is made up of single, randomly oriented magnetic moments. By application of an external field, these singular moments align with the field, increasing the net magnetisation $\vec{M}$ in the process (see Figure II.1.3). Hence, $\vec{M}$ is linearly dependent on the strength of the external field on weaker applied fields (see H-M graph in Figure II.1.3).[7] A paramagnet's susceptibility χ is small, but positive in the range of 10^{-5} to 10^{-3}.[13]
As soon as the external field is switched off, the single magnetic moments lose their coupled orientation, and the net magnetisation drops back to 0. According to the

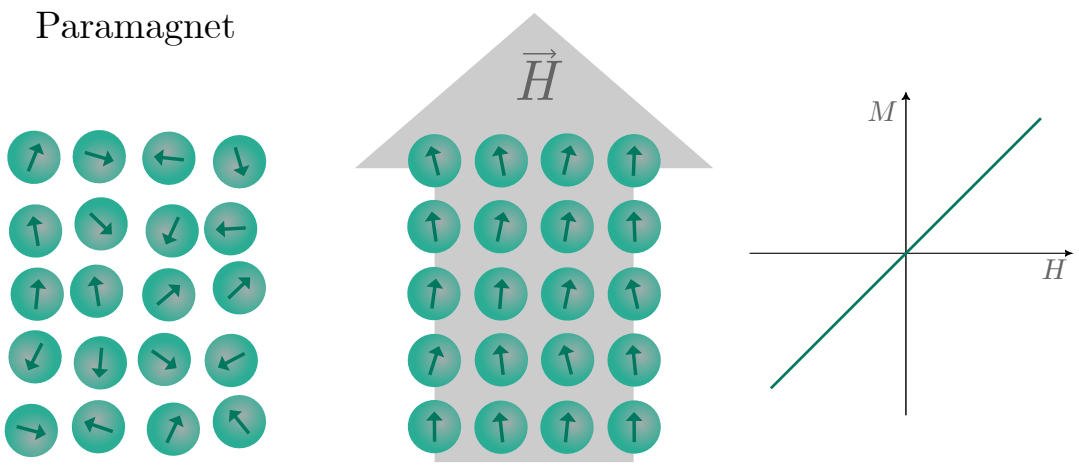

Figure II.1.3: Schematic depiction of a paramagnetic material in the absence and presence of an external magnetic field $\vec{H}$. For weak external fields, the magnetisation M of the material aligns with an external field H.

Langevin model, thermal energy exceeds the energy barrier that keeps the magnetic moment in an ordered orientation.[13] The presence of an external field raises this energy barrier and allows the paramagnet to sustain its magnetisation.[13]

II.1.2.2 Ordered Magnetism

Materials that are able to sustain their net magnetisation even in the absence of an external magnetic field are summarised under the broader term of *ordered* or *strong magnetic materials* – accordingly, dia- and paramagnetism can also be referred to as *weak magnets*. For strong magnetic materials, the temperature plays an important role since magnetic moments within the material can only become ordered below a specific critical transition temperature. Above this temperature, thermal energy prevents the single magnetic moments from remaining in line. This phenomenon will be described in more detail in the context of *superparamagnetism* in Section II.1.3.1. Namely, the ordered magnetic classifications are *ferro-*, *antiferro-*, and *ferrimagnets* (see Figure II.1.4) that will be described in the following paragraphs.

Ferromagnetism A *ferromagnet* is the incarnation of an everyday magnet. Ferromagnets can maintain their magnetisation even in the absence of an external field. Hence, it is possible to magnetise the material to create a permanent magnet (see Figure II.1.4). Usually, ferromagnets exhibit the strongest forms of magnetism, espe-

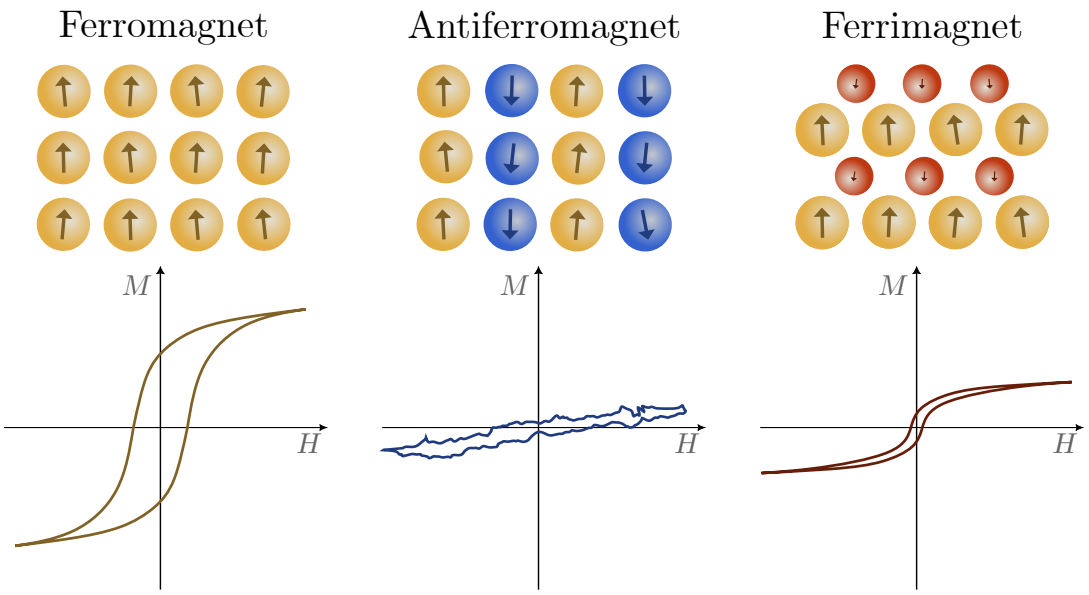

Figure II.1.4: Schematic depiction of ferro-, ferri-, and antiferromagnetic materials. At the bottom, typical H-M curves for each material are shown. As depicted here, saturation magnetisations of both ferri- and antiferromagnets are significantly smaller than that of ferromagnets (see also Figure II.1.7).[7]

cially in comparison to the temporarily induced fields in weak magnetic materials.[6] Ferromagnetism is usually observed in transition metals such as iron, cobalt, and nickel, as well as some lanthanoids and alloys of these metals.[7,10] It is caused by a quantum physical effect called *exchange coupling*. Through this effect, electron spins of neighbouring atoms interact with each other, leading to a stable alignment of magnetic moments across the material.[6]

As described in the previous chapter, magnets can only uphold their magnetisation below a specific critical temperature – in the case of ferromagnets, this temperature is also called *Curie temperature* T_C. Heating a ferromagnet above T_C leads to demagnetisation due to thermal agitation of the magnetic dipole moments in the material. In this state, the material will behave like a paramagnet. Only after cooling below T_C, the ferromagnet can be remagnetised.[5]

In ferromagnets, χ is highly dependent on various parameters such as temperature and material. While it follows paramagnetic behaviour above T_C, χ becomes non-linear below T_C. However, it can be noted that χ in ferromagnets is many magnitudes larger than that of paramagnets because of the strong exchange interactions.[13]

Excursion 2: Magnetic Domains

On the atomic scale, ordered magnetic materials are made up of crystals. An ideal material would consist of only one crystal with a perfect crystal lattice that has one uniform magnetic moment. However, due to imperfections in the lattice, single magnetic moments cannot align perfectly across one bulk magnet. Energetically, it is favourable for the material to form areas in which single magnetic moments are aligned in parallel, giving rise to the sum of the magnetisations $\vec{M}$. These areas are referred to as *Weiss domains* or *magnetic domains* (see left image in Figure II.1.5). Magnetic moments of multiple domains are not necessarily aligned and can potentially cancel each other out. Upon exposition to an external field, in-line domains grow at the expense of out-of-line domains through the orientation of single magnetic dipole moments in line with the external field. This leads to an increase of the net magnetisation.[14]

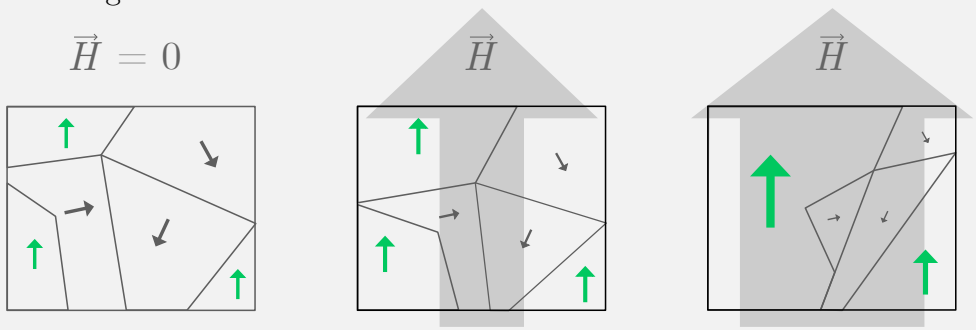

Figure II.1.5: Depiction of the magnetic domains, also known as Weiss domains, of an ordered magnetic material. Upon application of an increasing external magnetic field $\vec{H}$, in-line domains grow at the expense of out-of-line domains, increasing the material's net magnetisation.

Antiferromagnetism Some compounds, such as elemental manganese (Mn), have comparably high magnetic moments due to their atomic structure. Although such substances theoretically could exhibit a very high net magnetisation, the interatomic structure can disturb this expectation. Taking Mn as an example, due to *negative exchange interactions* between atoms, their magnetic moments align anti-parallel to each other (see Figure II.1.4). This then leads to the formation of two sub-lattices, cancelling out the magnetic fields of each other and, thus, to an effective magnetisation of 0 in pure Mn.[7,14]

This anti-parallel orientation of the two sub-lattices can only be sustained below a material-specific temperature – for Mn, this is 100 K.[15] At elevated temperatures, the magnetic moments of this *antiferromagnet* are thermally agitated, and hence, the material behaves similarly to a paramagnet. The temperature of this transition is referred to as the *Néel temperature* T_N of an antiferromagnet. Consequently, at T_N the material leaves the paramagnetic, randomly oriented state (for $T > T_N$) and enters the antiferromagnetic, ordered state (for $T < T_N$).[5]
Above T_N, χ follows the Curie-Weiss law:

$$\chi = \frac{C}{T + \Theta_D}, \tag{II.1.3}$$

where C is the material-specific *Curie constant* and Θ_D the Debye temperature.[16] Below T_N, the antiferromagnetic ordering increases and, hence, the material's susceptibility decreases.[13,16]

Ferrimagnetism Elaborating on the idea of antiferromagnets consequently leads to a material in which two opposing sublattices are present but not equally strong. Thus, the net magnetisation of the material is not cancelled out fully. This situation occurs in *ferrimagnets*. Macroscopically, ferrimagnets behave similarly to ferromagnets while below the transition temperature T_C. On a microscopic scale, however, they are closer to antiferromagnets: two (or potentially more) distinct species with different magnetic dipole moments form magnetic domains that are usually opposed to neighbouring domains (for details on magnetic domains see Excursion 2).[5,7] The susceptibility is large – comparable to ferromagnets – as long the material is below T_C.[13]
One prominent example of a ferrimagnetic material is the iron oxide *magnetite* (Fe_3O_4 or – more precisely – $Fe^{2+}Fe_2^{3+}O_4$). It crystallises in an inverse spinel structure. The iron atoms are located in either octahedral (six nearest neighbours) or tetrahedral (four nearest neighbours) lattice sites (see Figure II.1.6). The Fe^{3+} ions populate both octahedral and tetrahedral sites, while the Fe^{2+} ions are only present in tetrahedral sites. The ratio of this distribution is 1:1:1 (Fe^{3+}_{tetr}:Fe^{3+}_{oct}:Fe^{2+}_{oct}).

Within this structure, the magnetic moments of the two iron ions in the octahedral and tetrahedral sites interact with each other. In magnetite, the interactions between Fe^{3+}_{tetr} and Fe^{3+}_{oct} are antiferromagnetic and cancel each other out, hampering the net magnetic moment. Hence, magnetite would be antiferromagnetic if not

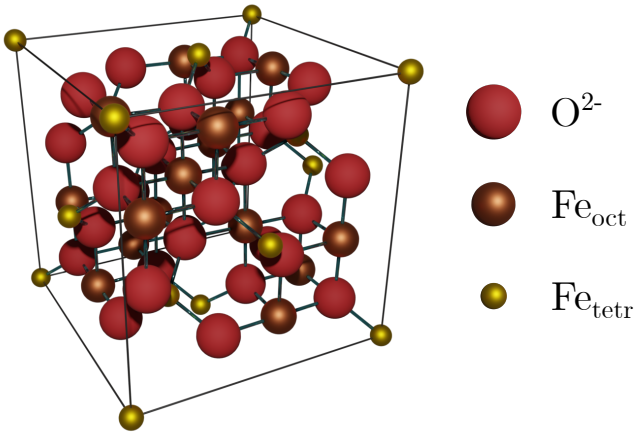

Figure II.1.6: Crystal structure for magnetite (Fe_3O_4), with oxygen atoms (O^{2-}) and iron atoms (Fe^{2+} and Fe^{3+}) that are on octahedral or tetrahedral positions.

for the remaining Fe^{2+} ions. Due to their orientation and magnetic moment, the material is classified as ferrimagnetic.[17]
Magnetoferritin, the main subject of this dissertation, was shown to contain iron oxide cores made of magnetite.[18] Therefore, magnetite plays a key role in this work. *Ferritin*, *Magnetoferritin* and the role of magnetite within will be introduced in more detail in Section II.3.2.4.

II.1.2.3 Magnetic Hysteresis

As described in the previous chapters, ferro- and ferrimagnetic materials are able to uphold a magnetisation in the absence of an external $\vec{H}$ field. The effect that these materials sustain magnetisation is defined by the lack of the ability to return to the initial, unmagnetised state. This effect is referred to as *magnetic hysteresis*.
As described in Excursion 1, H-M curves are a helpful tool in order to visualise and characterise magnetic properties of ordered magnetic materials (see also Figure II.1.4). An exemplary curve for a ferro- or ferrimagnet is shown in Figure II.1.7. Starting at the initial, non-magnetised state, the H field is applied (dotted, central curve). This causes the single magnetic dipole moments to gradually align with the external field. In this course, M increases up until the point where all magnetic domains are aligned parallel to each other – the saturation magnetisation M_S is reached. From there, H is decreased again until it reaches 0 and is technically

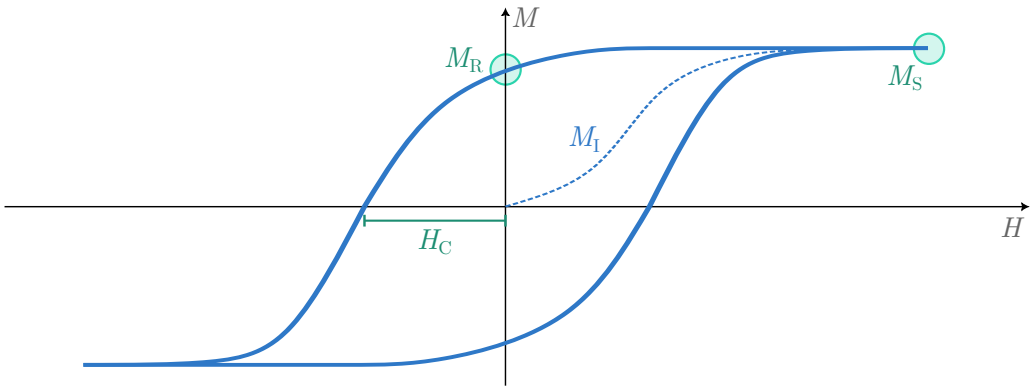

Figure II.1.7: Typical hysteresis curve of a ferri- or ferromagnet below T_C. The dotted line in the centre M_I shows the initial magnetisation curve that starts with the material not being magnetised. Additionaly shown are the saturation magnetisation M_S, the remanent magnetisation M_R and the coercive field H_C. Due to their characteristic shape, these curves are commonly referred to as *hysteresis loops*. For more details on how these curves are gathered, see Excursion 1.

turned off. Here, the hysteresis leads to the *remanent magnetisation* M_R, the actual magnetisation the material can retain. Through the sweeping of the external field, it switches direction at this point. The material is demagnetised when the H field reaches the *coercive field* H_C, which forces enough magnetic domains to reorient and cancel each other out for M to reach 0 again. From here on, the material will reach the opposites of M_S, M_R, and H_C. The continuous sweeping of the external field produces a characteristic loop, the so-called *hysteresis loop*.[5,6]

Magnetic hysteresis is a phenomenon that is highly dependent on temperature. As mentioned earlier, elevated temperatures can introduce enough thermal energy into the material that the energy barrier from magnetic exchange interactions of dipole moments can be exceeded, leading to a loss of magnetic orientation through the shrinkage and, eventually, the disappearance of magnetic domains. Thus, while still being present, magnetic moments are not able to stably sustain their orientation and align randomly, cancelling out each other. Hence, M_S decreases with increasing temperature, until it reaches 0 at T_C.[14]

II.1.3 Nanomagnetism

It was shown in Excursion 2 that ferri- and ferromagnetic materials are made up of finite magnetic domains, where all singular magnetic dipole moments are aligned in parallel. What happens, though, if the analysed material is small enough so that

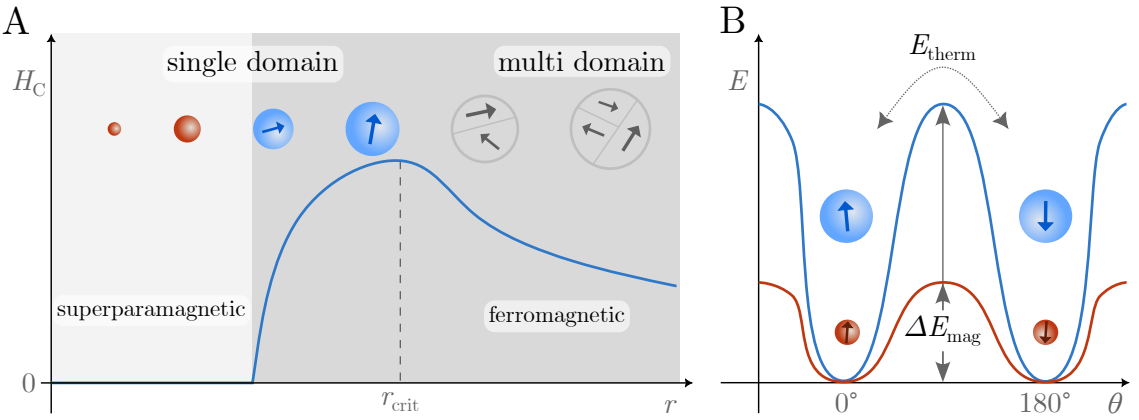

Figure II.1.8: Size dependencies of magnetic behaviour in nanoparticles. (A) Dependency of coercivity H_C on particle radius r. Below a material-specific critical size r_{crit}, MNPs will become single domain particles but retain their magnetic moment. Only at even smaller sizes they will become superparamagnetic.[13] (B) Energy E of an MNP in dependency of the orientation of its magnetic moment θ. Considering that the magnetic anisotropy of the particle is uniaxial, there are two energetic minima at opposite orientations to the magnetic moment. The energy barrier ΔE_{mag} prevents the orientation from flipping and decreases with the particle size. Once the thermal energy E_{therm} is sufficient to surpass ΔE_{mag}, orientation flips will occur.[19] In this context, particles can either be *blocked* and behave like a ferromagnet (blue particles, $E_{therm} < \Delta E_{mag}$) or in their superparamagnetic state (red particles, $E_{therm} > \Delta E_{mag}$).

only one magnetic domain can fit into its volume?
This question guides us to the phenomenon of *superparamagnetism*, which will be discussed in the next chapter.

II.1.3.1 Superparamagnetism

Superparamagnetism is a magnetic state that occurs in ferro- or ferrimagnetic materials if their size is reduced greatly (see Figure II.1.8). Below the critical size r_{crit} – for example 15 nm for iron[20] – particles of the material contain only one magnetic domain with an uniaxial magnetic anisotropy (see Figure II.1.8 A). At this point, the energy E of the particle will exhibit two minima for the two opposing magnetisation orientations (see Figure II.1.8 B). An energy barrier ΔE_{mag} prevents the magnetisation from flipping directions. Thus, the particle will act as a ferro- or ferrimagnet and retain its magnetisation.
ΔE_{mag} depends on the particle size and will decrease with it. If the particle becomes smaller than the superparamagnetic limit, ΔE_{mag} will be surpassed – for example, by thermal fluctuations, which will be discussed later in this chapter.[19] Here, the

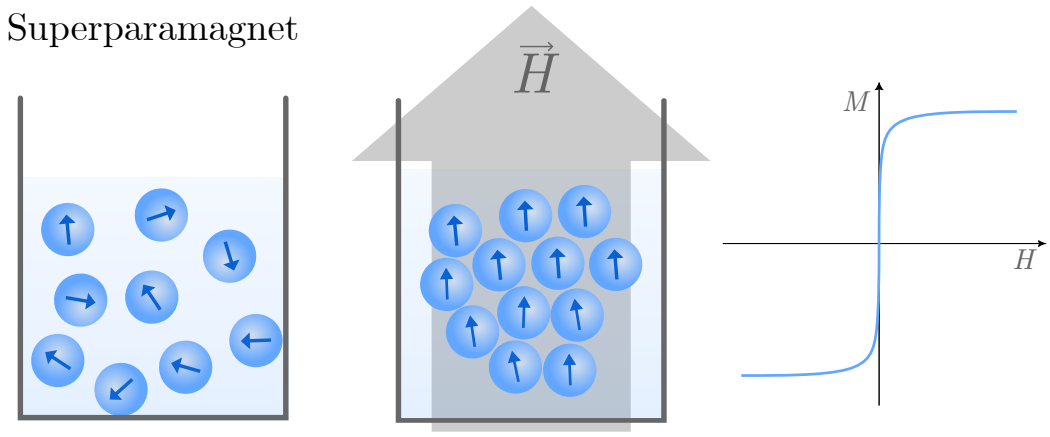

Figure II.1.9: Schematic depiction of superparamagnetic nanoparticles in solution in the absence and presence of an external magnetic field $\vec{H}$. The presence of the $\vec{H}$ field leads to rapid agglomeration of the particles. The H-M curve demonstrates the quick reaching of the saturation magnetisation and lack of remanence after magnetisation.

particle's magnetisation will lose its stability and start to fluctuate. This leads to a disordered, seemingly non-magnetic state, represented by the coercivity H_C being 0 (see Figure II.1.8A). The strong resemblance to paramagnetism in this state served as the origin for the term *superparamagnetism*. Due to the strict size restrictions, superparamagnetism is only observed in MNPs.[10]

However, when exposed to an external magnetic field, superparamagnets behave profoundly differently than their namesake. First, their magnetic dipole moment is extremely frail since it is basically isolated. External fields of lowest intensities are enough for a superparamagnet to reach M_S (see Figure II.1.9). Secondly, once a superparamagnet is sufficiently magnetised – *i.e.* its magnetic dipole moment oriented in line with the external field – it will reach a quasi-ferromagnetic state, where magnetic interactions lead to attractive forces between single magnetic domains. Hence, the superparamagnetic MNPs agglomerate and are pulled towards the source of the $\vec{H}$ field. Additionally, due to the instability of the magnetic dipole moment, superparamagnets lose their magnetisation immediately in the absence of an external field – M_R is 0. Therefore, superparamagnetic MNPs do not exhibit magnetic particle-particle interactions or agglomerate without being magnetically stimulated.[7,10]

As implied, temperature again plays a major role in the occurrence of this magnetic classification. A superparamagnetic system is governed by two distinct energies. On the one hand, the frequency of flips of the magnetic moment and the system's

dynamics are determined by the thermal energy E_{therm}:

$$E_{\text{therm}} = k_{\text{B}}T, \tag{II.1.4}$$

with the Boltzmann constant k_{B} and the temperature of the system T. On the other hand, the energy barrier that opposes these flips and therefore stabilises the system is defined as ΔE_{mag}:

$$\Delta E_{\text{mag}} = K_{\text{eff}}V, \tag{II.1.5}$$

with the volume of the particle V and the constant for the anisotropy of the particle K_{eff} (see Figure II.1.8).[20] Hence, as E_{therm} exceeds ΔE_{mag}, the system enters the superparamagnetic state. The temperature at which this transition takes place is the *blocking temperature* T_{B}. This can be interpreted as the equivalent to T_{C} in ferro- or ferrimagnets in the means, that the magnetic material transitions into a dynamic, unstable, (super)paramagnetic state, caused by thermal energy (see also Section II.1.2.2). While the superparamagnet is in this dynamic state, thermal fluctuations lead to random flips of the magnetic dipole and prevent the ensemble of MNPs from aligning their magnetic moments.
Equation II.1.5 also demonstrates the dependency of T_{B} on the particle size: the larger an MNP, the higher the energy barrier ΔE_{mag} will become. Thus, more thermal energy – meaning a higher temperature – is necessary to enter the superparamagnetic state (see also Figure II.1.8 B).
While T is below T_{B}, the aforementioned random flips of the magnetic dipole moments come to a halt and are, figuratively, *frozen* in place. In this blocked state, an MNP will behave comparably to a ferromagnet – the thermal energy is not sufficient anymore for magnetic dipole moments to flip spontaneously. Therefore, the material displays hysteresis, demonstrated by the non-zero M_{R} and H_{C}.
Another critical factor for observing superparamagnetism is the time scale at which the system is analysed. The time τ that magnetic dipole moments in MNPs need for flipping is defined by the Néel-Brown relation:[20]

$$\tau = \tau_0 \, exp\left(\frac{\Delta E_{\text{mag}}}{E_{\text{therm}}}\right). \tag{II.1.6}$$

Here, τ_0 is a material-specific time, also referred to as *attempt frequency*, and represents the frequency with which a system will attempt to switch its magnetic moment.

However, the actual transition will nevertheless depend on the energy barrier in the exponent. Generally, τ_0 has a value between 10^{-9} and $10^{-8}\,\mathrm{s}^{-1}$. ΔE_{mag} and E_{therm} are defined in Equation II.1.4 and II.1.5 respectively. τ is the relaxation time of the particle's magnetic moment, also called *Néel relaxation time*. When measuring superparamagnetic materials, it is important to keep the relaxation time in mind, since the experimental parameters, *e.g.* the frequency in a VSM (see also Excursion 1), determines the magnetic state that will be observed. If τ is shorter than the experimental time scales, the system will be in its superparamagnetic state. Otherwise, the system will be blocked since the magnetic moment lags behind the measurement parameters and, therefore, appears stable. The temperature at which both τ and the measurement time are equal is another definition for T_{B}.[20]
Conclusively, superparamagnetism occurs only under specific conditions. The bulk material needs to be ferro- or ferrimagnetic, with its size reduced to a certain critical size at which single-domain MNPs are formed. Plus, the temperature must be above the blocking temperature T_{B}, and the measurement's observation time should be longer than the MNP's Néel relaxation time τ.[9,20]

II.1.3.2 Magnetic Hyperthermia

In general, an astonishing aspect of superparamagnetism and MNPs is their ability to translate the energy from magnetic fields into thermal energy. This is achieved via *magnetic displacement* that induces *magnetic hyperthermia*.[7] This heat dissipation can only be triggered when superparamagnetic MNPs are subjected to an *alternating magnetic field* (AMF), with frequencies in the *radio frequency* (RF) range.*
The energy difference ΔU that is introduced into the MNP system by the AMF is related to the area within its hysteresis curve:

$$\Delta U = -\mu_0 \oint M dH. \tag{II.1.7}$$

Rephrasing the magnetisation M with Equation II.1.2 and expanding χ to its complex variant $\chi = \chi' - i\chi''$ results in an expression for the dissipated power P.

*Radio frequencies are usually between 30 kHz and 300 MHz. However, frequencies needed for magnetic hyperthermia are particle-dependent and can differ greatly with particles of different size, shape, or material.

$$P = f \cdot \Delta U = \mu_0 \pi \chi''(f) f H_0^2, \tag{II.1.8}$$

where f is the cyclic frequency of the external field and χ'' is the out-of-phase component of χ, which is dependent on f.[21] Hence, the dissipated heat reaches a maximum when the particle resonates with the AMF. As an example, magnetite MNPs can dissipate between $85\,\mathrm{W\,g^{-1}}$ and up to $\sim$$150\,\mathrm{W\,g^{-1}}$, depending on the particle size and the frequency of the applied AMF.[22,23]

II.1.3.3 Current Advances in Nanomagnetism

Besides the biophysical research on *magnetogenetics* – that will be discussed in great detail in Section II.3.3 –, other research fields use the magnetism of nanoscale materials. As a result of this, synthesis routes and applications for novel materials and the phenomena behind them are of high interest.
Besides the widely applied MNPs based on ferrites (Fe_2O_3, Fe_3O_4), researchers are always looking to overcome existing limits. Iron carbides, such as FeC_3 or Fe_5C_2, are explored as a base material for magnetic nanostructures. These compounds are more stable against heat and chemicals than ferrites and can exhibit higher saturation magnetisations – with maximal values up to 50 % above that of magnetite nanoparticles.[24,25]
Another recently debated subject is *two-dimensional magnetism*. This phenomenon occurs in atomically thin layers of material with suitable magnetic attributes. The most prominent property of these materials is the long-ranged magnetic interaction. In contrast to bulk magnets, where the three-dimensionality of the grain boundaries disrupt magnetic interactions over long ranges, the two-dimensional 'monolayer of magnetic moments' can exhibit ordered magnetism, such as ferro- or antiferromagnetism, over longer ranges. They are interesting for their sustainable generation of magnetic materials and might be used for data storage and quantum computing.[26–28]
Furthermore, *skyrmions* are of major interest in current research for innovative techniques to store data. Skyrmions are highly complex alignments of magnetic spins inside a material that give rise to a swirling magnetisation structure with sizes comparable to nanoparticles. These spin alignments are surprisingly stable, even have particle-like properties and can be trapped inside confined spaces.[29] Due to their

extremely small size, stability, and the fact that they can be manipulated with less energy than conventional magnetic domains on hard drives, they are a promising concept for future data storage devices.[30]

II.2 Cellular Signalling

What electrons are to magnetism, cellular signalling is to organisms. In order to react and adapt to internal signals, environmental changes, or stimuli in general, cells have developed complex signalling pathways. One key element of these pathways are membrane-bound receptors, that transmit information from the environment to the cell. With this vital role at the interface between a cell and its surroundings, malfunctions of receptors and, hence, signalling can have severe consequences. Cancer,[31–33] Alzheimer's disease,[33,34] Parkinson's,[35] and diabetes[36] are just a few examples for diseases that are closely related to defective signalling.
The following chapters outline signalling pathways that are relevant to this work.

II.2.1 Iron Homeostasis

Iron (Fe) serves as an important trace element in most living organisms. Thanks to its ability to easily accept and donate electrons, it is majorly involved in many elemental processes of life, such as oxygen transport as a crucial component of heme,[37] DNA synthesis, N_2 fixation, and photosynthesis.[38] However, the native element Fe^0 is neither available nor suitable for these applications. Hence, life adapted to iron in its ferrous (Fe^{2+}) or ferric (Fe^{3+}) state. In general, ferrous iron is more soluble than its oxidised counterpart and, therefore, readily available for the host. If not controlled, iron can be highly toxic. In the presence of *hydrogen peroxide* (H_2O_2), a common byproduct of a cell's life cycle,[39] ferrous iron can undergo Fenton's reaction:[40,41]

$$Fe^{2+} + H_2O_2 + H^+ \longrightarrow Fe^{3+} + H_2O + HO^\bullet \tag{II.2.1}$$

One product of this reaction is $HO^\bullet$, a *reactive oxygen species* (ROS) that is highly reactive and thus toxic for organisms.[42] Therefore, maintaining iron homeostasis precisely is crucial for proliferation and survival.[37]

Transferrin Receptor 1 In order to allow efficient iron uptake into cells in the human body, the circulating protein *transferrin* (Tf) is produced and secreted mainly by hepatocytes inside the liver. Tf can bind up to two ferric iron atoms in the plasma. The excess secretion of Tf allows for safe delivery of iron to points where it is needed. Thus, the coupling of ferric iron to Tf suppresses the formation of ROS.[38] Cell internalisation of diferric Tf is mediated by the membrane-bound *transferrin receptor* family (TfR). The most abundant member of the TfR family is TfR1, also known as *cluster of differentiation 71* (CD71), which is expressed at low levels in most human cells.[43] Expression of TfR1, and thus uptake into the cell, is regulated by intracellular iron levels. Elevated expression levels of TfR1 have been assigned to highly proliferating cells (such as epidermal cells) and cells with high needs for iron, such as placental trophoblasts that supply the fetus with blood.[44] Due to their high demand, TfR1 is also over-expressed on various cancerous cells and has even been identified as a universal marker for cancer cells.[45,46]
Apart from Tf, TfR1 was also shown to bind the iron storage protein *ferritin* and to internalise it. This uptake is achieved by clathrin-mediated endocytosis, which delivers ferritin into endosomes and lysosomes.[47] The protein ferritin will be discussed in more detail in Section II.3.2.4.

II.2.2 Apoptosis – Programmed Cell Death

Just as iron homeostasis maintains health and proliferation in the different life cycles of a single cell, cell death is essential to ensure the well-being of multicellular organisms. While various forms of injury- or disease-related cell death processes exist (such as necrosis or pyroptosis), *apoptosis* is the most natural form. Apoptosis is a genetically programmed cellular suicide that is meant to regulate the number of cells and remove excess or old cells.[48] As apoptotic cells undergo an intentional process, the dying mechanism is highly structured. It leads to the partitioning of cells into vesicles enclosed by parts of the cell's plasma membrane. This formation of protrusions is also referred to as *blebbing*. The formed vesicles prevent intracellular, potentially harmful material from affecting surrounding cells and instead ready this cellular waste for the digestive machinery.[49]
As described, programmed cell death is an essential process in multicellular organisms. Hence, malfunctions in the fine-tuning of apoptosis can lead to severe disease. While overshooting apoptosis is, for example, linked to neurodegenerative diseases

Excursion 3: Cell Surface Receptors

Cells receive messages and information from the outside using *cell surface receptors*. Most of these membrane-bound proteins are activated upon coupling to extracellular molecules, referred to as *ligands*. Receptors can be activated either passively by recognition of diffusing molecules or actively by signal transduction from membrane proteins on effector cells.
Depending on their functionality, membrane receptors can be categorised into three groups: (1) *ion channel linked receptors* are mainly employed by neurons, (2) *G protein-coupled receptors* activate further membrane-bound receptors using a mediator protein, and (3) *enzyme linked receptors* are either enzymatically active or activate an enzyme upon ligand coupling.[50] Receptors utilised in this work are part of group 3.

The basic structure of an enzyme-linked receptor is shown in Figure II.2.1. The ligand binds to its receptor at the extracellular domain with high specificity and activates it. Once the receptor is activated, the intracellular domain will initiate signalling.

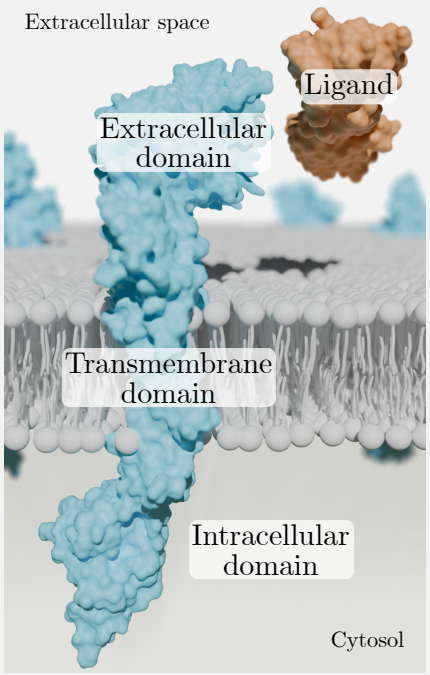

Figure II.2.1: Exemplary structure of an enzyme-linked membrane receptor, with the ligand-binding extracellular domain, the transmembrane domain and the enzymatic intracellular domain that initiates signal transduction.

such as Alzheimer's or Parkinson's,[51] insufficient apoptosis can lead to excessive cell proliferation, tumours, and, thus, cancer.[52]

Death Receptor – Cluster of Differentiation 95 The activation of apoptosis is mediated by members of the family of *tumour necrosis factor receptors* (TNF-R). Signalling is majorly transduced by the TNF-R *cluster of differentiation 95* (CD95,

also known as Fas or Apo-1). The receptor comprises two distinct domains: (1) the extracellular domain contains three *cysteine-rich domains* (CRD) that are responsible for ligand binding and (2) the intracellular domain which initiates the apoptotic signal and is thus also called *death domain* (DD).[49] CD95 without its death domain was shown to lack the ability to induce apoptosis.[53]
Naturally, CD95 is activated by cytotoxic T lymphocytes (*killer cells*) that express the trimeric *CD95 ligand* (CD95L).[49] Apart from its transmembrane receptor format, the extracellular domain of human CD95L can also be cleaved from the membrane and induce apoptosis as soluble CD95L.[54] It must be noted that the exact mechanism of CD95-mediated cell signalling is under debate to this date.[53,55–57] However, the common denominator is the formation of an oligomeric structure of multiple CD95 receptors triggered by CD95L. Only through this accumulation can apoptosis eventually be triggered.

II.3 Nanotechnology

In the late 1950s, the American physicist Richard Feynman held a talk that would initiate a whole new field of research. In his lecture, he stated that *there is plenty of room at the bottom*, meaning there is great potential in materials at small scales by manipulating single atoms and molecules.[58] This inspirational talk is nowadays regarded as the start signal of a new area of research: *nanotechnology*. The term is derived from the Greek word *nános*, meaning *dwarf*. The prefix *nano-* was first introduced as the billionth (10^{-9}) of a unit and further found its way into descriptions of all sorts of very little things.[59]
The fundamental idea of nanotechnology – that Feynman also addressed – is the drastic size reduction of conventional technology to manipulations at molecular or even atomic scales. Nanotechnology can, therefore, be seen as the link between bulk materials and single atoms and molecules. The size reduction frees an immense amount of space and opens new applications and properties of materials that are not comparable to their bulk variants.
Nanotechnology describes the application of materials that are within the nanoscale ($< 100\,\mathrm{nm}$) in at least one dimension. This includes coated surfaces (so-called *two-dimensional* nanomaterials), nanorods or -tubes (*one-dimensional*), or nanoparticles (*zero-dimensional*).[60]

The differences between nanomaterials and their bulky relatives are caused by several effects that come with the immense shrinkage of the material. This work is focused on zero-dimensional nanoparticles (NPs). Hence, the following chapters will concentrate on their properties and behaviours.

II.3.1 Nanoparticles

Due to the small number of atoms in a single NP, the ratio between surface and bulk atoms strongly shifts towards surface atoms. Consequently, dispersed NPs have a significantly higher volume-to-mass ratio than bulk materials. Additionally, more atoms are available for interactions with the environment. At the same time, surface atoms have fewer direct neighbours, leading to lower binding energy of single atoms to their corresponding NP. In summary, this highly increases the reactivity of nanoscale materials to the point where agglomeration can be more favourable for NPs than staying dispersed. Through agglomeration, NPs can reduce the number of high-energy surface atoms.[61]

As indicated, NPs are most commonly dispersed in (aqueous) solutions. The stability of such a *colloidal solution* can be described by the *Derjaguin-Landau-Verwey-Overbeek* (DLVO) theory. This theory combines several descriptions of particle interactions that occur when two particles are dispersed in a solvent. In general, the stability of a colloidal solution depends on the combined interaction energy between two particles V_T:

$$V_\mathrm{T} = V_\mathrm{A} + V_\mathrm{R} + V_\mathrm{S}, \tag{II.3.1}$$

with the attractive forces between single particles V_A, the repulsive forces caused by the electrical bilayer around the particle V_R (see Excursion 4), and the energy related to the specific solvent V_S. Since V_A and V_R are not only much stronger than V_S but also reach significantly further, V_S is commonly neglected in considerations of the colloidal stability.[62]

Attractive forces are mainly caused be van der Waals interactions and depend, among others, on the particles' structure. For two identical particles, V_A can be described as:

$$V_\mathrm{A} = -\frac{A \cdot r}{12D}, \tag{II.3.2}$$

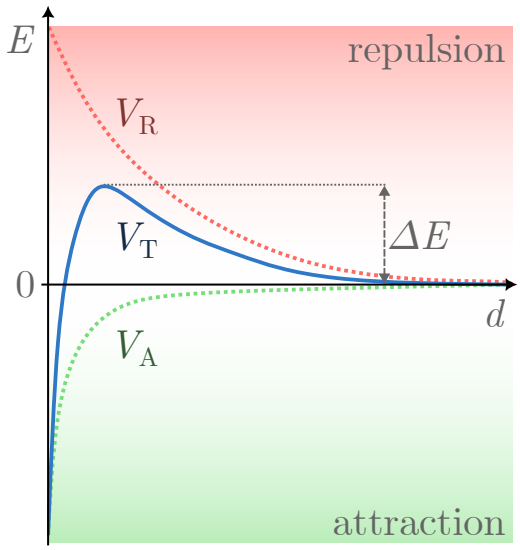

Figure II.3.1: Interaction energy E between two colloidal particles depending on their distance d. The combined total energy V_T consists of the repulsive forces V_R and the attractive forces V_A. The energy barrier ΔE prevents the particles from agglomerating.

with the particle radius r, distance D, and the Hamaker constant A, a material and solvent-dependent constant specific for van der Waals interactions. As shown in Equation II.3.2, V_A falls off rapidly with increasing distance with $\frac{1}{12D}$ but is highly attractive at short distances. Accordingly, V_R can be related to:

$$V_R \propto r \cdot \zeta^2 \cdot e^{-D}, \tag{II.3.3}$$

with the ζ potential (see Excursion 4), that mainly drives V_R due to electrostatic repulsion of the solvation shell's electric bilayer.

The linear DLVO theory assumes that V_A and V_R are additive, leading to the description of the interaction energy between two particles V_T in Equation II.3.1. The interaction energy, together with its components V_A and V_R, is displayed in Figure II.3.1.

If two colloidal particles are at an infinite distance, no attractive or repulsive forces are acting on them. Upon approach, V_R will dominate the interaction and the energy barrier ΔE prevents the particles from agglomerating – the colloidal solution is stable.

However, if the particles' energy exceeds ΔE, V_A will cause agglomeration and can lead to particle sedimentation. Factors that can influence the tendency of colloidal

systems to agglomerate are *e.g.* (1) the temperature, since increasing the thermal energy $k_\mathrm{B}T$ will allow the particles to pass ΔE, (2) alterations to the ionic strength or pH of the system can lower V_R and, consequently, ΔE or (3) magnetic forces between the particles that strengthen V_A and thus also lower ΔE.[63]

Excursion 4: ζ Potential

A helpful indicator of the colloidal stability of NPs is the ζ *potential* (see Figure II.3.2). In the demonstrated example, a negatively charged NP in solution will attract positively charged ionic species (salt ions, H_3O^+, etc.) that form a dense, positively charged layer – the *Stern layer*. The potential at the edge of this layer is the *Stern potential*. Beyond this edge, the negative surface charge of the NP is shielded by the Stern layer, which will, in turn, attract counterions. Hence, in the outer plane, anionic species (Cl^- ions, OH^-, etc.) will accumulate. At a certain distance from the NP surface, attractive forces will become too weak for the ions to be attracted to the NP. Instead, they will start to *slip* away from the surroundings of the NP and lose all interactions with it. At this point, the *slipping plane* is reached. The potential that remains at the edge of the slipping plane is the ζ potential; the diameter of NP with the slipping plane is called *hydrodynamic diameter* D_H.

Generally, the ζ potential of NPs lies within -100 to 100 mV. The higher the absolute value of the potential, the stronger the repulsive forces between single NPs, leading to higher colloidal stability.[64]

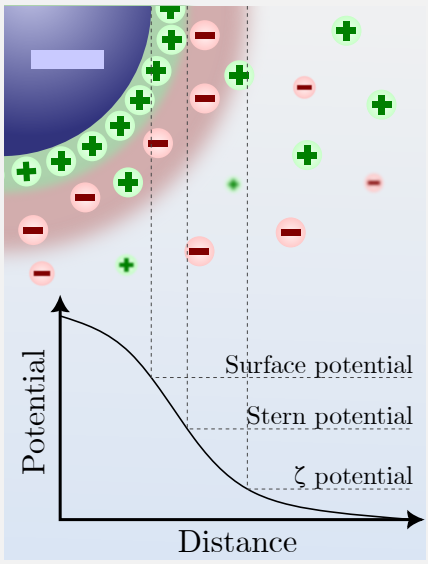

Figure II.3.2: Schematic description of the ζ potential of a negatively charged nanoparticle (blue). Through interaction with anions (red) and cations (green), it will exhibit surface, Stern and ζ potential at different distances from its surface.

Another method for altering interparticle interactions is the addition of polymers to the particles' surface. Polymers can either introduce attractive or repulsive forces.[65] One commonly used polymer is polyethylene glycol (PEG), a polyether with the general chemical formula of $H-(O-CH_2-CH_2)_n-OH$. Due to the introduced hydroxy and ether groups, PEG not only increases a particle's solubility in water, but it also significantly increases repulsive forces between particles. It can thus serve as an effective tool to improve the colloidal stability of an NP solution.[66]

II.3.2 Nanobiotechnology

For millennia, biology and medical research relied on observations in the *macroscale*. However, with the invention of the first microscope at the end of the 16$^{\text{th}}$ century by Zacharias and Hans Janssen,[2] it steadily became apparent that life's building blocks are working on much smaller scales. The discovery of cells led to the discovery of cell compartments and, finally, to the first description of proteins, membranes, and DNA – all of which are structures with sizes of several nanometres.[67] Hence, while Feynman dreamed about creating artificial cells rather than studying them,[58] nanotechnology was destined all along to be merged into biological research and technology.

Molecular biology has applied nanomaterials for decades in the form of proteins and other biomolecules, but with the rise of nanotechnology, new fields of research opened up: (1) the application of nanomaterials, such as nanoparticles, to investigate biological processes and better understand them and (2) the transfer of knowledge about nature's strategies to create novel, bio-inspired nanomaterials and -machines. This work is settled at the interface between those two disciplines – it applies semisynthetic, bio-inspired *ferritin nanoparticles* as a toolkit for investigations on cellular, nanoscopic mechanisms. The critical components of the employed nanomaterials will thus be introduced in the following chapters.

II.3.2.1 Green Fluorescent Protein GFP

The history of the *green fluorescent protein* (GFP) can easily be regarded as the most important story of (nano)biotechnology. The basis for its development is proteins from fluorescent animals that have been known and described for thousands of years. The first breakthroughs unravelling the molecular mechanisms behind GFP's

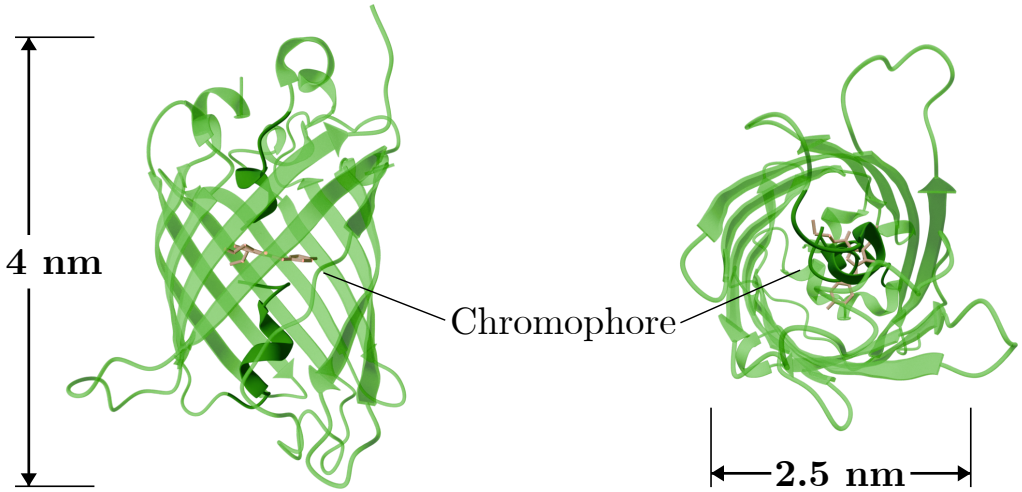

Figure II.3.3: Characteristic barrel-like tertiary structure (see Excursion 5) of GFP from front and top. Within the central α helix (dark green), the amino acids serine, tyrosine, and glycine at positions 65, 66, and 67, respectively, form GFP's chromophore, an aromatic hydrocarbon molecule (grey).[71]

fluorescence were made in the 1960s.[68] The modern usage of GFP started with the first isolation of the complete *gfp* gene from the jellyfish *Aequorea victoria* in 1992.[69] GFP was able to conquer molecular biology and become an indispensable tool because of its simplicity. By genetic engineering, a technique that was established in the early 1980s,[70] it was now possible to use GFP to make another protein fluorescent. This was achieved by genetically fusing *gfp* to the target protein and, subsequently, expressing this fusion construct in a target organism (for more details on genetic engineering, see also Excursion 7). The development of this technique revolutionised life sciences by allowing real-time observations of proteins in living cells via fluorescence microscopy without the need for preliminary – potentially harmful – labelling.

GFP's functionality is closely related to its structure (see also Excursion 5). While most proteins fold into amorphous, indistinguishable shapes at first glance, the structure of GFP is both perfectly adapted to its purpose and unique. The protein forms a characteristic barrel out of β sheets that covers the central α helix (see Figure II.3.3). The top and bottom are sealed with additional short peptide sequences, shielding the centre from environmental influences such as solvents. During the folding reaction of GFP, three amino acids in the central α helix (serine, tyrosine, and glycine) rearrange covalently to give rise to GFP's core: the *chromophore*, an aromatic hydro-

carbon. Without this chromophore, GFP is not fluorescent, but the chromophore is also not fluorescent without the protein shield. Thus, correct folding into the exact structure is of utmost importance for GFP.[71] This all gives rise to a fluorophore that absorbs light with peaks at 395 and 475 nm and emits light at a peak of 507 nm.[72] Natural GFP was an astonishing subject at the time; however, scientific demands quickly outgrew its capabilities. The molecular brightness of the fluorophore was too dim, photostability was too low, and the two absorption peaks were inconvenient,

Excursion 5: General Structure of Proteins

The basic building unit of proteins is amino acids, of which humans use 21. The structure of a protein is fundamentally connected to its functionality. Thus, the slightest structural deviation can have severe consequences on the protein and its host.

The *primary structure* is defined by the sequence of amino acids of a protein and forms its backbone. Depending on the last atoms of the exposed amino group, the two ends of the backbone are referred to as *N-terminus* or *C-terminus*. Interactions between amino acids – such as hydrogen bonds – form the *secondary structure*. Generally, it consists of α helices or β sheets. In the *tertiary structure*, additional interactions give rise to the protein's final structure. Polymeric proteins – such as ferritin – are combinations of multiple subunits that form a *quaternary structure*.

As indicated, mutations – additions, deletions, or replacements – of a protein's primary structure can have decisive consequences on its functionality. Structural changes can be beneficial and enhance the protein's performance, but they can also cause it to lose functionality or even become harmful.[73]

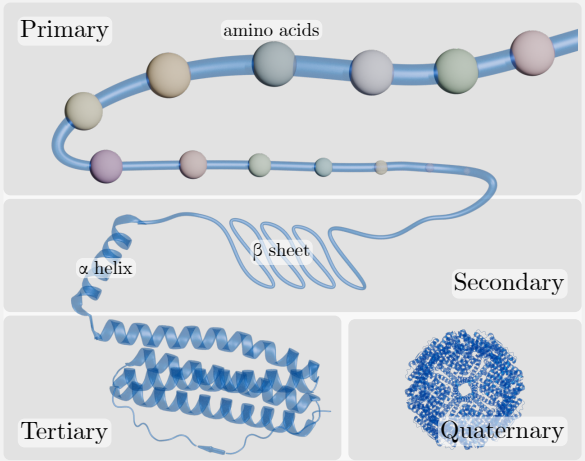

Figure II.3.4: The four dimensions of a protein's structure.

mainly since the absorbance at ∼475 nm was weaker than the second peak at 395 nm. Plus, wild-type GFP tends to form dimers and is lowly expressed in higher eukaryotes.[74]

In 1994, mutation studies addressed these issues that resulted in a more stable and brighter variant of GFP that only displayed one absorption peak at 475 nm.[75] To increase expression efficiencies, the codons of *gfp* were optimised to match higher eukaryotes. All these modifications resulted in the variant named *enhanced* GFP (EGFP).[76] In EGFP, the chromophore's serine at position 65 was replaced by threonine and phenylalanine at position 64 was replaced by leucine. Implementation of these mutations promoted the formation of the chromophore and, thus, accomplished the improvements mentioned above.[74]

Unfortunately, EGFP still tended to form dimers. This issue was attacked in 2002 by another point mutation that suppressed the coupling of two GFP monomers by replacing the hydrophobic alanine at position 206 with a positively charged lysine. This prevented hydrophobic interactions and, consequently, the formation of dimeric GFP. The resulting variant was named *monomeric* EGFP (mEGFP).[77]

The history of GFP culminated in 2008 when the Nobel Prize for Chemistry was awarded for the development and optimisation of this first scientifically used fluorescent protein.[78] Multiple fluorescent proteins of different colours emerged from the work with GFP. Some were derived directly from GFP by specific mutations,[79] while others – such as the red fluorophore *mCherry*[80] – were found in different organisms. Despite their different colours and origins, all fluorescent proteins share the barrel-like structure that is the hallmark of GFP.

II.3.2.2 Immunoglobulins

Whenever a potentially harmful invader (a *pathogen*) enters a human – or more generally, a vertebrate –, its immune system wields powerful defence mechanisms that are able to adapt to almost everything, be it bacteria, viruses, fungi, parasites, or other pathogens.[81] During an invasion, the *adaptive immune system* is responding to the attacker by producing *immunoglobulins*, also known as *antibodies* (Ab). An Ab is designed to specifically bind to a certain molecular pattern on the pathogen, the so-called *antibody generator* (antigen). Upon contact with the pathogen, Abs will cover the invader (*opsonisation*), block its interactions with the host, and pin it down until it can be destroyed by killer cells. The immense flexibility of Abs is

achieved via a process called *somatic hypermutation* in which antibody genes are spliced and rearranged. Different combinations during this process give rise to at least 10^{11} unique antibodies per organism.[82]

Thinking of antibodies brings their characteristic, widely known Y shape to mind. This structure, however, only represents one subclass of human antibodies: the *immunoglobulin G* (IgG). Other subclasses are IgA, IgD, IgE, and IgM, but IgG is the most abundant variant. Additionally, IgGs are commonly used for scientific and medical applications.

The structure of an IgG is shown in Figure II.3.5. Its backbone consists of two identical *heavy chains* (HC, ∼50 kDa) that are connected at a central hinge region via disulfide bridges. This backbone is referred to as the *fragment crystallisable* (Fc)

Excursion 6: Dissociation Constant K_D

In biotechnology, many binding processes between two species, A and B, are non-covalent, leading to both forward and reverse coupling reactions happening simultaneously:

$$x\mathrm{A} + y\mathrm{B} \rightleftharpoons \mathrm{A}_x\mathrm{B}_y \tag{II.3.4}$$

Under this condition, an equilibrium will form in which reaction rates for forward and reverse reactions will be balanced, leading to a net reaction rate of 0. In this equilibrium, the *dissociation constant* (K_D) can be determined to quantify the binding properties between A and B. Assuming monovalent binding, where $x = y = 1$ – as it is often used for binding of *e.g.* antibody to antigen or receptor to ligand – the K_D value can be determined by:

$$K_D = \frac{[\mathrm{A}] \cdot [\mathrm{B}]}{[\mathrm{AB}]}, \tag{II.3.5}$$

where [A] represents the concentration of A in equilibrium ([B] and [AB] accordingly). The K_D value also corresponds to the concentration of A at which 50 % of A is bound to B at excess concentrations of B.[83] Hence, the smaller the K_D, the more of AB will form in equilibrium and the stronger the bonding between A and B. Indeed, it has been shown that K_D is related to the physical binding strength between A and B.[84] For antibody–antigen bonding, K_D values typically lie in the range of 10^{-5} to 10^{-10} M.[83]

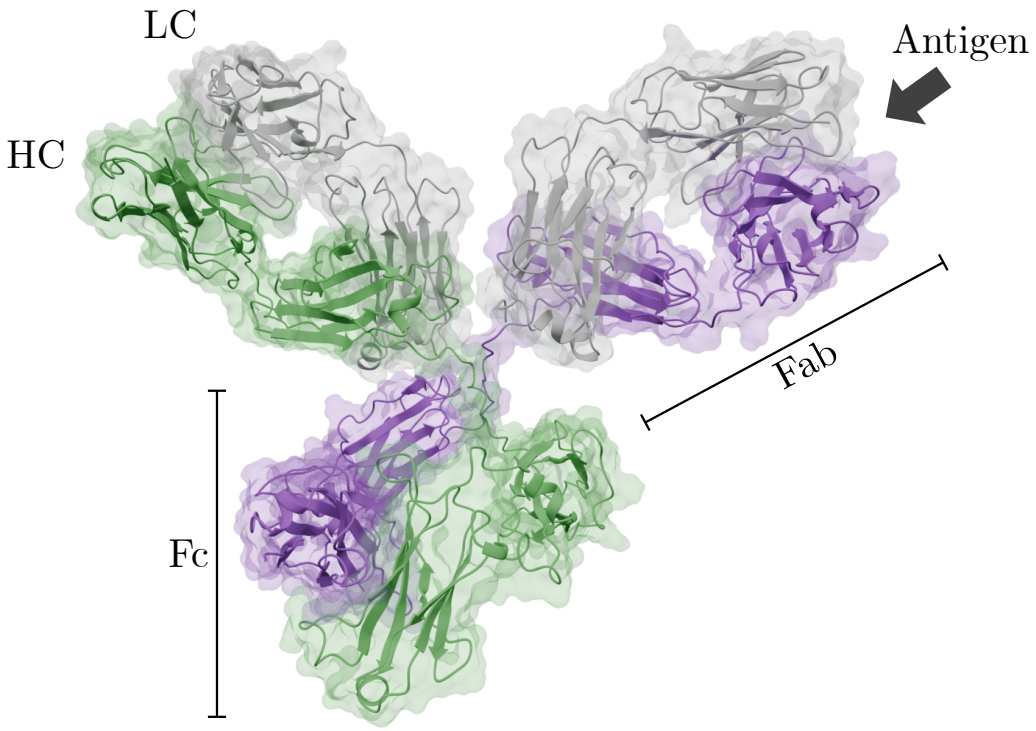

Figure II.3.5: Structure of an IgG antibody, with its typical Y shape. The antibody consists of two identical heavy chains (HC, for visibility coloured in green and purple) and two identical light chains (LC, grey). The two fragment antigen binding (Fab) regions (one HC and one LC) form one antigen-binding domain each, whereas the fragment crystallisable (Fc) region (two HCs) serves as the antibody's backbone.

region. At the top part, the two HCs are connected to one *light chain* each (LC, ∼25 kDa), creating two *fragment antigen binding* (Fab) regions.[83]

The axisymmetrical form of an antibody equips it with two separate antigen-binding domains. At the same time, the region around the hinge at the IgG's centre is highly flexible and can unfold to some extent to allow rotation of the binding domains. Thus, one IgG can bind two closely located antigens. This 'double binding' has two advantages. First, it enables the IgGs to interlink multiple pathogens and, therefore, immobilise them efficiently. Secondly, bonding between a multivalent binder (the antibody) and its target (two antigens on *e.g.* one bacterium) is entropically stabilised. This so-called *avidity effect* significantly increases the binding strengths of antibodies to their targets.

The connection between an antibody and its antigen is governed by non-covalent

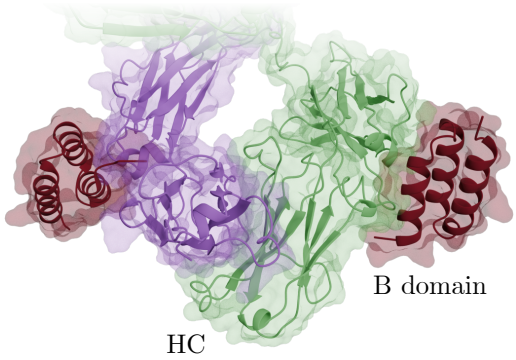

Figure II.3.6: Two isolated B domains of Protein A (red) binding to the *heavy chain* (HC) of an IgG in its Fc region. Due to the symmetrical structure of IgGs, one B domain can bind to one HC each. The complete structure of an IgG is shown in Figure II.3.5.

bondings. Namely, these are ionic or hydrophobic interactions, van der Waals forces, or hydrogen bonds.[83]

Besides medical applications, modern life sciences cannot imagine research without Abs. Due to their flexibility, Abs, in general, and IgGs, in particular, are commonly applied in all sorts of experiments for mediating the targeting of functional molecules, such as fluorescent dyes, to molecules of interest. Generally, Abs are used to locate or identify targets and can even be used within living cells and organisms.[83]

II.3.2.3 Protein A

Section II.3.2.2 described the beneficial binding properties of human antibodies and their impact on biotechnology. However, while Fab domains easily and strongly bind to their specific target, how is it possible to use antibodies to deliver *e.g.* NPs to a specific destination?

For this, it would be necessary to couple the Ab to the surface of the NP while leaving the Fab region free. This would basically 'turn around' the Ab's initial purpose. Luckily – or, depending on the perspective, unfortunately –, Nature has yet again developed a molecule that is capable of doing exactly that: grab an antibody at its rear, turn it around, and prevent it from fulfilling its original purpose. This molecule is *Protein A* (SpA) from *Staphylococcus aureus*.

SpA is found either anchored to the membrane of *S. aureus* or secreted in its soluble form. The protein is specifically binding to the Fc region of various types of Abs.[85–87] By doing so, SpA can deactivate Abs and thus circumvent parts of the host's immune

Excursion 7: Plasmids for Genetic Engineering

The powerhouse of genetic engineering is *plasmids* (or *vectors*), short, circular DNA strands that carry the genetic code of a protein of interest. In order to express foreign proteins in a cell or organism, plasmids containing the specific gene need to be transferred into the host. Here, according to the *central dogma of molecular biology*, the DNA will be transcribed to RNA and ultimately to the protein of interest. Generally, the transfer of plasmids into a bacterium or yeast is referred to as *transformation*, while genetically altering eukaryotic cells is named *transfection*.

Plasmids need to be equipped with specific sequences to ensure functionality. The expression of a fusion construct, *e.g.* to label a protein with GFP (see Section II.3.2.1), can be achieved by binding both genes directly next to each other at the specific location in the plasmid (see Figure II.3.7). Depending on the positioning, the labelling protein will either be added *N-terminally* or *C-terminally* (see also Excursion 5).[88]

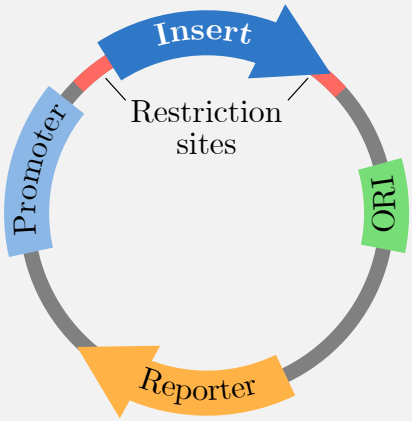

Figure II.3.7: Basic scheme of a plasmid. The arrows indicate the reading direction. The gene of interest (*insert*) is cloned between two restriction sites downstream of ('after') the *promoter*. Upon induction with a suitable molecule, the promoter will activate transcription and, thus, protein expression. An additional *reporter gene* (such as resistance against specific antibiotics) can help to select transformed cells. The *origin of replication* (ORI) is necessary for replication of the plasmid but is mostly relevant to genetic work with bacteria.

system.[89] The protein consists of five Ab binding domains (A, B, C, D, and E), each ∼58 amino acids long.[90] Each of these domains is made up of three α helices and is capable of individually binding to one HC of an Fc region (see Figure II.3.6).

In order to make SpA more accessible for biotechnology, efforts were made to isolate single domains to create a minimised Ab-binding protein.[91,92] Based on the B domain, a modified binding domain was created – the so-called Z domain. With the introduction of point mutations, the Z domain was designed to be more stable against various reducing and cleaving agents.[91] Its binding properties towards the

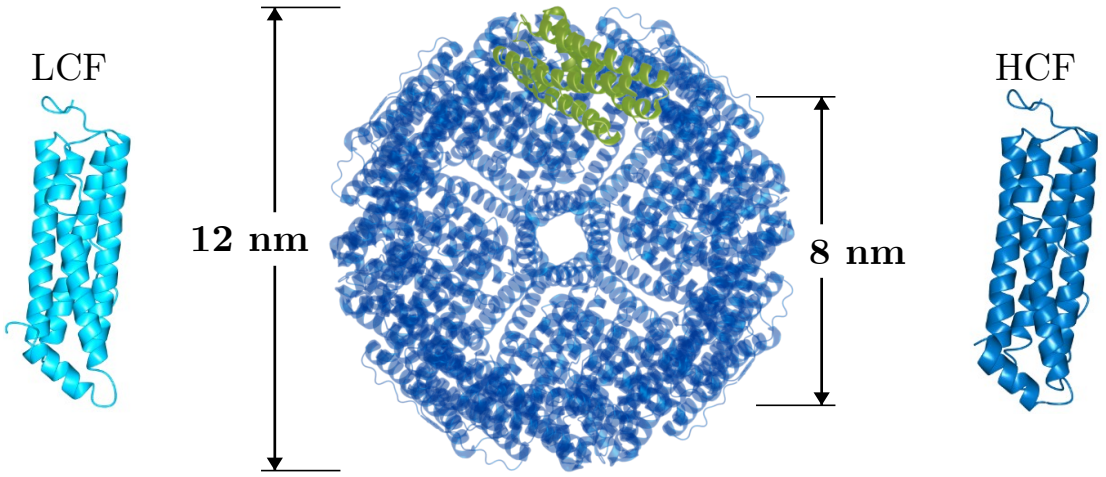

Figure II.3.8: Human ferritin in its 24-mer cage form, viewed at one of its six four-fold channels (centre) with its two subunits *light chain ferritin* (LCF) and *heavy chain ferritin* (HCF). The cage has an outer diameter of 12 nm and a diameter of the inner cavity of 8 nm. The position and orientation of a single subunit are highlighted in green.

Fc of human IgG1, represented by the K_D value (see Excursion 6), were measured to be ∼60 nM.[93] By genetically fusing the respective gene for the Z domain to a protein, it is possible to enable oriented Ab binding to the proteins surface.[94]

II.3.2.4 Fundamentals of Ferritin

One major protagonist in iron homeostasis (see also Section II.2.1) is the *ferritin* family. Ferritins are a class of proteins that exist in almost all branches of life. All ferritins share one distinct feature: they are spherical, self-assembling, polymeric protein complexes or cages. With their cage's inner cavity, ferritins serve as storage space for excess iron.[95] The diameter of the ferritin family ranges from 8 to 12 nm.[96–98]

Over the last years, *human ferritin* (Ft) has gained a lot of attention for its simplistic approach to creating multi-functional NPs. Ft cages are made up of two different subunits. While nowadays, they are commonly referred to as *heavy chain ferritin* (HCF) and *light chain ferritin* (LCF), historically, they have been named after the organ they were first discovered in – LCF was purified from liver tissue, while HCF was found in the heart. Coincidentally, LCF (19 kDa) was found to be a bit lighter than HCF (21 kDa), leading to the common reference as light and heavy chain.[98]

As shown in Figure II.3.8, LCF and HCF are structurally similar, both forming a

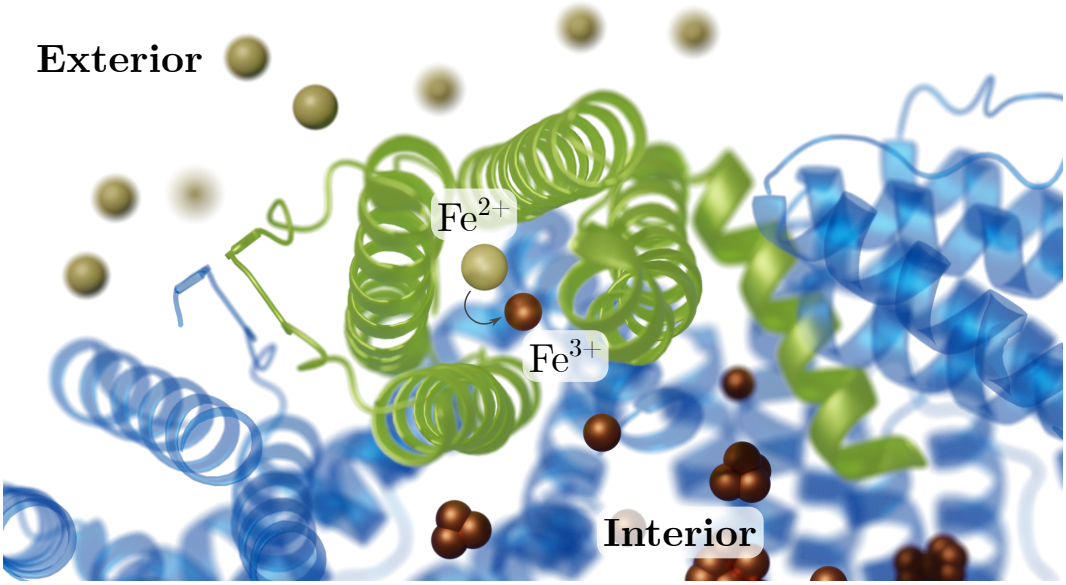

Figure II.3.9: Ferroxidase domain (marked in green) of heavy chain ferritin assembled in a 24-meric ferritin cage. Fe^{2+} ions (light brown) are oxidised to Fe^{3+} (dark brown), which in turn sediment and form ferritin's core in its interior.

bundle of four α helices. The most profound difference between the two subunits is a ferroxidase domain located within the α helices of HCF (see Figure II.3.9).[99] Here, ferrous iron is oxidised to ferric iron. Due to the drop in solubility caused by this oxidation, ferric iron ions will start to sediment within the cage and, hence, form ferritin's core. Although HCF is equipped with a ferroxidase domain and core formation rates are highly increased, cages containing LCF were shown to form both larger and more homogeneous iron oxide cores.[100]

Ferritin's subunits spontaneously form the 24-meric Ft cage with a diameter of 12 nm and an inner cavity of 8 nm (see Figure II.3.8) with enough room for up to 4500 iron atoms.[98] Ft cages display a 4-3-2 symmetry and, hence, give rise to eight 3-fold, six 4-fold, and twelve 2-fold channels (see Figure II.3.8).[95] Most prominently, the hydrophilic 3-fold channels are responsible for the internalisation of Fe^{2+}. From there, the ions are forwarded to the ferroxidase domain in HCF.[101,102]

Naturally, Ft's core consists of the ferric oxy-hydroxide *ferrihydrite*. It needs to be noted that the exact structure and composition of this compound, which was only recently discovered, is still under discussion.[103,104] However, it was shown to have para- and superparamagnetic properties in ferritin at temperatures above 12 K.[105]

II.3.3 Magnetogenetics

The relevance of cellular signalling pathways was elucidated in Section II.2. Also, it was discussed that these pathways can be fragile, and defects can have severe consequences for the organism's health and survival.[1] To this day, insights into a myriad of signalling pathways are scarce, and mechanisms are hardly understood. The lack of appropriate methods for observation and control on sub-cellular levels mainly accounts for these deficits. However, in order to shed light on these pathways and their ramifications, precise control over activation and deactivation, concentration thresholds, and structural deformations is essential. In the last decades, various techniques have been developed that apply chemistry, light, or other physical stimuli to gain control of cellular signalling. One promising method was brought to attention about two decades ago and will be introduced in the following chapter.

II.3.3.1 The Origins of Magnetogenetics

As described above, demands for coordinated and effective control over cellular signalling for both scientific as well as medical purposes were high. Generally, methods were needed to activate or inhibit specific proteins within pathways and observe the cell's reaction. To this end, several diverse techniques emerged that utilised different principles. Of course, pharmaceuticals have been applied for thousands of years that are able to affect cell signalling. However, since pharmaceuticals tend to cross-react in a network as complex as cellular signalling, they are often not the matching tool for gaining specific control.

The first attempts to precisely control signalling pathways were made by genetic engineering. Knocking out or artificially overexpressing genes selectively allowed basic studies of the role of specific proteins participating in a certain pathway.[106,107] This methodology was quickly extended by introducing modifications to proteins of interest to introduce *loss-of-function* or *gain-of-function* mutations. This culminated in the introduction of *chemogenetics*. Here, receptors are mutated genetically to implement interactions with small molecules the receptor naturally does not interact with. Essentially, the original ligand of the receptor is replaced with a new, synthetic molecule (for receptors and ligands, see also Excursion 3).

One example of chemogenetics is the use of *receptor activated solely by a synthetic ligand* (RASSL) and *designer receptors exclusively activated by designer drugs*

(DREADD) that are popular tools in neuroscience.[108] It was shown that muscarinic receptors could be engineered to only recognise the synthetic, inert molecule clozapine-*N*-oxide.[109]

In the early 2000s, another toolset was developed that relies not on chemical actuators but on light – it was therefore named *optogenetics*. The major advantage of this technique is that light, in contrast to chemicals, can be guided meticulously to its target location. Thus, control over signalling in single cellular compartments in time scales of milliseconds became possible.[110] Similar to chemogenetics, genetic modifications to the receptor of interest are necessary. More precisely, *opsins*, light-sensitive ion pumps from retinal cells of various animals, have been used to optically induce ion flux across the cell membrane, *e.g.* to turn neurons on and off. The first functional example was given in 2005 with *channelrhodopsin* from green algae *Chlamydomonas reinhardtii* expressed in mammalian neurons. Upon excitation with blue light (450–490 nm), the cation channels opened and, hence, induced neuronal spikes.[3] Soon, more channels responding to different colours were opened up with and for optogenetic applications, including *bacteriorhodopsin* and *halorhodopsin*.[111] After this initiation, the first implementation of optogenetics in living mammals followed. By operationally laying an optical fibre into the brain of freely moving mice, both light-induced activation and observation of neurons expressing channelrhodopsin were enabled.[4]

This experiment, however, highlights some of the critical drawbacks of optogenetics: While specificity and temporal resolution are high, penetration depths are only in the range of a few millimetres since biological tissue strongly absorbs visible light.[112] Thus, it is not possible to target deep tissue *in vivo*, such as deep brain neurons, without implants holding optical fibres. Aside from ethical concerns, animal stress, side effects after the operation, and photodamage during irradiation can influence the experiment's outcome. Additionally, the organism needs to be genetically modified so it is able to express the light-sensitive receptors.[113]

These downsides eventually promoted the development of another technique to tackle and overcome the disadvantages of its predecessors. For this, not light but magnetic fields were applied for the remote activation of cell signalling – *magnetogenetics* was born.

II.3.3.2 Basics of Magnetogenetics

There are two fundamental requirements for the magnetogenetic manipulation of a cell. On the one hand, a suitable magnetic actuator – most commonly an MNP – is needed that is able to interact with the target molecule selectively. On the other hand, an external magnetic field has to be applied that is precisely tailored to the MNP and the experiment. With these two combined, perturbation of a cellular system and specific control over a signalling pathway becomes possible.

Magnetic Nanoparticles An MNP should meet a handful of criteria in order to be suitable for magnetogenetic applications. First and foremost, the particle needs to be magnetic. Usually, iron-based MNPs are used, such as ferrites (magnetite and maghemite) with or without doping metals (cobalt, zinc, nickel, *etc.*).
Hard magnetic NPs (ferro- or ferrimagnets) with high magnetic anisotropy and coercivity (see also Section II.1.2.2) are commonly used for the mechanical actuation of receptors (twisting and shearing).[114] In general, these NPs need to consist of multiple magnetic domains and are, thus, larger. On the other hand, small and soft NPs that form superparamagnets (see Section II.1.3.1) are applied in redistributing ensembles of receptors, usually in the cytosol.[115,116]
Secondly, MNPs should be monodisperse, meaning uniform in size and structure. Plus, they should be equipped with identical surface modifications. Due to this uniformity of particle properties, consistent results can be recorded with the MNPs. Another requirement for applying MNPs in cellular contexts and *in vivo* is biocompatibility. Previous studies demonstrated the low toxicity of ferrite NPs when incubated with human cells at low concentrations (below $0.1\,\mu g\,mL^{-1}$).[117] Also, injection of 40 nm ferrite NPs into mice showed that the MNPs are removed from the bloodstream within 2 h. The MNPs are transported to the liver and spine within days, where they are degraded with a half-life of 21 days.[118] Administering ferrite MNPs into animals only leads to little to no toxic effects.[119]
Another desirable aspect of an MNP is its versatility. In order to simplify experimental procedures, the MNP should be easily modifiable, especially regarding its outer shell, which is responsible for interaction with the environment. By decorating the MNP with certain surface groups, fast and easy modifications are possible. One example of this is the usage of click-chemistry to *e.g.* assemble multiple MNPs on

the surface of polystyrene beads via triazole bonds.[114] Also, the colloidal stability, solubility, and biocompatibility of MNPs can be increased via functionalisation with polymers such as PEG (see also Section II.3.1).[120] The addition of specific binding proteins – such as antibodies[114] or binding tags[121] – to the MNP surface can mediate binding to organelles or proteins. Furthermore, a popular approach to creating MNPs with modifiable shells is using cage-like proteins to trap the magnetic core. This was done in iron-storage proteins from several organisms.[122,123] The protein shell of these MNPs can be readily altered and customised to the experimental needs by genetic modification, for example, to add GFP for straightforward MNP detection.[116,124]
Lastly, apart from modifications of the MNP's shell, it is also possible to adjust the properties of the core and, thus, its magnetic properties. Implementing dopants into the core's crystal structure can significantly alter saturation magnetisation, blocking temperature, and magnetic anisotropy.[18,125]

Magnetic Fields The magnetic field applied in magnetogenetic experiments needs to be well-adjusted to the respective measurement. A major advantage of magnetic fields in general – and their role in magnetogenetics – is that they are transmittable through biological tissue with almost no loss.[126] It is possible to apply both stable magnetic fields (*direct current*, DC) and AMFs (also called AC for *alternating current*) in magnetogenetics.
When the external magnetic field is a DC field with a gradient ($\nabla\vec{B}$), an MNP with a magnetic dipole moment $\vec{m}$ subjected to that field will start to move towards higher field strengths, namely the source of the field (Figure II.3.10 A). The force $\vec{F}_\mathrm{m}$ exerted on the particle will be:

$$\vec{F}_\mathrm{m} = (\vec{m} \cdot \nabla)\vec{B}, \tag{II.3.6}$$

given that the magnetic dipole moment of the MNP remains constant in space. For the MNP to move, it must overcome the hydrodynamic drag force F_d

$$F_\mathrm{d} \propto \eta \cdot D_\mathrm{H} \cdot v_\mathrm{D}, \tag{II.3.7}$$

with the viscosity of the medium – for cells, this is the cytosol – η, the hydrodynamic diameter of the MNP D_H (see also Excursion 4) and the MNP's drift velocity

v_D.[128] These assumptions do not include Brownian motion or other restrictive forces, such as unspecific interactions with cellular components. Also, if membrane-bound receptors or intracellular molecules are to be redistributed alongside the MNP, F_d will increase accordingly. In any way, if $F_m < F_d$, the particle will be immobile.
Gradient fields are necessary for precisely accumulating MNPs *in vitro* or pulling on membrane receptors. These fields can be generated with comparably simple setups, including small permanent magnets connected to string wire for single-cell studies. The attached wire directs the magnetic field of the permanent magnet to give rise to $\nabla\vec{B}$.[120,121]
Homogeneous DC fields will force MNPs to align their magnetic dipole with the external field. If sufficiently close (in the range of several nanometres)[127] this can lead to dipole-dipole interactions between single MNPs. The particles will then attract each other (Figure II.3.10 B). Accordingly, if the DC field is rotating, the magnetic moments of the MNPs – and the MNPs themselves – are forced to rotate as well. This motion can exert torque on structures that are linked to the MNPs (see Figure II.3.10 C).
Finally, as described in Section II.1.3.2, the application of an AMF can induce heat dissipation of MNPs (see Figure II.3.10 D).

II.3.3.3 Applications of Magnetogenetics

A basic overview of the different applications of magnetogenetics is shown in Figure II.3.10 and will be discussed in more detail in the following paragraphs.

Activation of mechano-sensitive receptors As described in the previous paragraphs, precise harmonisation of MNP and external magnetic field can exert different forces on cellular targets to induce their activation.
One of the first reports about magnetogenetic activation of an ion channel was published in 2008.[129] Here, Hughes *et al.* demonstrated the magnetically induced activation of TREK-1, a potassium channel mostly expressed in the neuronal system. Naturally, the ion channel is opened by mechanical forces exerted by fluctuations of the cellular membrane.[130] Genetic modification of one of TREK-1's extracellular loops allowed coupling of MNPs (250 nm) to the channel. The magnetic field was applied via permanent magnets that were placed close and far from the sample with a frequency of 0 to 1 Hz. The forces acting on TREK-1 in this setup (up to 40 pN)

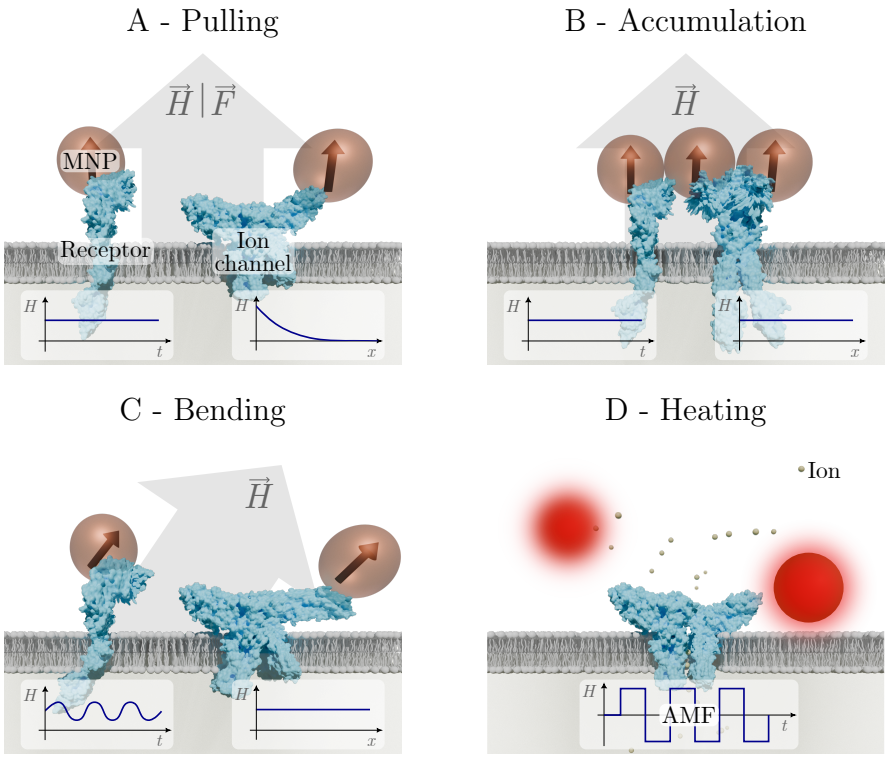

Figure II.3.10: Schematic overview of magnetogenetic techniques. (A) Applying a DC gradient field pulls the MNPs towards the source of the field. (B) A stationary and homogeneous DC field induces dipole-dipole interactions between MNPs and leads to accumulation. (C) By turning the direction of a homogeneous DC magnetic field, torque can be transferred from MNPs to the target. (D) An AMF will lead to heat being dissipated by the MNPs, *e.g.* activating thermosensitive channels.

were sufficient to induce changes in the channel's activity state.[129]

The potential of a static DC field was demonstrated by Cho *et al.*, summarised in Figure II.3.11. They created a precisely tuned gradient-free magnetic field that led to dipole-dipole attractive forces between single MNPs, estimated to be up to 30 fN. Zinc-doped ferrite MNPs were targeted via antibody-conjugation to *death receptor 4* (DR4) on cancer cells. The application of the static magnetic field led to the accumulation of MNPs and, hence, of DR4. This, in turn, significantly promoted apoptosis in sample cells. Using this setup, it was possible to induce apoptosis in zebrafish by targeting intrinsic death receptors.[131]

A similar approach was tested on *Frizzled*, a membrane receptor participating in Wnt-associated signalling. Wnt is a secreted ligand involved in various cellular

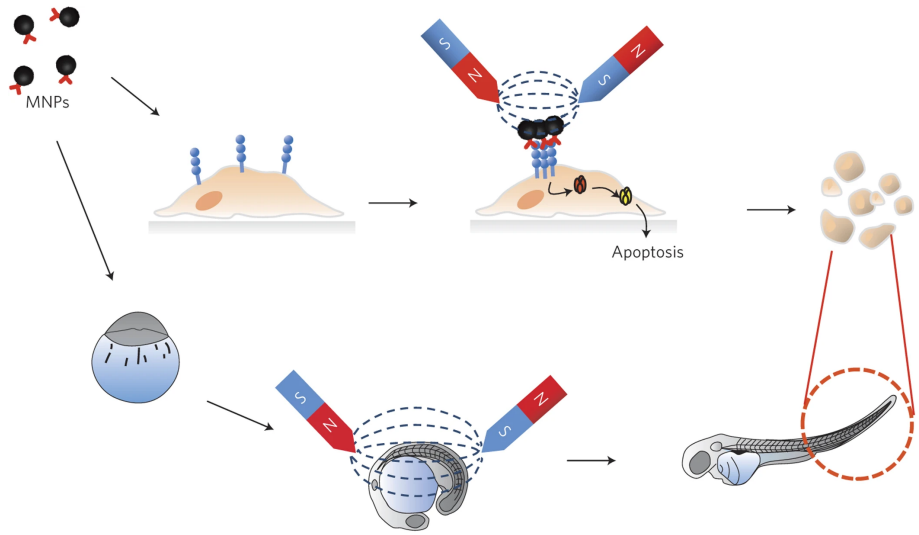

Figure II.3.11: Magnetic nanoparticles are used to target death receptors in cancer cells (top) and zebrafish (bottom). Applying a homogeneous, gradient-free magnetic field leads to accumulation and activation of death receptors, inducing apoptosis. Image was taken from Cho *et al.*[131] and reproduced with permission from *Springer Nature*.

pathways, including proliferation and differentiation of stem cells and osteogenic cells, which are responsible for bone formation.[132] Control over the Wnt signalling pathway is expected to lead the path to tissue engineering and regenerative medicine. Magnetogenetics was applied to this pathway to simplify its activation and circumvent the necessity of the complex and expensive production of Wnt proteins.[133] MNPs were functionalised with Ab against Frizzled and subjected to cells. Application of a DC gradient field with its source located below the examined cells induced Frizzled cluster formation and subsequent initiation of Wnt signalling.[132,133]

Further, it was shown that not only specific targeting of proteins can be used for magnetogenetic approaches. Tay *et al.* employed MNPs coated with starch to unspecifically bind to the membrane of primary neuronal cells from rats. After two weeks of cultivation, the neurons were incubated with the MNPs and subsequently subjected to magnetic fields. The pulling of the MNPs on the membrane was sufficient to open N-type calcium channels. N-type channels are a subclass of ion channels that were shown to be especially sensitive to magnetically induced deformation of the membrane. In a long-term study, it was also demonstrated that the expression of these ion channels increases when neurons are exposed to chronic magnetic stimulation. The overexpression of N-type channels was linked to the situation

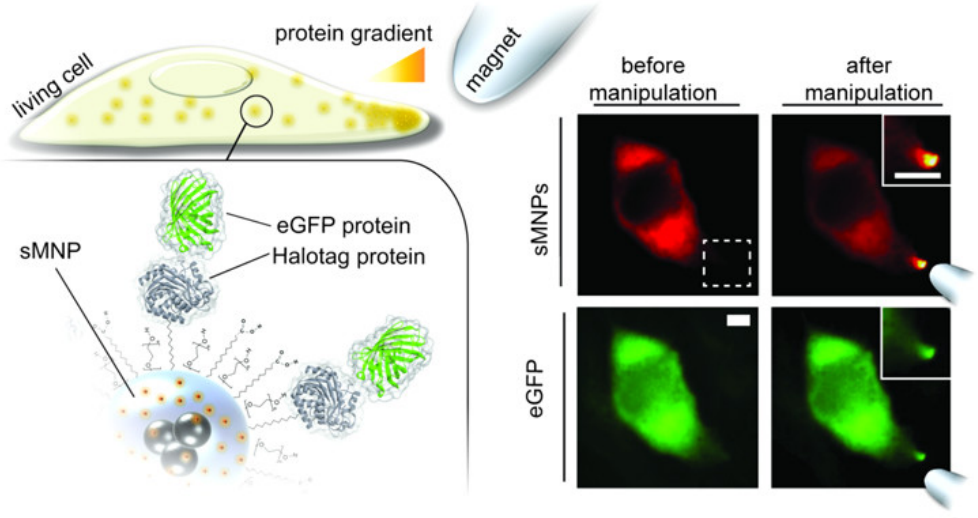

Figure II.3.12: Schematic depiction of magnetic accumulation of proteins inside a living cell by attachment to small MNPs (sMNP). The attachment to the sMNP is mediated by the highly specific *Halotag*. sMNPs are injected into living cells, overexpressing the target protein. A protein gradient at the cell membrane is created upon approaching a magnetic tip. Image is taken from Etoc *et al.*[115] and reprinted with permission from the *American Chemical Society*.

in various neurological diseases. Therefore, the presented technique can serve as a tool for mimicking conditions during these diseases.[134]

Apart from membrane-associated assays, magnetogenetic control of proteins was also realised in the cytosol by Etoc *et al.*[115,121] MNPs were functionalised with an affinity tag and microinjected into HeLa cells overexpressing the target protein *RhoGTPase*. This enzymatically active protein is involved in the formation and organisation of actin filaments. For this study, it was equipped with the counterpart of the affinity tag (see Figure II.3.12). Upon contact of the MNPs and target, both combined into a nanoplatform that could be moved through the cell using a magnetic tip that emits a gradient field. Accumulating the nanoplatform at the cell membrane activated the RhoGTPase and induced the formation of actin filaments and membrane protrusion.[115] In general, this study demonstrated the possibility of inducing local protein gradients within cells using magnetogenetics.

A combination of various ideas into one approach was created by Seo *et al.* in 2016.[135] They created Zn-doped ferrite particles with a plasmonic gold shell for magnetic stimulation and imaging, with a total diameter of 50 nm. The *magneto-plasmonic nanoparticles* (MPN) were used to target two membrane receptors that

are involved in cell–cell interactions: *Notch* and *VE-Cadherin*. The latter, VE-Cadherin, contributes to the formation of filaments and, thus, multicellular tissue and is sensitive to the application of force.[136] It was shown that accumulation of the receptor leads to clustering and, finally, to increased actin recruitment. Notch signalling is an initiator of various proliferation, physiological, and pathological processes. A key component of Notch signalling is the release of its intracellular domain, which ultimately influences gene expression in the nucleus. Conformational changes in the receptor promote this release.[137] It was demonstrated by Seo *et al.* that these changes can be induced by pulling on the extracellular domain using their designed MPNs.[135]

Activation of thermo-sensitive receptors The second major application of magnetogenetics is the localised generation of heat. As described in Section II.1.3.2, MNPs are dissipating heat when exposed to an AMF under suitable conditions.
One of the first applications of this phenomenon was published in 2010 by Huang *et al.*[138] The protein of interest in this work was a member of the *transient receptor potential cation channel subfamily V* – TRPV1. This ion channel is, among others, responsible for detecting capsaicin, the 'hot' molecule of chilli. In addition, TRPV1 was shown to be activated by increased temperatures.[139] The thermal activation threshold of TRPV1 is at approximately 43 °C.[140]
Huang *et al.* functionalised manganese-doped ferrite MNPs with a diameter of 6 nm to target the cellular membrane of human kidney cells expressing TRPV1 (see Figure II.3.13). Additionally, the MNPs were equipped with a thermo-sensitive fluorophore that loses fluorescence intensity upon temperature increase (drop by approximately 25 % for $\Delta T = 15\,^{\circ}\mathrm{C}$). Hence, temperature changes in the close proximity of the MNPs could be monitored.
It was shown through fluorescence microscopy that MNPs are exclusively present at the cellular membrane. Application of an AMF for up to 45 s led to local temperature increases of up to 18 °C at the membrane but not inside the cell. This approach was also used in neurons to open TRPV1 channels and activate calcium influx.[138]

A similar approach was used by Rosenfeld *et al.* for the activation of natural TRPV1 in the adrenal cells of rats.[141] However, they waived specific targeting of MNPs and instead injected them directly into the adrenal gland of living rats. By remote

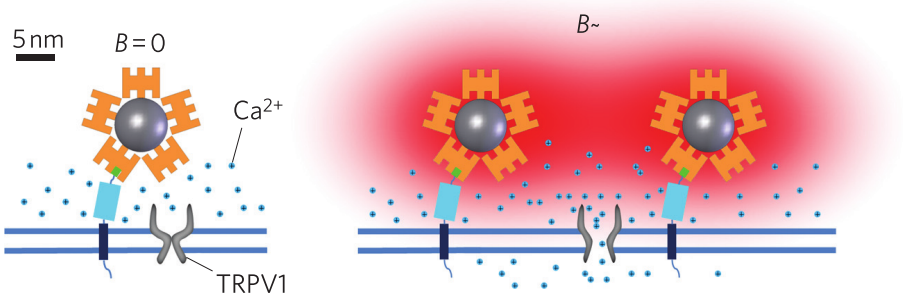

Figure II.3.13: Magnetothermal activation of the TRPV1 cation channel. MNPs are targeted to the cellular membrane and heated by applying an AMF. Upon temperature increase, the thermo-sensitive ion channels open and allow influx of Ca^{2+}. Image taken from Huang *et al.*[138] and reproduced with permission from *Springer Nature*.

magnetic actuation with an AMF, it was again possible to open thermo-sensitive ion channels. The consecutive uptake of calcium into the cells of the adrenal cortex after magnetic stimulation increased the secretion of adrenal hormones into the blood serum. Blood samples obtained from MNP-treated animals displayed significant differences in hormone levels compared to animals treated with paramagnetic iron NPs.[141] Imbalances of adrenal hormones are related to psychological diseases such as depression and post-traumatic stress disorder and are, therefore, a promising target for future studies.[142]

II.3.4 Ferritin as a Nanoagent

The previous chapters evaluated applications of magnetogenetics, especially regarding the properties of MNPs. As indicated by some examples in the previous chapters, ferritin – as a natural iron storage protein – has interesting intrinsic features for magnetogenetics. Ferritin's natural properties and tasks were described in Section II.3.2.4 and go in hand with various advantages for magnetogenetic applications. It is thus especially promising as a template for the design of a bio-inspired nanoagent.

First, the natural metal scavenging characteristics allow for a relatively easy and mild synthesis of ferrite NPs. Here, the hydrophilic gradient around ferritin's 3-fold channel not only enables quick internalisation of Fe^{2+} but also of other divalent, non-native metal ions[95] such as Co^{2+},[143] Mg^{2+},[144] Zn^{2+},[145] Pd^{2+}, but also Au^{3+}.[146] Through this, synthesis of not only doped ferrite MNPs but also various iron-free

constructs inside the ferritin cage can be accomplished.
Another advantage of ferritin's employment is the size constraint that it imposes on growing NPs. Hence, created particles are highly monodisperse and nearly identical in shape and size – consistency in their physical properties and experimental performances is therefore high. Plus, MNPs formed within the cage are smaller than 8 nm and are, thus, usually superparamagnetic. As described in Section II.1.3.1, superparamagnetism goes hand in hand with multiple further benefits for magnetogenetic applications.
Finally, the protein cage that covers ferritin NPs is a popular reason for using ferritin. Not only is the cage outstandingly stable at high temperatures of more than 60 °C[147] and against a multitude of chemicals,[148] it also increases water solubility and biocompatibility of NPs and, thus, provides availability for biological systems. Plus, genetic engineering allows for straightforward modification to equip the cage with tools for detection – fluorescence via GFP (see Section II.3.2.1)[116] – or site-specific targeting, even *in vivo*.[95]

II.3.4.1 Synthesis of semisynthetic Magnetoferritin

As mentioned, ferritin forms paramagnetic ferrihydrite cores under natural conditions (see Section II.3.2.4), which – with some exceptions – are uninteresting for biotechnological purposes. However, Meldrum *et al.* were the first to use ferritin as a template for the synthesis of a truly magnetic protein: *Magnetoferritin* (MFt) was born.[123]
With all the advantages described in the previous chapter in mind, it is unsurprising that ferritin entered the spotlight of research in the early 90s. The first attempt by Meldrum *et al.* of creating a semisynthetic ferritin MNP was made with horse spleen ferritin. To this end, it was first freed from residual ferrihydrite via dialysis at low pH. Subsequently, the produced empty ferritin (also referred to as *apoferritin*) was buffered at pH 8.5 and kept at 60 °C while adding ferrous iron and ambient air over the course of 200 min. During this reaction, the cages were steadily filled with magnetic cores with a mean diameter of 6 nm.[123]
Due to the narrow size distribution, MFt's core is an ideal sample for characterising the magnetic properties of such small ferrite NPs. Firstly, MFt was shown to be superparamagnetic under ambient conditions.[149] Electron diffraction measurements

revealed that the material inside MFt is either magnetite or maghemite with high crystallinity.[123,149] The blocking temperature T_B of the MFt cores was determined to be around 70 K. As comparison, for magnetite MNPs with a diameter of 11 nm T_B is approximately 120 K.[150] Hence, T_B of MFt lies within expectations since it decreases with the particle size (as discussed in Section II.1.3.1). Further, MFt's attempt frequency τ_0 (see Equation II.1.6) was 10^9 Hz and hence, comparable to previous results for similar MNPs (see Section II.1.3.1).[149]

The synthesis of ferritin's magnetic core steadily evolved. Switching to anaerobic synthesis made it possible to control oxidation processes more thoroughly. To start the reaction under these conditions, oxidising agents such as *trimethylaminoxid* (C_3H_9NO)[151] or *hydrogen peroxide* (H_2O_2)[152] are necessary. The equation for the formation of magnetite (Fe_3O_4) using H_2O_2 is given by:

$$3\,Fe^{2+} + H_2O_2 + 2\cdot H_2O \longrightarrow Fe_3O_4 + 6\cdot H^+ \tag{II.3.8}$$

Although at first glance, the formation of magnetite seems to be similar to Fenton's reaction (see Equation II.2.1), the elevated pH level during ferritin's core synthesis opposes the formation of ROS and favours Equation II.3.8.

Due to the steady formation of protons during the reaction, it is necessary to monitor and adjust the pH constantly. The solubility of ferric iron is highly dependent on pH and reaches a minimum at a pH of approximately 8.5.[153] Hence, basic milieus are ideal for sedimentation of Fe^{3+}. Additionally, the removal of H^+ from the system by neutralisation with OH^- shifts the equilibrium towards the products and suppresses the potentially harmful Fenton chemistry.

A major breakthrough in MFt production was achieved by Uchida *et al.* by isolating human *hcf* and cloning it into a prokaryotic expression vector. HCF expressed in *E. coli* was still able to self-assemble into a cage. However, this step removed the necessity to unload the ferritin cage prior to core synthesis. The synthesis reaction was performed in an oxygen-depleted N_2 atmosphere, at 65 °C, with ammonium iron sulfate ($(NH_4)_2Fe(SO_4)$) as iron precursor and H_2O_2 as oxidising agent. After the reaction, sodium citrate was added to the solution to chelate free iron ions and quench the reaction.[154] To this day, this procedure is commonly used for the synthesis of MFt.

II.3.4.2 Encapsulation of Nanoparticles with Ferritin

Apart from the uptake of single ions into ferritin's cage through its 3-fold channels for subsequent sedimentation, another highly interesting method of loading the cage with its cargo has been postulated. In 1986, Gerl and Jaenicke demonstrated that apoferritin can be disassembled at pH values around 2.[155] While this alone would not help in loading ferritin with cargo, it was also shown that upon raising the pH back to 7.9 in the presence of stabilising agents, cages started to reassemble.
This observation was first used by Webb *et al.* by incubating disassembled ferritin monomers with the pH indicator *neutral red* during reassembly. The small indicator molecules were trapped inside the ferritin cage during this process.[156] Unfortunately, ferritin cannot withstand the strongly acidic conditions during the disassembly without some damage. After reassembly, cages are disrupted and often contain holes. Hence, reassembly is not fully reversible using this method.[157]
This drawback was tackled by shifting from a pH-dependent disassembly to using urea at high concentrations of up to 8 M. By stepwise dialysis against urea-free buffers in the presence of the anti-cancer drug *doxorubicin*, ferritin cages formed around the molecules.[158]
This method established the generation of an almost universal nano-carrier system that was shown to host and deliver both hydrophobic and hydrophilic molecules, nucleic acids, proteins, and nanoparticles, such as semiconductor quantum dots.[159]

II.3.4.3 State-of-the-art Applications of Ferritin Nanoagents

As shown in the previous chapters, ferritin has become an essential element of nanobiotechnology. Nowadays, it is a vital component of diverse scientific advancements.

Targeted drug delivery After the first encapsulation of doxorubicin into ferritin's cage in 2014,[158] ferritin's self-assembly caught researchers' attention for all sorts of medical applications, with ferritin serving as a delivery system. Some examples are the delivery of photosensitising agents into tumour cells via TfR1 coupling (see Section II.2.1),[160] the delivery of pharmaceuticals such as the anticancer drug cisplatin,[161] or as a platform for vaccines against various diseases, including rabies,[162] SARS-CoV-2,[163] and even cancer.[164]

Diagnostics Another medical application of ferritin is its use in the detection of diseases. Here, it can be used as a mediator in a sandwich-format detection assay for phosphorylated p53 proteins secreted in early-stage cancer patients.[165] Also, ferritin is applied as an imaging agent in cancer, carrying graphene quantum dots with pH-responsive fluorescence.[166]

Magnetic resonance imaging Ferritin can further be used to develop new contrast agents for MRI. Here, it was employed to encapsulate gadolinium complexes to increase biocompatibility.[167] Also, it served as a helpful size regulator during the synthesis of MNPs with ultrafine iron oxide cores (diameter of $\sim$2 nm) as replacement of commonly used, toxic gadolinium compounds.[168]

Further applications Apart from these biomedical applications, ferritin was also used as a nanoreactor and carrier for palladium NPs for catalysis.[169,170] In the field of nanoelectric devices, ferritin can create highly ordered titanium arrays using two-dimensional ferritin matrices as templates – a promising candidate for novel data storage devices.[171]

Magnetogenetics Lastly, as noted earlier, ferritin has become a popular component of magnetogenetic appliations. One of the most prominent implementations of ferritin in this field was done by Wheeler *et al.* in 2016.[172] While the modifications that were done to TREK-1 (see Section II.3.3.3) only enabled binding to MNPs, they aimed at designing a magnetically sensitive actuator that requires only one combined component. To this end, they chose the cation channel *transient receptor potential cation channel subfamily V 4* (TRPV4). It was shown previously that TRPV4 can be opened by exerting pressure on the receptor, leading to an influx of cations.[173] TRPV4 was genetically fused to ferritin to give rise to the construct *Magneto2.0* (see Figure II.3.14).[172] Ferritin was attached to each of the intracellular domains of the four homomeric subunits of TRPV4 and expressed in cells of interest. Under these conditions, ferritin stores incoming iron in its natural, paramagnetic form (see also Section II.3.2.4). When a magnetic field is applied, the paramagnetic ferritins will be attracted towards the origin of the field. Plus, the magnetic field could induce dipole-dipole interactions between the ferritins, causing them to attract each other. Although the exact magnetic mechanisms are not clarified, it was shown that

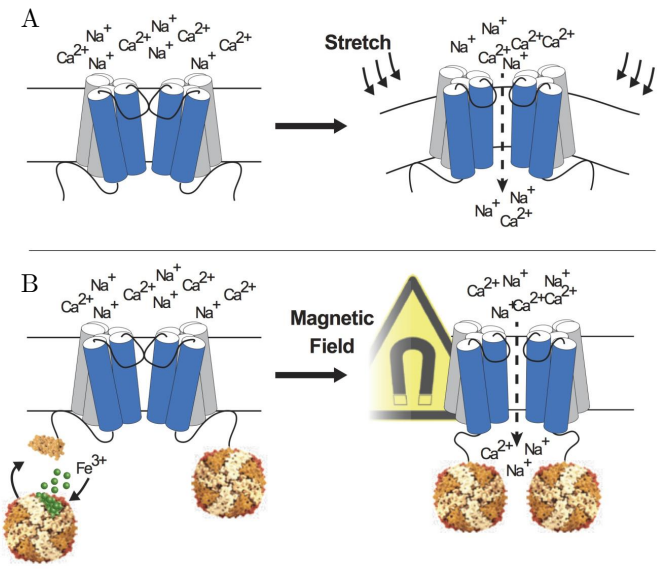

Figure II.3.14: Magnetogenetic activation of the semisynthetic ion channel Magneto2.0, a fusion protein of the cation channel TRPV4 and ferritin. (A) Naturally, TRPV4 is activated by bulging of the cellular membrane that opens the channel to let cations flow in. (B) By fusing ferritin to the channels, TRPV4 can be forced to open by introducing stretch via the forces acting on the natural, paramagnetic ferritins in the DC field. Image was taken from Wheeler *et al.*[172] and reproduced with permission from *Springer Nature*.

the forces acting on the four ferritin cages are transmitted to TRPV4, forcing the central channel to open and allowing cation influx. This was first demonstrated in human kidney cells as a proof of concept. Additionally, Magneto2.0 was expressed in neuronal cells of both zebrafish and mice. Subsequent exposure to an external magnetic field induced behavioural outputs in the genetically modified animals.[172] In accordance with the activation of thermo-sensitive receptors described in Section II.3.3.3, Stanley *et al.* employed endogenously expressed ferritin to target TRPV1. Application of an AMF was shown to regulate calcium influx into cells, similar to the work of Huang *et al.*[138] This method was then used to lower blood glucose levels in mice via induced insulin expression.[174]

Despite the various applications of ferritin in nanobiotechnology, its usage in magnetogenetics has been questioned. The presented results have been contested by theoretical considerations that demonstrad the physical limits of both magnetic heat dissipation and the forces transduced on cellular compartments by ferritin to be various magnitudes below necessary thresholds.[175] These considerations were re-

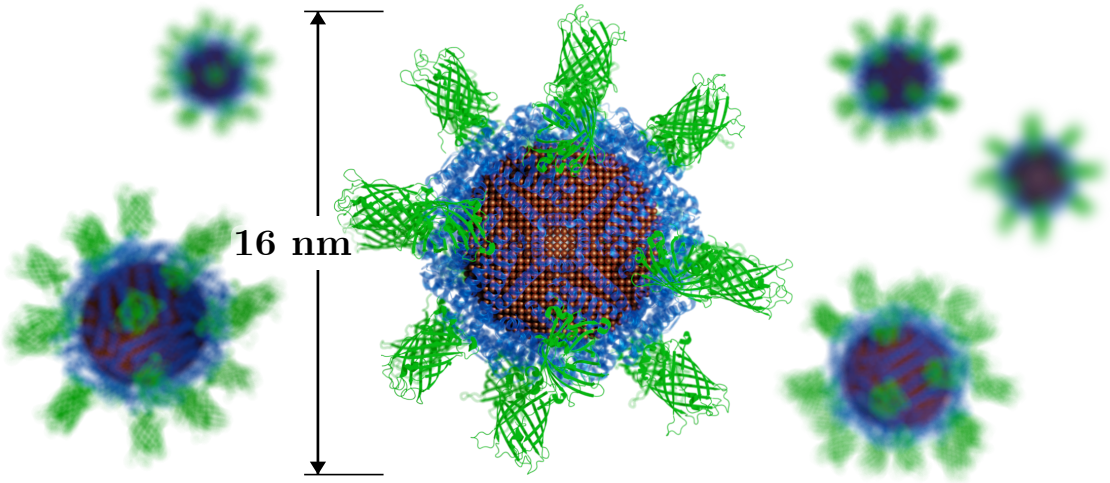

Figure II.3.15: Structure of Magnetoferritin, with its ferrite core in the central cavity (∼8 nm, brown), the ferritin shell (∼12 nm, blue), and the mEGFP subunits (green).

inforced by the lack of reproducibility of AMF-induced heating of ferritin MNPs.[176] Instead, other mechanisms that induced receptor or channel activation during magnetogenetic activation were postulated, which took a wider range of possible spin configurations within ferritin's core into account. The theories are described in more detail in the work of Mladen Barbic.[177] A more practical approach addressed the possibility that ROS generated at ferritin's core during AMF stimulation might, ultimately, be responsible for the magnetogenetic activation of TRPV1.[178]

In the wake of this discussion, a recently published work by Duret *et al.*[179] repeated and extended experiments with Magneto2.0. By fine-tuning TRPV4 in the construct, they ruled out that mechanical processes activate the channel and, thus, strengthened the claim that dissipated heat is responsible. In this light, they introduced the theory of magnetocaloric heating to the debate. Here, entropy reduction during the magnetisation of MNPs leads to heat dissipation. Calculations demonstrated that heating through magnetocaloric effects can, indeed, be sufficient for neuronal activation via TRPV4. Interestingly, this effect works in both directions – upon demagnetisation, entropy increases and heat will be taken up by the MNPs. Hence, the magnetocaloric hypothesis would enable the cooling of the surroundings of MNPs, an effect that previously suggested relaxation losses in AMFs cannot achieve. This theoretical model was put into use by activating the cold-responsive ion channel *transient receptor potential cation channel subfamily melastatin 8* in a construct similar to Magneto2.0. Although the magnetocaloric hypothesis would

provide an explanation for outcomes of previous studies and, additionally, open up a whole new area of applications, further work is needed to fully understand the thermal effects at ferritin's surface.[179]

In the context of this work, a semisynthetic MFt was used. The ferritin cage consists only of HCF subunits, each equipped with an N-terminal mEGFP. Thus, MFt can be reliably tracked using fluorescence microscopy or other optical methods. This MFt construct, its original plasmid, and the protocol for the magnetic core synthesis were initially established by Liße *et al.* for spatio-temporal control over intracellular proteins and even organelles. To this end, MFt was injected directly into the cytosol and redistributed using a DC gradient field emitted by a magnetic tip. With this setup, it was possible to redistribute cytosolic MFt within seconds and create local concentration gradients.[116]

II.4 Aim of this Dissertation

My dissertation focused on advancing magnetogenetical methods to manipulate cellular signalling pathways with external magnetic fields. Since MNPs are a fundamental component of magnetogenetics, demands for versatile MNPs with customised magnetic properties are high. As noted, magnetogenetics is intended as a tool to study living cells in both *in vitro* and *in vivo* settings. As a result, MNPs should be compatible with biological systems and flexibly applicable to easily adapt to changing experimental parameters.

With this in mind, I utilised and advanced a previously established MNP platform based on the iron storage protein ferritin. This cage-like protein is synthetically filled with a magnetic core to give rise to the semisynthetic Magnetoferritin. The protein cage surrounding this MNP's core effectively shields and introduces stealth-like properties against immunological and intracellular defence systems.

In its natural form, ferritin exhibits no unspecific interactions, but specifically, it couples only to its inherent receptors. Thus, the first part of this work focused on expanding ferritin's range of targets. To this end, I once again took advantage of ferritin's protein shell. I used genetic engineering to modify it to specifically bind to selected targets from a broad spectrum of proteins within or on a cell.

Furthermore, in the second part, I investigated the magnetic properties of the ferritin nanoagent. Generally, Magnetoferritin's magnetism is defined by the composition, crystallinity, and size of its core. Modifications to this core, hence, directly influence the magnetic performance of the ferritin MNPs. Therefore, I aimed at customising the magnetic properties of Magnetoferritin by altering its core.

These two modifications – the broadened range of targets and enhanced magnetic properties – should result in an ideal MNP that can be readily applied in all sorts of magnetogenetic applications.

Apart from optimising and generating ferritin MNPs, their characterisation has been a significant part of my work. To this end, I – on the one hand – utilised standard methods for MNP examination and – on the other hand – aimed at repurposing existing techniques to eventually analyse MNP morphology, composition, and biological and magnetic behaviour.

Chapter III

Nanobiotechnological Engineering of Ferritin

III.1 Publication I

Reference

Title Magnetic Nanoprobes for Spatio-Mechanical Manipulation in Single Cells

Authors Iuliia Pavlovna Novoselova* , Andreas Neusch*, Julia-Sarita Brand, Marius Otten, Mohammad Reza Safari, Nina Bartels, Matthias Karg, Michael Farle, Ulf Wiedwald, and Cornelia Monzel
* These authors contributed equally.

Journal details *Nanomaterials*, Volume 11, Issue 9

Date of Publication 31st August 2021

DOI https://doi.org/10.3390/nano11092267

Copyright

Contribution

As shared first author, I was involved in the conceptualisation of the publication and participated in regular progress report meetings. I produced all ferritin particles that we used in this work and was responsible for cell culture. Further, I performed viability assays and recorded magnetic manipulation of cells with fluorescence microscopy. I took part in writing the original draft of the paper and proof-reading. Figures were created by IPN and me.
My overall contribution to this publication amounts to approximately 40 %.

nanomaterials

MDPI

Article

Magnetic Nanoprobes for Spatio-Mechanical Manipulation in Single Cells

Iuliia P. Novoselova [1,*,†], Andreas Neusch [1,†], Julia-Sarita Brand [1], Marius Otten [2], Mohammad Reza Safari [1,3], Nina Bartels [1], Matthias Karg [2], Michael Farle [4], Ulf Wiedwald [4] and Cornelia Monzel [1,*]

1 Experimental Medical Physics, Heinrich-Heine University Düsseldorf, 40225 Düsseldorf, Germany; Andreas.Neusch@hhu.de (A.N.); jubra114@uni-duesseldorf.de (J.-S.B.); m.safari@fz-juelich.de (M.R.S.); Nina.Bartels@uni-duesseldorf.de (N.B.)
2 Colloids and Nanooptics, Heinrich-Heine University Düsseldorf, 40225 Düsseldorf, Germany; marius.otten@hhu.de (M.O.); karg@hhu.de (M.K.)
3 Peter Grünberg Institute, Electronic Properties (PGI-6), Forschungszentrum Jülich, 52425 Jülich, Germany
4 Center for Nanointegration (CENIDE), Faculty of Physics, University of Duisburg-Essen, 47057 Duisburg, Germany; michael.farle@uni-due.de (M.F.); ulf.wiedwald@uni-due.de (U.W.)
* Correspondence: Iuliia.Novoselova@hhu.de (I.P.N.); Cornelia.Monzel@hhu.de (C.M.)
† These authors contributed equally to this work.

Abstract: Magnetic nanoparticles (MNPs) are widely known as valuable agents for biomedical applications. Recently, MNPs were further suggested to be used for a remote and non-invasive manipulation, where their spatial redistribution or force response in a magnetic field provides a fine-tunable stimulus to a cell. Here, we investigated the properties of two different MNPs and assessed their suitability for spatio-mechanical manipulations: semisynthetic magnetoferritin nanoparticles and fully synthetic 'nanoflower'-shaped iron oxide nanoparticles. As well as confirming their monodispersity in terms of structure, surface potential, and magnetic response, we monitored the MNP performance in a living cell environment using fluorescence microscopy and asserted their biocompatibility. We then demonstrated facilitated spatial redistribution of magnetoferritin compared to 'nanoflower'-NPs after microinjection, and a higher magnetic force response of these NPs compared to magnetoferritin inside a cell. Our remote manipulation assays present these tailored magnetic materials as suitable agents for applications in magnetogenetics, biomedicine, or nanomaterial research.

Keywords: iron oxide nanoparticles; magnetoferritin; magnetogenetics; remote particle manipulation

Citation: Novoselova, I.P.; Neusch, A.; Brand, J.-S.; Otten, M.; Safari, M.R.; Bartels, N.; Karg, M.; Farle, M.; Wiedwald, U.; Monzel, C. Magnetic Nanoprobes for Spatio-Mechanical Manipulation in Single Cells. *Nanomaterials* **2021**, *11*, 2267. https://doi.org/10.3390/nano11092267

Academic Editor: Álvaro Somoza

Received: 30 July 2021
Accepted: 27 August 2021
Published: 31 August 2021

1. Introduction

Functional magnetic nanoscale particles (MNPs) are widely employed in biotechnology and nanomedicine to study fundamental biological processes as well as to develop enhanced diagnostic and treatment strategies, the most prominent examples being smart drug delivery, contrast enhancement in imaging, magnetic separation of molecules, magnetic particle hyperthermia [1], regenerative medicine concepts [2], and a combination of diagnostics and therapy [3]. In addition, for subcellular applications in fundamental studies, their manipulation via magnetic tweezers demonstrated benefit in the study of organelles, proteins, and biomolecules within the cell environment [4,5].

Iron oxide nanoparticles (NPs) are one of the most popular compounds for biomagnetics studies due to their versatile applicability and biocompatibility [6–9]. Interest in iron oxide NPs rises because they can be synthesized in various shapes, sizes, and in large amounts (e.g., via thermal decomposition or laser target evaporation) enabling cost-effective production. Previous studies demonstrated successful NP delivery into living tissues, their spatial manipulation by external magnetic fields [10,11], as well as their controlled heating [12]. Recent studies, however, indicate that these nanoprobes need to

reconcile a variety of demands which are difficult to achieve simultaneously [1,13]. First, NPs need to be biocompatible. Second, they need to be sufficiently monodisperse in terms of size, surface charge, and functional motifs in order to respond similarly to an external magnetic stimulus (DC or AC field). Finally, they need to be functionalized to specifically target particular biological sites as well as to make the particle chemically inert. Here, we characterize a new class of 'nanoflower'-shaped multicore iron oxide NPs, called synomag, and discuss possible applications.

Semisynthetic particles are another new class of NPs which can be tailored to meet the listed demands. Highly successful examples are NPs made of proteins belonging to ferritins, a group of proteins which naturally store iron in an organism to maintain its iron homeostasis [14,15]. For example, human ferritin (Ft) is a globular protein cage of this family, consisting of 24 subunits, 12 heavy and 12 light chains. Interestingly, the heavy-chain-ferritin (HCF) subunit exhibits ferroxidase activity [15,16] which can be exploited in Fenton-like reactions to synthesize a magnetic crystal into the cage. Previously, it was shown that a superparamagnetic iron oxide core can be grown within the cage [17]. This is particularly beneficial for subcellular applications where particle chain formation due to magnetic dipole–dipole interactions should be prevented. Moreover, due to their unique protein structure, these NP templates are biocompatible by nature and exhibit a well-defined size with a strict upper size limit along with shape uniformity [18]. In addition, the protein cage can serve as a scaffold for bio-orthogonal tagging, and, via genetically encodable tags, precise control over the tag number is achieved. Such genetically modified human ferritin, henceforth termed 'magnetoferritin' (MFt), is the second MNP presented in this work.

If an MNP exhibits the desired superparamagnetic, biofunctional, and biocompatible properties, it is imperative to evaluate the MNP in conjunction with an applied magnetic field. Any spatial, mechanical, or thermal stimulus to be transferred to a biological entity of interest will heavily depend on both the NP magnetic responses and the externally applied field. For example, for localized MNP heating, the dissipated heat is proportional to the AC susceptibility of the NP and the square of the magnetizing field [19]. In case of force applications, the product of the NP's magnetic moment and the magnetic field gradient have to be known. The localized heat or applied force may then be used to switch molecular activity states and to eventually influence a cellular function. Such a remote and finely tunable magnetic manipulation approach is commonly referred to as Magnetogenetics. Several recent studies demonstrate how these stimuli (heat, force, or spatial redistribution) enable active probing of fundamental cell signaling functions, such as action potential formation in neuronal cells [20], cell signaling for differentiation or migration [11,21], or tumorigenesis [22]. Hence, Magnetogenetics can provide a rich toolkit to study fundamental processes in individual cells. An overview of intriguing biological and medical questions is reviewed in Monzel et al. [23] and Pankhurst et al. [19], along with information about the required magnetic fields and gradients.

Here, we first characterized two new classes of MNPs: semisynthetic single core magnetoferritin (MFt) and multicore synomag MNPs. We then assessed their biocompatibility and uptake by cells. Finally, two different modes of MNP–cell transfer (microinjection and incubation) were applied. A magnetic tip for microscale MNP manipulation was characterized and used to subject MNPs to a magnetic attraction force for spatio-mechanical manipulation.

2. Materials and Methods

Ferritin Cage Expression and Purification: monomeric enhanced green fluorescent protein (mEGFP)-tagged heavy chain ferritin (HCF) plasmid (mEGFP::HCF) was a kind gift from the Coppey/Hajj Lab at Laboratoire Physico-Chimie, Institut Curie, Paris, France and Piehler Lab at University Osnabrück, Germany. For site-specific targeting of proteins, mEGFP was fused to the N-terminus of HCF containing 6 amino acids as linker by cassette cloning as described before [21]. For bacterial expression of mEGFP::HCF in *E.coli* BL21-

CodonPlus (DE3)-RIPL Competent Cells (Agilent Technologies, Santa Clara, CA, USA), the cDNA of the fusion protein was cloned in pET21a (Merck KGaA, Darmstadt, Germany). For preparative overexpression, the *E. coli* BL21 were transformed with the plasmid and the culture was grown from a single colony in 2xYT medium at 37 °C up to an OD_{600} of 0.6 to 0.8. Plasmid expression was induced with 1 mM IPTG (Sigma-Aldrich, St. Louis, MO, USA), and the culture was grown further at 16 °C overnight. Harvested cells were washed in Phosphate Buffered Saline (PBS) and finally resuspended in HEPES-1 buffer (50 mM HEPES, 150 mM NaCl, pH 8.0). The obtained cell suspension was treated with Protease Inhibitor Cocktail and PMSF to protect the protein from degradation during the following cell disruption via a homogenizer (M110P Microfluidizer, Microfluidics, Westwood, MA, USA). After centrifugation, the supernatant containing mEGFP::HCF was purified by heat shock (70 °C, 15 min). Subsequently, mEGFP-tagged ferritin particles were cleaned up using ammonium sulfate precipitation, first at 200 g/L, then at 300 g/L, to precipitate proteins of different solubility than the desired protein. After the last step, the pellet containing ferritin was resuspended and dialyzed overnight in HEPES-2 buffer (20 mM HEPES, 100 mM NaCl, pH 8.0). The resulting sample was loaded onto a size exclusion column (HiPrep 16/60 Sephacryl S400 High Resolution, GE Healthcare, Chicago, IL, USA) equilibrated with filtered (0.2 µm) and degassed HEPES-2 buffer. All chromatography steps were performed in an FPLC system (Äkta Explorer, GE Healthcare, Chicago, IL, USA). We used 12% sodium dodecyl sulphate–polyacrylamide gel electrophoresis (SDS-PAGE) to confirm the purity of the final product as well as the effectiveness of each individual purification step (Figure S1) [24].

Coupling of methoxy-PEG2000-NHS: methoxy-(polyethylene glycol)-*N*- hydroxysuccinimid (Molecular Weight (MW): 2000 Da) was purchased from Sigma-Aldrich (St. Louis, MO, USA). Methoxy-PEG2000-NHS (30 µL of 100 mM in dry DMSO) was added to 100 µL mEGFP::HCF (10 µM) in HEPES-2 buffer. The reaction mixture was incubated for 2 h at room temperature on a rotator. PEGylated mEGFP-tagged ferritin was purified with PD10 desalting columns (GE Healthcare) equilibrated with HEPES-2 buffer. The integrity and physicochemical properties of PEGylated mEGFP::HCF were examined by SDS-PAGE. The protein concentration was determined by UV-Vis absorption spectroscopy (NanoDrop 2000, Thermo Fisher Scientific Inc., Waltham, MA, USA).

Iron Oxide Core Synthesis in Ferritin Cages: purified PEGylated ferritin cages were used to synthesize a magnetite core inside the cage using 1 mg/mL protein concentration diluted in 25 mL of 100 mM NaCl (Sigma-Aldrich, St.Louis, MO, USA). A solution of 30 mM ammonium iron(II) sulfate hexahydrate (Sigma-Aldrich, St.Louis, MO, USA) was used as an iron source and added to the reaction vessel at a constant rate of 211 µL/min, at an excess of about 5000 Fe atoms per ferritin cage. Hydrogen peroxide H_2O_2 of 5 mM was simultaneously syringe-pumped into the vessel at the same rate. During the synthesis, the reaction vessel was kept at 65 °C under positive N_2 pressure and the pH was maintained dynamically at 8.5 with 100 mM NaOH by an automatic titrator (Titration Excellence T5, Mettler-Toledo, Columbus, OH, USA). During the oxidation process, the green-toned solution became evenly yellow-brown. Once magnetic loading was done, 200 µL of 300 mM sodium citrate was added to chelate any free iron. Synthesized MNPs were treated by centrifugation at 19,000× *g* for 30 min at 4 °C and 0.2 µm PTFE filtering to remove potential iron oxide aggregates formed outside of the cages. The final product was stored at −80 °C to prevent protein degradation till further experiments were performed.

Synomag NPs: 'nanoflower'-shaped iron oxide particles were commercially available from micromod GmbH (Rostock, Germany). Since some of the NPs exhibited free amine groups on their surface, coupling of PEG2000-COOH was performed to generate a passivation surface according to the protocol given above ('Coupling of methoxy-PEG2000-NHS').

Transmission electron microscopy (TEM): ferritin cages in buffer solution were dropped onto Formvar coated nickel grids (200 mesh, S162N-100, Plano GmbH, Wetzlar, Germany) and left to sediment for 1 min. Solution remaining on the grid was removed between each step using filter paper. After sedimentation, the sample was negatively

stained twice for 3 to 5 s and 30 s by subsequently placing the grid onto two separate drops of 2% uranyl acetate. The remaining solution was removed and the grid was left to air dry.

Imaging was performed on a Jeol JEM-2100Plus (Akishima, Tokyo, Japan), operating in bright field mode at an acceleration voltage of 80 kV. The average size, obtained by statistical analysis using Fiji [25], was 275-347 NPs for synomag, stained ferritin shells, and unstained magnetic cores in ferritin NPs, respectively.

Dynamic light scattering (DLS) and electrophoretic light scattering (ELS): measurements were carried out on Zetasizer Nano ZS (Malvern Panalytical Ltd., Malvern, UK) equipped with a He–Ne laser working at a wavelength of 633 nm. Data was recorded using a detection angle of 173°. For DLS, 5 subsequent measurements containing 50 sub-runs were taken (each sub-run duration was 10 s). Reported hydrodynamic diameters D_H refer to the peak value of the log-normal fit applied to the DLS number distributions. For ELS, stabilizing buffers showed a conductivity of about 10–15 mS/cm (measured conductivity of deionized water is below 0.1 mS/cm); thus, measurements were carried out at a reduced voltage of 40 V to protect measuring cell electrodes from deterioration. Reported results represent averages from 10 measurements; 30 sub-runs each along with standard deviations.

Magnetometry: buffers from the samples were diluted to reduce the amount of salts. Liquid samples were dried using a rotational evaporator. Dried powders (~10 mg) were compacted into synthetic sample holders for vibrating sample magnetometry (VSM) in a PPMS DynaCool system (Quantum Design GmbH, Darmstadt, Germany). The magnetic response was measured up to 4 T at 5–300 K, and zero-field-cooling/field-warming sequences (ZFC/FW) were recorded at 5 mT.

Cell Handling: HeLa wild type cells (ATCC® CCL-2™, ATCC, Manassas, VA, USA) were cultivated at 37 °C, 5% CO_2 in Dulbecco's Modified Eagle Medium (DMEM) supplemented with 10% fetal calf serum (FCS) and 1% PenStrep; all from Thermo Fisher Scientific. Cell splitting trypsin-based standard protocol was carried out once the cells density reached about 70% confluency. For experiments, cells were passaged no higher than passage 30.

Cell Viability Assay: to assess possible negative effects of MNPs on cell viability, a standard CellTiter-Blue (CTB) Assay from Promega (Fitchburg, WI, USA) was carried out for both empty ferritin cages and synomag samples. This assay is based on the conversion of resazurin to resorufin by living cells. This reduction causes a shift in the dye's fluorescence. In a 96-well plate, about 25,000 cells were seeded per well and grown in the incubator (37 °C; 5% CO_2) overnight. Afterwards, cells were incubated with increasing amounts of MNPs. Untreated cells and cells incubated only with the MNP-containing medium served as positive control. Incubation with MNPs was carried out for 24 h. As negative control, untreated cells were exposed to 0.1% Triton 30 min before CTB addition. After incubation, cells were washed with DPBS and incubated for 4 h in a mixture of DMEM and CTB (9:1). The emission of the supernatant at 590 nm was measured (excitation: 560 nm) in a plate reader (infinite M200 Pro, TECAN, Männedorf, Switzerland). The obtained signal was linearly proportional to the number of living cells inside the sample. CTB results were evaluated from 3 biological replicates. For each replicate, fluorescence intensity was determined from five separate measurements; each averaged over 25 flashes.

Imaging, nanoparticle incubation and microinjection; image analysis: for imaging and manipulation, HeLa wild type (WT) cells were plated on sterilized glass coverslips in 35 mM cell-culture dishes at about 50% confluency. Prior to experiments, cells were washed with a PBS buffer and re-incubated in preheated Leibovitz medium (L15, Thermo Fisher Scientific, Waltham, MA, USA), supplemented with 10% fetal calf serum (FCS) and 1% PenStrep (Thermo Fisher Scientific, Waltham, MA, USA). Imaging was performed in a heating chamber preheated to 37 °C and placed on an inverted microscope (IX83 from Olympus, Shinjuku, Tokyo, Japan) equipped with a 60× oil-objective with N.A. 1.25 and phase contrast Ph3. For fluorescent optical MNPs detection and microinjection, cells were seeded to adhere in 8-well rectangular chambers equipped with a glass bottom (Sarstedt, Nümbrecht, Germany) overnight in an incubator at 37 °C, 5% CO_2. MNPs were

centrifuged (19,000 g for 10 min) and filtered through PTFE filters with 0.2 µm cutoff (Filtropur S 0.2, Sarstedt, Nümbrecht, Germany). After this cleaning routine, cells were incubated for either 6 or 24 h with MNP concentrations of 0.1–1.0 mg/mL. Directly before microscope imaging, cells were washed with preheated PBS and immediately incubated in L15 medium supplemented with FCS and PenStrep as before. MNPs were injected into cells using a micro manipulation system (InjectMan 4 and FemtoJet 4i, Eppendorf, Hamburg, Germany) with microinjection capillaries (Femtotip II, inner diameter of 500 nm, Eppendorf, Hamburg, Germany). For injection, a concentration of 3 mg/mL for each MNP system was used and capillary pressures were set to a pressure difference between the needle tip and the environment of 10 to 20 hPa. The range of image intensities was adjusted manually to optimize visualization of MNPs localizations at the sites of interest.

The MNP uptake and temporal change inside the cells were analyzed using an in-house developed analysis routine written in Matlab (R2019b, The Mathworks Inc., Natick, MA, USA) and ImageJ (version 1.49v, U. S. National Institutes of Health, Bethesda, MD, USA). For their detection, phase contrast and fluorescence image recordings were used. Cells borders were detected using a canny edge detection algorithm. If necessary, cell borders were corrected manually. Single cells were then numbered, and cellular fluorescence intensity was attributed to each corresponding cell. The intensity by area was determined by the quotient of fluorescence intensity over cell area for each cell.

Magnetic Tip Configuration: the magnetic tip was constructed from two magnets (cube: NdFeB, side length 5 mM, gold-plated, product number W-05-G; cuboid: NdFeB, $10 \times 4 \times 1.2$ mM, gold-plated, product number: Q-10-4-1.2-G; both from supermagnete.de by Webcraft GmbH, Gottmadingen, Germany), with a 0.4 mM diameter polished steel wire (product number 1416, from Röslau Stahldraht, Röslau, Germany) attached to it. During the remote manipulation experiments, the magnetic tip was brought to the HeLa WT cell edge at a moderate distance of 10–20 µm for 10–15 min and removed thereafter.

Simulations of the magnetic tip stray field distribution were performed using COMSOL Multiphysics® software (COMSOL Inc., Stockholm, Sweden) with an AC/DC electromagnetics module. The magnetization curve of a neodymium magnet was implemented into the COMSOL library as material reference. According to the mentioned tip wire material, spring steel was chosen as material reference for the tip wire. This data was used to simulate the field distribution of the magnetic tip in the configuration used for remote manipulation experiments.

3. Results and Discussion

Magnetoferritins (MFts) and synomag are two structurally and bio-functionally complementary particles, which were chosen to test their suitability for the manipulation of biological functions inside cells. In case of MFts, the ferritin protein cages served as templates, which were further tailored to feature cytosolic stealth properties as well as to fluoresce for microscopic observation. To this end, we used a bacterial expression vector of the heavy chain subunit of the ferritin protein (HCF) with an mEGFP genetically fused to it. Note that the mEGFP was pointing away from the ferritin surface, as any encapsulation of the fluorescent molecules inside the cage structure was sterically inhibited. In order to render ferritin cages chemically inert and mobile within the living cell environment, a polyethylene glycol (PEG) coupling to its surface with 2 kDa PEG was performed as previously described [21]. The PEGylation was suggested to not only result in cytosolic stealth properties but also to improve cage stability during the magnetic core synthesis at 65 °C [18].

We synthesized a pure magnetic iron oxide core into the functionalized cage by taking advantage of the intrinsic ferroxidase activity of the heavy chain ferritin subunit in a Fenton-like reaction. For details of the MFt synthesis, refer to the Materials and Methods section of this work as well as Lisse et al. [21]. On the other hand, the fully synthetic core-shell MNPs, synomag, were used. These consist of iron oxide cores embedded into a dextran shell, forming an inhomogeneous sphere-like morphology [26]. Due to their production via

Nanomaterials **2021**, *11*, 2267

co-precipitation, synomag are produced at much higher quantities than MFt, albeit with a larger variety in size. Thus, in subsequent steps, their size distribution was narrowed via separation in high gradient magnetic fields. Synomag are commercially available with amine-reactive surface groups for covalent coupling of a biofunctional molecule such as carboxyl-polyethylene glycol (COOH-PEG). While synomag MNPs previously proved to be highly suitable for magnetic hyperthermia [27] and magnetic particle imaging [28,29], they are probed herein with regard to their force and spatial manipulation capability.

3.1. MNP Characterization

To characterize both MNPs, we performed structural and morphological analyses of MFt and synomag particles; the schematic representations are shown in Figure 1a partially created using the CCP4mg Molecular-Graphics Software [30]. Dynamic light scattering (DLS) was used to determine the hydrodynamic particle size and polydispersity. The data of both particles showed a narrow, monomodal size distribution (Figure 1b) from which the effective hydrodynamic diameter D_H was extracted. The peak value of the number distribution revealed a D_H of 39 ± 3 nm and 39 ± 2 nm for MFt and synomag, respectively. Moreover, from the DLS measurement, a polydispersity index (PDI) of 0.11 (MFt) and 0.17 (PEGylated synomag) was derived. Overall, both particles showed appropriate and comparable size homogeneity. Such size monodispersity is important to enable a robust determination of particle properties.

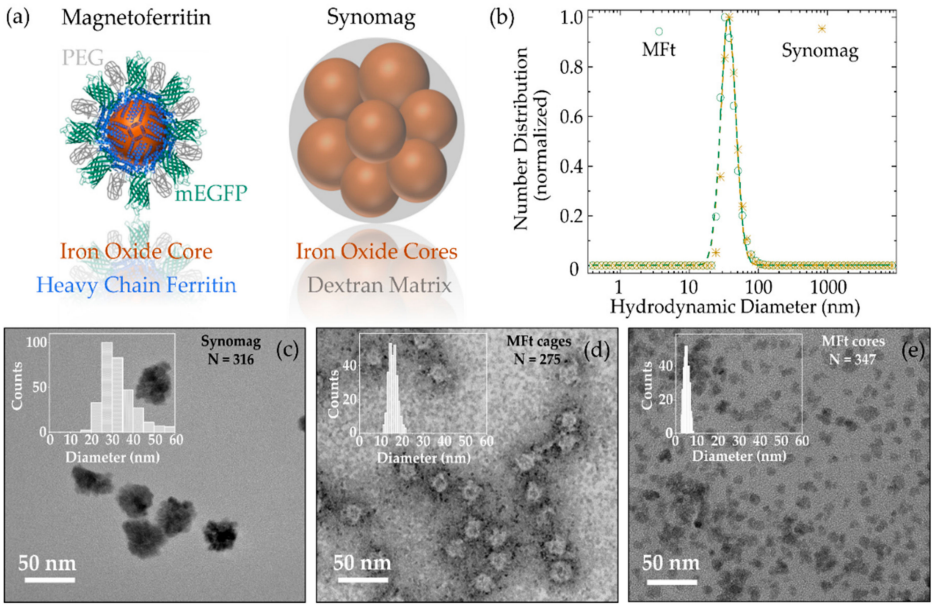

Figure 1. (**a**) Morphology sketches for magnetoferritin (MFt, parts created with permission of [30]) and synomag nanoparticles (NPs). (**b**) Number distribution for MFt (green) and PEGylated synomag (yellow) obtained by dynamic light scattering. Transmission electron microscopy images of (**c**) synomag, (**d**) MFt protein cages stained with uranyl acetate, and (**e**) MFt cores unstained. PEG = polyethylene glycol, mEGFP = monomeric enhanced green fluorescent protein, D_H = hydrodynamic diameter, N = number of evaluated NPs.

It is also essential for any bio-technological or bio-medical application, since the MNPs' response to a magnetic stimulus should be similar. The effective hydrodynamic diameter of <50 nm is suitable for subcellular applications, since cytoplasmic non-specific interactions

between a nanoprobe and the proteins/fibers in the cytoplasm dramatically increase above 50 nm, as previously reported [31–33].

Transmission electron microscopy (TEM) images in Figure 1c–e were recorded to determine particle sizes and morphologies. TEM images of synomag MNPs (Figure 1c) confirmed the 'nanoflower'-like structure of the NPs with irregular surface texture. MFt protein cages were visualized using uranyl acetate (Figure 1d) and showed the predicted uniform spherical structure. Note that mEGFP and PEG on the cage surface were likely to give rise to the increase in roughness of the outer cage. Magnetic cores, after their synthesis into MFts, were depicted in the unstained TEM sample (Figure 1e). Each TEM image was supplemented with a histogram of MNP size and the number of counted MNPs. The average diameter of synomag was 34 ± 8 nm, whereas dried MFt cores and cages were 5 ± 1 nm and 16 ± 2 nm, respectively (Table 1).

Table 1. Physical parameters for MFt and PEGylated synomag: polydispersity index (PdI) from dynamic light scattering (DLS), D_{TEM} solid NP diameter from transmission electron microscopy (TEM), D_{H} hydrodynamic diameter from DLS, and ζ-potential from electrophoretic light scattering (ELS). MFt was stabilized in HEPES-2 buffer, synomag in PBS (pH 7.4). Additional data can be found in Tables S1 and S2, Supplementary Information.

Sample	PdI	D_H, nm	D_{TEM}, nm	ζ-Potential, mV
PEGylated magnetoferritin	0.11 ± 0.01	39 ± 3	Cages: 16 ± 2 Cores: 5 ± 1	−3.7
PEGylated Synomag	0.17 ± 0.03	39 ± 2	34 ± 8	−2.0

In the case of MFt, the sizes compared well with the protein crystalline structure, with a cage inner diameter of 8 nm and an outer diameter of 12 nm [34]. Based on structural considerations, mEGFP and PEG were predicted to add ~3 nm to the surface thickness [21]. Hence, the theoretically expected outer diameter of 18 nm compares well with our TEM results [35]. A comparison with the hydrodynamic diameters showed that synomag exhibited an 8.3 nm smaller diameter than its hydrodynamic diameter, which may be well explained by a ~4 nm hydrodynamic shell around the NPs [26]. MFt cages turned out to be about two times smaller than the hydrodynamic diameter. This discrepancy may have arisen from the additional hydrodynamic drag the PEG shell causes, whereby the size is overestimated during the DLS measurement, as previously reported [36]. Other potential explanations are the presence of larger iron oxide cores which form outside of the protein cages during the core synthesis step, or from remaining particle–particle interactions wherever the PEG passivation was insufficient to suppress all non-specific interactions.

Finally, differences between the solid size and the size in the solution were expected from theoretical considerations, since the hydrodynamic size determination assumes diffusion of an ideal sphere, as reported before [37–39]. Subsequently, electrophoretic light scattering (ELS) measurements were performed to determine the NP surface potential; the so-called ζ-potential. For synomag and MFt, the ζ-potential distribution exhibited a monomodal peak, confirming their surface homogeneity (data not shown) [39]. For both NPs, the ζ-potential turned out to be weakly negative: −3.7 mV for MFt and −2.0 mV for synomag (Table 1). While both of these ζ-potential values deviate only slightly from zero, their negative charge may support colloidal stability, cellular uptake, and cytoplasmic stealth properties, given the negative charge of many membrane and intracellular molecules [40,41]. Colloidal stability of synomag NPs was qualitatively assessed over the duration of 1 month (Figure S2). In addition, NPs of weak negative ζ-potential between −2 to −15 mV were recently shown to exhibit high intracellular mobility [32,42].

A major challenge in realizing a remote and efficient manipulation of MNPs in the cell environment is to adjust the NPs' magnetic properties, such as their magnetization and

Nanomaterials **2021**, *11*, 2267

magnetic anisotropy, to the external magnetic fields. To characterize the magnetic response of the herein presented NPs, conventional magnetic field- and temperature-dependent vibrating sample magnetometry (VSM) were conducted. Figure 2a,b shows magnetization curves for MFt and synomag. At T = 300 K, both samples exhibited superparamagnetic behavior and saturation magnetizations of 42 Am^2/kg (MFt) and 69 Am^2/kg (synomag). The insets of Figure 2a,b present the low field region. The superparamagnetic behavior is essential to reduce magnetic dipole–dipole interactions between the particles and hence their propensity to form chains. Exhibiting this property at physiological temperatures is further important to enable a manipulation of each particle individually without any application of torque to the NPs. At T = 5 K, both samples exhibited a hysteresis loop with coercive fields of 31 mT and 8 mT for MFt and synomag, respectively. This is a typical signature of the ferrimagnetic nature of the respective Fe oxides. The saturation magnetization at T = 5 K was 56 Am^2/kg for MFt and 81 Am^2/kg for synomag, which are both higher than the values at T = 300 K, as expected, but lower than the volume magnetizations of bulk magnetite (92 Am^2/kg) and maghemite (82 Am^2/kg) [43].

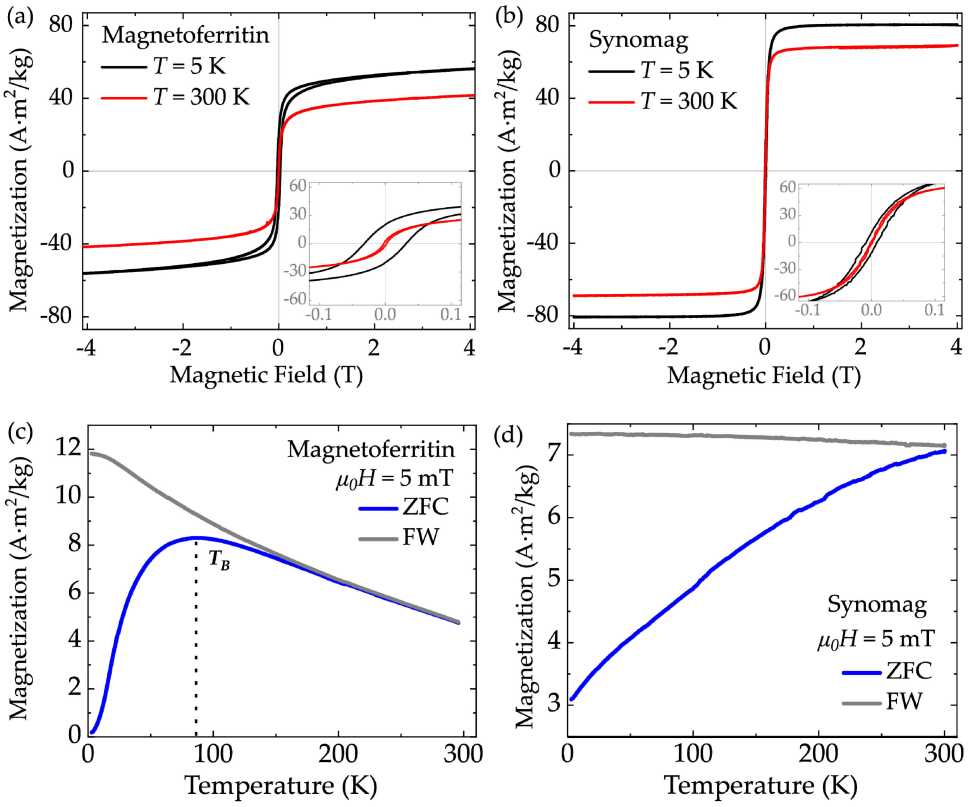

Figure 2. Magnetization as function of magnetic field for (**a**) magnetoferritin and (**b**) synomag nanoparticles. ZFC/FW for (**c**) magnetoferritin and (**d**) synomag measured in 5 mT. T_B = characteristic blocking temperature, ZFC = zero field cooling, FW = field warming.

Figure 2c,d shows zero-field-cooling/field-warming (ZFC/FW) experiments. MFt exhibited a broad maximum centered at 86 K, which indicates the effective blocking temperature T_B, and an irreversibility point at about 150 K. The MFt ZFC/FW maximum

at 86 K found in this work is significantly larger than the T_B reported in [44] (T_B = 40 K) and in [45] (T_B = 13 K). This shift in T_B may have resulted from reduced distances and dipole–dipole interactions between cores in the powdered samples after the drying process. Here, in order to minimize paramagnetic contributions to the VSM data, the salt in the medium was strongly diluted, which in turn may have affected protein cage stability. Other contributions may arise from interactions between cores synthesized outside of the cages. Since the relation $21 \cdot k_B T_B \approx K_{eff} V$ holds [45] for VSM measurements with an averaging time of 1 s and blocking temperature T_B, the effective magnetic anisotropy value K_{eff} can be estimated with the particle volume V. Using the mean particle diameter of 5–6 nm, we obtained K_{eff} = 2–4 · 10^5 J/m^3. This value is reasonable for Fe oxide MNPs of small sizes, exhibiting a large surface to volume ratio. Here, magnetic moments at the surface of an MNP experience broken symmetry and crystal deterioration leading to a larger surface anisotropy compared to volumetric magnetite [43,46]. Such increasing effective magnetic anisotropies are typically observed with reduced MNP sizes [47–49].

For synomag, experimental magnetic field and temperature dependencies of the magnetization obtained in this work complement the characterization previously reported in [27]. We obtained a broad distribution of blocking temperatures with an anticipated center slightly above physiological temperature (see Figure 2d). This indicates that synomag MNPs are designed to effectuate maximal hysteretic losses in radio-frequency alternating magnetic fields and thus exhibit good heating capabilities for magnetic particle hyperthermia [19,27]. Taken together, both MNP systems possessed the key magnetic properties (superparamagnetism, sufficient magnetic response) necessary to realize a remote manipulation in external magnetic fields.

3.2. MNP Cellular Uptake

Despite protective coatings, iron oxide MNPs are still cautiously applied in nanomedicine due to potential side effects they could implicate after being injected into living tissue or cells [1,50]. Here, HeLa WT cells were used with the CellTiter-Blue assay to test the cell viability of both MNP systems, within the concentration range of 0.1–4.0 mg/mL. MNPs were transferred into the cells via a standard incubation protocol. As controls, untreated cells in DMEM and cells treated with MNP buffers were used. As an additional control, cells were killed by addition of 0.1% Triton-X for 30 min before imaging was started. As shown in Figure 3, traceable harmful effects for both samples appeared only at concentrations above 1.0 mg/mL. For ferritin cages (Figure 3a), a small reduction in viability was also detected in the control measurement with HEPES-2 buffer. Similarly, a viability drop for synomag only occurred at concentrations above 1.0 mg/mL. Addition of PBS did not affect the cell viability. In conclusion, both MNPs can be safely brought into the cell environment at concentrations up to 2.0 mg/mL. Hence, for subsequent particle incubation experiments, the upper concentration limit was set to 1.0 mg/mL (equals to 6.4 µM for MFt and 18.3 pM for synomag) to rule out any negative MNP-related effect. Previous studies investigating the effects of iron oxide NPs on cell viability reported similar results, where multi-core iron oxide NPs passivated with citrate of up to 5 mM showed little negative effects on cells [51]. Additionally, PEGylation and passivation was reported to reduce cellular damage upon uptake [52,53], supporting our particle passivation strategy.

In order to characterize the process of particle incubation and uptake further, and in view of subsequent magnetic manipulation, where an efficient particle delivery into the cell is desirable, we evaluated the intracellular NP amount via image data analysis of their fluorescence. NP uptake by HeLa WT cells was monitored at distinct incubation times of 6 and 24 h to probe different long-time temporal effects as well as for concentrations between 0.1–1.0 mg/mL. In this study, PEGylated Ft cages without a magnetic core were used, since magnetoferritin is freshly produced only in small amounts and since the magnetic properties are not relevant for this assay. Care was taken to record the cell samples at identical imaging settings, in order to not bias the detected fluorescence intensities. Obtained data was evaluated using a custom-written Matlab algorithm. Therein, the

Nanomaterials **2021**, *11*, 2267

intensity per pixel inside each cell as a function of NP concentration was extracted and normalized to the amount of cells found (see Figure 4a for Ft cages and Figure 4d for synomag MNPs). Ft cages demonstrated a substantially larger cellular uptake compared to synomag, with an increase of the MNP concentration inside the cell if incubated with higher MNP concentration. Evaluation of the uptake for different concentrations after 6 h of incubation showed only a slight increase in the recorded intensity of both particles, even at the highest concentration of 1 mg/mL (Figure 4d). After 24 h, a higher amount of MNPs was taken up, and this increased with increasing particle concentration in the medium. Figure 4b,e show phase contrast images of the cells and Figure 4c,f are the corresponding fluorescence images indicating the MNP distribution after 24 h of incubation. In Figure 4c, Ft cages show a cloud-like accumulation around the nucleus. This is a typical signature of particles which are taken up via the endosomal pathway. Here, after initial encapsulation within the endosome, the cargo is transported towards the endoplasmic reticulum or Golgi apparatus, where it is further processed. In contrast, synomag MNPs were more sparsely distributed, accumulating around the nucleus as well as in spots across the cell (see Figure 4f). Interestingly, according to Figure 4a,d, Ft NPs were taken up more efficiently compared to synomag MNPs. This may be attributed to the twofold difference in their solid diameters. Previous studies already reported a positive effect of a decreasing particle size on cellular uptake [54]. The slight negative ζ-potential (see Tables S1 and S2) measured for both NPs may also enhance particle uptake, since most intracellular proteins and lipids are negatively charged. The negative surface charge can further protect NPs against non-specific interactions inside the cell, preventing their entrapment [32]. For our MNPs, the stealth properties were further enhanced by modifying the NPs surface using PEG as passivating agent, as previously suggested [38,42,54].

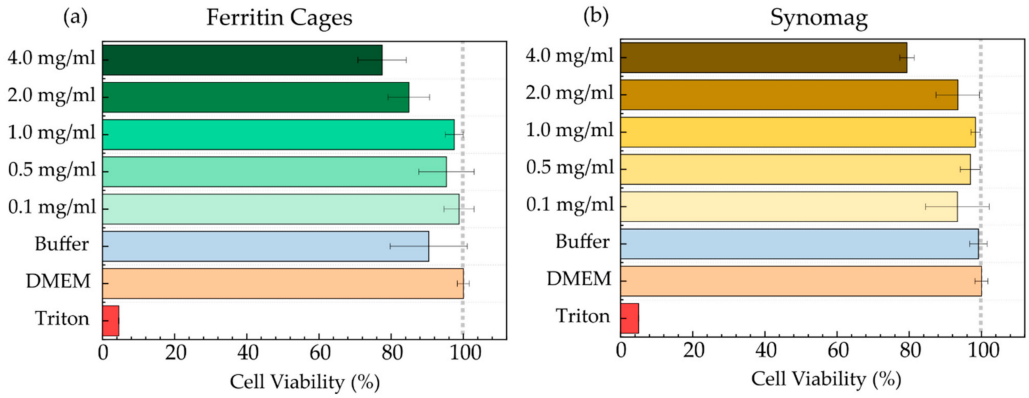

Figure 3. Cell viability Assay (CellTiter-Blue from Promega) measured after 24 h in HeLa WT cells for (**a**) ferritin cages and (**b**) synomag. Data was normalized to DMEM as positive control with untreated cells. Triton at 0.1% leads to cell death and was therefore used as negative control. The buffer control determines the effect of plain buffer on cell viability. The highest volume of MNP solution that was added during MNP addition was used here. Buffers were HEPES-2 for ferritin and PBS (pH 7.4) for synomag. Error bars represent the standard deviation of five measurements carried out for three biological replicates per concentration.

Nanomaterials **2021**, *11*, 2267

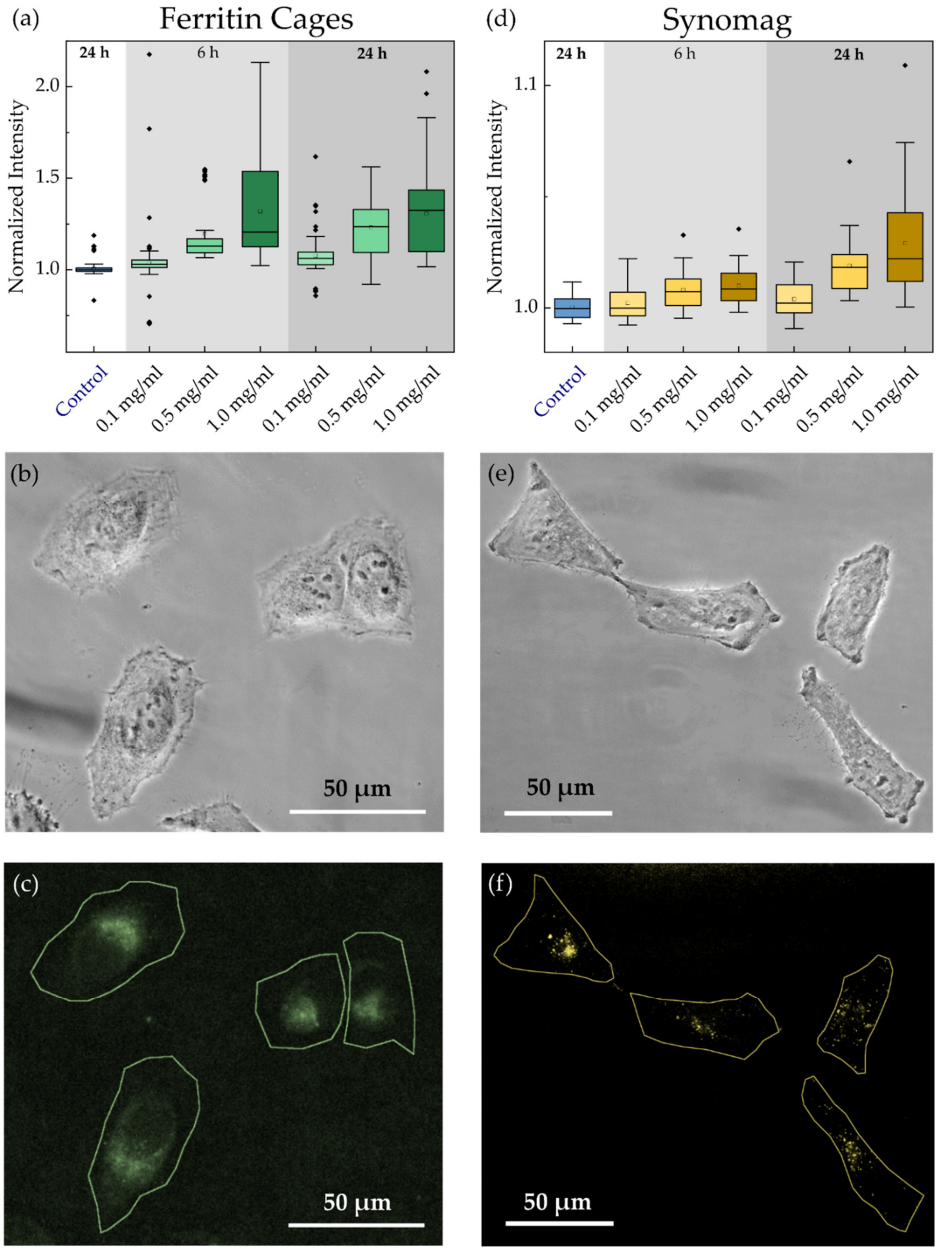

Figure 4. Normalized HeLa WT cellular uptake of (**a**) ferritin cages and (**d**) synomag nanoparticles (NH_2 surface) as function of concentration. Intensity is given as intensity per pixel inside the cell. Particle systems were transferred into the cells via incubation for 6 or 24 h. (**b**,**c**) Phase contrast image and corresponding fluorescent image with cell outlines recorded using 470/525 nm filter for ferritin cages. (**e**,**f**) Phase contrast image and corresponding fluorescent image with cell outlines recorded using 545/620 nm filter for synomag NPs. Box plots show the distribution of 100–260 cells recorded in each of five independent measurements per condition.

Nanomaterials **2021**, *11*, 2267

3.3. Magnetic Tip Characterization

After successful uptake, we then sought to realize the remote and localized manipulation of MNPs inside cells using a magnetic tip. To this end, first the magnetic tip and the generated magnetic flux density gradient had to be characterized. The magnetic tip was set up as a combination of two permanent magnets and a string wire was attached to the lower magnet (Figure 5a, inset). The string wire was made of spring steel and pulled into a tip of parabolic-like shape.

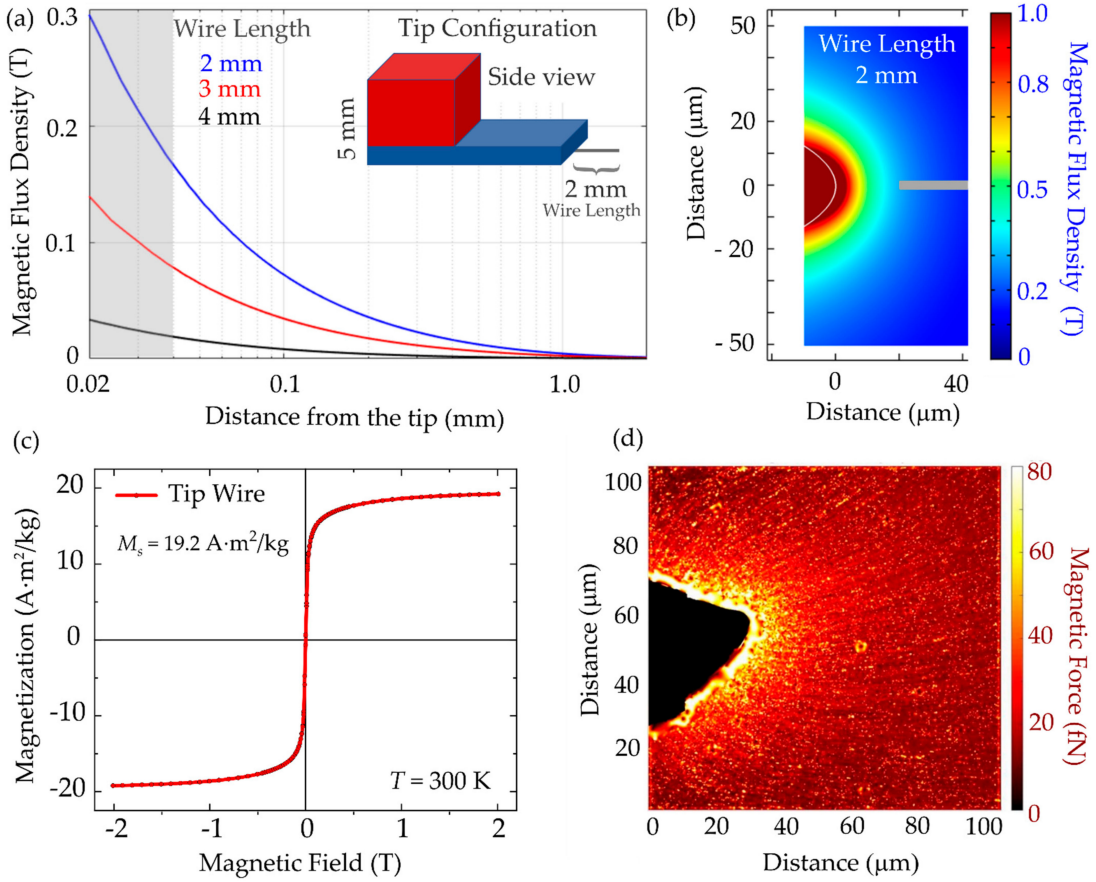

Figure 5. Magnetic tip for remote manipulation. Simulated magnetic flux density (**a**) for a tip wire extending 2, 3, or 4 mM from the magnet as a function of distance from the tip, and (**b**) as 2D projection from the top with 2 mM long tip wire. Grey line in (**b**) indicates the position from where the data in (**a**)—highlighted by the grey area—was extracted for the 2 mM tip wire. Inset in (**a**) shows a sketch of the tip configuration consisting of two magnets (red, blue) and a tip wire of 2 mM attached to the magnets. (**c**) Magnetization curves of the tip wire measured at T = 300 K. (**d**) Magnetic force measured via nanoparticle attraction to the magnetic tip with 2 mM tip wire. The line texture resulted from the tracked particles.

To characterize the magnetic flux density generated by the magnetic tip, 3D finite element modeling as well as an in vitro calibration assay were performed. In case of finite element modeling, the magnetic flux density was simulated for 2, 3, and 4 mM lengths of the tip wire and plotted against the distance from the tip (see Figure 5a). Unsurprisingly, the 2 mM long tip exhibited the highest magnetic flux densities at small distances that were critical for remote manipulation. Moreover, the strong dependency of the absolute magnetic

flux density values indicates how important an accurate choice of wire length is. The grey area in Figure 5a corresponds to the grey line in Figure 5b, where the simulated magnetic flux density around the magnetic tip is shown as 2D projection from the top. Figure 5c depicts the magnetization curve of the tip material with a saturation magnetization of 19.2 Am^2/kg and a coercive field of 1.2 mT. Figure 5d shows the result of an in vitro assay, which was introduced to measure the magnetic force generated by the magnetic tip over 100 µm distance. This is the relevant scale for particle manipulation experiments in single cells.

To realize this assay, precise positioning of the tip inside the sample was achieved using an InjectMan 4 micromanipulator, where the three spatial axes as well as the angle of the magnetic tip could be adjusted with 20 nm spatial precision. The tip was positioned in a mixture of 85% glycerin and 15% distilled water, to mimic intracellular viscosity conditions. As magnetic nanoparticle probes, Nanomag-D with 250 nm hydrodynamic diameter (micromod GmbH, Rostock, Germany) were used. These enabled individual detection and reliable tracking with phase contrast microscopy. MNPs within the glycerin–water mixture were attracted toward the tip, and the trajectories of several 100 particles were recorded. Thereafter, the Fiji plugin, TrackMate, and self-written routines were used to trace the particle trajectories and to calculate the velocity vectors along the particle trajectory [55]. Using Stokes' law,

$$F_{mag} = 6\pi\eta R v, \tag{1}$$

the magnetic force generated by the tip was calculated, which typically lay within the range of 10–100 fN. Here, η is the dynamic viscosity of the medium as determined in [32], R is the MNP radius, and v is the velocity of MNPs extracted from the single-particle trajectories.

3.4. MNP Manipulation in Cells

Having established the above prerequisites for the magnetic manipulation approach, we probed MNP transfer into HeLa WT cells and their subsequent intracellular mobility via two approaches: MNP injection using a microneedle (Figure 6) and MNP incubation (Figure 7).

In both cases, MNP localization was recorded via fluorescence microscopy in the presence of the magnetic tip for about 30 min followed by recordings in the magnetic tip's absence. Fluorescence intensity distribution inside a single cell was monitored and plotted as a function of time for regions within the magnetic tip's sphere of action. The mean intensity I for this region as a function of time was fitted by an exponential fit function to obtain the characteristic accumulation τ_{acc} and relaxation τ_{rel} times:

$$I_{acc} = -A \cdot e^{-\frac{(t+B)}{\tau_{acc}}} + C \tag{2}$$

and

$$I_{rel} = A \cdot e^{-\frac{(t-B)}{\tau_{rel}}} + C \tag{3}$$

where A is a fit parameter reflecting the intensity plateau of the exponential function on long time scales, B represents the temporal off-set of the starting point of attraction/relaxation, C stands for the intensity offset, and τ_{acc} and τ_{rel} are characteristic accumulation and relaxation times, respectively.

Injection was performed using a microinjector (FemtoJet 4i) in combination with a micromanipulator (InjectMan 4). For particle delivery, a microinjection capillary (Femtotip II) with an inner diameter of 500 nm was used. Dispersed particles should effortlessly pass through this capillary, underlining the importance of using a highly homogeneous and non-reactive MNP sample. MFt with PEGylated surface was readily injected. Synomag with a NH_2 coating was tested initially, but experienced aggregation inside the injection needle, which irreversibly blocked it. Since surface passivated MNPs are expected to exhibit reduced particle–particle interactions and to be less prone to aggregation, the PEGylation

Nanomaterials **2021**, *11*, 2267

protocol for MFt was also conducted for synomag NPs. The effective hydrodynamic diameter after PEGylation changed from 42 ± 1 to 39 ± 2 (Table S2, Supplementary Information) and was hence similar to the one of MFt (Figure 1). This PEG passivation indeed facilitated synomag microinjection.

Injected MFts (see Figure 6a–d) were instantaneously homogeneously distributed after microinjection into the cell. It was possible to both attract and accumulate particles using a magnetic tip. Once the magnetic tip was removed, MFts returned to the initial homogeneous distribution within minutes. Figure 6e shows the relatively fast kinetics with a characteristic accumulation time τ_{acc} of 2.2 ± 0.1 min and a relaxation time τ_{rel} of 3.1 ± 0.1 min. Very similar values were reported in a previous study, where PEGylated core-shell maghemite–silica particles with diameters of about 40 nm were accumulated within τ_{acc} of ~1 min, whereas the relaxation times τ_{rel} were ~10 min with a large distribution between 2 and 35 min [31].

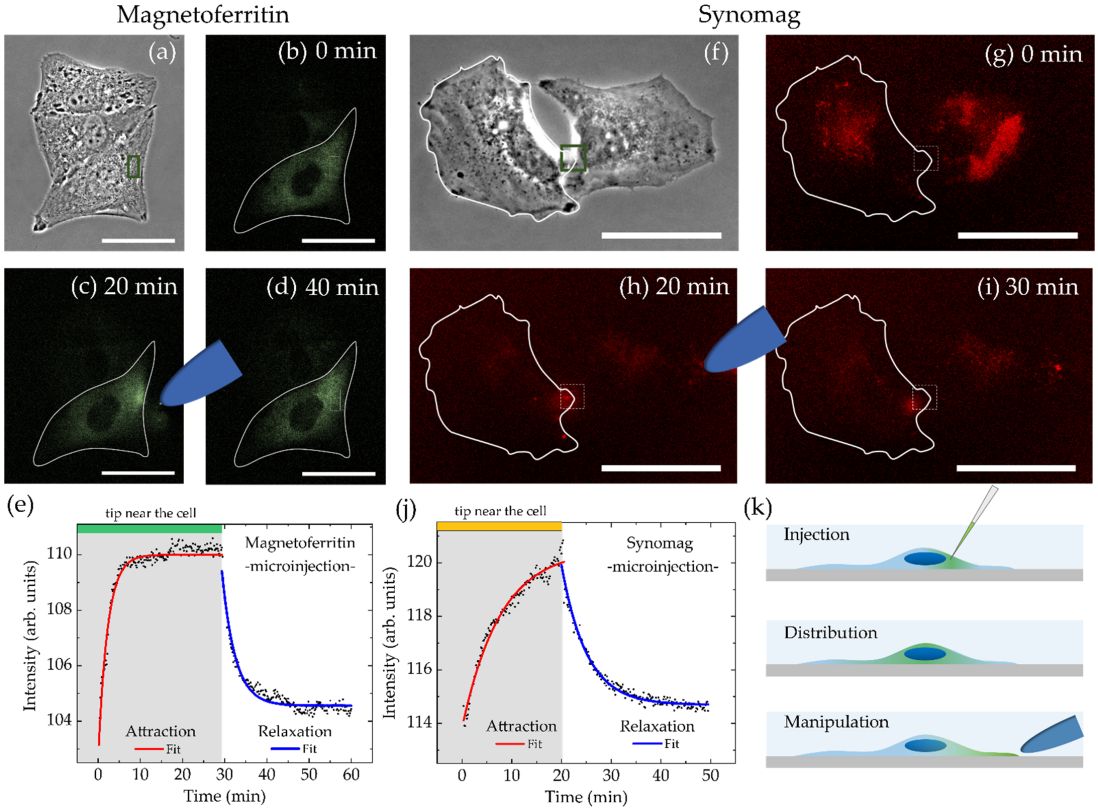

Figure 6. Spatial manipulation of (**a**–**d**) magnetoferritin and (**f**–**i**) synomag nanoparticles dispersed inside cytoplasm of living HeLa WT cells after microinjection recorded over 40 min. Scale bars are 50 µm. (**e**,**j**) show corresponding mean intensities over time with fit functions to characterize nanoparticle accumulation near the magnetic tip (green box in (**a**,**f**)) and relaxation after tip removal. Distance between magnetic tip and analyzed region was (MFt) 6 µm or (synomag) 75 µm, respectively. (**k**) illustrates the experimental setup for microinjection.

Nanomaterials **2021**, *11*, 2267

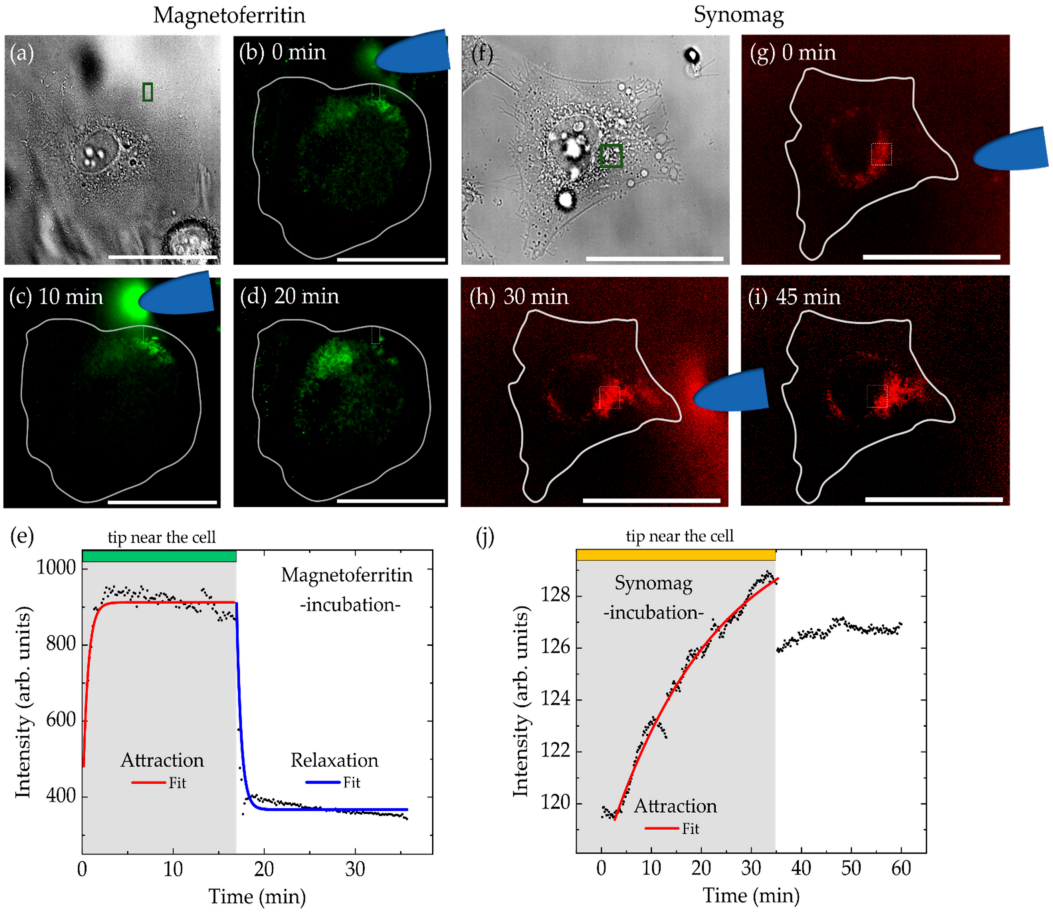

Figure 7. Spatial manipulation of (**a**–**e**) magnetoferritin and (**f**–**j**) synomag nanoparticles transferred by cellular uptake. MNPs were possibly localized on the outer membrane or within cellular vesicles of single HeLa WT cells after 5 and 24 h incubation, respectively. Scale bars are 50 µm. (**e**,**j**) show corresponding mean intensity over time along with the fit to characterize accumulation time near the magnetic tip (green box in (**a**,**f**)) and relaxation time after the tip removal. Distance between magnetic tip and analyzed region (green box in (**a**,**f**)) was (MFt) 10 µm or (synomag) 30 µm, respectively.

In contrast, obtaining a homogeneous particle distribution after synomag injection appeared to be more difficult than with MFt. An example of microinjection of PEGylated synomag into HeLa WT is given in Figure 6f–i. Synomag MNPs exhibited heterogeneous particle distribution inside cells and, despite the PEG passivation, were still prone to entrapment in the cytoplasm. Nevertheless, in some cases, MNPs could be attracted via the magnetic tip. After magnetic tip removal, the relaxation dynamics were recorded and exhibited significant loss in mobility for synomag compared to MFt. Attraction and relaxation times for the case shown in Figure 6 increased to τ_{acc} = 5.1 ± 0.1 min and τ_{rel} = 7.7 ± 0.2 min. Here, in contrast to magnetoferritin, particles did not fully redisperse but accumulated at a slightly different position inside the cell. Intriguingly, synomag attraction towards the magnetic tip could be monitored for distances up to 100 µm. This can be attributed to the higher saturation magnetization and magnetic moment (Figure 2b), corresponding to higher forces of synomag compared to MFt. Thus, higher forces can develop and attract particles across the cell over large distances, despite increasing non-

specific interactions. Qualitatively, successful particle attraction was observed in around 10% of the analyzed cells, of which 50% exhibited a relaxation of particle distributions after tip removal.

In the case of magnetic manipulation after particle incubation, we considered the results of our particle uptake study as presented in Figure 4. Choosing incubation conditions of 0.5 mg/mL of MFt in the extracellular medium over 24 h led to the expected high particle uptake. However, MFts could not be attracted by a magnetic tip, not even over distances less than 10 µm. Most probably this was due to increasing intracellular interactions and particle recognition by the cell's autophagy machinery on long time scales. Therefore, shorter incubation times of 1, 2, 3, 4, and 5 h with 0.5 mg/mL of MFt in the extracellular medium were tested. Cells were washed and, upon observation under the microscope, those cells exhibiting sufficient MFt signal were monitored for 1 h while approaching and removing a magnetic tip.

Figure 7a–d shows a cell after incubation with MFt for 5 h. Here, prior to magnetic manipulation, MFts were evenly distributed across the cell. Magnetic particles were attracted with a characteristic time of τ_{acc} = 0.56 ± 0.04 min and redistribution in absence of the magnetic tip occurred with a characteristic time of τ_{rel} = 0.53 ± 0.03 min. These values are distinctively smaller than values from injection studies. Changes in the attraction kinetics may, in general, also be attributed to variable distances between the magnetic tip and the MNPs, since the magnetic attraction force scales proportional to $1/r^2$, where r is the distance. However, in this case, both attraction and relaxation dynamics evolved on fast timescales, suggesting that MFts did not enter the highly viscous cytoplasm of the cell. Instead, after the short incubation time used, MFts may be attached on the outer side of the cell plasma membrane, wherefore particles could be more easily attracted towards the tip. In conclusion, manipulation of MFts after incubation was difficult to realize as, in most of the cases, MFt remained immobile. Thus, magnetic forces in the fN range will only attract the MNPs when the applied force surpasses any intracellular interaction. Note that for longer measurement times the magnetic tip became increasingly fluorescent due to freely moving MFt particles in the extracellular medium. These were present despite several washing steps prior to imaging. While this was disturbing during imaging, the MNP attraction by the tip provided evidence that the particles were still magnetic after 24 h incubation (see Figure 7c).

In Figure 7f–j, an example of incubation and manipulation of PEGylated synomag is shown. In contrast to MFt, synomag manipulation was possible even after 24 h of incubation. The cell shown in Figure 7f was incubated with a concentration of 0.5 mg/mL for 24 h, washed, and then analyzed under the microscope. Although being mostly located around the nucleus, PEGylated synomag MNPs were still attracted by the magnetic tip. The accumulation time τ_{acc} amounted to 21.8 ± 0.3 min, and was significantly higher than for MFt and synomag after MNP injection. As discussed in the context of Figure 4, this may be attributed to an entrapment of synomag inside cellular vesicles during particle uptake. In line with this interpretation, no intensity relaxation and particle redistribution after magnetic tip removal was observed (Figure 7j). Instead, similarly to Figure 7c, the magnetic tip gradually accumulated remaining MNPs from the extracellular medium and showed a fluorescent signal, confirming their magnetic response even after 24 h of incubation. However, as a result of this attraction, a distinct drop of intensity was observed upon tip removal, after which intensities remained constant (see Figure 7j). Accordingly, the fit for the relaxation time determination in this case became obsolete. Based on the aforementioned results concerning synomag, we hence conclude that higher magnetic forces exerted by PEGylated synomag—in contrast to MFt—can exceed the non-specific interaction forces. The particles, as well as any coupled molecule, may then be pulled across the cell. Such pulling may also affect the cytoskeletal organization in those cases, where MNPs encapsulated in endosomes would couple to cytoskeletal filaments. The measured attraction/relaxation kinetics are sufficiently slow to allow for some spatial relocalization.

Staining of intracellular filaments and their monitoring during manipulation may be of interest for further studies on cell cytoskeletal mechanics.

In both approaches, we cannot rule out that biodegradation would affect the success rate of our magnetic manipulation approach. However, successful manipulation experiments show that magnetically responding particles and the fluorescence signal are colocalized during attraction toward the magnetic tip. In addition, in a previous study [21], one of the authors showed how surface PEGylation on magnetoferritin helps to elude intracellular xenorecognition and biodegradation. To clarify the intracellular state of MNP integrity, further assays need to be developed.

The possibility to manipulate MNPs after incubation and uptake by cells is of particular interest, since MNP incubation affects multiple cells simultaneously and is considered a multicellular approach. Understanding MNP incubation and uptake is further useful in magnetic cell sorting studies, as suggested by Massner et al. [45]. In addition, the possibility to transfer localized forces to the cell is important whenever mechanical forces influence a cellular process. For example, Tseng et al. showed that the cell orientation during cell division is susceptible to MNP-mediated force application [56], and Seo et al. [11] demonstrated how mechanosensitive receptors on the cell surface influence cell expression. Here, MNP attraction was realized over distances as far as 100 µm, applying forces in the fN regime. An upscaling to larger manipulation distances might be achieved with a different magnetic manipulation setup, where similar magnetic field gradients (~10^4 T/m) at larger distances (~mm) are generated. In this case, an in vivo manipulation can also be envisaged. In this work, we have provided a proof of principle, under which conditions a spatial relocalization or a force stimulus can be applied. This may be further used for the manipulation of intracellular cell organization as well as for the stimulation of single cell signaling.

4. Conclusions

In this work, we compared two new classes of MNPs: semisynthetic single core magnetoferritin (MFt) and multicore synomag MNPs, in view of future magnetic manipulation studies in single cells. Both particles fulfilled the prerequisite of size monodispersity and high biocompatibility up to MNP concentrations of 2 mg/mL. Efficient intracellular transfer of MNPs was realized by simple MNP incubation, which is advantageous for nanomedicine applications compared to other transfer methods. We attributed higher transfer efficiencies in MFts compared to synomag to the smaller size and the slightly more negative ζ-potential. The difference in magnetic core size further gave rise to varying forces in in vitro experiments, with the larger magnetic moments of synomag developing higher magnetic force responses than MFts. These MNP characteristics were ultimately tested in two subcellular manipulation approaches: (1) particle microinjection, where free particle motion in the cell cytoplasm and reversible particle redistribution via a magnetic tip was realized. In this first approach, MFts exhibited higher mobility and reversible attraction–relaxation kinetics compared to synomag NPs. The second manipulation approach was based on (2) particle incubation and uptake by cells. In this second approach, most NPs accumulated at cell organelles and exhibited reduced mobility. Magnetic field gradients probed the NP mechanical force response, which successfully led to synomag attraction across the cell, whereas MFts remained immobile. Hence, MFts are more suitable for non-invasive spatial manipulation approaches in cells, whereas synomag are well utilized to mediate nanoscale forces. The experimental assays described and the values reported for MNPs provide benchmarks for future magnetic manipulation experiments, whenever a spatial or mechanical manipulation of a biological process is envisaged.

Supplementary Materials: The following are available online at https://www.mdpi.com/article/10.3390/nano11092267/s1, Figure S1: SDS-PAGE analysis of purification steps of ferritin shells; Table S1: Hydrodynamic size, polydispersity index and ζ-potential for subsequent steps of magnetoferritin synthesis; Table S2: Hydrodynamic size, polydispersity index and ζ-potential for synomag nanoparticles with three surface modifications. Figure S2: Qualitative assessment of the colloidal stability for synomag nanoparticles over time from 1 min up to 1 month.

Author Contributions: Conceptualization, C.M. and I.P.N.; methodology, C.M., I.P.N., A.N., U.W. and N.B.; software, A.N. and J.-S.B.; investigation, I.P.N., A.N., J.-S.B., U.W., M.R.S. and M.O.; resources, C.M., M.K. and M.F.; writing—original draft preparation, I.P.N.; writing—review and editing, C.M., I.P.N., A.N. and U.W.; visualization, I.P.N. and A.N.; supervision, C.M. and I.P.N.; project administration, I.P.N.; funding acquisition, C.M., M.K. and M.F. All authors have read and agreed to the published version of the manuscript.

Funding: C.M. acknowledges financial support of the Deutsche Forschungsgemeinschaft (DFG) through SFB1208 'Identity and Dynamics of Membrane Systems' (A12). C.M., I.N. and A.N. acknowledge financial support via the 'Freigeist fellowship' of VolkswagenFoundation. This work was performed on synomag particles purchased from Micromod Partikeltechnologie GmbH with financial support from Fonds der Chemischen Industrie. The authors acknowledge the DFG and the State of North Rhine–Westphalia for funding the cryo-TEM (INST 208/749-1 FUGG).

Data Availability Statement: We can provide original data upon request.

Acknowledgments: We acknowledge C. Seidel and L. Schmitt and their groups for sharing their biochemistry equipment and expert knowledge on its handling. We thank the group of M. Coppey and B. Hajj at the Laboratoire Physico-Chimie, Institut Curie, Paris, France for providing the mEGFP::HCF plasmid. C.M. acknowledges Maxime Dahan†, Institut Curie, for introduction to the topic. We thank Daniel Kuckla for microscopy support, optimization of magnetic core loading setup, and useful comments to improve the manuscript.

Conflicts of Interest: The authors declare no conflict of interest.

References

1. Anik, M.I.; Hossain, M.K.; Hossain, I.; Mahfuz, A.M.U.B.; Rahman, M.T.; Ahmed, I. Recent Progress of Magnetic Nanoparticles in Biomedical Applications: A Review. *Nano Sel.* **2021**, *2*, 1146–1186. [CrossRef]
2. Kim, C.; Kim, H.; Park, H.; Lee, K.Y. Controlling the Porous Structure of Alginate Ferrogel for Anticancer Drug Delivery under Magnetic Stimulation. *Carbohydr. Polym.* **2019**, *223*, 115045. [CrossRef] [PubMed]
3. Pavlov, A.M.; Gabriel, S.A.; Sukhorukov, G.B.; Gould, D.J. Improved and Targeted Delivery of Bioactive Molecules to Cells with Magnetic Layer-by-Layer Assembled Microcapsules. *Nanoscale* **2015**, *7*, 9686–9693. [CrossRef] [PubMed]
4. Moghram, W.I.; Kruger, A.; Sander, E.A.; Selby, J.C. Magnetic Tweezers with Magnetic Flux Density Feedback Control. *Rev. Sci. Instrum.* **2021**, *92*, 034101. [CrossRef] [PubMed]
5. Li, J.H.; Santos-Otte, P.; Au, B.; Rentsch, J.; Block, S.; Ewers, H. Directed Manipulation of Membrane Proteins by Fluorescent Magnetic Nanoparticles. *Nat. Commun.* **2020**, *11*, 4259. [CrossRef]
6. Pankhurst, Q.A.; Thanh, N.K.T.; Jones, S.K.; Dobson, J. Progress in Applications of Magnetic Nanoparticles in Biomedicine. *J. Phys. D Appl. Phys.* **2009**, *42*, 224001. [CrossRef]
7. Sangaiya, P.; Jayaprakash, R. A Review on Iron Oxide Nanoparticles and Their Biomedical Applications. *J. Supercond. Nov. Magn.* **2018**, *31*, 3397–3413. [CrossRef]
8. Kurlyandskaya, G.V.; Novoselova, I.P.; Schupletsova, V.V.; Andrade, R.; Dunec, N.A.; Litvinova, L.S.; Safronov, A.P.; Yurova, K.A.; Kulesh, N.A.; Dzyuman, A.N.; et al. Nanoparticles for Magnetic Biosensing Systems. *J. Magn. Magn. Mater.* **2017**, *431*, 249–254. [CrossRef]
9. Avugadda, S.K.; Wickramasinghe, S.; Niculaes, D.; Ju, M.; Lak, A.; Silvestri, N.; Nitti, S.; Roy, I.; Samia, A.C.S.; Pellegrino, T. Uncovering the Magnetic Particle Imaging and Magnetic Resonance Imaging Features of Iron Oxide Nanocube Clusters. *Nanomaterials* **2021**, *11*, 62.
10. Etoc, F.; Lisse, D.; Bellaiche, Y.; Piehler, J.; Coppey, M.; Dahan, M. Subcellular Control of Rac-GTPase Signalling by Magnetogenetic Manipulation Inside Living Cells. *Nat. Nanotechnol.* **2013**, *8*, 193–198. [CrossRef]
11. Seo, D.; Southard, K.M.; Kim, J.; Lee, H.J.; Farlow, J.; Lee, J.; Litt, D.B.; Haas, T.; Alivisatos, A.P.; Cheon, J.; et al. A Mechanogenetic Toolkit for Interrogating Cell Signaling in Space and Time. *Cell* **2016**, *165*, 1507–1518. [CrossRef] [PubMed]
12. Huang, H.; Delikanli, S.; Zeng, H.; Ferkey, D.M.; Pralle, A. Remote Control of Ion Channels and Neurons through Magnetic-Field Heating of Nanoparticles. *Nat. Nanotechnol.* **2010**, *5*, 602–606. [CrossRef] [PubMed]
13. Liang, Y.; Xie, J.; Yu, J.; Zheng, Z.; Liu, F.; Yang, A. Recent Advances of High Performance Magnetic Iron Oxide Nanoparticles: Controlled Synthesis, Properties Tuning and Cancer Theranostics. *Nano Sel.* **2021**, *2*, 216–250. [CrossRef]

14. Chasteen, N.D.; Harrison, P.M. Mineralization in Ferritin: An Efficient Means of Iron Storage. *J. Struct. Biol.* **1999**, *126*, 182–194. [CrossRef]
15. Aronovitz, N.; Neeman, M.; Zarivach, R. Ferritin Iron Mineralization and Storage: From Structure to Function. In *Iron Oxides: From Nature to Applications*, 1st ed.; Faivre, D., Ed.; Wiley-VCH: Weinheim, Germany, 2016; pp. 117–141.
16. Meldrum, F.C.; Heywood, B.R.; Mann, S. Magnetoferritin: In Vitro Synthesis of a Novel Magnetic Protein. *Science* **1992**, *257*, 522–523. [CrossRef]
17. Klem, M.T.; Resnick, D.A.; Gilmore, K.; Young, M.; Idzerda, Y.U.; Douglas, T. Synthetic Control over Magnetic Moment and Exchange Bias in All-Oxide Materials Encapsulated within a Spherical Protein Cage. *J. Am. Chem. Soc.* **2007**, *129*, 197–201. [CrossRef]
18. Yang, C.; Cao, C.; Cai, Y.; Xu, H.; Zhang, T.; Pan, Y. Effects of PEGylation on Biomimetic Synthesis of Magnetoferritin Nanoparticles. *J. Nanoparticle Res.* **2017**, *19*, 101. [CrossRef]
19. Pankhurst, Q.A.; Connolly, J.; Jones, S.K.; Dobson, J. Applications of Magnetic Nanoparticles in Biomedicine. *J. Phys. D Appl. Phys.* **2003**, *36*, R167–R181. [CrossRef]
20. Chen, R.; Romero, G.; Christiansen, M.G.; Mohr, A.; Anikeeva, P. Wireless Magnetothermal Deep Brain Stimulation. *Science* **2015**, *347*, 1477–1480. [CrossRef]
21. Liße, D.; Monzel, C.; Vicario, C.; Manzi, J.; Maurin, I.; Coppey, M.; Piehler, J.; Dahan, M. Engineered Ferritin for Magnetogenetic Manipulation of Proteins and Organelles Inside Living Cells. *Adv. Mater.* **2017**, *29*, 1700189. [CrossRef] [PubMed]
22. Fernández-Sánchez, M.E.; Barbier, S.; Whitehead, J.; Béalle, G.; Michel, A.; Latorre-Ossa, H.; Rey, C.; Fouassier, L.; Claperon, A.; Brullé, L.; et al. Mechanical Induction of the Tumorigenic β-Catenin Pathway by Tumour Growth Pressure. *Nature* **2015**, *523*, 92–95. [CrossRef]
23. Monzel, C.; Vicario, C.; Piehler, J.; Coppey, M.; Dahan, M. Magnetic Control of Cellular Processes Using Biofunctional Nanoparticles. *Chem. Sci.* **2017**, *8*, 7330–7338. [CrossRef]
24. Laemmli, U.K. Cleavage of Structural Proteins during the Assembly of the Head of Bacteriophage T4. *Nature* **1970**, *227*, 680–685. [CrossRef]
25. Schindelin, J.; Arganda-Carreras, I.; Frise, E.; Kaynig, V.; Longair, M.; Pietzsch, T.; Preibisch, S.; Rueden, C.; Saalfeld, S.; Schmid, B.; et al. Fiji: An Open-Source Platform for Biological-Image Analysis. *Nat. Methods* **2012**, *9*, 676–682. [CrossRef]
26. Gavilán, H.; Kowalski, A.; Heinke, D.; Sugunan, A.; Sommertune, J.; Varón, M.; Bogart, L.K.; Posth, O.; Zeng, L.; González-Alonso, D.; et al. Colloidal Flower-Shaped Iron Oxide Nanoparticles: Synthesis Strategies and Coatings. *Part. Part. Syst. Charact.* **2017**, *34*, 1700094. [CrossRef]
27. Bender, P.; Fock, J.; Frandsen, C.; Hansen, M.F.; Balceris, C.; Ludwig, F.; Posth, O.; Wetterskog, E.; Bogart, L.K.; Southern, P.; et al. Relating Magnetic Properties and High Hyperthermia Performance of Iron Oxide Nanoflowers. *J. Phys. Chem. C* **2018**, *122*, 3068–3077. [CrossRef]
28. Vogel, P.; Kampf, T.; Rückert, M.; Grüttner, C.; Kowalski, A.; Teller, H.; Behr, V. Synomag®: The New High-Performance Tracer for Magnetic Particle Imaging. *Int. J. Magn. Part. Imaging* **2021**, *7*, 1–6.
29. Griese, F.; Knopp, T.; Gruettner, C.; Thieben, F.; Müller, K.; Loges, S.; Ludewig, P.; Gdaniec, N. Simultaneous Magnetic Particle Imaging and Navigation of Large Superparamagnetic Nanoparticles in Bifurcation Flow Exper-Iments. *J. Magn. Magn. Mater.* **2020**, *498*, 166206. [CrossRef]
30. McNicholas, S.; Potterton, E.; Wilson, K.S.; Noble, M.E.M. Presenting Your Structures: The CCP4mg Molecular-Graphics Software. *Acta Crystallogr. Sect. D Biol. Crystallogr.* **2011**, *67*, 386–394. [CrossRef] [PubMed]
31. Etoc, F.; Vicario, C.; Lisse, D.; Siaugue, J.-M.; Piehler, J.; Coppey, M.; Dahan, M. Magnetogenetic Control of Protein Gradients Inside Living Cells with High Spatial and Temporal Resolution. *Nano Lett.* **2015**, *15*, 3487–3494. [CrossRef]
32. Etoc, F.; Balloul, E.; Vicario, C.; Normanno, D.; Liße, D.; Sittner, A.; Piehler, J.; Dahan, M.; Coppey, M. Non-Specific Interactions Govern Cytosolic Diffusion of Nanosized Objects in Mammalian Cells. *Nat. Mater.* **2018**, *17*, 740–746. [CrossRef] [PubMed]
33. Gupta, A.K.; Gupta, M. Synthesis and Surface Engineering of Iron Oxide Nanoparticles for Biomedical Applications. *Biomaterials* **2005**, *26*, 3995–4021. [CrossRef]
34. Harrison, P.M.; Arosio, P. The Ferritins: Molecular Properties, Iron Storage Function and Cellular Regulation. *Biochim. Biophys. Acta-Bioenerg.* **1996**, *1275*, 161–203. [CrossRef]
35. Fan, K.; Cao, C.; Pan, Y.; Lu, D.; Yang, D.; Feng, J.; Song, L.; Liang, M.; Yan, X. Magnetoferritin Nanoparticles for Targeting and Visualizing Tumour Tissues. *Nat. Nanotechnol.* **2012**, *7*, 459–464. [CrossRef]
36. Kusterle, M.; Jevsevar, S.; Porekar, V.G. Size of Pegylated Protein Conjugates Studied by Various Methods. *Acta Chim. Slov.* **2008**, *55*, 594–601.
37. Novoselova, I.P.; Safronov, A.P.; Samatov, O.M.; Medvedev, A.I.; Kurlyandskaya, G.V. Biocompatible Ferrofluids with Iron Oxide Nanoparticles Fabricated by Laser Target Evaporation. *IEEE Magn. Lett.* **2015**, *6*, 6–9. [CrossRef]
38. Debayle, M.; Balloul, E.; Dembele, F.; Xu, X.; Hanafi, M.; Ribot, F.; Monzel, C.; Coppey, M.; Fragola, A.; Dahan, M.; et al. Zwitterionic Polymer Ligands: An Ideal Surface Coating To Totally Suppress Protein-Nanoparticle Corona Formation? *Biomaterials* **2019**, *219*, 119357. [CrossRef]
39. Lim, J.; Yeap, S.P.; Che, H.X.; Low, S.C. Characterization of Magnetic Nanoparticle by Dynamic Light Scattering. *Nanoscale Res. Lett.* **2013**, *8*, 381. [CrossRef]

40. Forest, V.; Cottier, M.; Pourchez, J. Electrostatic Interactions Favor the Binding of Positive Nanoparticles on Cells: A Reductive Theory. *Nano Today* **2015**, *10*, 677–680. [CrossRef]
41. Schavemaker, P.E.; Śmigiel, W.M.; Poolman, B. Ribosome Surface Properties May Impose Limits on the Nature of the Cytoplasmic Proteome. *eLife* **2017**, *6*, e30084. [CrossRef] [PubMed]
42. Liße, D.; Richter, C.P.; Drees, C.; Birkholz, O.; You, C.; Rampazzo, E.; Piehler, J. Monofunctional Stealth Nanoparticle for Unbiased Single Molecule Tracking Inside Living Cells. *Nano Lett.* **2014**, *14*, 2189–2195. [CrossRef]
43. Coey, J.M.D. *Magnetism and Magnetic Materials*, 1st ed.; Cambridge University Press: Cambridge, UK, 2010.
44. Skoropata, E.; Desautels, R.D.; Falvo, E.; Ceci, P.; Kasyutich, O.; Freeland, J.W.; van Lierop, J. Intra–and Interparticle Magnetism of Cobalt-Doped Iron-Oxide Nanoparticles Encapsulated in a Synthetic Ferritin Cage. *Phys. Rev. B.* **2014**, *90*, 174424. [CrossRef]
45. Massner, C.; Sigmund, F.; Pettinger, S.; Seeger, M.; Hartmann, C.; Ivleva, N.P.; Niessner, R.; Fuchs, H.; Hrabě de Angelis, M.; Stelzl, A.; et al. Genetically Controlled Lysosomal Entrapment of Superparamagnetic Ferritin for Multimodal and Multiscale Imaging and Actuation with Low Tissue Attenuation. *Adv. Funct. Mater.* **2018**, *28*, 1706793. [CrossRef]
46. Aragón, R. Cubic Magnetic Anisotropy of Nonstoichiometric Magnetite. *Phys. Rev. B.* **1992**, *46*, 5334–5338. [CrossRef]
47. Efremova, M.V.; Nalench, Y.A.; Myrovali, E.; Garanina, A.S.; Grebennikov, I.S.; Gifer, P.K.; Abakumov, M.A.; Spasova, M.; Angelakeris, M.; Savchenko, A.G.; et al. SIze-Selected Fe3O4–Au Hybrid Nanoparticles for Improved Magnetism-Based Theranostics. *Beilstein J. Nanotechnol.* **2018**, *9*, 2684–2699. [CrossRef]
48. Phong, P.T.; Oanh, V.T.K.; Lam, T.D.; Phuc, N.X.; Tung, L.D.; Thanh, N.T.K.; Manh, D.H. Iron Oxide Nanoparticles: Tunable Size Synthesis and Analysis in Terms of the Core–Shell Structure and Mixed Coercive Model. *J. Electron. Mater.* **2017**, *46*, 2533–2539. [CrossRef]
49. Nayek, C.; Manna, K.; Imam, A.A.; Alqasrawi, A.Y.; Obaidat, I.M. Size-Dependent Magnetic Anisotropy of PEG Coated Fe_3O_4 Nanoparticles; Comparing Two Magnetization Methods. *IOP Conf. Ser. Mater. Sci. Eng.* **2018**, *305*, 012012. [CrossRef]
50. Jiang, Z.; Shan, K.; Song, J.; Liu, J.; Rajendran, S.; Pugazhendhi, A.; Jacob, J.A.; Chen, B. Toxic Effects of Magnetic Nanoparticles on Normal Cells and Organs. *Life Sci.* **2019**, *220*, 156–161. [CrossRef]
51. Lartigue, L.; Hugounenq, P.; Alloyeau, D.; Clarke, S.P.; Lévy, M.; Bacri, J.-C.; Bazzi, R.; Brougham, D.F.; Wilhelm, C.; Gazeau, F. Cooperative Organization in Iron Oxide Multi-Core Nanoparticles Potentiates Their Efficiency as Heating Mediators and MRI Contrast Agents. *ACS Nano* **2012**, *6*, 10935–10949. [CrossRef]
52. Guardia, P.; Di Corato, R.; Lartigue, L.; Wilhelm, C.; Espinosa, A.; Garcia-Hernandez, M.; Gazeau, F.; Manna, L.; Pellegrino, T. Water-Soluble Iron Oxide Nanocubes with High Values of Specific Absorption Rate for Cancer Cell Hyperthermia Treatment. *ACS Nano* **2012**, *6*, 3080–3091. [CrossRef]
53. Curcio, A.; Silva, A.K.A.; Cabana, S.; Espinosa, A.; Baptiste, B.; Menguy, N.; Wilhelm, C.; Abou-Hassan, A. Iron Oxide Nanoflowers @ CuS Hybrids for Cancer Tri-Therapy: Interplay of Photothermal Therapy, Magnetic Hyperthermia and PhotoDynamic Therapy. *Theranostics* **2019**, *9*, 1288–1302. [CrossRef]
54. Salatin, S.; Dizaj, S.M.; Khosroushahi, A.Y. Effect of the Surface Modification, Size, and Shape on Cellular Uptake of Nanoparticles. *Cell Biol. Int.* **2015**, *39*, 881–890. [CrossRef] [PubMed]
55. Tinevez, J.Y.; Perry, N.; Schindelin, J.; Hoopes, G.M.; Reynolds, G.D.; Laplantine, E.; Bednarek, S.Y.; Shorte, S.L.; Eliceiri, K.W. TrackMate: An Open and Extensible Platform for Single-Particle Tracking. *Methods* **2017**, *115*, 80–90. [CrossRef]
56. Tseng, P.; Judy, J.W.; Di Carlo, D. Magnetic Nanoparticle-Mediated Massively Parallel Mechanical Modulation of Single-Cell Behavior. *Nat. Methods* **2012**, *9*, 1113–1119. [CrossRef]

nanomaterials

MDPI

Article

Magnetic Nanoprobes for Spatio-Mechanical Manipulation in Single Cells

Iuliia P. Novoselova [1,*,†], Andreas Neusch [1,†], Julia-Sarita Brand [1], Marius Otten [2], Mohammad Reza Safari [1,3], Nina Bartels [1], Matthias Karg [2], Michael Farle [4], Ulf Wiedwald [4] and Cornelia Monzel [1,*]

[1] Experimental Medical Physics, Heinrich-Heine University Düsseldorf, 40225 Düsseldorf, Germany; Andreas.Neusch@hhu.de (A.N.); jubra114@uni-duesseldorf.de (J.-S.B.); m.safari@fz-juelich.de (M.R.S.); Nina.Bartels@uni-duesseldorf.de (N.B.)
[2] Colloids and Nanooptics, Heinrich-Heine University Düsseldorf, 40225 Düsseldorf, Germany; marius.otten@hhu.de (M.O.); karg@hhu.de (M.K.)
[3] Peter Grünberg Institute, Electronic Properties (PGI-6), Forschungszentrum Jülich, 52425 Jülich, Germany
[4] Center for Nanointegration (CENIDE), Faculty of Physics University of Duisburg-Essen, 47057 Duisburg, Germany; michael.farle@uni-due.de (M.F.); ulf.wiedwald@uni-due.de (U.W.)
* Correspondence: Cornelia.Monzel@hhu.de (C.M.); Iuliia.Novoselova@hhu.de (I.P.N.)
† These authors contributed equally to this work.

Ferritin Purification

Sodium dodecyl sulphate–polyacrylamide gel electrophoresis (SDS-PAGE, 12%) carried out to confirm ferritin quality after each purification step can be seen in Figure S1. A standard Coomassie blue staining protocol was used. Theoretical molecular weight (MW) for mEGFP::HCF monomer is 48.7 kDa. This expected band is clearly observed in all loaded gel pockets indicating the presence of the desired mEGFP::HCF. Bright green color of the solution further confirms the correct expression of the complex containing mEGFP. Sephacryl S400 16/60 size exclusion column (SEC) equilibrated in buffer (20mM HEPES pH 8.0, 100 mM NaCl, pH 8.0) was used for the final purification step.

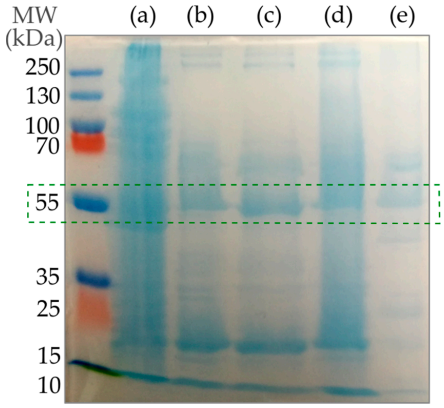

Figure S1. SDS-PAGE analysis of purification steps of ferritin shells. (**a**) directly after disrupting *E.coli* walls, (**b**) after heat denaturation at 70°C, (**c**) after 30% ammonium sulfate precipitation, (**d**) after 70% ammonium precipitation, (**e**) final product before loading on a size exclusion column (SEC).

Nanomaterials **2021**, *11*, 2267

Nanoparticles modification

Table S1. Hydrodynamic size D_H, polydispersity index (PdI), and ζ-potential for subsequent steps of magnetoferritin synthesis. Concentration c is presented after the filtering step (0.2 μm cut-off, PTFE). Stabilizing buffer (20 mM HEPES, 100 mM NaCl, pH 8.0) was used for all listed measurements. Conductivity of the medium was at 11 mS/cm for all samples while it was 0.1 mS/cm for milliQ water.

Sample	D_H, nm	PdI	ζ-Potential, mV
Non-PEGylated Ferritin Cages c = 0.5 mg/ml	15.3 ± 1.0	0.25 ± 0.00	−4.8 ± 0.7
PEGylated Ferritin Cages c = 1.0 mg/ml	20.5 ± 3.5	0.21 ± 0.01	−3.5 ± 0.7
PEGylated Magnetoferritin c = 0.7 mg/ml	39.1 ± 2.5	0.11 ± 0.01	−3.7 ± 1.2

Table S2. Hydrodynamic size D_H, polydispersity index (PdI), and ζ-potential for synomag nanoparticles with three different surface modifications. Concentration prior to filtering (0.2 μm cut-off, PTFE) was 1.0 mg/ml. Stabilizing buffer PBS (pH 7.4) was used for all listed measurements. Deviations from the ζ-potential are ascribed to the unpronounced phase plot prohibiting improvements of the final result disregarding the sub-runs increase.

Synomag	D_H, nm	PdI	ζ-Potential, mV
plain	48.1 ± 1.5	0.11 ± 0.01	−3.8 ± 0.6
NH_2	41.9 ± 0.5	0.05 ± 0.01	−1.2 ± 1.2
NH_2 - PEG_{2000}	39.1 ± 2.0	0.17 ± 0.03	−2.0 ± 2.3

Nanomaterials **2021**, *11*, 2267

Synomag colloidal stability

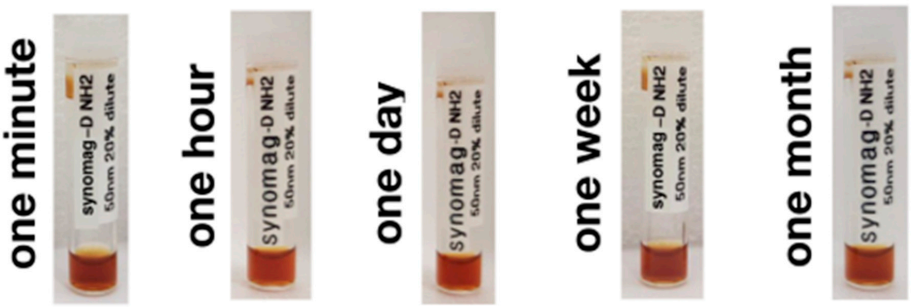

Figure S2. Qualitative assessment of the colloidal stability for synomag nanoparticles over time from 1 min up to 1 month.

III.2 Publication II – Preprint

Reference

Title Semisynthetic Ferritin Nanocages for Flexible, Site-specific Targeting, Cluster-formation and Activation of Membrane Receptors

Authors Andreas Neusch, Christina Siepe, Liesa Zitzke, Alexandra C. Fux, and Cornelia Monzel

Journal details *bioRxiv*

Date of Publication 3rd November 2024

DOI https://doi.org/10.1101/2024.11.01.621585

Copyright

Contribution

As first author, I took the lead in experimental planning and methodology of this work. I designed, performed, and analysed all experiments with support from CS, LZ, and ACF. Furthermore, I created all figures and wrote the original draft.
My overall contribution to this publication amounts to approximately 90 %.

Semisynthetic ferritin nanocages for flexible, site-specific targeting, cluster-formation and activation of membrane receptors

Andreas Neusch,[1] Christina Siepe,[1] Liesa Zitzke,[1] Alexandra C. Fux,[2] Cornelia Monzel [1,]*

AUTHOR ADDRESS

[1] Experimental Medical Physics, Heinrich-Heine University Düsseldorf, 40225 Düsseldorf, Germany.

[2] Department of Biosciences & Medical Biology, Paris Lodron University of Salzburg, 5020 Salzburg, Austria.

[*] Corresponding author, E-mail: Cornelia.Monzel@hhu.de

KEYWORDS

membrane receptors; ferritin; nanoparticle; targeting; CD95; TfR1

ABSTRACT

Homopolymerization and cluster formation of cellular membrane receptors (MR) is closely related to their signaling activity. However, underlying mechanisms and effects of clustering are often hardly understood. This lack of knowledge is due to the lack of suitable tools which enable to specifically target and activate distinct MRs, without causing side-effects. In this study, we

designed a fluorescent semisynthetic nanoparticle (NP) based on the iron-storage protein ferritin and *S. aureus* Protein A, that is readily equipped with a variety of antibodies with K_D values below 5 nM. Specificity of the NP antigen recognition was evaluated in cell experiments with cells expressing Transferrin Receptor 1 or the death receptor CD95, both of which displayed rapid cluster formation upon contact with the NP. Lastly, it was possible to induce apoptosis solely by induced clustering of CD95 via our engineered NP.

MAIN TEXT

Living cells are constantly facing multitudes of incoming information through all sorts of extracellular molecules. In order to process these signals effectively, intricate signaling pathways have developed around membrane receptors (MR) that are specifically recognizing distinct extracellular molecules, so called ligands.[1] To this date, more than 1350 MRs were identified in the human proteome.[2] Upon ligand recognition, MRs initiate signaling pathways, that can involve complex, multilayered chemical cascades that ultimately trigger a cellular reaction. Malfunction of signaling pathways was shown to be closely related to various diseases.[3–6]

Signaling pathways are often initiated by homopolymerization of MRs. In this context, the role of supramolecular structures and spatial arrangements of receptors involved in signaling has been highlighted in several studies.[7–12] However, the exact mechanisms behind the formation of these clusters and the subsequent signaling are largely unknown. This might partly be because of the lack of molecular tools that can trigger distinct MRs specifically, without affecting the cell through off-target effects.[13,14] Among the recent approaches to induce MR clustering, photoactivatable reagents,[15,16] magnetogenetics,[17–19] and optogenetics,[20,21] constitute powerful tools to locally control the protein activity of cells and to learn about the signal initiation mechanism. However,

these approaches often require genetic modifications of the proteins of interest and the application of sophisticated stimuli.

Among all known MRs, the tumor necrosis receptor family (TNF-R) is considered one of the best known. It is responsible for cell proliferation, survival, immune homeostasis, and the programmed cell death, apoptosis.[11,22] Cluster of differentiation 95 (CD95) is one death receptor of the TNF-R family, that is able to trigger apoptosis upon binding to its ligand CD95L.[23] Prior to initiation of apoptosis, some CD95 may form small oligomers[12] and lipid rafts containing CD95 were shown to promote receptor clustering. After ligand binding CD95 oligomerizes at least to dimers and trimers at characteristic distances and initiates the subsequent apoptosis signal.[24–27] However, it was also shown that pre-ligand assembly domains (PLADs) are promoting dimerization and signal initiation in TNF-Rs in the absence of ligand.[28] While excessive apoptosis has been linked to diseases such as Alzheimer's and Parkinson's, insufficient apoptosis can lead to excessive cell growth and, thus, cancer.[29,30] Therefore, tools that are able to specifically trigger and control cell death, are of high medical interest.

Another membrane receptor that is connected to cancer is Transferrin Receptor-1 (TfR1). TfR1 is responsible for cellular iron uptake and iron homeostasis in general, by binding and internalizing the iron transporter Transferrin.[31] Furthermore, TfR1 has been found to be overexpressed in cancer cells, making it a suitable marker for tumor cells.[32]

Here, we designed a nanoparticle (NP) platform, that is able to site-specifically target membrane-bound receptors. We focused on receptors that were shown to be overexpressed in cancer cells. After receptor targeting, our NP is designed to induce receptor clustering and, if applicable, MR activation.

One highly promising approach for efficient targeting is the ferritin family, an ubiquitous class of iron-storage proteins. Present in nearly all forms of life, ferritins feature a spherical, hollow protein cage that is highly conserved and serves as storage for iron ions.[33,34] For scientific application, the most commonly used member is human ferritin, with a diameter of 12 nm, while its inner cavity is 8 nm in size.[35] Here, the protein cage consists of 24 subunits of an arbitrary combination of either L chain ferritin (LCF) or H chain ferritin (HCF),[36,37] named after the locations where the subunits were first isolated from: liver and heart.[38] Coincidentally, LCF (19 kDa) is also slightly lighter than HCF (21 kDa), thus the two subunits are often referred to as light and heavy chain. The main difference between the two subunits is HCF's ferroxidase domain, that oxidizes toxic ferrous iron to insoluble, harmless ferric iron.[39]

There are several advantages of applying ferritin as a platform for MR targeting. As a protein, it can fairly easily be modified through genetic engineering. To this end, its 24-mer cage can be equipped with different tags, in order to create a multi-functional nanoparticle (NP). Due to ferritins human origin, it has low immunogenicity and is, in contrast to many synthetic NPs, biodegradable. Plus, ferritin was shown to be a natural ligand to TfR1.[40] More specifically, the coupling is mediated by HCF.[41] Upon binding, TfR1 initiates endocytosis of both itself and ferritin.

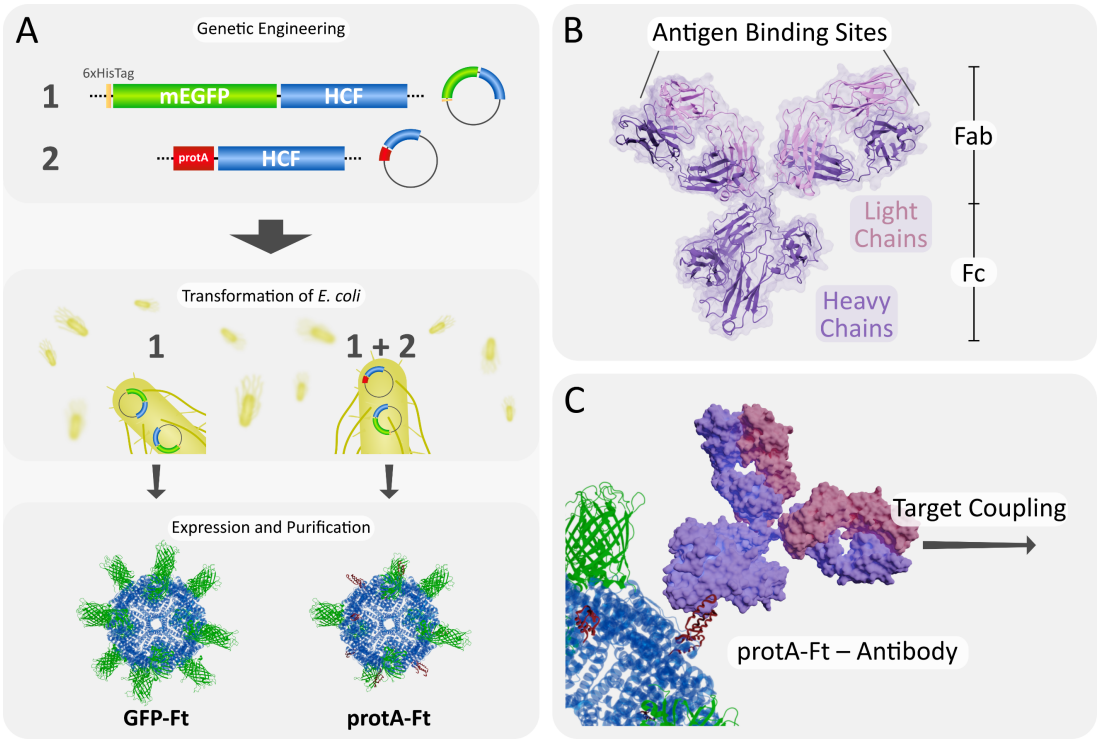

Figure 1. (A) Schematic display of the generation of ferritin nanoagents. Two constructs were genetically engineered: His6-mEGFP-HCF and protA-HCF (see Figure S3 and S4). Plasmid DNA was expressed in E. coli and subsequently purified to obtain both forms, GFP-Ft and the hybrid protA-Ft. (B) Structure of an IgG antibody. (C) Basic principle of protA-Ft activation via antibody coupling. Activated protA-Ft is able to specifically couple to the antibody's target.

In this study, we focused on the development of an NP platform for specific targeting. One feasible approach is to use antibodies as targeting mediators (see Figure 1). Immunglobulin G (IgG) is the most common antibody (Ab) and consists of two light and two heavy chains that combine to form the characteristic Y-shape with a molecular mass of ~ 150 kDa (see Figure 1B).[42,43] The specific binding site is formed between a heavy and a light chain at the outer edge of the protein, the so-called fragment antigen-binding (Fab) region. The constant region consists of two heavy chains that form the fragment crystallizable (Fc) region, that serves as a backbone to stabilize the structure.[44] In order to allow the antibody to retain its antigen-binding capabilities after coupling

to an NP, it is crucial to connect the two via the Fc region. This leaves the target binding sites free of steric hindrance and, hence, functional. One way to establish such an oriented connection is through Protein A (SpA) from the bacterium *Staphylococcus aureus*.[45] This 42 kDa protein consists, among others, of five domains of about 58 amino acids each that form one antibody binding domain.[46] One of these domains, the B-domain, was isolated and modified to give rise to the Z-domain (from here on named protA) that is capable of binding antibodies on its own with a K_D value of 20 nM.[47,48] Genetically fusing this domain to ferritin allows direct coupling of IgG to the protein's surface via incubation (see Figure 1C). This flexible approach enables a quick and straightforward creation of highly specific NPs, with the only constraint being the need for a compatible antibody.[49]

In addition, guiding NPs to their target is as important as detecting and observing them. To this end, we chose to attach a fluorescent probe in the form of monomeric enhanced green fluorescent protein (mEGFP) to our NPs.[50,51] Using genetic engineering, two ferritin-based constructs were created: (1) mEGFP coupled to HCF (see Figure S3),[52] and (2) protA coupled to HCF (see Figure S4). Through the nature of ferritin's self-assembling properties, we produced both a control cage consisting only of mEGFP-HCF (hereafter GFP-Ft) and a hybrid cage combining both constructs, resulting in a mEGFP-protA-ferritin cage (hereafter protA-Ft, see also Figure 1A). This hybrid form is easily trackable via its fluorescent subunits and can also be easily equipped with a matching antibody to direct it to any specific target on – or even in – a cell (see Figure 1C)

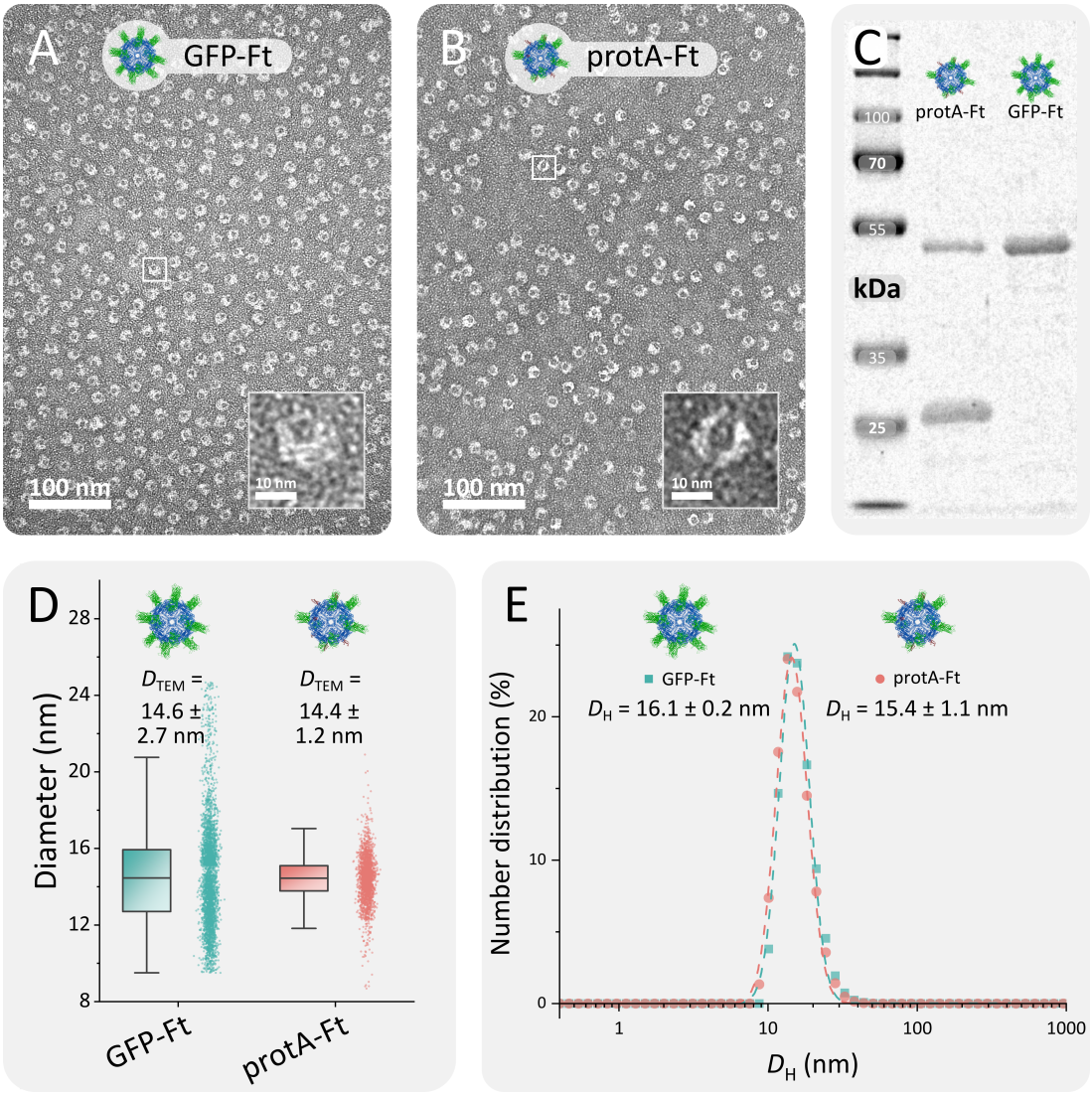

Figure 2. Characterization of ferritin NPs. (A) and (B) show TEM images of GFP-Ft and protA-Ft with an inlet showing an enlarged single cage. (C) SDS-PAGE of both constructs. The first lane shows a protein standard ladder with components of known size (shown in kDa). Background of the image was subtracted using a sliding paraboloid with a radius of 50 pixels. (D) Size distribution of NPs from TEM images. (E) DLS data showing the number distribution of the size of both NP constructs.

The two ferritin constructs were expressed in the *E. coli* strain BL21-CodonPlus (DE3)-RIPL and purified using IMAC. In order to analyze the particles' physical properties, they were analyzed

using transmission electron microscopy (TEM), dynamic light scattering (DLS) and sodium dodecylsulphate polyacrylamide-gel electrophoresis (SDS-PAGE) (see Figure 2 and Table 1). Most notably, all three methods demonstrated the high purity and monodispersity of the ferritin samples. Molecular weights of the monomers matched our expectations. TEM and DLS data revealed cage structures consistent with previously reported (recombinant) ferritins.[52–54] The observed size difference between TEM and DLS is explained by the experimental setup: while TEM captures the dry protein shell, DLS measures particle properties in solution, hence also including the particle's hydration shell. Consequently, this leads to a larger detected particle size, namely the hydrodynamic diameter D_H. Furthermore, all data suggests that no significant changes in both cage size as well as cage morphology were introduced by the shift from homo- to heteropolymeric ferritin. The successful creation of heteropolymeric ferritin is evident from the two bands that appeared in SDS-PAGE, representing GFP-HCF and protA-HCF (see Figure 2C).

Table 1. Composition and properties of ferritin constructs used in this study. Since the exact composition of protA-Ft is unkown, the molecular weight can only be estimated. (MW: molecular weight, D_{TEM}: diameter obtained from TEM imaging, D_H: hydrodynamic diameter and PdI: Polydispersity index, both from DLS)

Name	**Monomer**	**MW (kDa)**		***D*TEM (nm)**	***D*H (nm)**	**PdI**
		Monomer	Cage			
GFP-Ft	His6-mEGFP-HCF	49.8	1194.7	14.6 ± 2.7	16.1 ± 0.2	0.13 ± 0.01
protA-Ft	His6-mEGFP-HCF protA-HCF	49.8 28.5	~900	14.4 ± 1.2	15.4 ± 1.1	0.11 ± 0.04

The two ferritin constructs were further characterized by spectroscopically measuring the degree of labeling (DoL), a measure for the number of fluorescent species coupled to a NP. The DoL of ferritin and mEGFP can be calculated using Beer-Lambert's law[55]

$$DoL = \frac{\varepsilon_{488,GFP}}{\varepsilon_{280,Ft}} \frac{A_{488}}{(A_{280} - A_{488} \cdot CF_{GFP})},$$

with the absorbance *A*, the molar extinction coefficient $\boldsymbol{\varepsilon}$, both at the specified wavelength and the correction factor CF_{GFP} that is given by

$$CF_{GFP} = \frac{A_{280,GFP}}{A_{488,GFP}}.$$

The DoL for GFP-Ft was measured to be 11.2 ± 0.5 GFP/Ft (see Figure S1). While these values strongly deviate from theoretically possible values of up to 24 GFP/Ft, they give an insight into the surface functionalization of our ferritin constructs. It seems, that despite consisting of 24 GFP-labeled HCF subunits, only about 50% of the GFP subunits are indeed actively fluorescent. Explanations for the decreased activity states include (1) steric hindrance on ferritin's limited surface area, that disturbs GFP structure and hence hampers its activity, (2) post-translational cleavage between the two fused subunits HCF and GFP, (3) HOMO-FRET events that influence absolute absorbance values or (4) intrinsic folding and activity deficits when expressing GFP homologues in *E. coli*.[56] Nonetheless, a distinct difference was detectable between GFP-Ft and protA-Ft with a DoL of 3.0 ± 0.0 GFP/Ft (see Figure S1). This difference can be seen as an indication that the composition of the heteropolymeric protA-Ft is roughly 1 to 3 (GFP-HCF to protA-HCF). This estimation is supported by SDS-PAGE that shows a ratio of GFP-HCF to protA-HCF of roughly 1 to 2. It seems therefore, that the hybrid protA-Ft cage consists to a notable excess of protA-HCF, giving rise to more than twelve antibody-binding sites.

After the initial characterization, we assessed whether the natural binding capabilities of ferritin towards TfR1 are constrained. In order to precisely monitor coupling and changes of cells coming in contact with protA-Ft, we used a microshower system to incubate single cells with protA-Ft

(see Figure 3A). A solution of protA-Ft was loaded into a microcapillary and then placed several µm above the cell of choice while maintaining a constant outflow. This created a stable cloud of ferritin NPs around the cell, similar to localized, cell-specific incubation in NP-loaded media.

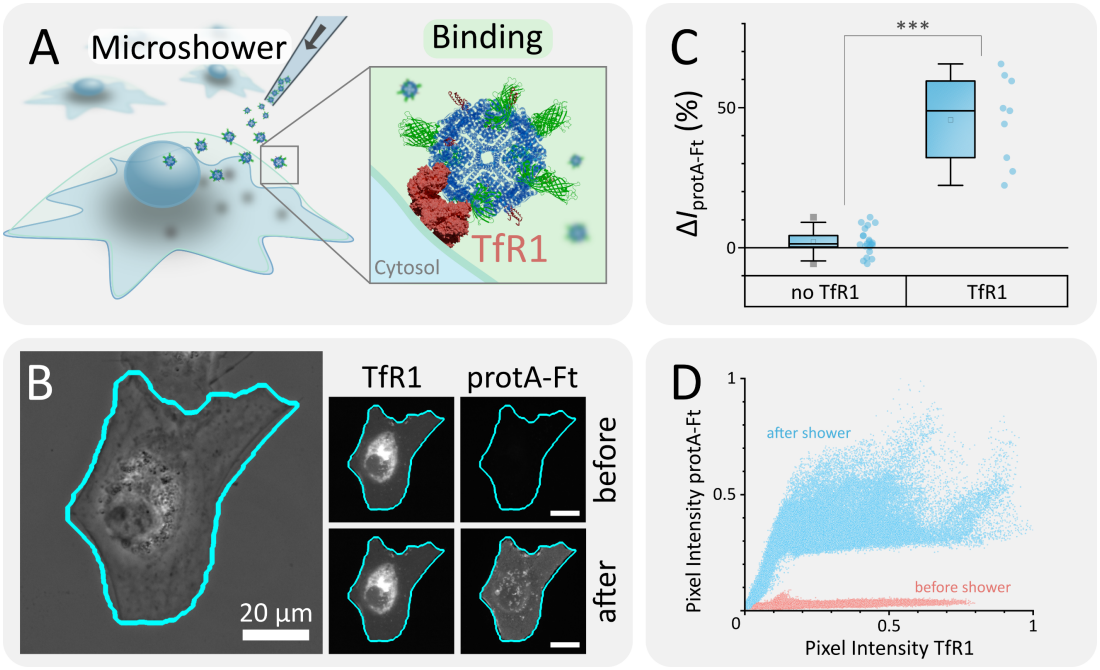

*Figure 3. Targeting of TfR1 using protA-Ft. (A) Schematic experimental setup. Cos7 cells were showered with a microcapillary filled with protA-Ft for 15 min. Binding to cells occurs on cells that are overexpressing TfR1. (B) Microscopy data of exemplary cell before and after protA-Ft microshower. Shown are phase contrast image, red channel (TfR1 – pHuji, contrast enhancement of 1 %), and green channel (ferritin, mEGFP). (C) Intensity increase ΔI in protA-Ft's fluorescence channel after microshower for 15 min in wild type cells ('no TfR1') and cells overexpressing TfR1 ('TfR1'). A one-way ANOVA was performed to test for differences between groups (*** = p < 0.001). (D) Scatter plot of pixel values from TfR1 channel vs. protA-Ft channel, both normalized.*

In contrast to wild type cells, protA-Ft clearly bound to the membrane of TfR1-overexpressing cells after a microshower of 15 min (see Figure 3B). Fluorescence intensity in ferritin's green channel significantly increased by a mean of 46 ± 16 % when showering cells with TfR1, while intensities in wild type cells hardly changed by 2 ± 5 % (Figure 3C). Note that due to the nature of epifluorescent microscopy, intensity values include out-of-focus. Hence, pixel values represent –

to some extent – Z-scans across the cell and are therefore brighter towards its thicker center, where the nucleus and endoplasmic reticulum (ER) are located.

Direct comparison of pixel values of the red (pHuji on TfR1) and green (mEGFP on protA-Ft) channels showed that after the microshower, a linear dependency of the two emerged, while *a priori*, those two variables were basically independent (see Figure 3D). We have deliberately not applied Pearson's Correlation to our microscopic data to avoid misinterpretation due to background signal and cellular autofluorescence in the green channel, but this pixel-wise comparison nonetheless demonstrates high colocalization of TfR1 and protA-Ft. Therefore, we can conclude that despite our implemented modifications, the natural binding capabilities between TfR1 and ferritin are still present. On the other hand, we saw that further modification to the ferritin cage, namely the passivation using polyethylene glycol (PEG), disturb binding to TfR1 and suppresses the correlated intensity increase (data not shown). It is therefore advisable to find an ideal state of modification to not hamper ferritins binding behavior.

After the initial characterizations and testing, we proceeded towards the application of protA-Ft as a targeting hybrid NP. To activate protA-Fts targeting capabilities, antibodies are conjugated to the protA domains on the NPs surface. For characterization of this coupling, a fluorescence-linked immunosorbent assay (FLISA) was performed.[57] Here, target antibody was immobilized on the wells of a 96-well plate, followed by incubation with protA-Ft. After washing off any excess protein, the fluorescence of protA-Ft remaining inside each well could be measured to evaluate the binding capabilities between protA-Ft and the target antibody. In order to demonstrate the versatility of our hybrid ferritin construct, we characterized the binding of various control antibodies: human IgG1, murine IgG2a and a fluorescently labeled IgG1-APC antibody. As shown in Figure S2, protA-Ft bound to all examined antibodies with K_D values in the range from 1.6 to

3.7 nM. This even undercuts previously reported K_D values for the minimalized protA from *S. aureus* by almost one magnitude.[48] This decrease can be explained by the avidity effect: protA binds to the antibody's heavy chain in its Fc region. Since antibodies in general consist of two heavy chains (see also Figure 1), there are two potential binding sites for protA.[58] Our hybrid protA-Ft cage is equipped with multiple protA subunits. Thus, the antibody is not only bound to one binding site but chelated by two subunits. This in turn entropically strengthens the bond between ferritin and antibody. We observed bonding between protA-Ft and each of the tested antibodies, regardless of species or antibody labels. In contrast, no binding was observed when testing GFP-Ft under the same conditions (data not shown). We can therefore safely assume that the hybrid protA-Ft can be equipped with any IgG as long as the antibody has sufficient affinity towards SpA.[49]

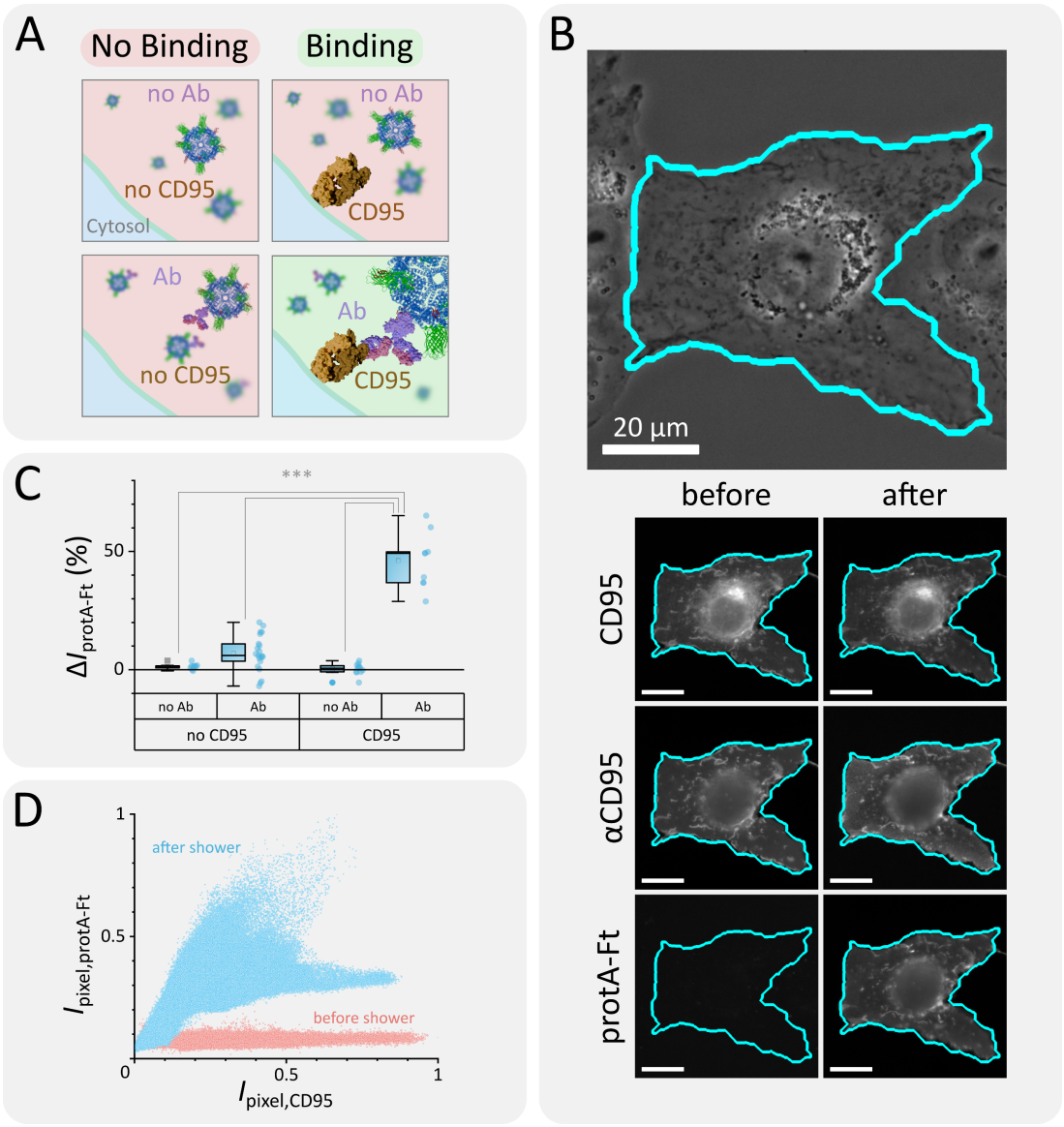

*Figure 4. Targeting of CD95 using protA-Ft in combination with αCD95 antibody. (A) Schematic experimental setup. Cos7 cells were incubated with αCD95 for 15 min and subsequently showered with a microcapillary filled with protA-Ft for 15 min. Binding to cells occurs on cells that are overexpressing CD95 and only in the presence of the antibody. (B) Microscopy data of exemplary antibody-treated cell before and after protA-Ft microshower. Shown are phase contrast image, red channel (CD95 – mCherry, far-red channel (αCD95 – APC), and green channel (Ferritin – mEGFP). (C) Intensity increase in protA-Ft's fluorescence channel after microshower for 15 min in wild type cells (no CD95) and TfR1-overexpressing cells (CD95) with and without previous antibody-treatment (Ab, no Ab). A one-way ANOVA was performed to test for differences between groups (*** = $p < 0.001$). (D) Scatter plot of pixel values from CD95 channel vs. protA-Ft channel.*

We demonstrated the performance of the activated hybrid protA-Ft by targeting the extracellular domain of the death receptor CD95. Here, protA-Ft's binding capabilities only come in to play in the presence of an αCD95 antibody (see Figure 4A). Thus, prior to the microshower with protA-Ft, cells were incubated with respective antibody for 15 min. Afterwards, a microshower as described previously (Figure 3A) was applied for 15 min. While no binding was observed in cells not treated with antibody, a slight increase occurred when showering antibody-treated wild type cells with protA-Ft. This minimal increase might be caused by the intrinsic presence of natural CD95 receptor on the cell's membrane.

However, treatment of CD95-overexpressing cells with antibody followed by protA-Ft led to a significantly larger rise of signal by 46 ± 12 % (see Figure 4B and C). Hence, it becomes apparent, that protA-Ft binding to CD95 is indeed enabled by the antibody. This is also confirmed by comparing pixel values of protA-Ft and CD95 (Figure 4D). As seen for the binding of protA-Ft to TfR1, the two intensities are linearly dependent and thus strongly co-localized. As for TfR1 experiments, no binding was observed with PEGylated protA-Ft, regardless of presence or absence of antibody (data not shown).

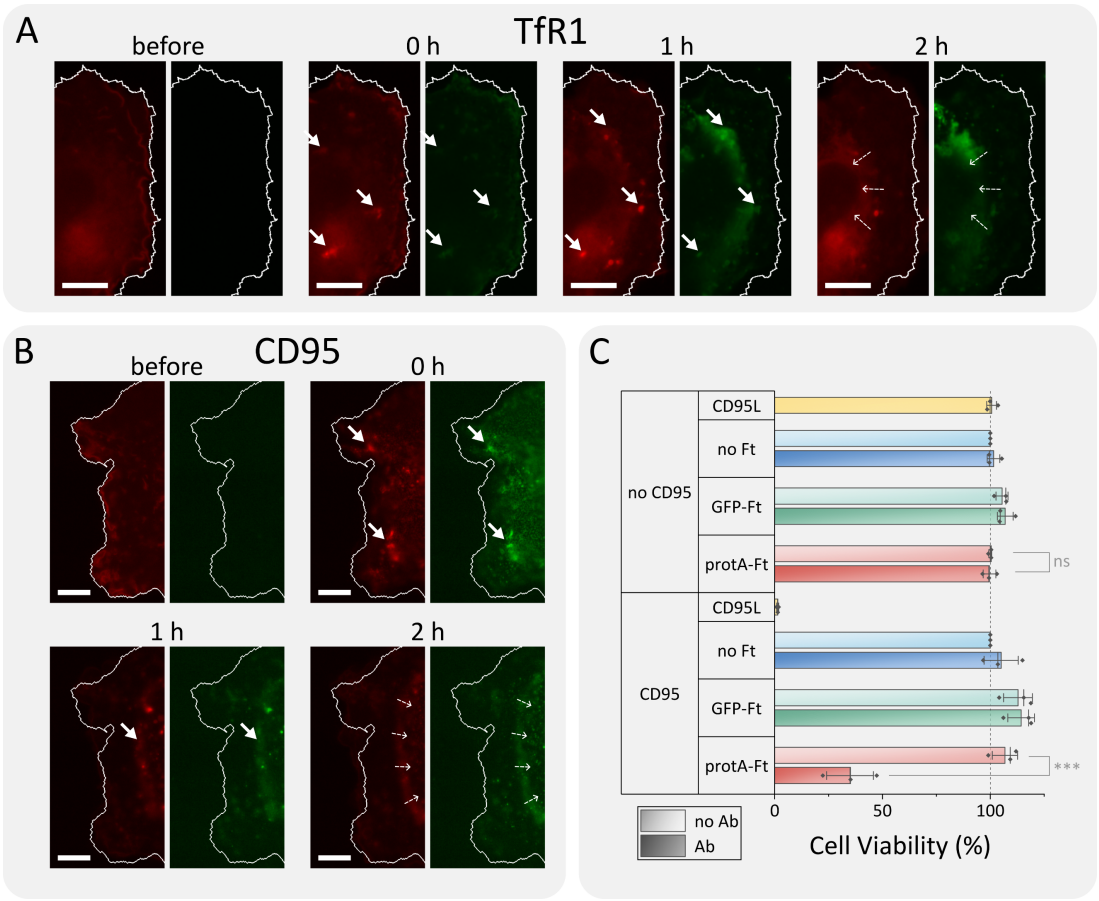

*Figure 5. Exemplary Cos7 cells over-expressing (A) TfR1 (red), and (B) overexpressing CD95 (red) and treated with αCD95 antibody. Images were taken before or at denoted timepoints after a 15 min microshower with protA-Ft (green). Solid arrows are pointing to formed clusters. Dotted arrows indicate movement of protA-Ft and the respective receptor towards the cell nucleus. All scale bars are 10 µm. (C) CTB Viability assay of HeLa cells overexpressing CD95 ('CD95') or with CD95 being knocked out ('no CD95'). Cells were incubated overnight with or without αCD95 antibody and with or without protA-Ft or GFP-Ft. CD95L served as negative control, that triggers apoptosis upon contact with CD95. A one-way ANOVA was performed to test for differences between groups (ns = not significant, *** = $p < 0.001$).*

The key points of this work are the specific targeting of MRs and, if applicable, the subsequent activation, namely of CD95, by incubation with protA-Ft. It was shown in Figure 3 and Figure 4 that protA-Ft is able to specifically target both its natural receptors, demonstrated by the exemplary receptor TfR1, as well as other MRs through antibody-mediated binding. Figure 5 shows two examples for cells over-expressing TfR1 or CD95 respectively, before and at certain timepoints after microshower with protA-Ft. In TfR1 cells, the presence of protA-Ft leads to rapid formation

of clusters of TfR1, illustrated by the transition of homogenous fluorescence signal to a granular image directly after the shower. Within 2 h, these clusters grow and steadily move towards the cell's nucleus.

A similar behavior was observed on CD95 cells: immediately after protA-Ft initiation, clusters appeared in both the CD95 and protA-Ft channels. Rapidly after the microshower, a ring of CD95 and protA-Ft formed in the periphery of the cell that moved towards the nucleus within 1 h. Due to the highly synchronized and directed movement, it seems that endocytotic vesicles containing both protA-Ft as well as CD95 are being transported towards the center of the cell.

Probing of CD95 activation via protA-Ft incubation was performed using a cell viability assay. To this end, two cell lines were used – a knockout cell line without CD95 and a cell line stably overexpressing CD95. Both cell lines were incubated with different combinations of CD95-specific Ab, protA-Ft, GFP-Ft or no Ft. As a positive control, CD95L which induces apoptosis in the presence of CD95, was added to the cells. As shown in Figure 5B only the combination of CD95, protA-Ft and the CD95-specific Ab was able to induce apoptosis. Cell survival rates under these conditions dropped to 35 ± 13 %, while all other conditions remained at survival rates within the margin of error of the negative control. In the positive control with CD95L in the presence of CD95, 1.4 ± 0.5 % of all cells survived. This demonstrates, that only through the clustering of CD95 using our engineered protA-Ft, apoptosis can be initiated.

In this comprehensive study we assessed the potential of ferritin as a targetable NP. Due to its protein nature, stability and biocompatibility, ferritin serves as an excellent targeting system. By creating hybrid ferritin cages, multifunctionality can be readily introduced to the NP without the

need for downstream chemical modifications. We demonstrated this by fusing mEGFP- and protA-labeled subunits that combined the capabilities of both modifications into one cage. The implementation of protA, a minimal binding model of the antibody-binding SpA, gave rise to a targeting system that can be easily adapted to experimental needs by simple means of incubation with antibodies. We demonstrated its targeting capabilities by targeting our hybrid protA-Ft to both TfR1 overexpressing cells via natural binding of ferritin and to CD95 via antibody-mediated binding, two receptors that are connected to cancer. Through both targeting routes, protA-Ft induced cluster formation of the targeted receptor. The intensive accumulation of CD95 through protA-Ft was enough to exceed cellular thresholds and ultimately induce apoptosis.

Conclusively, our manufactured hybrid protein cages are an easily operatable, highly flexible nanosystem for site-specific cellular targeting. Combination of this system with methods for loading small molecules into ferritin, such as anti-cancer drugs,[59–61] could create a potent carrier for targeted drug delivery.[62] Our cellular studies gave indications, that protA-Ft was internalized by the targeted cells, a useful property for drug delivery.[63] Furthermore, by implementation of a magnetic core into the hybrid ferritin cage, a versatile tool for spatial manipulation and accumulation of MRs in living cells can be created.[17,52–54,64] Such a tool would have the potential to explore previously unknown mechanisms underlying the signaling pathways of membrane receptors.

ASSOCIATED CONTENT

Supporting Information: Detailed description of materials and methods and supplementary figures.

AUTHOR INFORMATION

Author Contributions: The manuscript was written through contributions of all authors. All authors have given approval to the final version of the manuscript.
Conceptualization: CM
Methodology: AN
Software: AN
Validation: AN, CM
Formal analysis: AN
Investigation: AN, CS, LZ, ACF
Resources: CM
Data Curation: AN
Writing-original draft: AN
Writing-review & Editing: AN, CS, LZ, ACF, CM
Visualization: AN
Supervision: CM
Project administration: CM
Funding acquisition: CM

Notes: The authors declare no competing financial interest.

ACKNOWLEDGMENT

CM acknowledges financial support by the DFG Collaborative Research Center 1208 “Identity and dynamics of biological membranes” (project ID 267205415), the DFG Collaborative Research Center 1535 ‘MiBiNet’ (project ID 458090666). CM and AN acknowledges financial support by the ‘Freigeist-fellowship’ of VolkswagenFoundation. The authors acknowledge the DFG and the State of North Rhine–Westphalia for funding the cryo- TEM (INST 208/749-1 FUGG) hosted by the Centre of Advanced Imaging (CAi, Heinrich-Heine University). We thank the Institute of Molecular Physical Chemistry (University of Düsseldorf) of Prof. Seidel for providing lab space and laboratory equipment, the Institute of Computational Pharmaceutical Chemistry (University of Düsseldorf) of Prof. Gohlke for providing the plate reader, the Institute of Synthetic Membrane Systems of Prof. Kedrov (University of Düsseldorf) for providing lab space and equipment, the Institute of Biochemistry I (University of Düsseldorf) of Prof. Schmitt for providing the cell disruptor, and the Institute of Macromolecular Chemistry of Prof. Hartmann (University of Düsseldorf) for providing the Zetasizer.

ABBREVIATIONS

MR – membrane receptor; SpA – Protein A from S. aureus; protA – engineered Z-domain of *S. aureus* Protein A; mEGFP – monomeric Enhanced Green Fluorescent Protein; Ft – Ferritin; protA-Ft – ferritin with mEGFP and protA subunits fused to its cage; GFP-Ft – ferritin with mEGFP subunits fused to its cage; HCF – Heavy Chain Ferritin; LCF – Light Chain Ferritin; GFP-HCF – HCF subunits fused to mEGFP; protA-HCF – protA subunit fused to HCF; TEM – Transmission Electron Microscopy; DLS – Dynamic Light Scattering; SDS-PAGE – Sodiumdodecly Sulphate-Polyacrylamide Gel Electrophoresis

REFERENCES

1 N. C. Hartman and J. T. Groves, *Curr. Opin. Cell Biol.*, 2011, **23**, 370–376.
2 M. S. Almén, K. J. Nordström, R. Fredriksson and H. B. Schiöth, *BMC Biol.*, 2009, **7**, 50.
3 G. S. Martin, *Cancer Cell*, 2003, **4**, 167–174.
4 F. Müller-Pillasch, C. Wallrapp, U. Lacher, H. Friess, M. Büchler, G. Adler and T. M. Gress, *Gene*, 1998, **208**, 25–30.
5 K. Scheuer, A. Maras, W. F. Gattaz, N. Cairns, H. Förstl and W. E. Müller, *Dement. Geriatr. Cogn. Disord.*, 1996, **7**, 210–214.
6 A. Ulloa-Aguirre, T. Zariñán and E. Jardón-Valadez, *Int. J. Mol. Sci.*, 2021, **22**, 12329.
7 D. B. Nikolov, K. Xu and J. P. Himanen, *Biochim. Biophys. Acta - Proteins Proteomics*, 2013, **1834**, 2160–2165.
8 L. Balagopalan, V. A. Barr, R. L. Kortum, A. K. Park and L. E. Samelson, *J. Immunol.*, 2013, **190**, 3849–3853.
9 F. Henkler, E. Behrle, K. M. Dennehy, A. Wicovsky, N. Peters, C. Warnke, K. Pfizenmaier and H. Wajant, *J. Cell Biol.*, 2005, **168**, 1087–1098.
10 A. S. Yap, W. M. Brieher and B. M. Gumbiner, *Annu. Rev. Cell Dev. Biol.*, 1997, **13**, 119–146.
11 É. S. Vanamee and D. L. Faustman, *Sci. Signal.*, 2018, **11**, 4910.
12 N. Bartels, N. T. M. van der Voort, O. Opanasyuk, S. Felekyan, A. Greife, X. Shang, A. Bister, C. Wiek, C. A. M. Seidel and C. Monzel, *Sci. Adv.*, 2024, **10**, eadn3238.
13 A. Ashkenazi, *Nat. Rev. Cancer*, 2002, **2**, 420–430.
14 B. B. Aggarwal, *Nat. Rev. Immunol.*, 2003, **3**, 745–756.
15 G. Mayer and A. Heckel, *Angew. Chemie Int. Ed.*, 2006, **45**, 4900–4921.
16 N. Umeda, T. Ueno, C. Pohlmeyer, T. Nagano and T. Inoue, *J. Am. Chem. Soc.*, 2011, **133**, 12–14.
17 C. Monzel, C. Vicario, J. Piehler, M. Coppey and M. Dahan, *Chem. Sci.*, 2017, **8**, 7330–7338.
18 D. A. Kuckla, J.-S. Brand, B. Czech, A. Asharion, J. V. Jüttner, I. P. Novoselova, A. Neusch, P. Hagemann, M. Getzlaff and C. Monzel, *J. Phys. D. Appl. Phys.*, 2023, **56**, 505002.
19 L. Toraille, K. Aïzel, É. Balloul, C. Vicario, C. Monzel, M. Coppey, E. Secret, J. M. Siaugue, J. Sampaio, S. Rohart, N. Vernier, L. Bonnemay, T. Debuisschert, L. Rondin, J. F. Roch and M. Dahan, *Nano Lett.*, 2018, **18**, 7635–7641.
20 A. Remorino, S. De Beco, F. Cayrac, F. Di Federico, G. Cornilleau, A. Gautreau, M. C. Parrini, J.-B. Masson, M. Dahan and M. Coppey, *Cell Rep.*, 2017, **21**, 1922–1935.
21 A. Levskaya, O. D. Weiner, W. A. Lim and C. A. Voigt, *Nature*, 2009, **461**, 997–1001.
22 T. Hehlgans and K. Pfeffer, *Immunology*, 2005, **115**, 1–20.
23 P. H. Krammer, *Nature*, 2000, **407**, 789–795.
24 P. Legembre, S. Daburon, P. Moreau, F. Ichas, F. de Giorgi, J.-F. Moreau and J.-L. Taupin,

Mol. Cell. Biol., 2005, **25**, 6811–6820.
25 J. R. Muppidi and R. M. Siegel, *Nat. Immunol.*, 2004, **5**, 182–189.
26 G. S. Gülcüler Balta, C. Monzel, S. Kleber, J. Beaudouin, E. Balta, T. Kaindl, S. Chen, L. Gao, M. Thiemann, C. R. Wirtz, Y. Samstag, M. Tanaka and A. Martin-Villalba, *Cell Rep.*, 2019, **29**, 2295-2306.e6.
27 R. M. L. Berger, J. M. Weck, S. M. Kempe, O. Hill, T. Liedl, J. O. Rädler, C. Monzel and A. Heuer-Jungemann, *Small*, 2021, **17**, 2101678.
28 F. K. M. Chan, H. J. Chun, L. Zheng, R. M. Siegel, K. L. Bui and M. J. Lenardo, *Science*, 2000, **288**, 2351–2354.
29 C. B. Thompson, *Science*, 1995, **267**, 1456–1462.
30 S. Kumari, R. Dhapola and D. H. Reddy, *Apoptosis*, 2023, **28**, 943–957.
31 T. R. Daniels, T. Delgado, J. A. Rodriguez, G. Helguera and M. L. Penichet, *Clin. Immunol.*, 2006, **121**, 144–158.
32 A. Essaghir and J.-B. Demoulin, *PLoS One*, 2012, **7**, e39666.
33 D. He and J. Marles-Wright, *N. Biotechnol.*, 2015, **32**, 651–657.
34 Y. Zhu, Y. Zhu, T. Cao, X. Liu, X. Liu, Y. Yan, Y. Shi and J. C. Wang, *Med. Rev.*, 2023, **3**, 49–74.
35 Y. Zhang and B. P. Orner, *Int. J. Mol. Sci.*, 2011, **12**, 5406–5421.
36 N. K. Lee, S. Cho and I. S. Kim, *Exp. Mol. Med.*, 2022, **54**, 1652–1657.
37 P. M. Harrison and P. Arosio, *Biochim. Biophys. Acta - Bioenerg.*, 1996, **1275**, 161–203.
38 E. C. Theil, R. K. Behera and T. Tosha, *Coord. Chem. Rev.*, 2013, **257**, 579–586.
39 N. D. Chasteen and P. M. Harrison, *J. Struct. Biol.*, 1999, **126**, 182–194.
40 D. F. Wallace, C. McDonald and V. N. Subramaniam, *Gastroenterology*, 2010, **139**, 1052–1053.
41 L. Li, C. J. Fang, J. C. Ryan, E. C. Niemi, J. A. Lebrón, P. J. Björkman, H. Arase, F. M. Torti, S. V. Torti, M. C. Nakamura and W. E. Seaman, *Proc. Natl. Acad. Sci. U. S. A.*, 2010, **107**, 3505–3510.
42 G. M. Edelman, *Science*, 1973, **180**, 830–840.
43 S. Cohen and C. Milstein, *Nature*, 1967, **214**, 449–452.
44 S. Dübel, F. Breitling, A. Frenzel, T. Jostock, A. L. J. Marschall, T. Schirrmann and M. Hust, *Rekombinante Antikörper*, Springer Berlin Heidelberg, Berlin, Heidelberg, 2019.
45 P. L. Ey, S. J. Prowse and C. R. Jenkin, *Immunochemistry*, 1978, **15**, 429–436.
46 T. Moks, L. Abrahmsen, B. Nilsson, U. Hellman, J. Sjoquist and M. Uhlen, *Eur. J. Biochem.*, 1986, **156**, 637–643.
47 B. Nilsson, T. Moks, B. Jansson, L. Abrahmsén, A. Elmblad, E. Holmgren, C. Henrichson, T. A. Jones and M. Uhlén, *Protein Eng. Des. Sel.*, 1987, **1**, 107–113.
48 M. D. Levasseur, S. Mantri, T. Hayashi, M. Reichenbach, S. Hehn, Y. Waeckerle-Men, P. Johansen and D. Hilvert, *ACS Chem. Biol.*, 2021, **16**, 838–843.
49 S. Hober, K. Nord and M. Linhult, *J. Chromatogr. B*, 2007, **848**, 40–47.
50 G. Zhang, V. Gurtu and S. R. Kain, *Biochem. Biophys. Res. Commun.*, 1996, **227**, 707–711.
51 D. A. Zacharias, J. D. Violin, A. C. Newton and R. Y. Tsien, *Science*, 2002, **296**, 913–916.
52 D. Liße, C. Monzel, C. Vicario, J. Manzi, I. Maurin, M. Coppey, J. Piehler and M. Dahan, *Adv. Mater.*, 2017, **29**, 1–7.
53 I. P. Novoselova, A. Neusch, J. S. Brand, M. Otten, M. R. Safari, N. Bartels, M. Karg, M. Farle, U. Wiedwald and C. Monzel, *Nanomaterials*, 2021, **11**, 1–20.
54 A. Neusch, U. Wiedwald, I. P. Novoselova, D. A. Kuckla, N. Tetos, S. Sadik, P. Hagemann,

M. Farle and C. Monzel, *Nanoscale*, 2024, **16**, 15113–15127.
55 D. F. Swinehart, *J. Chem. Educ.*, 1962, **39**, 333.
56 H. C. Chang, C. M. Kaiser, F. U. Hartl and J. M. Barral, *J. Mol. Biol.*, 2005, **353**, 397–409.
57 E. Matsukuma, Z. Kato, K. Omoya, K. Hashimoto, A. Li, Y. Yamamoto, H. Ohnishi, H. Hiranuma, H. Komine and N. Kondo, *Allergol. Int.*, 2006, **55**, 49–54.
58 M. Ultsch, A. Braisted, H. R. Maun and C. Eigenbrot, *Protein Eng. Des. Sel.*, 2017, **30**, 619–625.
59 J. F. Hainfeld, *Proc. Natl. Acad. Sci.*, 1992, **89**, 11064–11068.
60 L. Conti, S. Ciambellotti, G. E. Giacomazzo, V. Ghini, L. Cosottini, E. Puliti, M. Severi, E. Fratini, F. Cencetti, P. Bruni, B. Valtancoli, C. Giorgi and P. Turano, *Inorg. Chem. Front.*, 2022, **9**, 1070–1081.
61 C. Gu, T. Zhang, C. Lv, Y. Liu, Y. Wang and G. Zhao, *ACS Nano*, 2020, **14**, 17080–17090.
62 Z. Tu, P. Timashev, J. Chen and X. Liang, *BMEMat*, 2023, **1**, e12022.
63 F. Tang, L. Li and D. Chen, *Adv. Mater.*, 2012, **24**, 1504–1534.
64 F. Etoc, E. Balloul, C. Vicario, D. Normanno, D. Liße, A. Sittner, J. Piehler, M. Dahan and M. Coppey, *Nat. Mater.*, 2018, **17**, 740–746.

SI - Hybrid ferritin nanocages for flexible, site-specific targeting, cluster-formation and activation of membrane receptors

Andreas Neusch,[1] Christina Siepe,[1] Liesa Zitzke, [1] Alexandra C. Fux,[2] Cornelia Monzel [1,]*

AUTHOR ADDRESS

[1] Experimental Medical Physics, Heinrich-Heine University Düsseldorf, 40225 Düsseldorf, Germany.

[2] Department of Biosciences & Medical Biology, Paris Lodron University of Salzburg, 5020 Salzburg, Austria.

[*] Corresponding author, E-mail: Cornelia.Monzel@hhu.de

Content

MATERIALS AND METHODS

Bacterial transformation and genetic engineering

As described in the main text, one ferritin cage consists of 24 subunits. For this study, cages only comprised of modified heavy chain ferritin (HCF; PDB code: 2FHA) subunits. Through genetic engineering two constructs were prepared: HCF with an N-terminal mEGFP (as a generous gift from the Coppey/Haji laboratory at the Laboratoire Physico-Chimie, Institut Curie, Paris, France and the Piehler laboratory at the University of Osnabrück, Germany), denoted GFP-HCF (see Figure S3) and HCF with an N-terminal protA (see Figure S4), a minimal binding domain of Protein A from *S. aureus*,[1–3] denoted protA-HCF. Additionally, GFP-HCF was equipped with a His-tag at its N terminus. cDNA of GFP-HCF was inserted into the vector pET21a (reporter gene: *ampR*), protA-HCF was inserted into pET24a (reporter gene: *kanR*).

Homopolymeric Ferritin

In order to produce Ferritin cages consisting of only one subunit, *E. coli* from the strain BL21-CodonPlus (DE3)-RIPL (Agilent, Santa Clara, CA, USA), were transformed with one of the two HCF constructs as described previously.[4]

Heteropolymeric Ferritin

A two-step bacterial transformation was performed to create a hybrid ferritin cage consisting of both GFP-HCF and protA-HCF. In the first step, bacteria were transformed as previously established.[4] After transformation, bacteria were plated on LB-agar plates containing the respective antibiotic and incubated at 37 °C overnight. The next day, a single colony was picked and transferred into 5 ml of LB containing 1 g/l of glucose for an overnight culture. Afterwards, 500 µl of the overnight culture were used to inoculate 50 ml of LB medium without antibiotics. The culture was grown up to an OD_{600} of 0.4 to 0.5. Bacteria were then transferred into a centrifuge tube, chilled on ice for 15 min, and then centrifuged at 4 °C and 4,000 g for 10 min. The cell pellet was resuspended in ice-cold resuspension buffer (100 mM $CaCl_2$). After another 15 min on ice, bacteria were again centrifuged at 4 °C and 4,000 g for 10 min and collected in 2 ml of competence buffer (100 mM $CaCl_2$, 15 % v/v glycerol). As referenced earlier, the subsequent transformation was performed with 50 µl of these competent bacteria.[4] With this method, bacteria were first transformed with GFP-HCF and then, after rendering the transformed bacteria competent, with protA-HCF, to express both subunits simultaneously and produce hybrid ferritin cages.

Protein expression and purification

Production of protein and the subsequent purification were performed as referenced earlier.[4] Owing to the incorporated His-tag in both ferritin constructs, after heat denaturation of unwanted proteins and the subsequent centrifugation, the protein solution was purified using immobilized metal affinity chromatography (IMAC) in an NGC system (Bio-Rad, Hercules, CA, USA). The system – together with a Ni^{2+} activated HisTrap HP column (Cytiva, Marlborough, MA, USA) – was flushed with binding buffer BB (20 mM HEPES, 100 mM

NaCl, 20 mM imidazole, pH 8.0, filtered through 0.2 µm mesh, degassed) and elution buffer EB (20 mM HEPES, 100 mM NaCl, 300 mM imidazole, pH 8.0, filtered through 0.2 µm mesh, degassed) followed by another flush with BB. In preparation for IMAC, 20 mM imidazole was added to the sample solution. The sample was then loaded onto the column and washed with BB, to remove unspecifically bound protein. The target protein was eluted by applying an elution gradient from 0 to 100 % of EB over 10 column volumes (CV). Eluate was collected with a fraction size of 3 ml. Fractions containing the target protein were combined, reconcentrated, washed with HEPES buffer (20 mM HEPES, 100 mM NaCl, pH 8.0, filtered through 0.2 µm mesh, degassed), and aliquoted for further needs.

Transmission electron microscopy (TEM)

For TEM analysis, samples were diluted to 0.05 mg/ml and a droplet of 7 µl was placed on a Ni grid with Formvar coating (S162N, PLANO GmbH, Wetzlar, Germany). Proteins were left to sediment for 1 min and then removed from the grid using filter paper. The grid was then dipped for 3 s into a droplet of uranyl acetate solution (2 %), dried with filter paper and placed on top of a second drop of uranyl acetate. After 30 s, the grid was removed from the drop, dried using filter paper, and left to dry for 15 min.

Samples were imaged using a Jeol JEM-2100Plus (Akishima, Tokyo, Japan) at an acceleration voltage of 80 kV. Images were analyzed using Gatan Micrograph Suite (Gatan Inc., Pleasanton, CA, USA) and Matlab 2023a (Mathworks, Natick, MA, USA).

Fluorescence linked immunosorbent assay (FLISA)

The binding behavior between the ferritin constructs and target antibodies was assessed using FLISA. For this, 50 µl of antibody solution (1 µg/ml) were added into the wells of a 96-well plate (half area, black, medium binding, REF 675076, Greiner Bio-One, Kremsmünster, Austria) and incubated for 1 h at room temperature. The analyzed antibodies were a human IgG1 control antibody (REA Control Antibody, human IgG1, pure, 130-129-977, Miltenyi Biotec, Bergisch Gladbach, Germany), a murine IgG2a (Art. No. 130-106-546, Miltenyi Biotec), and an APC-labeled human IgG1 (Art. No. 130-113-446, Miltenyi Biotec). Wells were then filled to their maximum by adding 130 µl of blocking buffer (20 mM HEPES, 100 mM NaCl, pH 8.0, 2 % (w/v) BSA) and incubated overnight at 4 °C. The next day, serial dilutions of ferritin samples were prepared freshly. Afterwards, wells were emptied and washed three times with 180 µl of HEPES-T (20 mM HEPES, 100 mM NaCl, pH 8.0, 0.05 % (v/v) Tween20). After the last washing step, it is highly important to remove all traces of liquid from each well. Then, 50 µl of the ferritin constructs' dilution series were added to each corresponding well and incubated at room temperature for 1 h in the dark. Wells were then washed again three times and afterwards filled with 50 µl of HEPES buffer (20 mM HEPES, 100 mM NaCl, pH 8.0).

The FLISA was analyzed using a Tecan Infinite M Plex (Tecan Group, Männedorf, Switzerland) in fluorescence mode (Excitation: 488 nm | Emission: 540 nm). The obtained data was analyzed using Matlab. Normalized data was fitted using four-parameter logistic regression:

$$I(x) = D + \frac{A - D}{1 + \left(\frac{x}{C}\right)^{B}},$$

with the plateau at infinite concentration *A*, the asymptote at zero concentration *D*, the slope parameter *B* and the point of inflection – or K_D value – *C*. The fit was forced to stay within the Interval of 0 to 1, since the data sets were background subtracted and normalized to the positive control (ferritin incubated directly in the well).

Dynamic light scattering (DLS)

DLS measurements were performed using a Zetasizer Nano ZS (Malvern Panalytical Ltd, Malvern, UK). Prior to measurement, all samples were centrifuged at 10,000 g for 10 min and only the supernatant was analyzed. 20 µl of sample solution at a concentration between 0.1 and 1.0 mg/ml was placed into a Ultra-Micro-cuvette, placed in the Zetasizer, and left to equilibrate to 25°C for 3 min. The sample was analyzed in five measurement cycles, each containing 15 runs of 10 s. The delay between each measurement cycle was 1 min. The measurement angle was set to 173° backscatter. The obtained data was analyzed according to the number distribution in order to realistically weight the measured nanoparticles.

Spectroscopy and degree of labeling

In order to determine the concentration and degree of labeling (DoL; number of fluorophores per nanoparticle) of our ferritin constructs, spectroscopical analyses were conducted. In this work, it was determined spectroscopically using a NanoPhotometer NP80 (Implen, Munich, Germany). The absorbance of samples was measured in the range of 200 to 900 nm and the mean of 550 to 900 nm was subtracted from each curve as background. As described in the main text, Lambert-Beer's law was used for the analysis:

$$DoL = \frac{\varepsilon_{488,GFP}}{\varepsilon_{280,Ft}} \frac{A_{488}}{(A_{280} - A_{488} \cdot CF_{GFP})},$$

with the following parameters: $\varepsilon_{488,GFP}$ = 56,000 M-1cm-1, $\varepsilon_{280,Ft}$ = 462,860 M-1cm-1, A_{280} and A_{488} as measured absorbances of the sample at wavelength 280 and 488 nm respectively, and the correction factor CF_{GFP} as the ratio of A_{280} over A_{488}. This correction factor was determined from a separately, pure sample of mEGFP to be 0.54.

SDS-PAGE

Protein samples were mixed in a 1:1 ratio with 2x Laemmli buffer (Cat. No. 42526.01, Serva, Heidelberg, Germany) denatured for 5 min at 100 °C and centrifuged for 15 min at 4 °C and 15,000 g. The supernatant was loaded onto a self-cast 11% SDS gel and run at 100 V for 90 to 120 min. Afterwards, the gel was washed with water several times and then stained using Coomassie blue stain (SimplyBlue™ SafeStain, Thermo Fisher Scientific, Waltham, MA, USA) for 1 h on a horizontal shaker. After staining, the gel was washed with water and destained for 1 h in water, also shaking. Gels were then imaged using a GelDoc Go Imaging System (Bio-Rad).

The images were processed in Fiji.[5] After background subtraction (rolling ball radius: 50 px, sliding paraboloid) Fiji's gel analysis tool was used to plot band intensities. The area under the peaks was used for estimations of protein contents.

Cell culture and transient transfection

Adherent Cos7 cells, HeLa CD95-Knockout cells, and HeLa overexpressing CD95 were cultivated at 37 °C in a 5 % CO_2 atmosphere. Cells were cultured in Dulbecco's Modified Eagle Medium (DMEM) supplemented with 10 v% fetal calve serum (FCS) and 1 v% PenStrep (all from Thermo Fisher Scientific). Cos7 cells were seeded onto imaging dishes 24 h before transfection. Transfection of Cos7 was carried out the day before imaging using the transfection agent ViaFect (Promega, Madison, Wisconsin, USA) according to the manufacturer's protocol. During imaging, cells were kept in Leibovitz's L-15 Medium (L-15) without phenol red. HeLa cells for CTB assay were seeded in a 96-well plate 24 h before the experiment.

Microscopy and microshower

Images were taken with an inverted epifluorescence microscope (IX83 by Olympus, Shinjuku, Tokyo, Japan) in combination with a 60x oil objective (N.A. = 1.25, PH3, Olympus UPLFLN60XOIPH/1,25, Olympus). Microshower of protA-Ft was performed using a microinjection setup, consisting of a micromanipulator (InjectMan 4, Eppendorf, Hamburg, Germany), a pump system (FemtoJet 4i, Eppendorf), and matching microcapillaries (Femtotip II, inner diameter of 500 nm, Eppendorf). The loaded ferritin solution was at a concentration of 1 mg/ml and centrifuged for 10 min at 10,000 g to remove any agglomerates before loading into the capillary. The pump system's compensation pressure was adjusted to sustain a constant flow out of the microcapillary during the microshower. For CD95 experiments, cells were incubated for 15 min with CD95-specific antibody (Art. No. 130-108-066, Miltenyi Biotec) at a dilution of 1:50 in L-15 medium. Then, cells were washed with Dulbecco's Phosphate Buffered Saline PBS (DPBS, Thermo Fisher Scientific) and imaged in L-15 medium.

CellTiter-blue® viability assay

Apoptosis evaluation was performed using CellTiter®-blue (CTB) assay (Promega, Fitchburg, WI, USA) according to the manufacturer's manual and as described previously.[6] In short, HeLa CD95-Knockout and HeLa stably overexpressing CD95 were seeded into 96-well plates, with 25,000 cells per well, the day before. Cells were washed with DPBS, once and incubated in DMEM and the respective mixture of CD95-specific antibody (Miltenyi), protA-Ft, GFP-Ft, and CD95 ligand (CD95L), all at concentration of 1 µg/ml in DMEM. After 16 h, cells were washed once and incubated for 3 h in a 1:10 mix of DMEM and CTB solution. Well plates were analyzed using Infinite M Plex plate reader (Tecan, Männedorf, Switzerland) with 560 nm excitation and 590 nm emission over 25 flashes and 5 repetitions. Three biological replicates were analyzed. Data was background subtracted (control well with all cells killed using 0.1% of Triton X-100 (PanReac AppliChem, Darmstadt, Germany) for 30 min, as 0 % cell viability) and normalized to the positive control (cells only incubated with DMEM, as 100 % cell viability).

SUPPLEMENTARY FIGURES

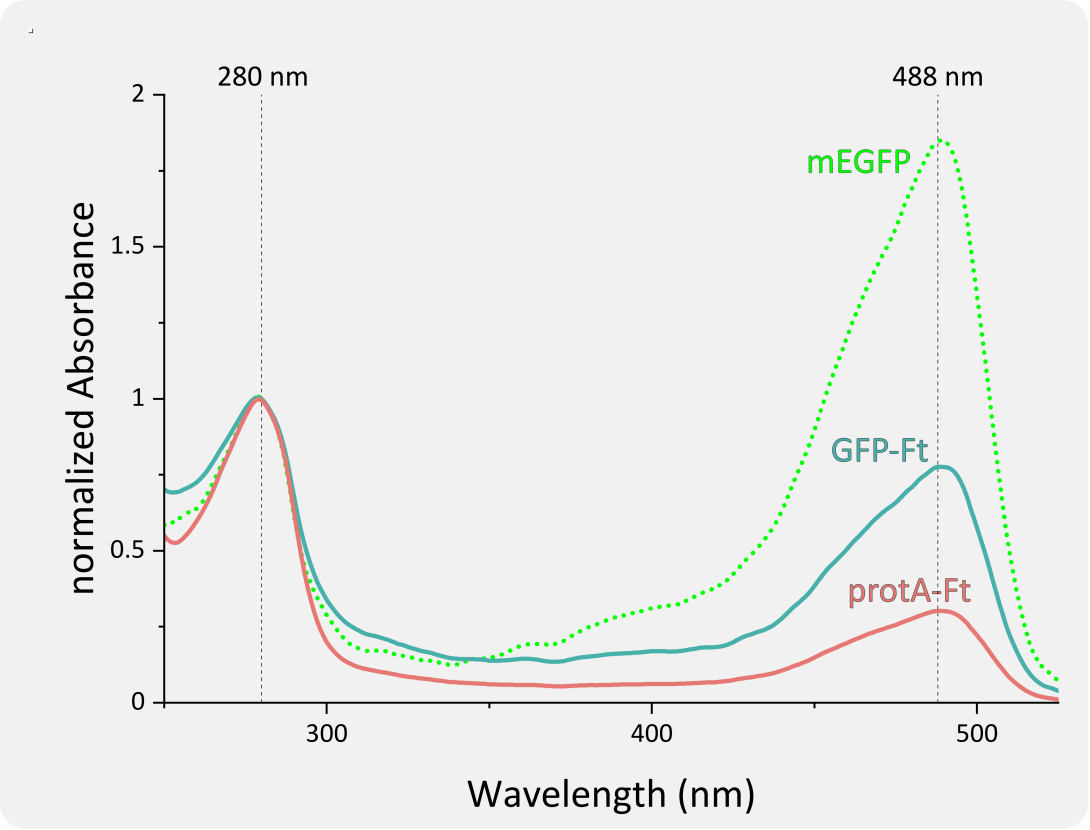

Figure S1 – Absorption spectra of pure GFP-Ft and protA-Ft for determination of the degree of labeling (DoL). Pure mEGFP was measured as a reference for the calculation of the correction factor of mEGFP. All spectra are normalized to the absorbance at 280 nm.

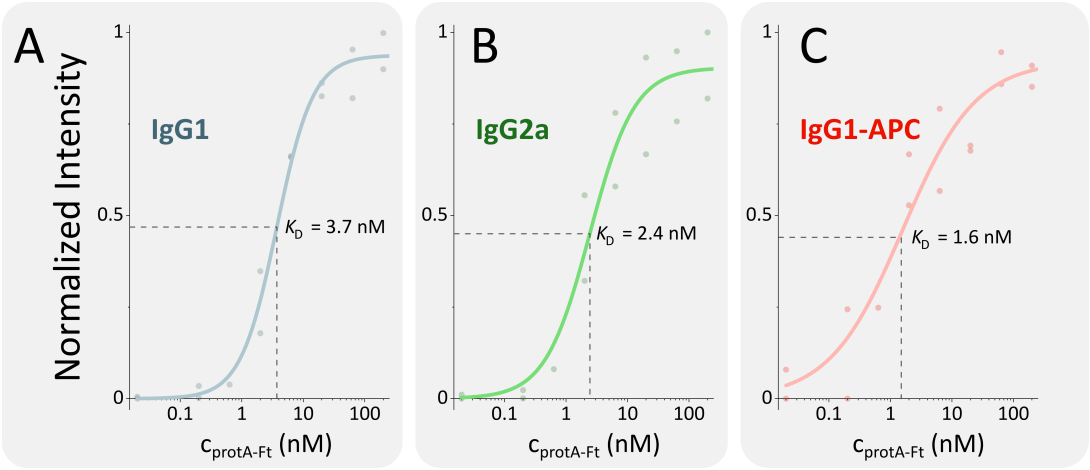

Figure S2 – Results of FLISA with three different antibodies and incubation with protA-Ft in different concentrations. The K_D was obtained by fitting a 4PL curve (see Materials and Methods) to the data. Data were obtained as three technical replicates.

Figure S3 – Sequence of His6–mEGFP–Linker–HCF

His6

mEGFP

Linker

HCF

DNA Sequence

ATGCATCATCATCACCATCACGGCAGCGGC-
GTGAGCAAGGGCGAGGAGCTGTTCACCGGGGTGGTGCCCATCCTGGTCGAGCTGGACGGCGACGTAAACGG
CCACAAGTTCAGCGTGTCCGGCGAGGGCGAGGGCGATGCCACCTACGGCAAGCTGACCCTGAAGTTCATCTG
CACCACCGGCAAGCTGCCCGTGCCCTGGCCCACCCTCGTGACCACCCTGACCTACGGCGTGCAGTGCTTCAGCC
GCTACCCCGACCACATGAAGCAGCACGACTTCTTCAAGTCCGCCATGCCCGAAGGCTACGTCCAGGAGCGCAC
CATCTTCTTCAAGGACGACGGCAACTACAAGACCCGCGCCGAGGTGAAGTTCGAGGGCGACACCCTGGTGAA
CCGCATCGAGCTGAAGGGCATCGACTTCAAGGAGGACGGCAACATCCTGGGGCACAAGCTGGAGTACAACTA
CAACAGCCACAACGTCTATATCATGGCCGACAAGCAGAAGAACGGCATCAAGGTGAACTTCAAGATCCGCCAC
AACATCGAGGACGGCAGCGTGCAGCTCGCCGACCACTACCAGCAGAACACCCCCATCGGCGACGGCCCCGTG
CTGCTGCCCGACAACCACTACCTGAGCACCCAGTCCAAGCTGAGCAAAGACCCCAACGAGAAGCGCGATCACA
TGGTCCTGCTGGAGTTCGTGACCGCCGCCGGGATCACTCTCGGCATGGACGAGCTGTACAAG-
GGATCCGGTGCAGAATTC-
ATGACGACCGCGTCCACCTCGCAGGTGCGCCAGAACTACCACCAGGACTCAGAGGCCGCCATCAACCGCCAGA
TCAACCTGGAGCTCTACGCCTCCTACGTTTACCTGTCCATGTCTTACTACTTTGACCGCGATGATGTGGCTTTGA
AGAACTTTGCCAAATACTTTCTTCACCAATCTCATGAGGAGAGGGAACATGCTGAGAAACTGATGAAGCTGCA
GAACCAACGAGGTGGCCGAATCTTCCTTCAGGATATCAAGAAACCAGACTGTGATGACTGGGAGAGCGGGCT
GAATGCAATGGAGTGTGCATTACATTTGGAAAAAAATGTGAATCAGTCACTACTGGAACTGCACAAACTGGCC
ACTGACAAAAATGACCCCCATTTGTGTGACTTCATTGAGACACATTACCTGAATGAGCAGGTGAAAGCCATCAA
AGAATTGGGTGACCACGTGACCAACTTGCGCAAGATGGGAGCGCCCGAATCTGGCTTGGCGGAATATCTCTTT
GACAAGCACACCCTGGGAGACAGTGATAATGAAAGCTAG

Protein Sequence

MHHHHHHGSG-
VSKGEELFTGVVPILVELDGDVNGHKFSVSGEGEGDATYGKLTLKFICTTGKLPVPWPTLVTTLTYGVQCFSRYPDH
MKQHDFFKSAMPEGYVQERTIFFKDDGNYKTRAEVKFEGDTLVNRIELKGIDFKEDGNILGHKLEYNYNSHNVYIM
ADKQKNGIKVNFKIRHNIEDGSVQLADHYQQNTPIGDGPVLLPDNHYLSTQSKLSKDPNEKRDHMVLLEFVTAAGI
TLGMDELYK-GSGAEF-
MTTASTSQVRQNYHQDSEAAINRQINLELYASYVYLSMSYYFDRDDVALKNFAKYFLHQSHEEREHAEKLMKLQN
QRGGRIFLQDIKKPDCDDWESGLNAMECALHLEKNVNQSLLELHKLATDKNDPHLCDFIETHYLNEQVKAIKELGD
HVTNLRKMGAPESGLAEYLFDKHTLGDSDNES

Figure S4 – Sequence of protA–Linker–HCF

protA

Linker

HCF

DNA Sequence

ATGGTTGACAACAAATTCAACAAAGAACAGCAGAACGCGTTCTACGAAATCCTGCACCTGCCGAACCTGAACG
AAGAACAGCGTAACGCGTTCATCCAGTCTCTGAAAGACGACCCGTCTCAGTCTGCGAACCTGCTGGCGGAAGC
GAAAAAACTGAACGACGCGCAGGCGCCGAAA-GGATCCGGTGCAGAATTC-
ATGACGACCGCGTCCACCTCGCAGGTGCGCCAGAACTACCACCAGGACTCAGAGGCCGCCATCAACCGCCAGA
TCAACCTGGAGCTCTACGCCTCCTACGTTTACCTGTCCATGTCTTACTACTTTGACCGCGATGATGTGGCTTTGA
AGAACTTTGCCAAATACTTTCTTCACCAATCTCATGAGGAGAGGGAACATGCTGAGAAACTGATGAAGCTGCA
GAACCAACGAGGTGGCCGAATCTTCCTTCAGGATATCAAGAAACCAGACTGTGATGACTGGGAGAGCGGGCT
GAATGCAATGGAGTGTGCATTACATTTGGAAAAAAATGTGAATCAGTCACTACTGGAACTGCACAAACTGGCC
ACTGACAAAAATGACCCCCATTTGTGTGACTTCATTGAGACACATTACCTGAATGAGCAGGTGAAAGCCATCAA
AGAATTGGGTGACCACGTGACCAACTTGCGCAAGATGGGAGCGCCCGAATCTGGCTTGGCGGAATATCTCTTT
GACAAGCACACCCTGGGAGACAGTGATAATGAAAGCTAG

Protein Sequence

MVDNKFNKEQQNAFYEILHLPNLNEEQRNAFIQSLKDDPSQSANLLAEAKKLNDAQAPK-GSGAEF-
MTTASTSQVRQNYHQDSEAAINRQINLELYASYVYLSMSYYFDRDDVALKNFAKYFLHQSHEEREHAEKLMKLQN
QRGGRIFLQDIKKPDCDDWESGLNAMECALHLEKNVNQSLLELHKLATDKNDPHLCDFIETHYLNEQVKAIKELGD
HVTNLRKMGAPESGLAEYLFDKHTLGDSDNES*

BIBLIOGRAPHY

1 B. Nilsson, T. Moks, B. Jansson, L. Abrahmsén, A. Elmblad, E. Holmgren, C. Henrichson, T. A. Jones and M. Uhlén, *Protein Eng. Des. Sel.*, 1987, **1**, 107–113.

2 M. D. Levasseur, S. Mantri, T. Hayashi, M. Reichenbach, S. Hehn, Y. Waeckerle-Men, P. Johansen and D. Hilvert, *ACS Chem. Biol.*, 2021, **16**, 838–843.

3 A. C. Braisted and J. A. Wells, *Proc. Natl. Acad. Sci. U. S. A.*, 1996, **93**, 5688–5692.

4 A. Neusch, U. Wiedwald, I. P. Novoselova, D. A. Kuckla, N. Tetos, S. Sadik, P. Hagemann, M. Farle and C. Monzel, *Nanoscale*, 2024, **16**, 15113–15127.

5 J. Schindelin, I. Arganda-Carreras, E. Frise, V. Kaynig, M. Longair, T. Pietzsch, S. Preibisch, C. Rueden, S. Saalfeld, B. Schmid, J. Y. Tinevez, D. J. White, V. Hartenstein, K. Eliceiri, P. Tomancak and A. Cardona, *Nat. Methods*, 2012, **9**, 676–682.

6 I. P. Novoselova, A. Neusch, J. S. Brand, M. Otten, M. R. Safari, N. Bartels, M. Karg, M. Farle, U. Wiedwald and C. Monzel, *Nanomaterials*, 2021, **11**, 1–20.

Chapter IV

Magnetic Actuation of Magnetoferritin

IV.1 Publication III

Reference

Title An efficient magnetothermal actuation setup for fast heating/cooling cycles or long-term induction heating of different magnetic nanoparticle classes

Authors Daniel Alexander Kuckla, Julia-Sarita Brand, Bastian Czech, Amirarsalan Asharion, Jan Vinzenz Jüttner, Iuliia Pavlovna Novoselova, Andreas Neusch, Philipp Hagemann, Mathias Getzlaff, and Cornelia Monzel

Journal details *Journal of Physics D: Applied Physics*, Volume 56, Issue 50

Date of Publication 29th September 2023

DOI https://doi.org/10.1088/1361-6463/acfb8f

Copyright

Contribution

I recorded nanoparticles via TEM, determined the size distributions and prepared the data for visualization. Additionally, I proof-read the article together with the other authors.
My overall contribution to this publication amounts to approximately 5 %.

OPEN ACCESS
IOP Publishing
Journal of Physics D: Applied Physics
J. Phys. D: Appl. Phys. **56** (2023) 505002 (14pp)
https://doi.org/10.1088/1361-6463/acfb8f

An efficient magnetothermal actuation setup for fast heating/cooling cycles or long-term induction heating of different magnetic nanoparticle classes

Daniel Alexander Kuckla[1], Julia-Sarita Brand[1], Bastian Czech[2], Amirarsalan Asharion[1], Jan Vinzenz Jüttner[1], Iuliia Pavlovna Novoselova[1], Andreas Neusch[1], Philipp Hagemann[1], Mathias Getzlaff[2] and Cornelia Monzel[1,*]

[1] Experimental Medical Physics, Heinrich-Heine University, Duesseldorf, Germany
[2] Institute of Applied Physics, Heinrich-Heine University, Duesseldorf, Germany

E-mail: cornelia.monzel@hhu.de

Received 15 April 2023, revised 7 September 2023
Accepted for publication 20 September 2023
Published 29 September 2023

Abstract

Alternating magnetic fields (AMFs) in the ∼100 kHz frequency regime cause magnetic nanoparticles (MNPs) to dissipate heat to their nanoscale environment. This mechanism is beneficial for a variety of applications in biomedicine and nanotechnology, such as localized heating of cancer tissue, actuation of drug release, or inducing conformational changes of molecules. However, engineering electromagnetic resonant circuits which generate fields to efficiently heat MNPs over long time scales, remains a challenge. In addition, many applications require fast heating/cooling cycles over $\Delta T = 5$ °C–10 °C to switch the sample between different states. Here, we present a home-built magnetothermal actuation setup maximized in its efficiency to deliver stable AMFs as well as to enable fast heating/cooling cycles of MNP samples. The setup satisfies various demands, such as an elaborate cooling system to control heating of the circuit components as well as of the sample due to inductive losses. Fast cycles of remote sample heating/cooling (up to ±15 °C min^{-1}) as well as long-term induction heating were monitored via contact-free thermal image recording at sub-mm resolution. Next to characterizing the improved hyperthermia setup, we demonstrate its applicability to heat different types of MNPs: 'nanoflower'-shaped multicore iron oxide nanoparticles, core shell magnetite MNPs, as well as magnetosomes from magnetotactic bacteria (*Magnetospirillum gryphiswaldense*). MNPs are directly compared in their structure, surface charge, magnetic properties as well as heating response. Our work provides practical guidelines for AMF engineering and the monitoring of MNP heating for biomedical or nano-/biotechnological applications.

* Author to whom any correspondence should be addressed.

J. Phys. D: Appl. Phys. **56** (2023) 505002 D A Kuckla *et al*

Supplementary material for this article is available online

Keywords: hyperthermia, nanoparticles, magnetic nanoparticles, Synomag®, BNF, magnetosomes

(Some figures may appear in colour only in the online journal)

1. Introduction

Magnetic nanoparticles (MNPs) have been utilized in a variety of approaches to control material properties or biological functions in a defined manner [1–6]. Of particular interest is their remote, inductive heating by the application of alternating magnetic fields (AMFs). Thus, a contact-free generation of nanoscale hotspots with high temperature control is realized. Hitherto, this approach has been employed across a range of biomaterial applications including cancer hyperthermia [7–10], spatially controlled drug release [11–15], the control of cell functions [16–18], as well as the creation of heat responsive material [17, 19, 20]. However, the MNP heating response highly depends on the AMF generating setup and a thorough description of it exists only in few cases [21–23]. Moreover, to maximize the heating performance and range of applications, further optimization with regard to its implementation is needed [24]. For example, (i) to expand AMF applications to heterogeneous MNP distributions and to monitor their local effect requires recording of spatially resolved temperature data. (ii) For nanotechnological or cell biological applications, the generation of higher and stable magnetic field amplitudes ($\geqslant$40 mT) over long time scales is important. Here, small MNPs ($\leqslant$50 nm) need to be used, which naturally exhibit a lower magnetic response. (iii) Precise temperature variations, e.g. in the form of oscillations, are very useful to change the state of heat-sensitive matter. E.g. biomolecules can be switched between their active and inactive state and biological membranes can change from a phase separated to a homogenously mixed state. Towards realizing these applications in addition to characterizing the classical homogeneous MNP samples, this work presents solutions to advance the hyperthermia setup.

The generation of heat at the MNP site requires sufficient magnetization of the MNP by magnetic field amplitudes of typically $H \approx 10\,\mathrm{kA\,m^{-1}}$ [16, 18]. The magnetic moment then couples to the AMF and follows the orientation of the external field (in phase or with a certain phase lag), the latter exhibiting frequencies of typically 100 kHz–1 MHz. The relative orientation of the magnetic moment and the external field give rise to an effective hysteresis loop [25], whose area is proportional to the heat produced by the MNPs. The dissipated power P_H in form of heat is calculated according to

$$P_\mathrm{H} \propto f \oint H(f)\,\mathrm{d}B, \tag{1}$$

where f is the AMF frequency, H the external magnetic field amplitude and B the magnetic flux density generated by the MNP. In case of superparamagnetic particles, which lack an apparent hysteresis loop and hence resemble 'paramagnetic' particles within a certain temperature range, the generated heat can be calculated from the linear-response theory [26]

$$P_\mathrm{H} = \mu_0 \pi f \chi''(f) H(f)^2, \tag{2}$$

where χ'' is the imaginary part of the AC magnetic susceptibility, a measure of how much the material becomes magnetized, and P_H, f, H as before. Of note, $\chi(f)''$ is a particle inherent property and $H(f)$ is defined by the hyperthermia setup, with both depending on the AMF frequency. The lack of an apparent hysteresis loop for superparamagnetic particles is a result of the fact, that the magnetic moment is not blocked but can oscillate due to thermal fluctuations. Here, after an initial magnetization pulse, a relaxation of the orientation of the magnetic moment is observed. Two different processes contribute to this relaxation mechanisms, the Néel and Brownian relaxation. Néel relaxation describes the reorientation of the magnetic moment relative to the particle due to thermal fluctuations, whereas Brownian relaxation occurs due to interactions of the particle with the surrounding medium (figure 1(a)). The in our case faster Néel relaxation then dominates the effective relaxation time of the particle's magnetic moment. The effective relaxation time is directly reflected in the alternating current magnetic susceptibility (AC-susceptibility), χ, and its imaginary part χ'' has to be maximized, to maximize P_H. Overall, the strong dependence of P_H on f, $H(f)$ and $\chi(f)''$ suggests a critical examination and adjustment of the AMF setup and MNP properties for optimal performance.

To design an efficient hyperthermia setup, one needs to overcome severe constraints, primarily arising from the substantial power dissipated as Joule heating. The resistive losses in the material not only impede the long-time stability of the AMF setup, but also cause substantial side effects, such as immediate heating of the sample and the surrounding. Also, additional input power may be required to reach target magnetic flux densities.

So far, different magnetic hyperthermia setups were constructed, generating magnetic fields of several 10 mT at frequencies around 100 kHz within an electromagnetic gap of few mm in size [21–23]. These works reported substantial improvements with regard to the choice of the electromagnet core and the generation of higher magnetic flux densities [23], the capability of life cell imaging during magnetic stimulation [18], or the realization of gap sizes up to 11 mm [21]. Yet, reconciling these partly countervailing demands in one setup remains a challenge. In particular, setups exhibiting long-time stability of the AMF at high magnetic flux densities as well as

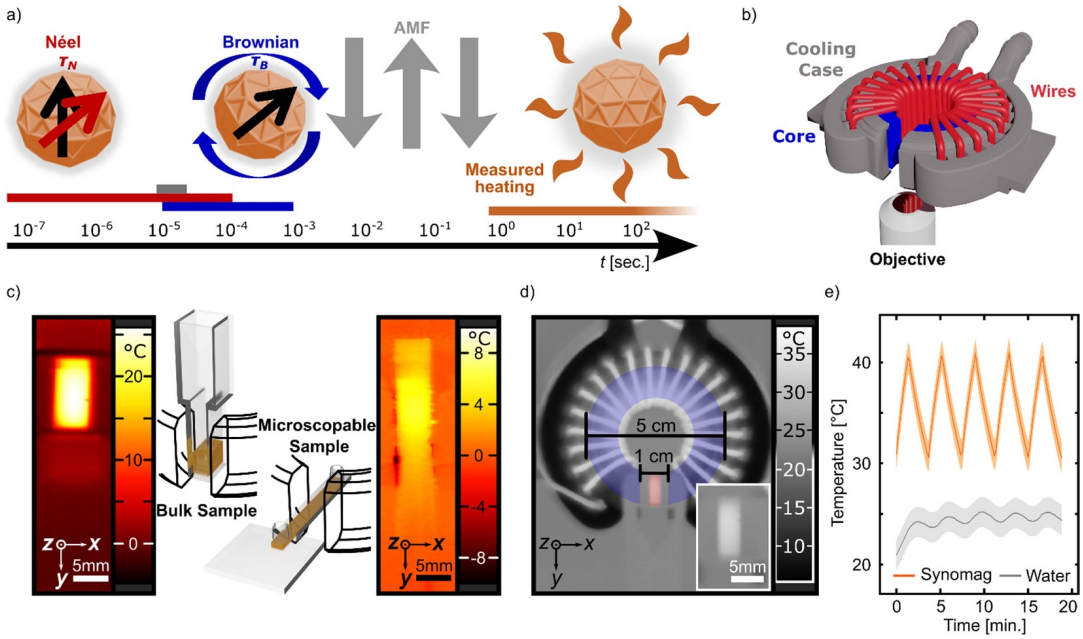

Figure 1. (a) Scheme of characteristic time scales of the AMF, the magnetization relaxation mechanisms of MNPs (Néel and Brownian relaxation) and the observed heating. (b) Scheme of the magnet setup with color coded components. (c) Sketch of samples for bulk measurements and microscopy measurements. The black wire model indicates the magnetic core around the samples. Typical sample volumes of 200 μl (bulk) and 50 μl (microscopable) are shown in orange. Thermography images show the difference in steady-state temperature of Synomag® (5 mg ml^{-1}) versus water sample for each sample type. Note, that the temperatures of the microscopable sample are underestimated due to the plastic sealing on top of the channel. Scale bar 5 mm. (d) Thermography image of the magnet while running. The core position is indicated in blue, the sample position in red. The inset is a zoomed view of the sample area. Scale bar 5 mm. (e) Fast heating/cooling cycles of Synomag® (5 mg ml^{-1}) and water measured with the setup presented in this work. Errors are shown as shaded areas around the data.

efficient, repetitive heating-cooling cycles are lacking. These would be desirable for a variety of applications in material science, such as the switching of thermo-sensitive molecules [12, 27, 28], or the triggering of biological signaling processes via temperature responsive proteins [16–18]. Another desirable aspect is the availability of a hyperthermia setup which is effective in terms of costs and technological equipment.

Here, we present a home-built hyperthermia setup addressing the aforementioned needs to demonstrate long-term stability of gap magnetic flux densities in the 45–50 mT regime over 30 min. Our work provides practical guidelines for AMF engineering to sufficiently magnetize MNPs. We demonstrate long-term measurements of MNP heating up to steady state temperatures at 70 °C as well as fast MNP heating/cooling cycles with temperature gradients up to ±15 °C min^{-1}. With this setup we demonstrate optimized heat generation from three types of (superpara-)MNPs: next to 'nanoflower'-like magnetite MNPs (so called Synomag®), we probe bionized nanoferrite core shell particles (so called BNF) as well as magnetosomes. Synomag® and BNF were readily available from micromod (micromod Partikel-technologie, GmbH, Rostock, Germany), whereas Magnetosomes are formed by the magnetotactic bacteria species *Magnetospirillum gryphiswaldense* through biomineralization and were isolated thereafter (see methods). Figures 1(b)–(e) provide an overview of the setup and measurement procedure with direct temperature mapping at sub-mm resolution.

2. Methods

2.1. MNPs

Synomag® 70 and BNF 100 were purchased from micromod. Magnetosomes were isolated from the bacteria species *M. gryphiswaldense*. Magnetosomes are single-domain MNP. In bacteria, they are encapsulated by a protein shell that prevents agglomeration and aligns the MNP in chains. Bacteria were cultivated in complex medium (15 mM potassium lactate, 10 mM sodium nitrate, 0.7 mM monopotassium phosphate, 0.6 mM magnesium sulfate, 3 g l^{-1} peptone, 0.1 g l^{-1} yeast extract, 0.15 mM iron(III) citrate, 20 mM HEPES (pH 7.0)) for 39 h at 28 °C without shaking and without air exchange. Cultures were fed with supplementary medium (0.75 M potassium lactate, 1 M sodium nitrate, 37 mM

monopotassium phosphate, 30 mM magnesium sulfate, 5 mM iron(III) citrate) after 24, 30, 33, 36, and 39 h. Afterwards, bacteria were collected by centrifugation at 4000 g for 7 min and resuspended in HEPES buffer (0.2 M, pH 7.0). Bacteria were lysed with an ultrasonic sonotrode (UP 200S, Hielscher Ultrasonics GmbH, Teltow, Germany) at 30 W for 120 min in an ice bath, to isolate but maintain the magnetosome chains. After lysis, magnetosome chains were collected and washed with a neodymium magnet and resuspended in HEPES buffer (0.2 M, pH 7.0). In some cases, the magnetosome cores were extracted from the chains, wherefore the encapsulating protein shells were denatured at 90 °C for 5 h in a water bath.

2.2. MNP sample preparation

For transmission-electron-microscopy (TEM) imaging of Synomag® and BNF particles the stock solution was diluted to a concentration of 0.125 mg ml^{-1} in phosphate buffered saline. Afterwards the sample was sonicated in an ultrasonic bath for 10 min and filtered through a syringe filter (Filtropur S, membrane: polyethersulfone, filtration area: 6.2 cm^2, pore size: 0.2 μm, sarsted AG & Co. KG, Nümbrecht, Germany). 7 μl of the prepared samples were dropped onto a formvarni-grid and sedimented for 2 min. The remaining solution was removed using filter paper and the grids were left to dry on air. Images were taken with a Jeol JEM-2100plus (Akishima, Tokyo, Japan) in brightfield mode at 80 kV acceleration voltage. Isolated magnetosomes were diluted 1:20 before transferring a single droplet onto a carbon-cu-grid. The solution was left to sediment for 1 min, then removed using filter paper and the grid was left to dry on air. Images were taken using a Zeiss EM902 (Carl Zeiss Microscopy GmbH, Jena, Germany) at an acceleration voltage of 80 kV. Average particle diameters were determined using FIJI [29].

For dynamic light scattering (DLS) measurements magnetosomes, Synomag® and BNF particles were diluted with HEPES buffer (0.2 M, pH 7.0) to a concentration of 0.2 mg ml^{-1} (magnetosomes) or 1 mg ml^{-1} (Synomag® and BNF particles). Please note that for Synomag® and BNF the concentration is given for particles while for magnetosomes the iron concentration is given throughout this work. All solutions were filtered through a 200 nm polytetrafluoroethylene filter (514-0068, VWR, Radnor, USA). The DLS measurements were performed with a Zetasizer Nano ZS (Malvern Panalytical, Malvern, UK). Prior to the measurement, a waiting time of 100 s served to balance the temperature (25 °C). For each sample 5 runs with 15 sub-runs (10 s) were recorded. A break of 100 s was taken between runs. Hydrodynamic diameters of particles were calculated from the mean size of the number distribution and averaged over 5 runs. The error is the standard deviation.

For ζ-potential measurement the sample was identically prepared as for DLS measurements. Since the particles were kept in buffer the 'monomodal mode' was used. Five runs with 15 sub-runs (10 s) were used per sample. Between the runs the lag time was 50 s. The ζ-potential was averaged over all runs and mean and standard deviation values are reported.

For hyperthermia measurements, MNPs dissolved in water or buffer at the indicated concentration were used.

2.3. Thermography measurements

Thermography measurements were performed using a VarioCam HD (Infratec GmbH, Dresden, Germany) with an IR 1,0/30 JENOPTIK objective (Supplied by Infratec GmbH, Dresden, Germany). A distance of 40 cm was kept from the magnet to prevent damaging the camera resulting in a $\sim$300 pixel measurement area of 5 $\times$ 10 μm^2 for the sample. Over this area, the sample temperature was averaged. The typical pixel size was $\sim$300 $\times$ 300 μm^2. A measurement cycle consisted of 1 image before applying the field, 90 images of heating period and 90 images of cooling period taken at a framerate of 0.1 Hz. For each sample the measurement was repeated $\geqslant$3 times.

2.4. Data analysis and evaluation

Images were evaluated using the IRBIS3 plus software (Infratec GmbH, Dresden, Germany). The temporal behavior of the sample temperature was extracted accounting for the sample emission coefficient of 0.95 in comparison to a blackbody, which was calibrated beforehand from the emission of a sample with known temperature. The reflected temperature was identified with the room temperature. The room temperature exhibited only slight fluctuations by $\pm$0.3 °C during the measurement and was considered to have negligible influence on the sample temperature. The heating and cooling kinetics were fitted with self-written routines in Matlab (The Mathworks Inc., Natick, MA, USA, Version: R2020b) using the least squares method lsqcurvefit. The mean fit parameters and respective error were calculated from each sample.

3. Implementation of an advanced AMF setup

3.1. General setup and resistive losses

The electric circuit is based on a series resonance circuit which enables the reuse of energy stored in the magnetic field that otherwise would need to be provided by the power supply. The general circuit design was reported before [23], where the setup consists of a function generator, an amplifier, a shunt resistor, a transformer, and an RLC series resonance circuit (figure 2(a)). To operate efficiently, the driving frequency is set to the circuit's resonant frequency where the impedance is at its minimum.

The main cause of energy dissipation in the resonance circuit are resistive losses resulting in heating of the electrical components, even when highly optimized material is used. This heat radiation causes elevated, gradually changing temperatures in the sample environment, thus preventing any measurement of small temperature changes. In order to prevent such effects and to limit the magnet temperature to $\sim$1 °C above room temperature, specialized circuit

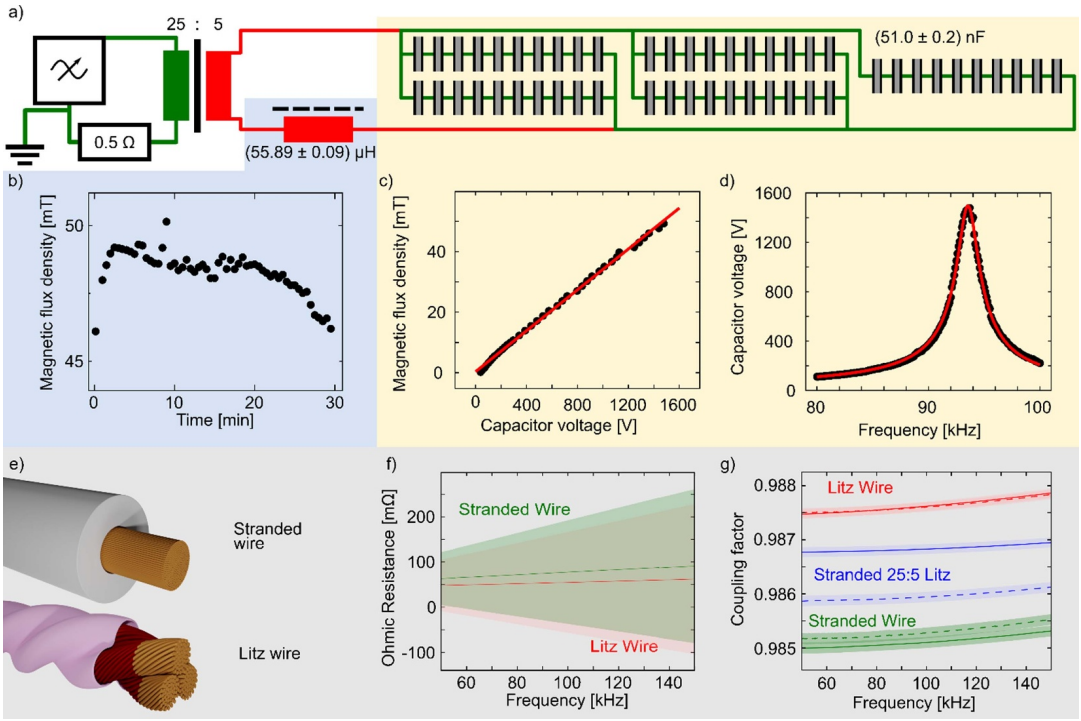

Figure 2. (a) Diagram of the resonance circuit with measured inductance and capacitance values for the electromagnet and whole array of 50 capacitors, respectively. Parts where the Litz and stranded wire are used, are marked in red and green, respectively. (b) Temporal evolution of the magnetic flux density measured in the center of the gap. The measured change amounts to less than 10%. (c) Magnetic flux density, B, as function of the peak-to-peak-voltage, x, measured at the capacitor array. The magnetic flux density follows the linear relation $B(x) = (33.78 \pm 0.49)\ \mathrm{mT/V} \cdot x + (0.33 \pm\ 0.37)\ \mathrm{mT}$ (d) measured resonance behavior of the capacitor peak-to-peak-voltage (black). From a Lorentzian function fit (red) the resonance frequency and quality factor are determined. (e) Rendered sketches of wire types used. Stranded wire consisting of 510 individual wire strands (orange) and outer insulation (light gray). Litz wire consisting of 3 bundles of 54 individually insulated wire strands (orange). Outer insulation (pink), insulation of individual wires (dark red). (f) Frequency dependent change of ohmic resistance of the different wires. (g) Frequency dependent coupling factor of a transformer consisting of a N87 core with winding ratios 25:5 (solid lines) and 5:25 (dashed lines). Coupling factors of Litz wire (red) and stranded wire (green) alone in comparison to the combination of stranded and Litz wire (25:5 solid blue line and 5:25 dashed blue line). The latter is used in this work. For all diagrams where applicable the errors are depicted as shaded areas around the data.

components minimizing eddy currents or proximity effects together with an elaborate cooling system need to be used.

3.2. Optimized circuit components and characterization

The central component of the AMF setup is the electromagnet which consists of a ferrite core and a wire coil around it ($N = 22$ turns). As core material MnZn-based SIFERRIT N87 (Tokyo denkikagaku kogyo (TDK), Tokyo, Japan) is chosen, a soft ferrimagnetic ceramic minimizing eddy currents, although losses from hysteresis occur. It exhibits a low power loss (e.g. 120 kW m^{-3} at 100 mT for 100 kHz frequencies around room temperature [30] compared to other optimized ferrites, such as 3F3 ferroxcube with 170 kW m^{-3} at identical conditions [31]). A downside of using the ferrite is the comparably low thermal conductivity (e.g. 1–5 W m^{-1} K^{-1} compared to iron 74 W m^{-1} K^{-1} at room temperature [32]). Due to the higher magnetic flux density inside the core in combination with the poor thermal conductivity, active cooling is needed to keep the core and surrounding wires from substantially heating up (see section 3.3). The toroidal magnet exhibits a gap of 10 mm × 20 mm × 10 mm ($w \times h \times l$), which enables mounting of different *in vitro* samples (e.g. fitted microscopy slides, vials or microfluidic channels) without direct contact between the sample container and magnet (figure 1(c)). These dimensions were also chosen to keep the flux leakage at minimum. The same ferrite core without gap is used for the transformer, which transmits the source signal to the resonance circuit by inductive coupling.

It is interesting to estimate the conditions at which a particular magnetic flux density at the center of the electromagnet's gap is reached. In case of a toroidal core, which channels

the AMF into a small gap (as in this work), it is given by [23]

$$H_g \approx \frac{NI}{w}, \tag{3}$$

where H_g is the amplitude of the magnetic field generated inside the gap, N is the number of turns, I is the peak current, and w is the width of the gap. For an anticipated $H_g \approx 36$ kA m^{-1} resulting in a flux density of $B = 45$ mT with $N = 22$ turns, this approximation shows that substantial currents of $I \approx 17$ A are needed. Of note, since this approximation is invalid for gap sizes $\gg 1$ mm, where leakage flux plays a role, even higher currents will be needed to reach the yield H_g. In fact, when measuring magnetic flux densities $\geqslant$45 mT at the center of the electromagnet's gap (figure 2(b)), a sinusoidal feed signal of 300 m V_{PP} was applied to the circuit. This signal was generated by a function generator (Agilent 33220A, Agilent Technologies, Santa Clara CA, USA) and amplified by (53.0 $\pm$ 1.5) dB using a 1020L radio frequency power amplifier (Electronics and Innovations Ltd, Rochester NY, USA). An input signal of this magnitude at resonance frequency gives rise to a peak-to-peak voltage of (1478 $\pm$ 2) V_{pp} at the capacitor array (figure 2(c)) and a calculated current of (44.4 $\pm$ 0.2) A.

Next to reaching the desired magnetic flux densities in the gap, an important aspect of a reliable AMF stimulus is the temporal stability of the magnetic field in the center of the gap. For the described setup a magnetic flux density of (48 $\pm$ 1) mT was maintained over 20 min and showed less than 10% deviation over the time range of 30 min (figure 2(b)). Such field stability is important, as it enables the recording of heating/cooling kinetics up to the point where a steady-state is reached.

Depending on the input voltage, the capacitor in the resonance circuit can be subject to high voltages in the kV regime (figure 2(c)) and steep voltage rises on the order of 4 $\cdot 10^8$ V s^{-1}.To account for these demands, high end film capacitors (FKP1 0.1 μF, WIMA, Mannheim, Germany) are used. To distribute the voltage among the capacitors in each branch and to divide the current among the different branches, an array of five parallel branches each containing ten capacitors in series, was implemented. Although similar setups can be realized using mica capacitors, the film capacitors are preferred as they allow for a better distribution of dissipated power and can operate free of any additional cooling. Another benefit is the option to alter the overall capacitance and hence the resonance frequency by selectively removing or adding capacitors. Important is the linear relation between the input voltage and measured magnetic flux density in the gap of the electromagnet (figure 2(c)). This behavior is favorable since it provides scalability of the AMF during experiments. Given these values, it is important to note, that the generation of higher voltages imposes a risk for the experimenter, wherefore additional safety measures as well as shielding and insulation of the setup needs to be installed. In addition, these values show, that the resonance circuit is unmatched in its efficiency to provide a high apparent power of $P = U(\omega_r)\cdot I = 65$ kW.

The resonance circuit components (figure 2) were measured with a four-port measurement using an E4990A-030 impedance analyzer (Keysight Technologies, Inc., Santa Rosa, CA, USA). The measured capacitance for the capacitance array amounted to (51.2 $\pm$ 0.3) nF, while the measured inductance for the magnet was (55.89 $\pm$ 0.09) μH. This led to a calculated resonance frequency of 94.26 kHz. These measurements provide a good estimate of the component properties, although their value in the circuit may differ during operation due to the heating of the setup. To determine the resonance frequency experimentally, a resonance curve was measured. To this end, the capacitor voltage $U(\omega)$ at different angular frequencies $\omega = 2\pi f$ was recorded and fitted with the theoretical relation

$$U(\omega) = \frac{\frac{U_{in}}{LC}}{\sqrt{\left(\frac{1}{LC} - \omega^2\right)^2 + \left(\omega\frac{R}{L}\right)^2}}, \tag{4}$$

where U_{in} is the input voltage, R is the ohmic resistance, L is the inductance, and C is the capacitance. The resonance frequency derived from the fit function was (93.54 $\pm$ 0.01) kHz (figure 2(d)), which is 0.51 kHz lower than the theoretical value. Experimentally, the magnetic field in the electromagnet's gap turned out to be slightly higher at 93.75 kHz, a value in between the initial theoretical and experimental value. For this reason, this latter optimal frequency was used. From the fit function also the quality-factor Q was determined, defined as

$$Q = \frac{\omega_r}{\Delta\omega} = \frac{f_r}{\Delta f}, \tag{5}$$

where f_r is the resonance frequency and $\Delta f$is the bandwidth at $1/\sqrt{2}$ of the maximum voltage $U(\omega)$ amounting to (3.3 $\pm$ 0.2) kHz. This resulted in a quality-factor of $Q = (29 \pm 2)$. While this high quality-factor signifies an efficient, underdamped operation of the circuit, it limits the accessible bandwidth of the signal amplification at the same time. To still enable flexible adjustments of the frequency range, interchangeable capacitors can be used.

To handle the currents mentioned above, special wires are required. The central wire forming the coil to generate the magnetic field is a special Litz wire (New England Wire Technologies, Lisbon NH, USA). The Litz wire consists of 3 bundles of 54 wire strands of American wire gauge 38, corresponding to a 50.5 μm radius (figure 2(e)). It is designed to minimize the influence of the frequency dependent skin effect, which signifies the current density distribution in a conductor, exponentially decreasing from the edge towards the center. A mitigation of the skin effect is achieved by adapting the size of individually insulated wires to the skin depth δ, the depth below the conductor surface at which the current density has fallen to its 1/e value [33]. δ amounts to $\sim$213 μm at the 93 kHz resonance frequency used in this work. Another aspect of optimization is the proximity effect, where a change in the current density in one conductor arises due to AC-currents in a nearby conductor. The proximity effect is diminished by 'braiding' the wire strands to distribute the position of each

individual strand throughout the wire. The Litz wire was used in parts of the secondary circuit of the setup, where high currents develop. A different, stranded wire consisting of 510 copper strands (LIFY 1.00/2.6; supplied by Bürklin GmbH & Co. KG, Oberhaching, Germany) was used in regions of the circuit where lower currents develop, i.e. the primary circuit of the setup and the capacitance array in the secondary circuit. Here, the necessity of using the Litz wire was reduced and combining these wires helps to lower the cost of the whole setup. To compare the performance of both wires, the wire impedance was measured and the corresponding ohmic resistance calculated, the main cause of wire heating. The ohmic resistance over a 50–150 kHz frequency regime showed a continuous resistance increase from 65 to 90 mΩ for the stranded wire, while the resistance of the Litz wire changed only from 48 to 52 mΩ (figure 2(f)). In addition, the coupling factor of the transformer for each wire was determined, using a transformation ratio of 25:5 measured in forward and backward direction (figure 2(g), solid and dashed lines respectively). Both wires exhibited a high coupling of >98% with almost negligible frequency dependence in the 50–150 kHz regime. With 98.8%, the inductive coupling of the Litz wire is marginally higher compared to the stranded wire, with 98.5%. Moreover, to ensure a homogeneous exposure of the sample to AMFs, the flux density value within the gap volume was measured with a hall probe in <1 cm steps (figure 3).

3.3. Mitigating heat dissipation by active cooling

To mitigate the heat dissipation by the system, a water-cooling system was developed. To this end, 3D printed housings for the electromagnet and the transformer core were designed with a 3D-computer aided design software and fabricated out of 3D resin (Gray Resin, Formlabs, Somerville, MA, USA). To limit the temperature rise, water of 5 °C temperature was provided by a thermostat and was constantly circulated through the cooling housings. By limiting the magnet temperature around ambient temperatures throughout the measurement, we minimized the influence of the magnet temperature on the sample heating. Moreover, cooling of the electromagnet, the transformer core, and the 0.5 Ω shunt resistor, decreases the strain on these components and increases their temporal stability and lifetimes. An image of the magnet generating 45 mT magnetic flux densities in the gap can be seen in (figure 1(d)).

4. Evaluation of three MNP classes

4.1. Characterization of MNP physical properties

To determine the suitability of different MNPs for hyperthermic heating, we first characterized the three MNP classes used in terms of their physical core size, their hydrodynamic size, their charge, as well as their AC susceptibility (figure 4). TEM images revealed a nanoflower shape of Synomag® MNP, consisting of a quasi-spherical morphology combined with a rough surface due to the nanocrystalline substructure embedded in a dextran matrix. BNF cores exhibited parallelepiped shapes, also encapsulated in a dextran shell. In case

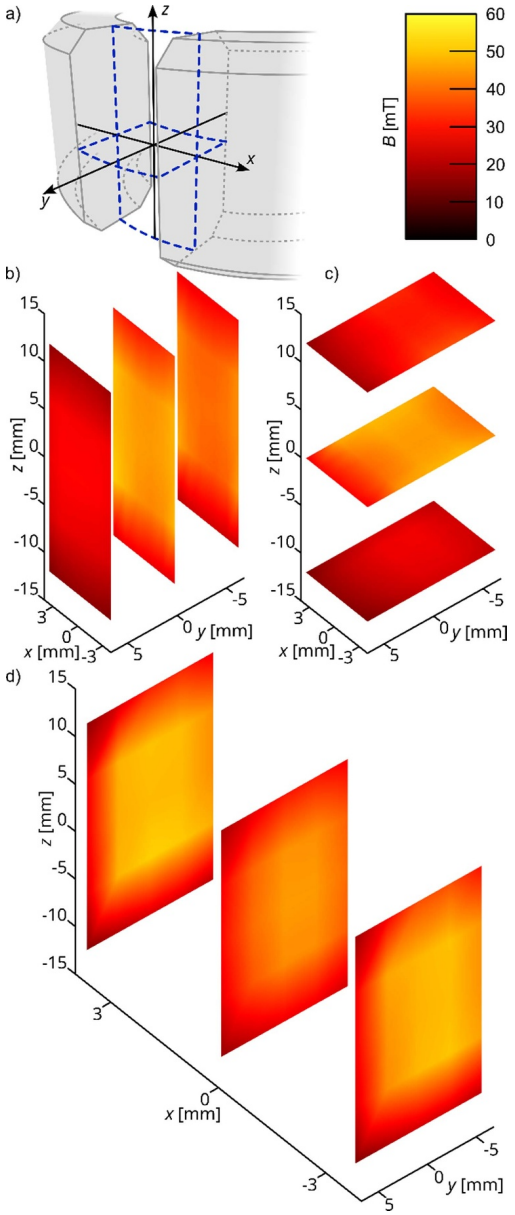

Figure 3. Magnetic flux density in the electromagnet gap. (a) Scheme of the used coordinate system and color scale of magnetic flux density. (b)–(d) Measured magnetic flux density shown in different planes. In (d) the x-axis is stretched for visibility reasons.

of magnetosomes, a cuboctahedral shape surrounded by a bio-membrane layer was found, in line with previous reports [34]. Particle size analysis of TEM images revealed a physical diameter of (32 ± 4) nm for Synomag®. The magnetic cores of

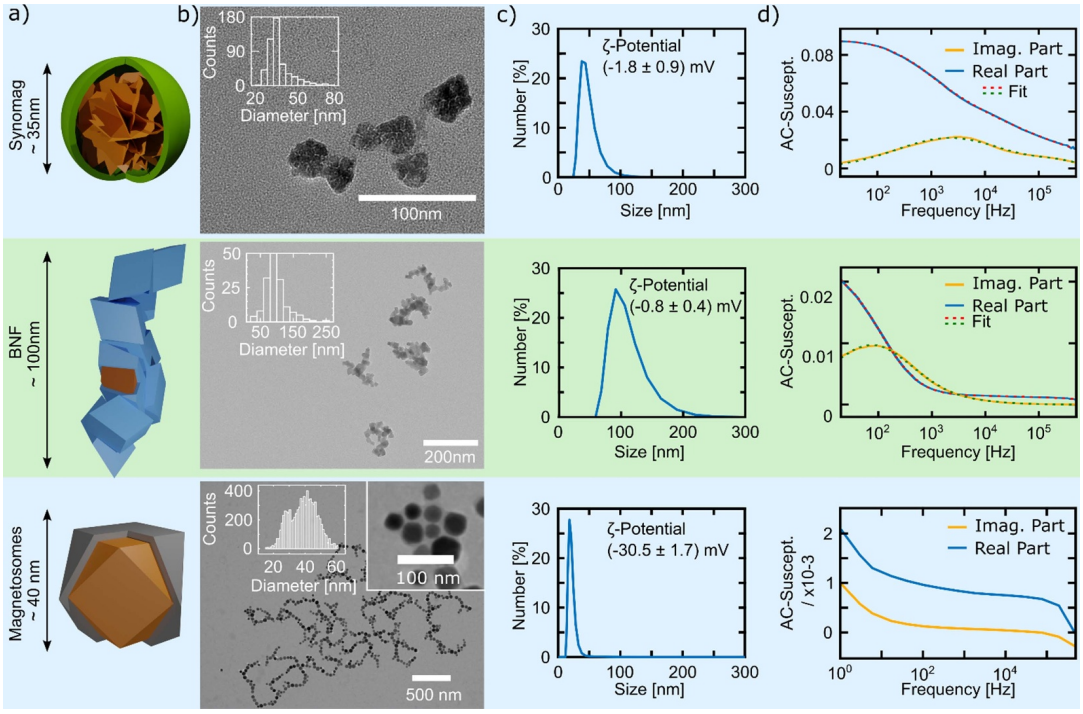

Figure 4. Characterization of different MNP classes (from top to bottom): Synomag®, BNF, and magnetosomes. (a) Sketch of the different MNPs and their composition: Synomag®—nanoflower multicore; BNF—core shell particles with dextran shell; magnetosomes—magnetic core with bio-membrane layer. Sketches indicate MNP sizes as determined by TEM measurements. (b) TEM images of MNPs at different magnification and inset with size distribution. (c) Dynamic-light-scattering measurement yields the number distribution of MNP sizes. Here, the hydrodynamic size is measured. In addition, the values of ζ-potential measurements are provided. (d) Real and imaginary part of the AC-susceptibility. Note the different y-axes.

BNF comprise several crystallites of magnetic iron oxide having a nominal diameter of 92 ± 19 nm. Both are comparable with previously reported sizes [35, 36]. Magnetosomes preserved within chains exhibited an average diameter of (39 ± 7) nm, not accounting for the protein rich membrane, which naturally surrounds the magnetosomes regulating the crystal maturation [37]. The hydrodynamic size was measured with DLS and the ζ-potential was determined with a Zetasizer. In case of Synomag®, the hydrodynamic diameter from the number distribution was (46.8 ± 0.6) nm (smaller than the intensity distribution based hydrodynamic size of (64.0 ± 0.4) nm); poly-dispersity-index (PDI) (0.048 ± 0.006) and the ζ-potential was slightly negative (-1.8 ± 0.9) mV. In case of BNF, the hydrodynamic size by number distribution was (103 ± 2) nm (smaller than the intensity distribution based hydrodynamic size of (132 ± 2) nm); PDI (0.04 ± 0.01) and the ζ-potential was slightly negative with (-0.8 ± 0.4) mV. The hydrodynamic sizes of Synomag® and BNF are larger than the size of the MNPs determined by TEM and can be explained by the surrounding dextran shell which is not visible in TEM as well as the layer of solvent molecules surrounding the particle. In case of magnetosomes, DLS measurements of preserved chains indicated a polydisperse sample and could only be performed after filtering the sample with a 200 nm cutoff filter. The hydrodynamic size amounted to (23 ± 9) nm (significantly smaller than the intensity distribution based hydrodynamic size of (202 ± 35) nm; PDI (0.295 ± 0.004). Please note that the PDI is calculated based on the intensity distribution and not the number distribution shown in figure 4). The small number distribution value compared to TEM measurements may arise from the additional filtering step. The ζ-potential was substantially negative with (-31 ± 2) mV (figure 4(c)). The negative surface potential determined for all MNPs is beneficial for their long-term stability as well as for their biocompatibility. For example, a negative ζ-potential was shown to prevent unspecific interactions and MNP mobility inside cells [38, 39].

AC susceptibility measurements (figure 4(d)) revealed the MNP dynamic response of the magnetic moment to an AMF. The imaginary part of the AC susceptibility corresponds to the energy 500 of the particle system. An optimal phase lag between the MNP magnetization and the excitation field for energy absorption exists at the frequency where the imaginary part of the AC susceptibility exhibits a maximum, $\chi''_{\max}$. This

primary relaxation frequency also indicates the effective relaxation time τ_{eff} according to

$$f_{\max} = \frac{1}{\tau_{\text{eff}}}, \tag{6}$$

which is dominated by the faster of the two, the Néel or the Brownian relaxation time $\tau_{\text{N/B}}$. It is important to note, that in contrast to single domain crystals, no simple expression for τ_{eff} exists. Instead $\tau_{\text{N/B}}$ are determined directly from an AC susceptibility data fit. Since MNPs used in this study did not exhibit single domain crystals, the AC susceptibility data was fitted with the extended multicore model. Here, the Brownian relaxation is given by the Debye model integrated over the particle size distribution, whereas the cole–cole expression is used to model the Néel relaxation part [40]:

$$\chi(\omega) = \chi_{0_{\text{B}}} \int \frac{1}{(1 + i\omega\tau_{\text{B}}(r_{\text{H}}))} f(r_{\text{H}})\, \mathrm{d}r_{\text{H}} + \frac{\chi_{0_{\text{N}}}}{1 + (i\omega\tau_{\text{N}})^{\alpha}}. \tag{7}$$

$\chi_{0_{\text{B}}}$ is the directed current (DC) susceptibility for particles that undergo Brownian relaxation, $\chi_{0_{\text{N}}}$ the DC susceptibility for particles that undergo Néel relaxation, $\omega = 2\pi f$ is the angular frequency, r_{H} the hydrodynamic radius of the particles and α describes the degree of distribution of the Néel relaxation times (due to size distribution of the single-domains and/or magnetic interactions between the single-domains). The advantage of this model is that the Néel relaxation does not have to be at higher frequencies than the Brownian relaxation as in other models and that both time scales may overlap.

For Synomag® particles (measured at 5 mg ml^{-1}) the imaginary part of the AC susceptibility exhibited a maximum at 3.8 kHz and a shallow plateau around 100 kHz. The real part of the AC susceptibility decayed slowly and exhibited a 0.02 value at 100 kHz. At low frequencies compared to the principal relaxation frequency at 3.8 kHz, the magnetization followed the excitation field. Here, the real part of the susceptibility was at its maximum and the imaginary part close to zero. At high frequencies compared to 3.8 kHz the real and the imaginary part decreased slowly, maintaining a significant phase lag with slow decrease of the magnetization. The rather broad distribution and slow decrease at higher frequencies reflected the multicore nature of Synomag® and indicated relaxation of internal disordered spins in line with previous reports [41]. Moreover, it has been speculated that the phenomenal heating of Synomag® is primarily a result of an exchange coupling between the cores, which leads to a superferromagnetic magnetization state [42]. In case of BNFs, the imaginary part of the AC susceptibility χ'' exhibited a single maximum at 0.1 kHz, orders of magnitudes lower compared to Synomag® MNP, together with a steep drop of the real part χ' around this frequency. At high frequencies the magnetization vanished quickly. This behavior resembled single-domain crystals, albeit the magnetization lagged the external field already at low frequencies. For magnetosomes the real and imaginary part of the AC-susceptibility decayed in parallel over the whole frequency range with small absolute values on the order of 10^{-3}, yet sufficiently above the resolution limit of the volume AC susceptibility of 10^{-5}. This data indicates, that magnetosomes get only barely magnetized by the 0.5 mT field of the AC susceptometer. Over the whole frequency range magnetosomes follow the external field only with a substantial phase lag. With increasing frequency, also the magnetosome magnetization gets more and more reduced. This indicates that magnetosomes are in a blocked and not a superparamagnetic state anymore. Due to the small $\chi(\omega)$ values, a determination of $\tau_{\text{N/B}}$ was not possible. Table 1 provides an overview of the analysis of the fit according to equation (7). In case of Synomag® and BNF particles Néel and Brownian relaxation times differed by more than an order of magnitude. Néel relaxation was the faster and dominating process, thus accounting for most of the power dissipation as shown before for maghemite particles [43]. Yet, it should be noted, that relaxation times were determined for an excitation field of $\leq$0.5 mT in the AC susceptometer, which is two orders of magnitude smaller than the excitation field of our home-built magnetothermal actuation setup. While $\tau_{\text{N/B}}$ are often provided in the zero-field limit, their value and in particular τ_{N} was reported to be dependent on the magnetic field strength [44].

Table 1. Iron concentration, number of particles and effective relaxation time for particle concentrations of 1 mg ml^{-1}.

	Synomag®	BNF	Magnetosomes
c_{Fe} (mg ml^{-1})	0.6	0.6	0.72
Particles [#]	2.2×10^{12}	6.0×10^{11}	5.7×10^{15}
$f_{\max}$ (Hz)	3.8×10^{3}	84	NA
τ_{N} [s] @ 0.5 mT	1.0×10^{-6}	6.5×10^{-6}	NA
τ_{B} [s] @ 0.5 mT	9.6×10^{-5}	1.7×10^{-3}	NA

Based on this study, τ_{N} is expected to become even smaller than reported in table 1, when MNPs are placed in higher external fields. Another consequence is, that the apparently small χ values will highly underestimate the actual magnetization and heating response obtained in the home-built AMF setup.

4.2. MNP heat response during heating/cooling cycles

To determine MNP heating responses correctly, samples were subjected to the AMF until an equilibrium between the heat generated by the particles and heat dissipated to the surrounding was established. Samples evaluated in this work reached this steady state within <15 min. For this reason, the time intervals of heating or cooling the sample were set to 15 min, except for fast cycle measurements. Absolute temperatures were recorded via thermal imaging at 0.1 Hz. The radiation emitted from the sample surface in the infrared range was recorded and converted into absolute temperatures accounting for the different opacities of the material in the visible and infrared spectrum as well as for the reflection and transmission coefficients of the sample (see methods). Thus, thermal imaging, in comparison to a thermal probe, offers undisturbed non-contact measurements of the sample and recording of

spatially resolved data (e.g. detecting heterogeneities or temperature gradients in the sample). Moreover, thermal imaging enabled simultaneous monitoring of the sample environment as well as control over temperature changes of the hyperthermia setup during measurements. The measured temporal behavior of the MNP solutions was analyzed by Newton's law of cooling, which proposes an exponential change of the temperature over time:

$$T_{\text{heat}}(t) = \Delta T\left[1 - \exp\left(-\frac{t}{\tau_{\text{h}}}\right)\right] + T_{\text{env}} \tag{8}$$

for the heating process and

$$T_{\text{cool}}(t) = \Delta T \exp\left(-\frac{t - t_0}{\tau_{\text{c}}}\right) + T_{\text{env}}. \tag{9}$$

For the cooling process, where $T_{\text{h/c}}$ is the sample surface temperature for heating and cooling, respectively. ΔT is the maximum temperature change, τ is the heating constant, t_0 is the starting time of the cooling process and T_{env} is the environmental temperature.

The heating kinetics of the three investigated particle classes and its analysis is shown in figure 5. Figure 5(a) shows an example measurement of a magnetosome sample and fits of equations (8) and (9) together with the temperature change of the magnet side faces as well as the background. As a result of the elaborate cooling system, the temperature of the magnet is kept below room temperature in absence of any AMF application and can be limited to ∼21 °C, which is 1 °C above room temperature, during AMF application. This is important as the magnet temperature and emitted radiation affects the sample temperature. In our case, the near room temperature of the magnet causes no effect on the maximum steady-state temperatures of the sample, while the temperature rise and fall in the first few minutes during and after AMF application is beneficial to accelerate heating/cooling rates of the sample. As a control, the background temperature is depicted. The background temperature remains constant except for a $\leqslant$1 °C variation, which arises from radiation of the magnet which is reflected by the surface in the background.

To test the effect of different active cooling of the magnet, a switch was installed in the cooling setup to enable an immediate exchange of the cooled water for water at ambient temperature (see SI figure 1). The heating kinetics of Synomag® using (i) constant magnet cooling were compared to the kinetics when (ii) the cooling case around the magnet was flushed with 20 °C water in absence of the AMF and flushing it with 5 °C water during AMF application, as well as with heating kinetics (iii) flushing the cooling system with 20 °C water constantly. This measurement nicely demonstrates the influence of the magnet temperature on the measured sample value, since the sample heating rates became lower and the maximum reachable sample temperature increased due to additional immediate heating by the magnet. This data also confirmed that our MNP data was free from any direct heating influence by the hyperthermia setup.

A comparison of the heating kinetics of the three particle classes is shown in figure 5(b). Intriguingly, the three particle classes measured at identical concentration exhibit distinct heat dissipation kinetics. Magnetosomes reached highest steady-state temperatures of ∼70 °C, whereas Synomag® and BNF were heated to ∼40 °C and ∼38 °C, respectively. All samples reached the steady-regime during heating or cooling within 15 min and the heating rate was with up to +15 °C min^{-1} highest for magnetosomes, followed by Synomag® with up to +6.7 °C min^{-1} and BNF with up to +5 °C min^{-1}. Fastest cooling rates were −15 °C min^{-1} in case of magnetosomes, up to −10 °C min^{-1} and up to −6.7 °C min^{-1} in case of Synomag® and BNF, respectively. Each of the heating/cooling kinetics was fitted with equations (8) and (9) and the parameters $T_{\text{max}} = \Delta T + T_{\text{env}}$ (figure 5(c)) and characteristic time constant $\tau_{\text{h/c}}$ of the heating/cooling process (figure 5(d)) extracted. Using the initial slope of the heating curve $\mathrm{d}T/\mathrm{d}t_{t=0}$, we further determined the specific absorption rate (SAR), as a measure of the heating power generated per unit mass

$$\text{SAR} = C \cdot \frac{m_{\text{H}_2\text{O}}}{m_{\text{MNP}}} \cdot \frac{\mathrm{d}T}{\mathrm{d}t}_{t=0}, \tag{10}$$

where $C = 4.19\ J(\text{g}\cdot\text{K})^{-1}$ is the heat capacity of water, $m_{\text{H}_2\text{O}}$ = mass of water in sample, and m_{MNP} = total mass of magnetic material (i.e. all elements contributing to the magnetic cores) in the sample. SAR values for Synomag®, BNF, and magnetosomes measured in different samples are shown in SI figure 2. On average, Synomag® exhibited an SAR of (170 ± 13) W g^{-1}, BNF an SAR of (126 ± 10) W g^{-1}, and magnetosomes an SAR of (307 ± 21) W g^{-1}.

The maximum steady-state temperatures increased linearly with sample concentration (figure 5(c)) due to the higher effective heat capacity of the sample. Magnetosomes were measured in three different conditions to probe effects of different extraction steps on their heating response. When living magnetotactic bacteria were exposed to AMFs the maximum reachable temperature was a factor 1.2–1.5 higher compared to magnetosome chains extracted from bacteria or when the chains were disrupted in addition. This behavior is expected as for the free chains a maximum single strand length, and therefore a maximum magnetic moment will be reached. When protein chains were denatured, interactions between magnetosomes led to a reduction of the effective magnetization and hence the maximally reachable steady-state temperature. For Synomag® and BNF MNPs the maximum reachable temperatures are a factor 1.3–1.7 lower than magnetosomes, but still in a regime suitable for bio-and nanotechnological applications. In addition, Synomag® and BNF are readily synthesized with identical properties and with the possibility to systematically alter their properties (e.g. by fluorescent labeling, material composition). The characteristic heating/cooling time constant $\tau_{\text{h/c}}$ exhibited a similar trend as T_{max}: magnetosomes heat/cool fastest ($\tau_{\text{h/c}} \sim$ 115–200 s) whereas $\tau_{\text{h/c}}$ of magnetosomes with denatured chains ($\tau_{\text{h/c}} \sim$ 140–230 s), Synomag® ($\tau_{\text{h/c}} \sim$ 150–250 s), and BNF ($\tau_{\text{h/c}} \sim$ 200–240 s) were successively longer. Time constants were usually shorter than the water control ($\tau_{\text{h/c}} \sim$ 245–270 s).

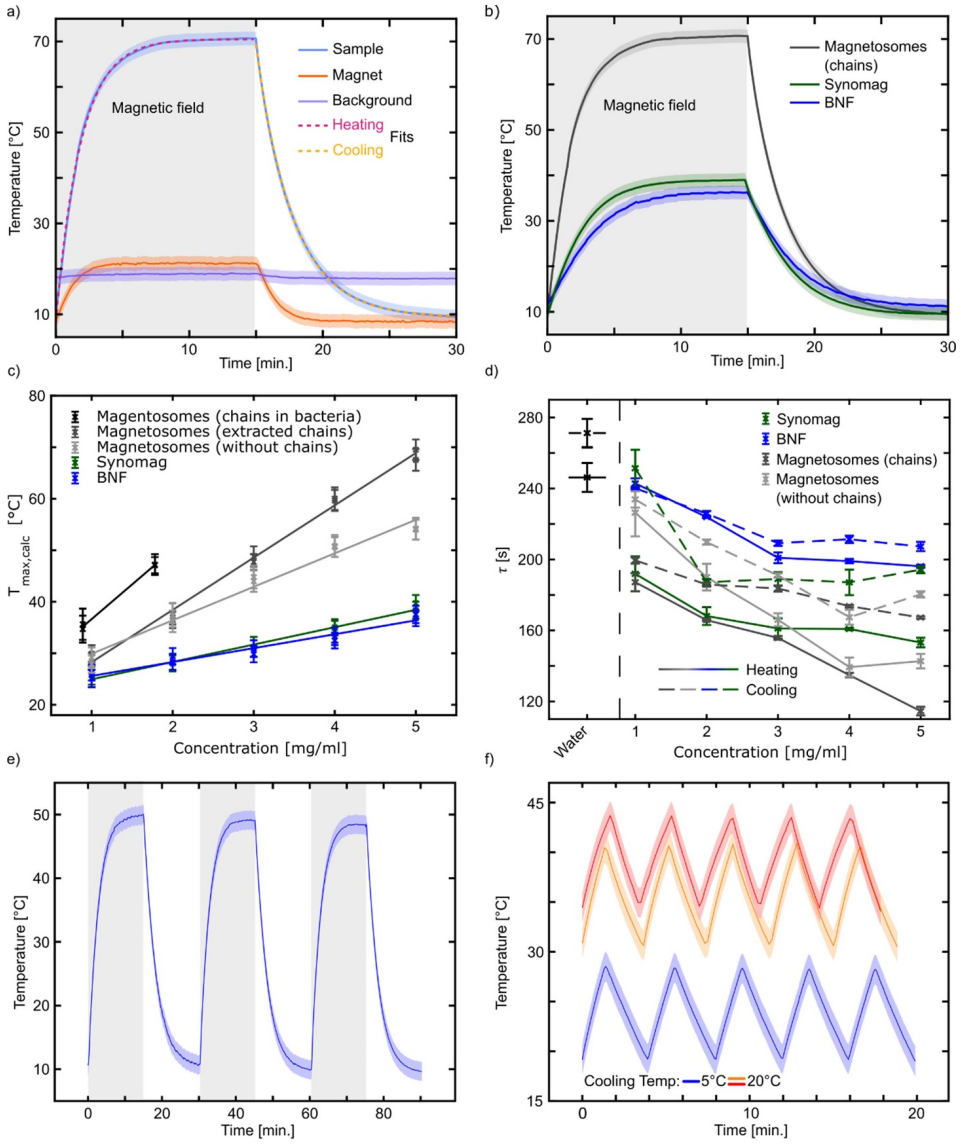

Figure 5. Comparison of MNP heating/cooling response. (a) Exemplary measurement of heating/cooling kinetics of magnetosome MNP sample, background, and magnet. For long-term induction heating the kinetics were recorded until the steady-state was reached. The fits for heating and cooling (dashed lines) overlay the measured data. (b) Comparison of heating/cooling kinetics of different MNPs at 5 mg ml^{-1} concentration each. (c) Maximum steady-state temperature of Synomag® and BNF particles as a function of concentration and using different solvents. Maximum steady-state temperature of magnetosomes as a function of concentration and at different purification stages. Please note that for Synomag® and BNF the concentration is the particle concentration while for magnetosomes it is the iron concentration. (d) Sample temperature for standard 5 °C cooling, switched cooling for constant magnet temperature and ambient temperature cooling water. (e) Three consecutive heating/cooling cycles of magnetosome MNP measured at 3 mg ml^{-1} concentration. (f) Fast heating/cooling cycles for characteristic target temperature intervals of Synomag® MNP at 5 mg ml^{-1} concentration. (a), (b), (e) Grey shaded areas indicate the time the AMF was applied. Kinetics were recorded until the steady-state was reached. In (f) the indication is not possible since the on-times are slightly different for all samples. For all graphs where applicable the errors are shown as shaded area.

Table 2. Comparison of the herein reported setup with previous works. EM = electromagnet, C = induction coil (as far as the work and values were accessible). Note, that in most cases selected parameters (for different measurements) are reported, but gap size, max. *B*, and continuous operation time depend on each other. Continuous operation time in this work corresponds to the time where temporal field stability is guaranteed. For other works typical reported operation times are stated.

Reference	EM gap size or C diameter (mm)	Measured max. *B* within gap (mT)	Frequency (kHz)	Continuous operation time (min)	Microscope mountable	Biocompatible	Heat map spatial resolution, i.e. IFOV (mrad)
This work	10 (EM)	48	∼94	20	Yes	Yes	0.8
[45]	0.4 (EM)	53	300	>60	Yes	No*	1.7
[23]	7.5 (EM)	75 & 20	100 & 500	2	Yes	Yes	1.3
[21]	11 (EM)	19.3 & 4.8	100 & 500	5	No	NA	NA
[22]	15 (C)	44 27.6	149 $>10^3$	NA	No	NA	NA
[46]	35 (C)	20	∼129	NA	Yes	Yes	NA

*cell measurements were performed, but here the electromagnet is in contact with the medium.

To demonstrate two important measurement settings for biological and nanotechnological applications, on the one hand the long-term, repetitive heating/cooling over 1.5 h was tested (figure 5(e)) and, on the other hand, fast heating/-cooling cycles for repetitive switching between states with $\Delta T = 10$ °C was probed (figure 5(f)). For comparison in both cases Synomag® MNP at 5 mg ml^{-1} were used. For long-term measurements, MNPs were heated up to steady-state temperatures at 50 °C and cooled to 10 °C starting conditions in three successive cycles. Heating/cooling time constants remained constant over the whole measurement and T_{max} was reduced only by $\Delta T = 1$ °C per cycle (i.e. every 30 min; in line with magnetic flux density measurements in figure 2(b)).

For fast heating/cooling cycles Synomag® MNP at 5 mg ml^{-1} were recorded over five cycles over time intervals until a temperature change by $\Delta T = 10$ °C was reached. This is a typical temperature interval needed to switch polymers between distinct conformational states (e.g. thermoresponsive elastin-like peptides between 15 °C and 35 °C [27], poly(N-isopropylmethylacrylamide) thermoresponsive hydrogel material 35 °C–50 °C [28], or thermal decomposition of a thermo-sensitive molecule between 20 °C and 80 °C, namely, azobis [N-(2-carboxyethyl)-2-methylpropion-amidine] [12]).

Since the switching behavior also depends on absolute temperatures, we used different settings of the cooling system to shift the average temperature between (I) 39 °C, (II) 36 °C, and (III) 24 °C. Heating/cooling rates were fast in the (I) 11 °C min^{-1}, (II) 10.6 °C min^{-1}, and (III) 10.1 °C min^{-1} regime.

5. Conclusion

In this work we present an advanced hyperthermia setup, which outcompetes previously available systems by producing 100 kHz AMFs, which fulfil the partly contradictory demands for (i) sufficient magnetic field amplitudes (48 mT), (ii) high temporal stability (⩾20 min), and (iii) sufficiently large working volumes (2 cm^3) at the same time. Moreover, the setup is designed to offer spatially resolved heat maps with an instantaneous field of view resolution of 0.8 mrad and enables microscopic observation of MNPs and biological samples for biomedical/nanotechnological studies (see table 2).

We compare the heating response of three structurally different MNPs, namely nanoflower-like and core shell magnetite MNPs, as well as magnetosomes. The latter exhibited highest heating rates and a maximal saturation temperature of 70 °C at 5 mg ml^{-1} concentration. Yet, considering aspects of particle monodispersity, availability, the possibility of biofunctionalization as well as heating response, nanoflower-like MNPs turn out to be primarily suitable for nanotechnological applications. The realization of long-time (30 min) field stability as well as the option to perform fast reversible heating/cooling cycles (with gradients up to ±15 °C min^{-1}), of MNPs with microscopic observation bears high potential of this setup for biomedical assays as well as for biosensor applications in nanotechnology.

Data availability statement

All data that support the findings of this study are included within the article (and any supplementary files).

Funding information

C M acknowledges financial support of the Deutsche Forschungsgemeinschaft (DFG, German Research Foundation) through CRC1208 ‘Identity and Dynamics of Membrane Systems’ (A12, Project ID 267205415) and CRC1535 ‘Microbial Networks’ (A09, Project ID 458090666). C M and A N acknowledge financial support via the ‘Freigeist fellowship’ of VolkswagenFoundation. This work was performed with financial support from Fonds der Chemischen Industrie. The authors acknowledge the DFG and the State of North Rhine–Westphalia for funding the cryo-TEM (INST 208/749-1 FUGG).

ORCID iD

Cornelia Monzel https://orcid.org/0000-0003-0892-3427

References

[1] Seo D *et al* 2016 A mechanogenetic toolkit for interrogating cell signaling in space and time *Cell* **165** 1507–18

[2] Liße D, Monzel C, Vicario C, Manzi J, Maurin I, Coppey M, Piehler J and Dahan M 2017 Engineered ferritin for magnetogenetic manipulation of proteins and organelles inside living cells *Adv. Mater.* **29** 1700189

[3] Monzel C, Vicario C, Piehler J, Coppey M and Dahan M 2017 Magnetic control of cellular processes using biofunctional nanoparticles *Chem. Sci.* **8** 7330–8

[4] Mai B T, Fernandes S, Balakrishnan P B and Pellegrino T 2018 Nanosystems based on magnetic nanoparticles and thermo- or pH-responsive polymers: an update and future perspectives *Acc. Chem. Res.* **51** 999–1013

[5] Keizer V I P *et al* 2022 Live-cell micromanipulation of a genomic locus reveals interphase chromatin mechanics *Science* **377** 489–95

[6] Rajan A and Sahu N K 2020 Review on magnetic nanoparticle-mediated hyperthermia for cancer therapy *J. Nanopart. Res.* **22** 319

[7] Pankhurst Q A, Connolly J, Jones S K and Dobson J 2003 Applications of magnetic nanoparticles in biomedicine *J. Phys. D: Appl. Phys.* **36** R167

[8] Pankhurst Q A, Thanh N T K, Jones S K and Dobson J 2009 Progress in applications of magnetic nanoparticles in biomedicine *J. Phys. D: Appl. Phys.* **42** 224001

[9] Makridis A, Tziomaki M, Topouridou K, Yavropoulou M P, Yovos J G, Kalogirou O, Samaras T and Angelakeris M 2016 A novel strategy combining magnetic particle hyperthermia pulses with enhanced performance binary ferrite carriers for effective *in vitro* manipulation of primary human osteogenic sarcoma cells *Int. J. Hyperth.* **32** 778–85

[10] Gavilán H, Avugadda S K, Fernández-Cabada T, Soni N, Cassani M, Mai B T, Chantrell R and Pellegrino T 2021 Magnetic nanoparticles and clusters for magnetic hyperthermia: optimizing their heat performance and developing combinatorial therapies to tackle cancer *Chem. Soc. Rev.* **50** 11614–67

[11] Thomas C R, Ferris D P, Lee J-H, Choi E, Cho M H, Kim E S, Stoddart J F, Shin J-S, Cheon J and Zink J I 2010 Noninvasive remote-controlled release of drug molecules *in vitro* using magnetic actuation of mechanized nanoparticles *J. Am. Chem. Soc.* **132** 10623–5

[12] Riedinger A, Guardia P, Curcio A, Garcia M A, Cingolani R, Manna L and Pellegrino T 2013 Subnanometer local temperature probing and remotely controlled drug release based on azo-functionalized iron oxide nanoparticles *Nano Lett.* **13** 2399–406

[13] Huang J, Li Y, Orza A, Lu Q, Guo P, Wang L, Yang L and Mao H 2016 Magnetic nanoparticle facilitated drug delivery for cancer therapy with targeted and image-guided approaches *Adv. Funct. Mater.* **26** 3818–36

[14] Noh S-H, Moon S H, Shin T-H, Lim Y and Cheon J 2017 Recent advances of magneto-thermal capabilities of nanoparticles: from design principles to biomedical applications *Nano Today* **13** 61–76

[15] Cazares-Cortes E, Cabana S, Boitard C, Nehlig E, Griffete N, Fresnais J, Wilhelm C, Abou-Hassan A and Ménager C 2019 Recent insights in magnetic hyperthermia: from the "hot-spot" effect for local delivery to combined magneto-photo-thermia using magneto-plasmonic hybrids *Adv. Drug Deliv. Rev.* **138** 233–46

[16] Huang H, Delikanli S, Zeng H, Ferkey D M and Pralle A 2010 Remote control of ion channels and neurons through magnetic-field heating of nanoparticles *Nat. Nanotechnol.* **5** 602–6

[17] Stanley S A, Gagner J E, Damanpour S, Yoshida M, Dordick J S and Friedman J M 2012 Radio-wave heating of iron oxide nanoparticles can regulate plasma glucose in mice *Science* **336** 604–8

[18] Chen R, Romero G, Christiansen M G, Mohr A and Anikeeva P 2015 Wireless magnetothermal deep brain stimulation *Science* **347** 1477–80

[19] Yakacki C M, Satarkar N S, Gall K, Likos R and Hilt J Z 2009 Shape-memory polymer networks with Fe_3O_4 nanoparticles for remote activation *J. Appl. Polym. Sci.* **112** 3166–76

[20] Criado M, Sanz B, Goya G F, Mijangos C and Hernández R 2017 Magnetically responsive biopolymeric multilayer films for local hyperthermia *J. Mater. Chem.* B **5** 8570–8

[21] Lacroix L M, Carrey J and Respaud M 2008 A frequency-adjustable electromagnet for hyperthermia measurements on magnetic nanoparticles *Rev. Sci. Instrum.* **79** 093909

[22] Garaio E, Collantes J M, Plazaola F, Garcia J A and Castellanos-Rubio I 2014 A multifrequency eletromagnetic applicator with an integrated AC magnetometer for magnetic hyperthermia experiments *Meas. Sci. Technol.* **25** 115702

[23] Christiansen M G, Howe C M, Bono D C, Perreault D J and Anikeeva P 2017 Practical methods for generating alternating magnetic fields for biomedical research *Rev. Sci. Instrum.* **88** 084301

[24] Myrovali E, Papadopoulos K, Charalampous G, Kesapidou P, Vourlias G, Kehagias T, Angelakeris M and Wiedwald U 2023 Toward the separation of different heating mechanisms in magnetic particle hyperthermia *ACS Omega* **8** 12955–67

[25] Eggeman A S, Majetich S A, Farrell D and Pankhurst Q A 2007 Size and concentration effects on high frequency hysteresis of iron oxide nanoparticles *IEEE Trans. Magn.* **43** 2451–3

[26] Rosensweig R E 2002 Heating magnetic fluid with alternating magnetic field *J. Magn. Magn. Mater.* **252** 370–4

[27] Vogele K, List J, Pardatscher G, Holland N B, Simmel F C and Pirzer T 2016 Self-assembled active plasmonic waveguide with a peptide-based thermomechanical switch *ACS Nano* **10** 11377–84

[28] Zhao J, Su H, Vansuch G E, Liu Z, Salaita K and Dyer R B 2019 Localized nanoscale heating leads to ultrafast hydrogel volume-phase transition *ACS Nano* **13** 515–25

[29] Schindelin J *et al* 2012 Fiji: an open-source platform for biological-image analysis *Nat. Methods* **9** 676–82

[30] © TDK Electronics 2023 Ferrites and accessories—SIFERRIT material N87 (available at: www.tdk-electronics.tdk.com/download/528882/990c299b916e9f3eb7e44ad563b7f0b9/pdf-n87.pdf) (Accessed 22 March 2023)

[31] Ferroxcube 2008 3F3 material specification (available at: www.ferroxcube.com/upload/media/product/file/MDS/3f3.pdf) (Accessed 22 March 2023)

[32] Shanks H R, Klein A H and Danielson G C 1967 Thermal properties of armco iron *J. Appl. Phys.* **38** 2885–92

[33] Keller R B (ed) 2023 Skin effect *Design for Electromagnetic Compatibility–In a Nutshell: Theory and Practice* (Springer) pp 135–43

[34] Schüler D 1999 Formation of magnetosomes in magnetotactic bacteria *J. Mol. Microbiol. Biotechnol.* **1** 79–86

[35] Dennis C L, Krycka K L, Borchers J A, Desautels R D, van Lierop J, Huls N F, Jackson A J, Gruettner C and Ivkov R 2015 Internal magnetic structure of nanoparticles dominates time-dependent relaxation processes in a magnetic field *Adv. Funct. Mater.* **25** 4300–11

[36] Novoselova I P, Neusch A, Brand J-S, Otten M, Safari M R, Bartels N, Karg M, Farle M, Wiedwald U and Monzel C 2021 Magnetic nanoprobes for spatio-mechanical manipulation in single cells *Nanomaterials* **11** 2267

[37] Uebe R and Schüler D 2016 Magnetosome biogenesis in magnetotactic bacteria *Nat. Rev. Microbiol.* **14** 621–37

[38] Etoc F, Balloul E, Vicario C, Normanno D, Liße D, Sittner A, Piehler J, Dahan M and Coppey M 2018 Non-specific interactions govern cytosolic diffusion of nanosized objects in mammalian cells *Nat. Mater.* **17** 740–6
[39] Debayle M *et al* 2019 Zwitterionic polymer ligands: an ideal surface coating to totally suppress protein-nanoparticle corona formation? *Biomaterials* **219** 119357
[40] RISE 2017 DynoMag manual.pdf (available at: www.ri.se/sites/default/files/2019-09/DynoMag%20manual.pdf) (Accessed 27 January 2023)
[41] Bender P *et al* 2018 Relating magnetic properties and high hyperthermia performance of iron oxide nanoflowers *J. Phys. Chem.* C **122** 3068–77
[42] Lartigue L, Hugounenq P, Alloyeau D, Clarke S P, Lévy M, Bacri J-C, Bazzi R, Brougham D F, Wilhelm C and Gazeau F 2012 Cooperative organization in iron oxide multi-core nanoparticles potentiates their efficiency as heating mediators and MRI contrast agents *ACS Nano* **6** 10935–49
[43] Fortin J P, Wilhelm C, Servais J, Ménager C, Bacri J C and Gazeau F 2007 Size-sorted anionic iron oxide nanomagnets as colloidal mediators for magnetic hyperthermia *J. Am. Chem. Soc.* **129** 2628–35
[44] Deissler R J, Wu Y and Martens M A 2014 Dependence of Brownian and Néel relaxation times on magnetic field strength *Med. Phys.* **41** 012301
[45] Connord V, Clerc P, Hallali N, El Hajj Diab D, Fourmy D, Gigoux V and Carrey J 2015 Real-time analysis of magnetic hyperthermia experiments on living cells under a confocal microscope *Small* **11** 2437–45
[46] nanoThericslLive cell exposure option (available at: www.nanotherics.com/live-cell-exposure-option/) (Accessed 25 August 2023)

Supplementary Information

An efficient magnetothermal actuation setup for fast heating/cooling cycles or long-term induction heating of different magnetic nanoparticle classes

Daniel Alexander Kuckla,[a] Julia-Sarita Brand,[a] Bastian Czech,[b] Amirarsalan Asharion[a], Jan Vinzenz Jüttner,[a] Iuliia Pavlovna Novoselova,[a] Andreas Neusch,[a] Philipp Hagemann,[a] Mathias Getzlaff, [b] and Cornelia Monzel[a,] *

a. Experimental Medical Physics, Heinrich-Heine University, Düsseldorf, Germany

b. Institute of Applied Physics, Heinrich-Heine University, Düsseldorf, Germany

* Corresponding author: cornelia.monzel@hhu.de

Figure S1: Effect of cooling on heating/cooling dynamics

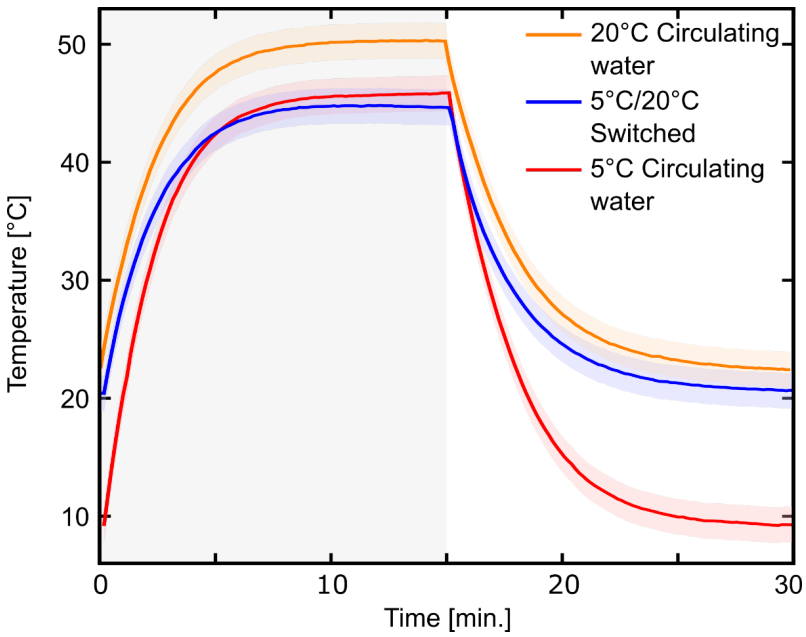

Figure S1 *Showing the heating of 5mg/ml Synomag 70 for different cooling settings. Where the cooling water is either the whole measurement time circulating at the same temperature (5°C/20°C). The third measurement is done with water at both temperatures where the 20°C water is used before the measurement to keep the magnet close to ambient temperature. Before the field is switched on the water is switched to a 5°C water supply. Due to the limited cooling capability of the cold water reservoir the water temperature is risen above 5 °C resulting in a slightly higher magnet temperature. Before the field is switched of the water is switched back to the 20°C supply. The water needs to be switched before the field is switched because and dependent on the tube length. The slightly higher magnet temperature also leads to a slightly higher sample temperature.*

Figure S2: Specific Absorption Rate (SAR) values

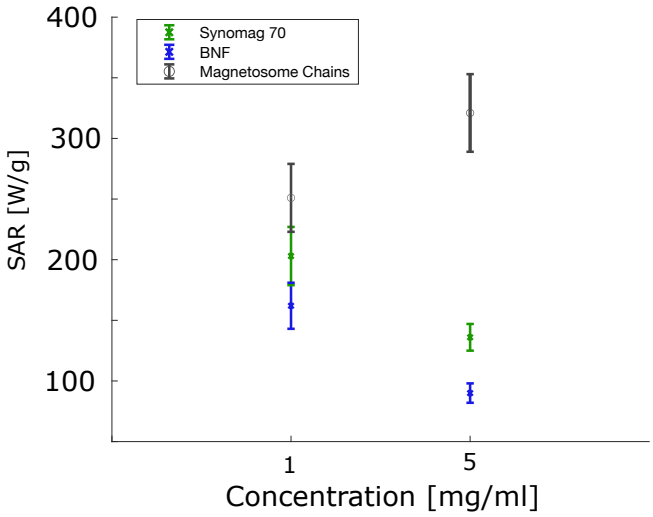

Figure S2 *Determination of Specific Absorption Rate (SAR) using the initial slope method. The heating power generated per unit mass is calculated for the three different particles according to the following expressions:*

$$SAR = C \cdot \frac{m_{H_2O}}{m_{MNP}} \cdot \frac{dT}{dt}_{t=0} \quad ;$$

$$D = \frac{dT}{dt}_{t=0} \quad ;$$

$$\Delta SAR = \sqrt{\left(\Delta m_{H_2O} \cdot \frac{CD}{m_{MNP}}\right)^2 + \left(\Delta C \cdot \frac{m_{H_2O} D}{m_{MNP}}\right)^2 + \left(-\Delta m_{\mathrm{p}} \cdot \frac{m_{H_2O} CD}{m_{\mathrm{MNP}}^2}\right)^2 + \left(\Delta D \cdot \frac{m_{H_2O} C}{m_{MNP}}\right)^2} \quad ;$$

where C = 4.19 J/(g·K) is the heat capacity of water, m_{H_2O} = mass of water in sample, and m_{MNP} = total mass of magnetic material (i.e. all elements contributing to the magnetic cores) in the sample.

Error Evaluation

The errors for magnetic field strength B, voltages U, impedance Z, phase angle Θ, inductances L_{s} and L_{o}, and temporal temperature evolutions are given by the instrument's measurement error.

The accuracy of the coupling factor, k, is calculated by

$$\Delta(k) = \sqrt{\left(\left(\frac{L_{\mathrm{s}}}{2L_{\mathrm{o}}^2\sqrt{1-\frac{L_{\mathrm{S}}}{L_0}}}\right)\Delta(L_{\mathrm{O}})\right)^2 + \left(\left(\frac{1}{2L_{\mathrm{o}}\sqrt{1-\frac{L_S}{L_o}}}\right)\Delta(L_{\mathrm{s}})\right)^2}$$

Where L_{s} is the short circuit inductance, and L_{o} is the open circuit inductance. The description open and short circuit refer to the secondary side.

For heating/cooling constants, temperature changes $\Delta(\Delta T)$, environmental temperature $\Delta(T_{\mathrm{env}})$, resonance Frequency from fit, environmental temperatures ΔT_{env}, and linear fits the error is given by the 95% confidence intervals of the fit, by nlparci.m. Calculated by MATLAB (2020b, The MathWorks Inc., Natick, MA, USA)

The error for the maximum temperatures is calculated by

$$\Delta(T_{\max}) = \sqrt{(\Delta(T_{\text{env}}) + \Delta(\Delta \text{T})}$$

The error of the ohmic resistance is calculated by

$$\Delta(R) = \sqrt{\left((-Z \cdot \sin(\theta))\, \Delta(\Theta)\right)^2 + \left((\cos(\Theta)\,)\Delta(Z)\right)^2}$$

Where Z is the impedance, and Θ is the phase angle.

IV.2 Publication IV

Reference

Title Semisynthetic Ferritin-based Nanoparticles with High Magnetic Anisotropy for Spatial Magnetic Manipulation and Inductive Heating

Authors Andreas Neusch, Ulf Wiedwald, Iuliia Pavlovna Novoselova, Daniel Alexander Kuckla, Nikolaos Tetos, Sarah Sadik, Philipp Hagemann, Michael Farle, and Cornelia Monzel

Journal details *Nanoscale*, Volume 16, Issue 32

Date of Publication 11th July 2024

DOI https://doi.org/10.1039/d4nr01652a

SI Supplementary videos are available online.

Copyright

Contribution

In my role as first author I was majorly involved in conceptualisation and experimental design. I synthesised ferritin nanoparticles used for this study and acquired TEM images. I recorded and analysed DLS data with PH, performed hyperthermia measurements together with DAK and analysed both afterwards. I performed the droplet assay for magnetic characterisation of our Magnetoferritin and analysed the data. I created Figures 1-7 and all figures in the supplementary information and was involved in writing the original draft.
Additionally, I designed the cover art that was chosen by *Nanoscale* to be printed onto the front cover of Volume 16, Issue 32, published on 28$^{\text{th}}$ August 2024.
My overall contribution to this publication amounts to approximately 70 %.

Volume 16
Number 32
28 August 2024
Pages 14963-15406

Nanoscale

rsc.li/nanoscale

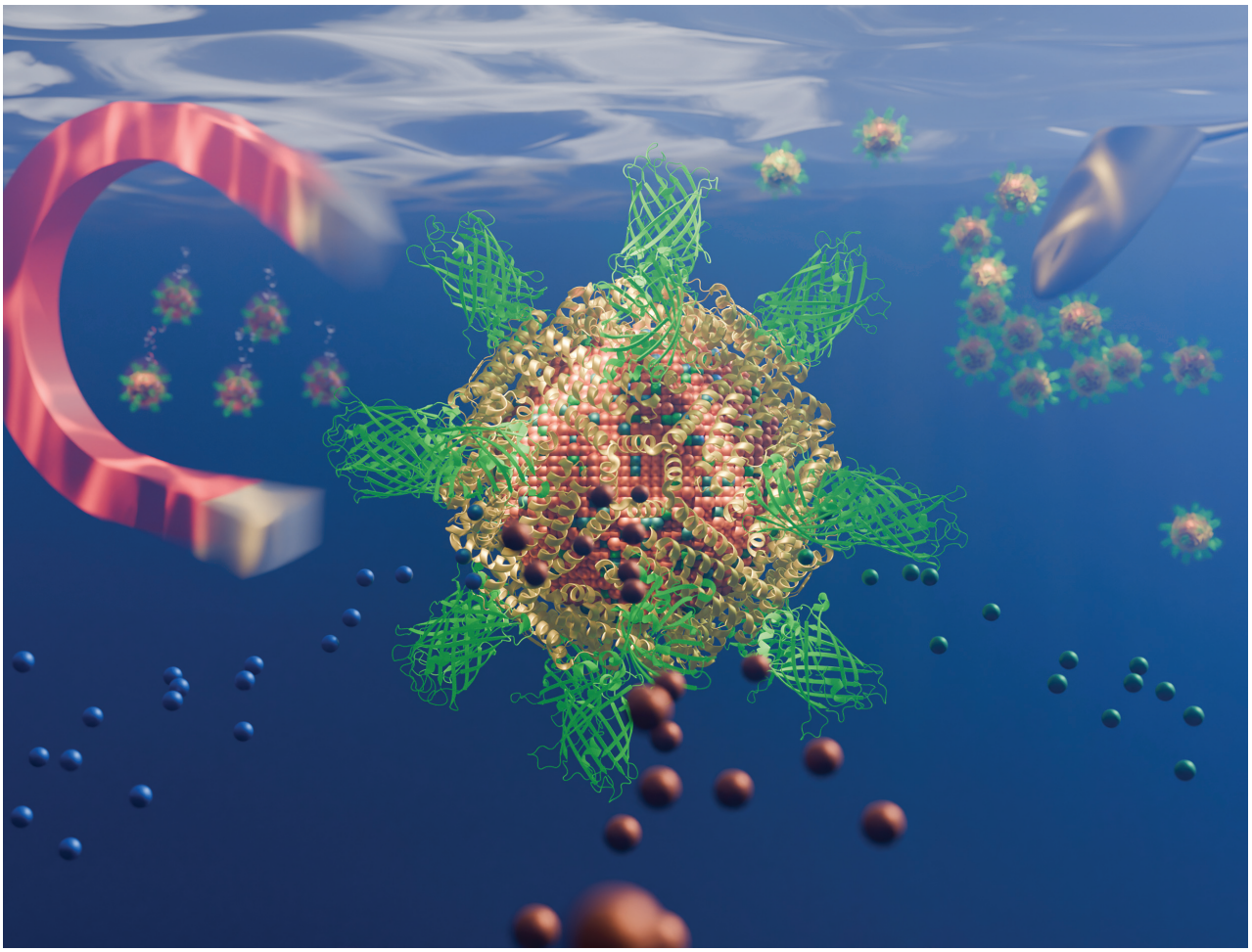

ISSN 2040-3372

ROYAL SOCIETY OF CHEMISTRY

PAPER
Cornelia Monzel *et al.*
Semisynthetic ferritin-based nanoparticles with high magnetic anisotropy for spatial magnetic manipulation and inductive heating

NCNST

Nanoscale

ROYAL SOCIETY OF CHEMISTRY

PAPER

View Article Online
View Journal | View Issue

Cite this: *Nanoscale*, 2024, **16**, 15113

Semisynthetic ferritin-based nanoparticles with high magnetic anisotropy for spatial magnetic manipulation and inductive heating†

Andreas Neusch, [a] Ulf Wiedwald, [b] Iuliia P. Novoselova,‡[a] Daniel A. Kuckla,[a] Nikolaos Tetos,[b] Sarah Sadik, §[a] Philipp Hagemann, [a] Michael Farle [b] and Cornelia Monzel*[a]

The human iron storage protein ferritin represents an appealing template to obtain a semisynthetic magnetic nanoparticle (MNP) for spatial manipulation or inductive heating applications on a nanoscale. Ferritin consists of a protein cage of well-defined size (12 nm), which is genetically modifiable and biocompatible, and into which a magnetic core is synthesised. Here, we probed the magnetic response and hence the MNP's suitability for (bio-)nanotechnological or nanomedical applications when the core is doped with 7% cobalt or 7% zinc in comparison with the undoped iron oxide MNP. The samples exhibit almost identical core and hydrodynamic sizes, along with their tunable magnetic core characteristics as verified by structural and magnetic characterisation. Cobalt doping significantly increased the MNP's anisotropy and hence the heating power in comparison with other magnetic cores with potential application as a mild heat mediator. Spatial magnetic manipulation was performed with MNPs inside droplets, the cell cytoplasm, or the cell nucleus, where the MNP surface conjugation with mEGFP and poly(ethylene glycol) gave rise to excellent intracellular stability and traceability within the complex biological environment. A magnetic stimulus (smaller than fN forces) results in the quick and reversible redistribution of the MNPs. The obtained data suggest that semisynthetic ferritin MNPs are highly versatile nanoagents and promising candidates for theranostic or (bio-)nanotechnological applications.

Received 15th April 2024,
Accepted 10th July 2024

DOI: 10.1039/d4nr01652a

rsc.li/nanoscale

Introduction

Over the last few decades, magnetic nanoparticles (MNPs) have become indispensable tools in nanomedicine for delivery,[1,2] imaging,[3–6] therapy,[5,7,8] or combined approaches. More recently, (bio)nanotechnology-based approaches have used the specific coupling of MNPs to biomolecules: (1) to inductively heat them to create nanoscale hot spots[9–11] (2) to spatially redistribute molecules,[12,13] since the spatiotemporal distribution of molecules plays a key role in biological signalling processes,[14,15] or (3) to apply forces to molecules for their controlled conformational change. The particular advantage of combining such nanoparticle-based approaches with a remote magnetic stimulus is to actively change biomolecular states in a contact-free and controlled manner. This is in contrast to what is hitherto possible by only observing the system's passive response.

The active stimulation provided by cases (1)–(3) is highly relevant for biomaterial development, subcellular signalling or biomechanical studies,[16–19] as well as for applying a stimulus in a whole organism. The aforementioned nanomedical approaches always aim at an *in vivo* application. The use of MNPs in such a biological context, however, requires their biocompatibility, to endow them with specific targeting properties, and a magnetic core which is sufficiently magnetisable and tuneable with regard to its magnetic anisotropy. In addition, the overall particle size should be below 100 nm.[20] As a result, partly contradictory demands need to be reconciled, which generally is a difficult task.

Here, we synthesised ferritin-based MNPs, commonly referred to as magnetoferritin (MFt), which have attracted considerable attention due to their semi-synthetic and multifunctional nature.[21–26] We show how MFts meet most of the abovementioned demands and scrutinise their suitability for spatial

[a]*Experimental Medical Physics, Heinrich-Heine University Düsseldorf, 40225 Düsseldorf, Germany. E-mail: Cornelia.Monzel@hhu.de*
[b]*Faculty of Physics and Center for Nanointegration (CENIDE), University of Duisburg-Essen, 47057 Duisburg, Germany*

†Electronic supplementary information (ESI) available. See DOI: https://doi.org/10.1039/d4nr01652a

‡Present address: Institute of Human Genetics, University Hospital Düsseldorf, Heinrich-Heine-University Düsseldorf, 40225 Düsseldorf, Germany.
§Present address: Cell Biology and Cancer, UMR 144 CNRS, Institute Curie, 75248 Paris cedex 05, France.

View Article Online
Paper Nanoscale

magnetic manipulation and inductive heating approaches, the latter also as a response to a recent discussion in the field.[27,28]

MFts are based on the human iron storage protein ferritin, which forms a well-defined hollow sphere with an internal and external diameter of 8 nm and 12 nm, respectively.[29,30] As such, the protein serves as a template, into which magnetic nanocrystals of high homogeneity, in terms of their shape and size, are synthesised. This semi-synthetic design using a protein shell as a template has several advantages for theranostic or (bio-)nanotechnological applications, which include excellent solubility and stability in physiological solutions as well as a low toxicity. Moreover, due to their well-defined, small size, they remain mobile in various biological environments.[9,17,31] Furthermore, MFts can be easily modified by genetic engineering or chemical reactions involving one of the primary amines, carboxylates or thiols exposed to their exterior. Thus, fluorescent labels or tags for site-specific targeting can be attached.[32–34] Previously, MFts were shown to couple to other biomolecules without apparent alteration of their natural function.[12,35,36] Finally, ferritin exhibits an exceptional stability over a wide range of temperatures (up to ~80 °C) and pH (3–10).

Ferritin is the most abundant iron-storage protein and its globular, hollow structure is conserved in most organisms. It is responsible for mediating iron homeostasis and to prevent oxidative stress.[22] Human ferritin forms a 24-mer protein[37] composed of two subunits: heavy chain ferritin (HCF) and light chain ferritin (LCF).[22,38] Due to their structural similarities, cages can be formed by any numerical combination of the two subunits. Although LCF and HCF are almost identical in structure, only HCF is equipped with a ferroxidase domain capable of oxidising toxic, soluble Fe(II) to insoluble and less harmful Fe(III) upon intake. The oxidised iron atoms sediment inside the cage and can fill it up to approximately 4500 iron atoms.[39] Naturally occurring ferritin cores are ferrihydrites and were reported to exhibit paramagnetic or superparamagnetic properties above 12 K.[40]

With regard to the core, a wide choice of inorganic materials have so far been mineralised inside the ferritin cage, such as Fe_3O_4,[41–44] Co_3O_4,[45,46] Mn_3O_4,[47] CoPt,[48] Pd,[49] Ag,[50] CdS,[51] CdSe,[52] and ZnSe.[53] Here, the inner cage diameter of 8 nm naturally confines the core and gives rise to a narrow size distribution. The synthesised MNPs are generally superparamagnetic at ambient or higher temperature, as they exhibit a magnetocrystalline anisotropy with an energy density that cannot block the particle's magnetic dipole moment at an upper size limit of 8 nm given by the ferritin cage. Superparamagnetism is particularly advantageous for many applications, since the nanoparticles do not show significant particle–particle (magnetic dipole–dipole) interactions. As a result, they do not form chains or aggregates in suspension and are more stable over time. On the other hand, the constraint to the growth of the inorganic core imposed by the ferritin size represents an important limitation to its magnetic properties. In particular, the applicability of ferritin for the hyperthermic heating of malignant cells or for the switching of thermally sensitive molecules was recently questioned.[27] Theoretical and experimental studies have indeed demonstrated that the maximum efficiency of hyperthermic heating is achieved for magnetite MNPs of 15–18 nm diameter and that it drops off sharply upon MNP size reduction.[19,54–57]

It is hence important to show that the MFts' properties can be tuned to maximise their efficiency for hyperthermic heating and their suitability for spatial magnetic remote manipulation. A viable route is to increase the magnetic anisotropy of the inorganic core, which can be simply realised through the replacement of ferrous ions in Fe oxides with dopants.[11] A prominent example is cobalt-doped ferrite nanoparticles, whose magnetocrystalline anisotropy can be up to 20 times larger than that of the undoped ferrite, retaining a good heat dissipation property down to a size of about 8 nm.[58] Interestingly, the highest values of magnetic anisotropy in ferritin were previously obtained using cobalt (Co) doping at a small percentage.[9,59,60] When ferrite nanoparticles were doped with a small percentage of zinc (Zn), the saturation magnetisation was shown to increase slightly.[61] Additional changes in the magnetic behaviour of the particles may arise, due to the inverse spinel structure of Co-doped ferrites (with Co^{2+} ions in octahedral sites and Fe^{3+} ions equally distributed between tetrahedral and octahedral sites) and the normal spinel structure of Zn-doped ferrites (with Zn^{2+} ions in tetrahedral and Fe^{3+} in octahedral sites).[62] On the basis of these findings, MFt is a highly interesting nanoagent for spatial redistribution studies in external magnetic fields and has been controversially discussed as a candidate to mediate inductive heating processes.[9,27,63]

In this work, we probed the characteristics of MFt and doped the magnetic core to tailor its magnetic properties (*i.e.*, to increase the magnetic anisotropy energy density or saturation magnetisation) for these applications. Former studies showed a strong improvement concerning heat dissipation in hyperthermia assays of MFt between no doping and 5% of Co doping, while 10% led to less heat dissipation.[9] Accordingly, the effective anisotropy of γ-Fe_2O_3 MNPs reaches a plateau at doping levels >5% of Co^{2+}.[64] Hence, we chose to investigate the effect of doping MFt cores with 7% Co or 7% Zn with respect to Fe. The manuscript is structured as follows: first, the structural and magnetic properties of pure and doped MFts were determined. Thereafter, an example to increase the MFts' inductive heating response is presented. The spatial manipulation of MFts applying magnetic field gradients is then shown for simple droplets and inside living cells. In the cell cytoplasm and in the cell nucleus, a repetitive and reversible tuning of MFts' spatial distributions was achieved. In cellular environments, the protein shell of MFts allows the MNPs to remain biocompatible despite the presence of Co^{2+}, as demonstrated previously in the absence and presence of external magnetic fields.[9,31] Overall, the comparison of different MFts and their applications provides important guidelines for their use as biomedical or nanotechnological agents as a possible strategy for improved spatial manipulation and magnetic hyperthermia to fully exploit the multiple advantages that ferritin MNPs offer.

View Article Online

Nanoscale Paper

Materials and methods

Ferritin purification

A semi-synthetic ferritin nanoprobe was prepared as previously described.[31] In short, the ferritin cage was genetically engineered so that each subunit of the 24-homomer consisted of the heavy chain ferritin subunit with mEGFP fused to its N-terminus. The cDNA of this fused subunit was inserted into the pET21a(+) vector (reporter gene: *ampR*, see Fig. S1†). The construct was a generous gift from the Coppey/Hajj laboratory at the Laboratoire Physico-Chimie, Institut Curie, Paris, France and the Piehler laboratory at the University of Osnabrück, Germany.

The engineered protein was expressed in BL21-CodonPlus (DE3)-RIPL competent cells (Agilent, Santa Clara, CA, USA). Bacteria were transformed *via* heat shock and plated on LB-Agar containing ampicillin (0.1 μg mL^{-1}). A single colony was chosen and used to grow a preculture and later the main culture in 2×YT medium (containing 0.1 μg mL^{-1} ampicillin). Bacteria were grown at 37 °C and 230 rpm in an orbital shaking incubator up to an OD_{600} of 0.6 to 0.8. At this point, expression was induced by the addition of the *lac* operon activator IPTG (isopropyl β-D-1-thiogalactopyranoside) at a final concentration of 1 mM. Cultures were incubated for 16 h at 16 °C and 160 rpm in a shaking incubator. Bacteria were then harvested at 8000*g* for 10 min, washed in PBS, collected at 19 000*g* for 5 min and finally resuspended in HEPES-2 buffer (50 mM HEPES, 150 mM NaCl, pH 8.0, filtered 0.2 μm). To prevent unwanted protein degradation, protease inhibitors were added to the bacteria according to the manufacturer's advice (cOmplete EDTA-free protease inhibitor cocktail, Roche, Basel, Switzerland). To that, 0.2 mg mL^{-1} of both DNAse I (Roche) and lysozyme (PanReac AppliChem, Darmstadt, Germany) were added. Bacteria were homogenised using a microfluidiser (M110P microfluidizer, Microfluidics, Westwood, MA, USA). After cell disruption, PMSF (phenylmethylsulfonyl fluoride, Merck, Darmstadt, Germany) was added to the solution at a final concentration of 5 mM. The lysate was then centrifuged for 40 min at 19 000*g* and 4 °C. The released proteins were further purified by heat denaturation in a water bath at 70 °C for 15 min and ammonium sulphate precipitation at 30% and 70% at 4 °C. After desalting *via* dialysis (20 kDa cut-off) against buffer HEPES-1 (20 mM HEPES, 100 mM NaCl, pH 8.0, filtered 0.2 μm), the protein solution was separated using a size exclusion column (HiPrep Sephacryl S-400 HR, Cytiva, Marlborough, MA, USA) in a FPLC system (NGC, Bio-Rad, Hercules, CA, USA). The purified ferritin cages were then PEGylated using *O*-[(*N*-succinimidyl)succinyl-aminoethyl]-*O*′-methylpolyethylene glycol 2′000 (Sigma Aldrich, St Louis, MO, USA) in DMSO at a molar excess of 3500 PEG units per ferritin cage. The mixture was left to react at room temperature for 2 h on a rotary shaker and cleaned afterwards using a PD-10 desalting column (Cytiva).

Magnetic core synthesis

Ferritin was loaded with a magnetic core consisting of ferrihydrite including cobalt or zinc as dopants. For the synthesis, 25 mL of PEGylated ferritin was heated to 65 °C in 100 mM NaCl at a ferritin concentration of 50 nM. The pH was kept constant at 8.5 by the addition of 100 mM NaOH using an autotitrator (Titration Excellence T5, Mettler-Toledo, Columbus, OH, USA). The whole reaction was performed under a constant stream of N_2 to suppress unwanted oxidation.

Table 1 Doping of magnetoferritin prepared from an ammonium iron(II) sulphate hexahydrate ($(NH_4)_2Fe(SO_4)_2{\cdot}6H_2O$) precursor for Fe, cobalt(II) chloride ($CoCl_2$) for Co, and zinc chloride ($ZnCl_2$) for Zn. All precursors were dissolved in degassed 100 mM NaCl

		Molarity of the precursor		
Sample	Dopant	Fe (μM)	Dopant (μM)	Final %
Pure	—	1034	—	—
Zn7	Zn	983	52	6.7 ± 1.3
Co7	Co	983	116	6.4 ± 2.2

To produce magnetic cores, both the ferrous precursor (iron(II) sulphate hexahydrate, Honeywell, Charlotte, NC, USA; see also Table 1) and H_2O_2 (5.5 mM, Merck) were dissolved in 2 mL of 100 mM NaCl and filtered through a 0.2 μm syringe filter. These two reagents were then added to the reaction vessel at a rate of 200 μL min^{-1} over a course of 10 min. In this setup, the soluble Fe^{2+} diffuses into the core and can be oxidised to the insoluble form in a controlled manner *via* the HCF's ferroxidase centre. The oxidised Fe^{3+} ions sediment inside the protein cage to form the MFt core, leading to brown colouration of the solution. In order to dope MFt cores, parts of the ferrous precursor were replaced with precursors of either Co^{2+} ($CoCl_2$, Honeywell) or Zn^{2+} ($ZnCl_2$, Acros Organics, Waltham, MA, USA; for detailed compositions see Table 1). This method enabled the implementation of doping ions into the core structure during its formation.[9,65]

After complete addition of the precursors and upon completion of the reaction, the reaction was quenched with trisodium citrate (Sigma Aldrich) at a final concentration of 2 mM. The fresh product was centrifuged at 19 000*g* at 4 °C for 30 min, then filtered through a 0.2 μm syringe filter and concentrated using Amicon Ultra centrifugal filters (100 kDa cut-off, Merck).

For further characterisation of the MNPs (X-ray diffraction and vibrating sample magnetometry), the samples were dialysed against low concentration HEPES buffer (0.2 mM HEPES, 1 mM NaCl, pH 8.0) to reduce the amount of salt and buffering agent in the sample. The samples were then plunge frozen in liquid nitrogen and lyophilised. For all other characterisation studies, the samples were kept in HEPES-1.

Transmission electron microscopy

Protein cages and magnetic cores were imaged by transmission electron microscopy (TEM). Cages and cores were recorded separately, since organic materials such as proteins are hardly visible by TEM. Protein cages were hence stained with uranyl acetate, while magnetic cores were recorded without additional staining.

For TEM measurements, freshly prepared samples of both ferritin and differently doped magnetoferritin (MFt) were

diluted to 0.05 μM. A droplet was placed on a TEM grid (Ni grid, Formvar carbon film, Plano GmbH, Wetzlar, Germany) and left to sediment for 1 min. Excess solution was removed using filter paper. Unstained samples were left to dry under ambient conditions. For uranyl acetate staining, the grid was dipped into a drop of 2% uranyl acetate for 3 s after sample sedimentation and the remaining liquid was removed using filter paper. Afterwards, the grid was placed onto a second drop of 2% uranyl acetate and left for 30 s. Excess solution was removed using filter paper and the grid was left to dry in air.

Stained images were taken with a JEOL JEM-2100Plus (Akishima, Tokyo, Japan) with an acceleration voltage of 80 kV. Unstained bright-field (BF) high-resolution TEM (HRTEM) and scanning TEM (STEM) images were acquired with a JEOL 2200FS transmission electron microscope at an acceleration voltage of 200 kV using a 2k × 2k GATAN UltraScan1000XP CCD camera. The local chemical composition was determined using EDX in STEM mode with an Oxford windowless 80 mm^2 SDD X-MaxN 80 TLE detector with a 0.21 sr solid angle. HRTEM and EDX data were analysed using Gatan Micrograph Suite and Oxford's Aztec software.

X-ray diffraction

X-ray diffraction (XRD) patterns were recorded using a PANalytical X'Pert PRO diffractometer equipped with a spinner for powders using Cu-K_α radiation and an X'Celerator detector. The background of the XRD patterns was subtracted and further data processing was performed using OriginPro. A 50-point moving average smoothing was applied to the diffractograms. Due to the small step width, the MFt peak width remained unchanged while the sharp NaCl peaks exhibited slightly smaller intensities.

Vibrating sample magnetometry

The magnetic properties of all samples were studied using Vibrating Sample Magnetometry (VSM) with a PPMS DynaCool system (Quantum Design, San Diego, CA, USA). The measurements were taken on powder samples within the field range of ±9 T at various temperatures ranging from 5 K to 330 K and normalised to the total sample mass.

Dynamic light scattering and electrophoretic light scattering

For characterisation of the nanoparticles in solution and, hence, under biological conditions, magnetoferritin was analysed using dynamic light scattering (DLS) and electrophoretic light scattering (ELS). Prior to measuring, the samples were diluted to 1 μM in HEPES-1 buffer (pH 8.0, see the Ferritin purification section) and filtered through a 0.2 μm filter to remove agglomerates. All measurements were performed using a Zetasizer Nano ZS (Malvern Panalytical Ltd, Malvern, UK). Each sample was characterised by averaging over 75 sub-runs (5 subsequent runs, each containing 15 sub-runs) with 10 s measurements per sub-run. A log–normal fit was applied to the measured number distribution to calculate the hydrodynamic diameter D_H, representing the diameter of a sphere with the same diffusion properties as the analysed particle.

ELS measurements were performed at 40 V to account for the high conductivity of saline buffers and to prevent damage of the measuring cell's electrodes. For each sample, 300 sub-runs (10 subsequent runs, each containing 30 sub-runs) were recorded.

Alternating magnetic field-induced heating

Magnetic hyperthermia measurements were performed in a custom-made alternating magnetic field (AMF) setup described previously.[66] In short, 200 μL of magnetoferritin solution was placed in a single-use cuvette and subjected to an AC magnetic field (45 mT induction amplitude at 93.75 kHz or 104.5 kHz). Thermal changes were monitored by recording the solution surface with a thermal imager (VarioCam HD, InfraTec GmbH, Dresden, Germany) with an IR 1.0/30 JENOPTIK objective (InfraTec GmbH). Measurements were performed every 10 s over a duration of 30 min. The magnetic field was switched on directly after the first image and switched off after 15 min (91 images). To obtain the sample's temperature, the average temperature of the sample surface in the cuvette (approximately 5 × 10 mm^2 or 300 pixels) was determined. The measurement was repeated three times for all samples. Images were evaluated using the software IRBIS 3 plus (InfraTec GmbH).

Droplet assay for quantification of magnetic forces

In order to characterise the forces that can be applied to MFt, a droplet assay on coverslips was performed. In a first step, coverslips were coated with a PDMS layer (SYLGARD 184 Silicone Elastomer Kit, Dow Europe GmbH, Wiesbaden, Germany) to reduce unspecific binding of MFt to the glass surface. For this, a 1 : 10 mixture (curing agent to elastomer by weight) of PDMS was diluted in twice the amount (by weight) of hexane.[67] A coverslip (22 × 22 mm^2, thickness: 170 ± 5 μm) was sonicated in an ultrasonic bath for 10 min in isopropanol, followed by another sonication step in ultrapure water. In between treatments, the coverslip was thoroughly flushed with ultrapure water. Afterwards, the coverslip was blown dry using pressurised N_2. The coverslip was then mounted onto a spin coater and 100 μL of the PDMS mixture was placed on top. The spin coater was run for 150 s at 6000 rpm with an acceleration of 100 rpm s^{-1}. After spin coating, the coverslip was cured at 110 °C for 20 min.

For the droplet assay, MFt was diluted to 0.1 μM in HEPES-1 with 25 V% of glycerol. A droplet of 1 μL was placed onto a PDMS-coated coverslip and a magnetic tip was brought close to it. The magnetic tip consisted of two magnets (cube: NdFeB, side length: 5 mm, gold-plated, product number: W-05-G; cuboid: NdFeB, 10 × 4 × 1.2 mm^3, gold-plated, product number: Q-10-4-1.2-G; both from supermagnete.de by Webcraft GmbH, Gottmadingen, Germany) and a steel wire (diameter: 0.4 mm, product number: 1416, Röslau Stahldraht, Röslau, Germany) attached to the magnets.[31] The attraction of the fluorescent MFt was observed using an inverted epifluorescence microscope (IX83 by Olympus, Shinjuku, Tokyo, Japan) equipped with a 60× oil-objective with a numerical aperture N.A. = 1.25 and phase contrast PH3 (Olympus UPLFLN60XOIPH/1,25, Olympus). Data analysis was performed using Matlab (R2023a, The Mathworks

View Article Online
Nanoscale Paper

Inc., Natick, MA, USA). A horizontal line scan (thickness: 1 μm) over the intensity in the fluorescence channel was performed starting from the position of the magnetic tip. Position 0 was placed at the edge of the drop with the inside of the drop in the positive direction. A linear background ($y = mx + c$) was fitted to intensities at higher positions and subtracted from the line scan to obtain the final intensity curve.

Spatial magnetic manipulation

For imaging and manipulation, Cos7 cells were plated on sterilised glass coverslips in 35 mm cell-culture dishes at about 50% confluency. Prior to experiments, the cells were washed with PBS buffer and re-incubated in preheated Leibovitz medium (L15, Thermo Fisher Scientific, Waltham, MA, USA) supplemented with 10% foetal calf serum (FCS) and 1% PenStrep (Thermo Fisher Scientific). Imaging was performed in a heating chamber (TempController 2000-2, PeCon GmbH, Erbach, Germany) set to 37 °C and mounted on an inverted microscope (IX83 from Olympus) equipped with a 60× oil-objective with N.A. = 1.25 and phase contrast PH3 (Olympus UPLFLN60XOIPH/1,25, Olympus). MFts were centrifuged (10 000*g* for 10 min) and the supernatant was used. MNPs were injected into the cells using a micromanipulation system (InjectMan 4 and FemtoJet 4i, Eppendorf, Hamburg, Germany) with microinjection capillaries (Femtotip II, inner diameter of 500 nm, Eppendorf). For injection, MFt with a concentration of 1 μM was used. After microinjection, the sample was washed with the previously mentioned Leibovitz medium to remove the remaining MFt in the medium. Thereafter, a home-built magnetic tip (described in the Droplet assay for quantification of magnetic forces section and in the study by Novoselova *et al.*[31]) was approached to the cell using InjectMan 4 of the micromanipulation system. Videos of MFt redistribution in the fluorescence channel were acquired typically every 10 s over 30–45 min at a 200 ms camera exposure time (Prime BSI, Photometrics, Tucson, AZ, USA, see also Videos S1–S3†). Phase contrast and fluorescence image recordings were analysed using in-house developed analysis routines written in Matlab (R2023a, The Mathworks Inc.) and ImageJ (version 1.49v, U. S. National Institutes of Health, Bethesda, MD, USA).[68] A background subtraction was applied to the fluorescence videos.

Cell viability assay

For evaluation of the toxicity of MFt on the cells, standardised CellTiter-Blue (CTB) assay from Promega (Fitchburg, WI, USA) was performed as described previously.[31] Cos7 cells were seeded in a 96-well plate (25 000 cells per well) one day in advance. The next day, they were incubated with varying concentrations of MFt for 1 h in a mixture of 100 μL of both Dulbecco's Modified Eagle's Medium (DMEM) supplemented with 10% fetal calf serum and 1% PenStrep (all from Thermo Fisher Scientific) and HEPES-1. As the negative control, the cells were treated with 0.1% of Triton X-100 (PanReac AppliChem) for 30 min, and the positive control was treated only with DMEM. All conditions were used in triplicate. After incubation, cells were washed and incubated in 190 μL of a mixture of CTB solution and DMEM (1 : 9 by volume) for 4 h. Afterwards, 100 μL of each cell supernatant was transferred to a fresh well and the plate was analysed using an Infinite M Plex plate reader (Tecan, Männedorf, Switzerland). Each well was excited at 560 nm and fluorescence was detected at 590 nm over 25 flashes and 5 repetitions. The measured intensity is proportional to the number of living cells inside the corresponding well.

Results and discussion

Synthesis and structural characterisation

A set of three MFts was prepared using a ferritin cage based on only HCF subunits fused N-terminally to mEGFP. For the magnetic core synthesis, either pure Fe^{2+} or Fe^{2+} doped with a final doping ratio of 7% (mol mol^{-1}) Co^{2+} or doped with 7% (mol mol^{-1}) Zn^{2+} with respect to the total metal amount was used (see Fig. 1, 2 and Table 1). The dopant molarity used during the synthesis differed by small percentage (see the Materials and methods section), but effectively gave rise to the 7% doping reported here (see also Fig. 3). The biomineralisation reaction was carried out inside the purified and PEGylated ferritin. The obtained MFts were first characterised by transmission electron microscopy (see Fig. 1 and 2) and dynamic light scattering to probe the protein and core size, respectively.

The mean diameter of all MFt cages measured with TEM was 13.9 ± 2.2 nm (see Fig. S2†), whereas the mean hydrodynamic diameters of MFts measured with DLS were 36.7 ± 1.9 nm for pure MFt, 44.7 ± 3.3 nm for Co^{2+}-doped MFt, and 43.4 ± 7.1 nm for Zn^{2+}-doped MFt (Fig. 1 and Table 2). The polydispersity index was ≤0.17 for all MFts, confirming the expected small size distribution within the sample (Table 2). The diameter values are in accordance with previous reports,[31] where the TEM size of the protein structure matches the theoretically calculated mEGFP-decorated protein diameter (12 + 2 × 2.3 = 16.6 nm).[69] The larger hydrodynamic size in comparison with the physical size was typically observed after surface PEGylation and core synthesis, giving rise to an increased hydrophilicity. This effective hydrodynamic diameter is particularly suitable for subcellular applications, since cytoplasmic non-specific interactions between a nanoprobe and the proteins/fibres in the cytoplasm dramatically increase above 50 nm, as previously reported.[13,70] In addition, the measured negative ζ-potential of around −5 mV (Table 2) prevents non-specific interactions within the primarily negatively charged biological environment.

The mean diameter of all cores was 6.3 ± 1.8 nm (Fig. 2), which is in accordance with previously reported values of synthetically loaded ferritin cages.[17,31] There were no systematic differences in size after loading the cages with Fe or together with Co or Zn as dopants. The reproducibility of the magnetic core synthesis was evaluated by three separate syntheses (called runs in the following) and analysed separately, unless stated otherwise.

The doping levels of Co and Zn were determined by energy dispersive X-ray spectroscopy in scanning transmission electron microscopy (EDX-STEM). Fig. 3 shows high-resolution STEM images in the upper row, along with Fe, Co, and Zn

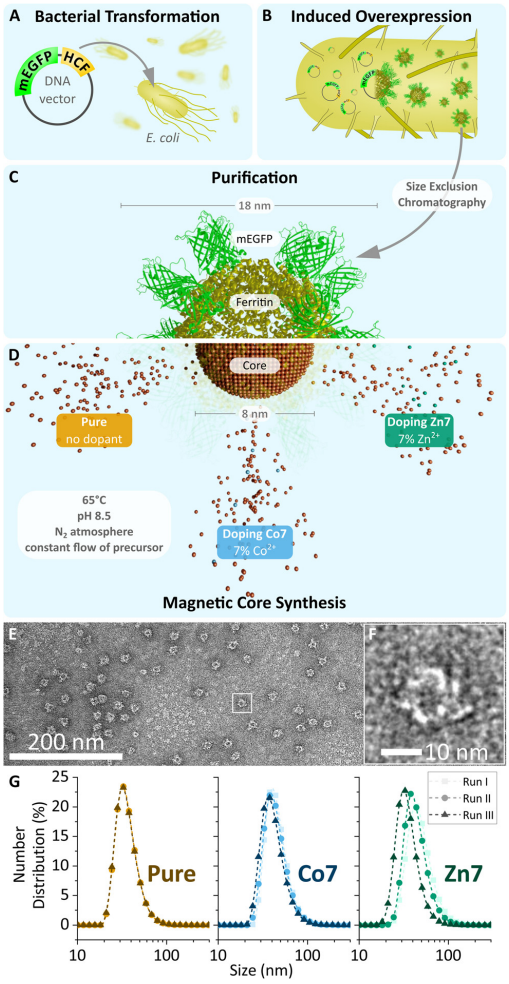

Fig. 1 (A–D) Schematic overview of MFt production. Apoferritin (yellow, PDB code: 1FHA), genetically fused to mEGFP (green, PDB code: 2Y0G, created with Avogadro v. 1.2.0[90] and blender v.2.93.2, Blender Foundation, Amsterdam, Netherlands), is expressed in transformed *E. coli* and then purified by size exclusion chromatography. Empty cages are filled with their respective metal oxide core (brown) during magnetic core synthesis. (C and D) Schematic illustration of the semi-synthetic MFt cage. The three different cores used in this study are indicated. (E) Transmission electron microscopy image of pure MFt's protein shell stained with 2% uranyl acetate. (F) Magnified image of (E) displaying one single ferritin cage. (G) Hydrodynamic diameter obtained using dynamic light scattering for MFt with three differently doped cores over three independent synthesis runs.

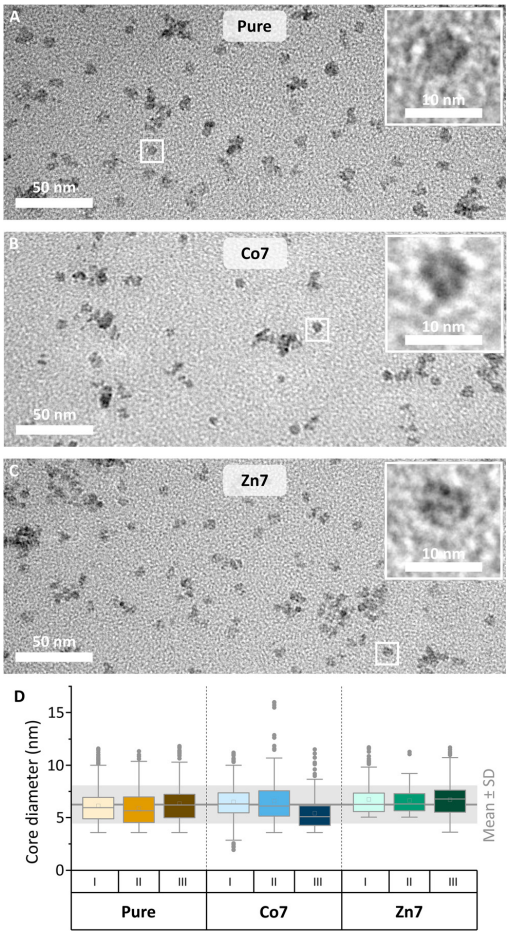

Fig. 2 (A–C) Transmission electron microscopy images of magnetoferritin. Images of all doping conditions were taken without staining to visualise metallic cores. (D) Box plots showing the diameters of cores from three independent synthesis runs (I, II and III) of all three doping conditions (each $N \geq 93$; mean ± SD = 6.3 ± 1.8 nm). Mean values are shown as boxes and median values are shown as horizontal lines.

elemental maps in the middle and lower rows. High-resolution STEM images appear blurry, due to the organics surrounding the magnetic cores. Under the focused electron beam, significant amounts of amorphous carbon grew, thus limiting the resolution and acquisition time for the elemental maps of Fe, Co, and Zn. Nonetheless, individual cores are visible in the pure MFt samples, while core accumulations yielded larger EDX signals. The elemental maps in Fig. 3 clearly show the colocalisation of Co or Zn with Fe. For the quantification of Co and Zn doping levels with respect to Fe, more than ten EDX spectra, each over small areas, were measured including about 20–30 magnetic cores. The results of each run are summarised in the graph in Fig. 3. The desired low doping levels of 6.8 ± 1.3 at% for Co and 6.4 ± 1.9 at% for Zn relative to the Fe intensity in the EDX spectra were obtained, with error bars indicating their standard deviation. We are the first to measure this

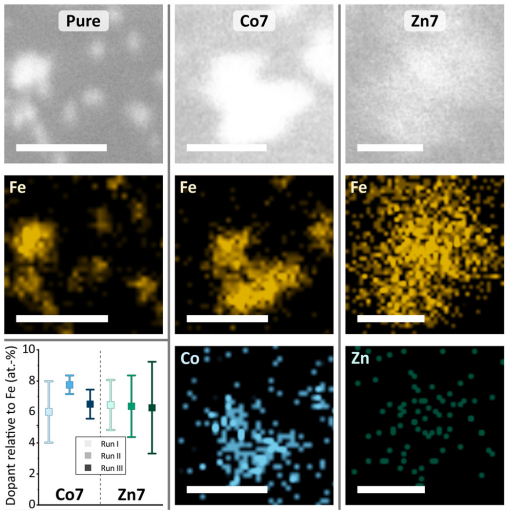

Fig. 3 Representative EDX-STEM images of MFt (pure) and doped (Co7 and Zn7) samples and elemental maps of indicated elements Fe, Co, and Zn (scale bar: 50 nm). The graph shows the dopant concentration relative to Fe of individual runs I–III.

Table 2 Properties of doped MFts. D_H: hydrodynamic diameter and PdI: polydispersity index, both obtained from DLS measurements, and ζ-Potential. For more details see Table S1†

Sample	D_H (nm)	PdI	ζ-Potential (mV)
Pure	36.7 ± 1.9	0.16 ± 0.01	−5.1 ± 0.7
Co7	44.7 ± 3.3	0.17 ± 0.02	−4.7 ± 1.1
Zn7	43.4 ± 7.1	0.17 ± 0.01	−4.8 ± 0.8

in the case of MFts and find that the effective dopant molarities of 6.8 (Co) and 6.4 (Zn) are slightly different from the amount applied during the synthesis (5% for Zn and 11% for Co). This deviation shows that it is necessary to determine the exact doping state in the core after the synthesis. All three individual runs of Co-doped (from now on called Co7) or Zn-doped (Zn7) samples contained only cores with doping elements, excluding the presence of pure iron or cobalt and zinc oxide. At this point, we can state that Co and Zn doping of MFt cores is possible and reproducible with a fairly homogeneous distribution of dopants from core to core.

To further investigate the crystal structure of MFts, we used X-ray diffraction. Three individual samples for each dopant (runs I–III) were pooled to increase the signal intensity. Since the small size of MFts and the large amount of organic material gave rise to a background signal, Fig. 4 presents the X-ray diffractogram using Cu-K_α radiation after background removal and smoothing.

Overall, the diffractograms of pure and doped MFt samples are similar and consist of two sets of sharp and broader peaks. The sharp peaks (indicated by asterisks) originate from NaCl

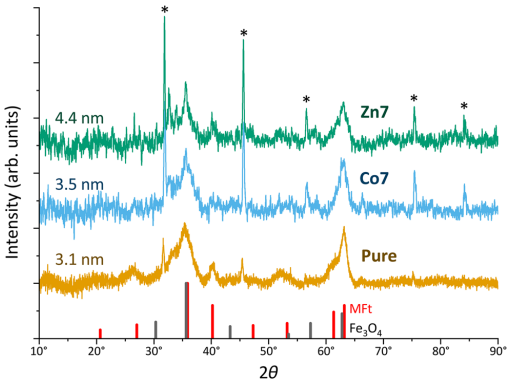

Fig. 4 X-ray diffraction patterns of magnetoferritin (pure) and doped (Co7 and Zn7) samples using Cu-K_α radiation. Runs I–III were pooled. Sharp peaks indicated by asterisks originate from residual NaCl after drying. Crystallite sizes obtained from the Scherrer analysis are given on the left. Sticks in black and red indicate the angles and intensities for Fe_3O_4 and MFt powder samples, respectively. Diffractograms are shifted vertically for better visibility.

crystallising during the drying process. However, more interesting are the broader peaks of the diffractogram of few-nm crystallites, *i.e.*, the pure MFt and Co7- and Zn7-doped samples. The crystallite sizes of 3–4 nm given in Fig. 3 were evaluated from the two largest peaks of each diffractogram using Scherrer's approach.[71] Considering the average core diameter of 6.3 nm and 3–4 nm crystallite sizes, it is estimated that each MFt consists of 4–9 crystallites regardless of doping. These numbers are realistic in light of the number of the HCF crystallisation points in a cage.[72] The diffractograms have a close relationship to those of 6-line ferrihydrite[73,74] while ferrites including the often-observed ferrimagnetic magnetite (Fe_3O_4) or maghemite (Fe_2O_3) can be excluded from the peak positions and relative intensities. For this comparison, powder-like samples[75,76] were assumed and the patterns of standard bulk cobalt ferrite (PDF-00-0221086), magnetite (PDF-00-019-0629) and maghemite (PDF-00-039-1346) were used. While different structures of ferrihydrite have been suggested over the decades, it is clear from previous studies that defects and relative site occupancies slightly modify the XRD response.

Magnetic characterisation

The structural characterisation of MFts in terms of their size and core composition showed a high homogeneity and similar properties between the three different samples. Any change in terms of their suitability for spatial manipulation and inductive heating approaches should thus depend on their magnetic properties. In Fig. 5A, the zero field-cooling (ZFC) and field-cooling (FC) magnetisation curves at B = 5 mT are displayed. For direct comparison of the blocking temperature, all curves are normalised to the FC value at T = 5 K. For clarity, we show only one curve for the pure MFt and Co7- and Zn7-doped samples as indicated by the run number while the values given below are

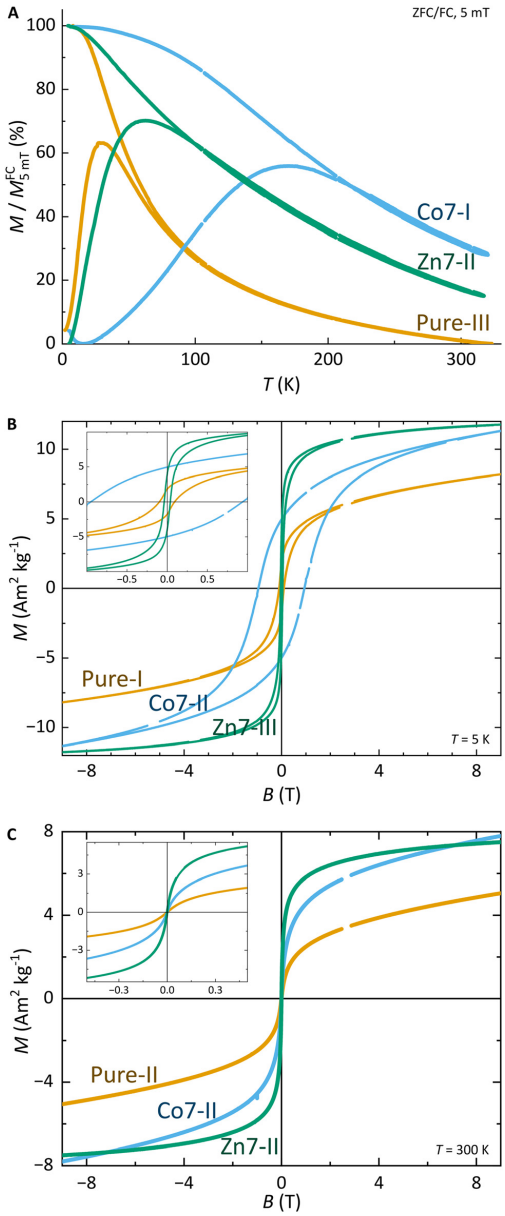

Fig. 5 Magnetometry results of pure and Co7 and Zn7 doped samples. The run number behind the doping conditions reflects the individual sample. Statistics are given in the text. (A) ZFC/FC curves in B = 5 mT. (B) Hysteresis loops at T = 5 K and (C) superparamagnetic response at T = 300 K. Insets show magnification at the origin in identical units. Voids in the curves are a technical feature of VSM resetting the sample position by a touchdown to the end position switch giving no data while the field is constantly swept.

accompanied by the statistics of the three independent runs. All individual runs confirm the trends. It is obvious from Fig. 5A that both the ZFC/FC maximum and the irreversibility point shift with doping towards higher temperatures, reflecting an increased magnetic anisotropy energy density (MAE) at a constant volume given by the MFt nanocompartments (*cf.* Fig. 2D). Taking the ZFC maxima as a measure of the blocking temperature T_B, we obtained 35 ± 5 K for pure MFt, 130 ± 37 K for Co7 and 74 ± 14 K for Zn7. The statistics hereby also reflect the individual doping levels achieved (*cf.* graph in Fig. 3). For pure MFt in our semisynthetic approach, T_B = 35 K is about 3 times higher than that usually observed for horse spleen ferritin (T_B = 10 K)[6] likely signalling different crystallisation mechanisms. While Zn doping doubles T_B as compared to pure MFt, it is striking that a low Co doping of 7% significantly increases the blocking temperatures to 130 K and thus the effective MAE K_{eff} correspondingly; T_B can be translated in K_{eff} for single-domain nanoparticles using the following equation:

$$\ln\frac{\tau}{\tau_0}k_B T_B = A \cdot k_B T_B = K_{eff} V.$$

where k_B is the Boltzmann constant and V is the particle volume. The prefactor $A = \ln(\tau/\tau_0)$ accounts for the measurement time (for VSM 1 s) with respect to the inverse of the intrinsic attempt frequency (typically 10^{-9} s). Using a prefactor A of 21 for VSM, K_{eff} values are 0.8×10^5 J m^{-3} for pure MFt, 2.9×10^5 J m^{-3} for Co7 and 1.6×10^5 J m^{-3} for Zn7 assuming a constant volume of V = 131 nm^3. Such 3.5 times larger T_B is very attractive for inductive heating since the increased anisotropy may lead to blocking effects at frequencies of 100 kHz at constant particle volume and thus to higher heat losses *via* Néel relaxation processes. A rough estimate can be drawn when comparing the prefactors A_{VSM} = 21 for VSM and A_{ind} = 9 for inductive heating at 100 kHz. Then, we compare $A_{VSM} \cdot T_B = A_{ind} \cdot T_{B,ind}$ and expect a $T_{B,ind}$ = 21/9 · 130 K ≈ 303 K for Co7 in inductive heating experiments. Thus, hysteresis losses can be expected at 100 kHz, leading to better heating in magnetic hyperthermia. Note that this estimate assumes a frequency-independent magnetic susceptibility which is generally not the case.

Furthermore, we discuss the important features: (1) magnetisation and (2) coercive field dependence on doping. Fig. 5 presents hysteresis loops at (B) T = 5 K and (C) T = 300 K. All curves are normalised to the total mass of the dried sample powder including the organic shell and residual salts. For the whole particle, we obtained magnetisations of 7–13 Am^2 kg^{-1} in B = 9 T and, as expected, the values decrease with increasing temperature. However, we cannot define the saturation magnetisation with regard to the magnetic cores only since the magnetic content is not exactly known. Instead, we used Langevin fitting as discussed below. None of the hysteresis loops reaches saturation, which points to additional paramagnetic Fe salts or antiferromagnetic contributions in the MFt MNPs. Taking the saturation magnetisation of 6 nm Fe_3O_4 MNPs of 45 (30) Am^2 kg^{-1} at T = 5 K (300 K)[57] as an upper limit, we obtained a ferrimagnetic fraction of at least 20–50 mass% in the samples. This is also in line with XRD measurements

View Article Online
Nanoscale Paper

showing sharp peaks (large crystallites) of NaCl after drying (*cf.* Fig. 4), giving a significant contribution to the total mass.

The coercive fields $\mu_0 H_C$ at T = 5 K are 99 ± 29 mT for pure MFt, 977 ± 64 mT for Co7 and 35 ± 4 mT for Zn7. These results follow earlier studies showing magnetic softening and higher magnetisation for Zn-doped ferrites and strong hardening at slightly reduced magnetisation for Co-doped ferrites.[77,78] At 300 K, all MNPs show a superparamagnetic response as expected. MFts can thus be treated as single domain and weakly interacting particles following the Néel–Brown model.[79]

Finally, the magnetisation of the MNPs can be extracted from the Langevin fitting of superparamagnetic magnetisation at T = 300 K. Fig. S3† presents the results for pure MFt and Co7 samples. Here, we used the Langevin function and an additional linear slope accounting for add-on contributions of salts and organics and paramagnetic or antiferromagnetic contributions in the samples. For simplicity, we fit the data with a single parameter in the Langevin function omitting the distribution of the product of magnetisation and volume. The resulting volume magnetisation values are 2824 ± 704 μ_B per particle (200 ± 50 kA m^{-1}) for pure MFt, 2973 ± 931 μ_B per particle (211 ± 66 kA m^{-1}) for Co7 and 5620 ± 3611 μ_B per particle (398 ± 255 kA m^{-1}) for Zn7. Pure MFt and Co7 yield similar values which are about 40% of bulk Fe_3O_4 magnetisation at ambient temperature. For Zn7, the larger value and larger variation of the fitting results of the three independent runs are ascribed to the larger number of agglomerates in Zn7 (*cf.* Fig. 2).

For further use of doped MFt in biomedical applications, magnetometry suggests that all the generated MNPs exhibit magnetisation values suitable for spatial manipulation in external fields. For applications in magnetic hyperthermia, however, especially the Co-doped MFts appear suitable due to their enhanced MAE, leading to magnetic blocking close to ambient temperature. This behaviour is consistent with the substitution of Co ions for Fe ions, since cobalt is well known to increase the magneto-crystalline anisotropy and correspondingly the blocking temperature.[9,59,65]

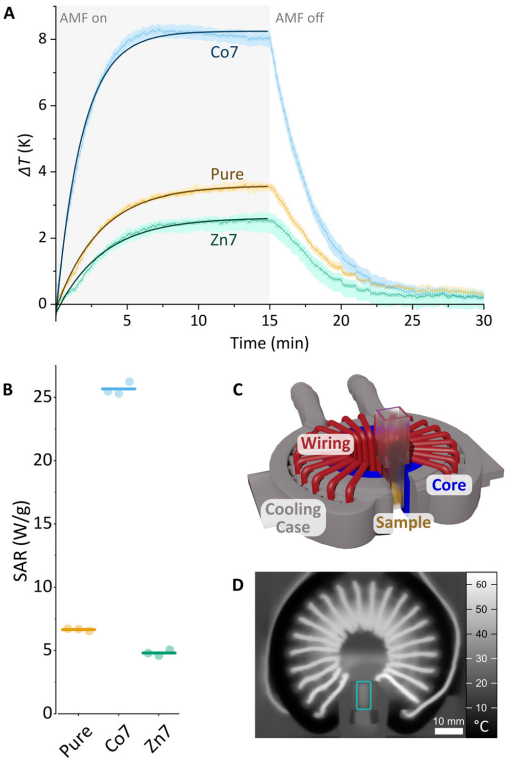

Fig. 6 (A) Hyperthermia measurement. Temperature kinetics of pure, Co7, and Zn7 MFt samples (each 35 μM) during exposure to an alternating magnetic field (45 mT, 93.75 kHz). Each curve is an average of three runs. The absolute temperature change ΔT refers to the temperature increase above the temperature of pure buffer solution. All MFt and buffer solution samples were measured in an identical manner. (B) Specific absorption rate (W g^{-1}) of each run (coloured dot) and average value (coloured line). (C) Custom-made hyperthermia setup. (D) Selected thermal image that was taken during the hyperthermia measurement with the sample (blue box) in the centre of the magnet gap.

Magnetic hyperthermia

The heating capabilities of the MNPs were evaluated by recording their temperature kinetic curves and hyperthermic efficiency. To this end, the MFts in HEPES-1 buffer solution were exposed to alternating magnetic fields (AMFs) of 93.75 kHz and 104.5 kHz and B = 45 mT amplitude using a custom-made hyperthermia setup. Due to extensive cooling and mitigation of inductive losses in the electromagnet, this setup allows for accurate measurements of the MNPs' dissipated power. The total particle concentration in the sample was 35 μM, corresponding to 55 mg mL^{-1} and 16% (w/w) of total metal ions. Fig. 6 and Fig. S4† show the average heating curves of three repeats for pure, Co7, or Zn7 MFts. From each measurement, the temperature kinetics of buffer measured under identical conditions were subtracted, yielding ΔT. Care was taken to measure each sample up to the steady-state conditions during the heating and cooling stages (10–15 min after switching the AMF on or off). At 93.75 kHz, the pure MFt sample exhibits a temperature increase above the buffer reference up to ΔT = 3.6 K during exposure to the AMF. The Zn7 sample exhibits a lower temperature increase of ΔT = 2.5 K during inductive heating. This lower response, however, is not significantly different from that of the pure MFt sample given the ±2 K absolute temperature accuracy of the IR-camera. Single heating curves were highly robust, since repetitions were near identical and hence did not contribute to the uncertainty (see Fig. 6A, where the coloured envelope indicates the error arising from repeated measurements). Intriguingly, Co7 samples led to an inductive heating of ΔT = 8 K after 300 s in the AMF. Such a significant temperature increase provides evidence that doped MFts can act as heat mediators. At 104.5 kHz

AMF frequency, all three MFt samples exhibited slightly lower heating rates compared to those at 93.75 kHz (see Fig. S4†). While the pure MFt sample again heated up to ΔT_{max} = 3 K, the Zn7 sample showed ΔT_{max} = 1.2 K and the Co7 sample showed ΔT_{max} = 6.1 K. Previous tests using horse spleen ferritin as a reference led to no measurable heating,[28] corroborating our finding that the synthesis of a particular magnetic core is critical to maximise the heating response.

The trend observed in the calorimetric experiments can be explained with MFt's magnetic properties. In the linear response regime, the power losses are described by the specific absorption rate (SAR). It is proportional to the frequency, f, to the square of the external magnetic field amplitude, H_0, and to the out-of-phase component of the magnetic susceptibility, $\chi''(f)$:[80]

$$\mathrm{SAR} \propto f\mu_0 {H_0}^2 \chi''(f).$$

χ'' depends non-linearly on f, increases with the MFt's magnetic moment, and reaches a maximum when the Néel relaxation time τ_N (*i.e.*, the magnetic moment reversal time above the energy barrier) matches the period of the alternating magnetic field. This latter condition is, in our experiments, best satisfied for the Co7 sample, with increased magnetic anisotropy as compared to that of pure and Zn7 samples.

Since all measurements were performed using identical settings, the slightly lower inductive heating in the case of Co7 and Zn7 at 104.5 kHz could arise from a lower AC susceptibility χ'', which is directly proportional to the dissipated power.

Our data reveal an overall low inductive heating of MFts, which manifests itself in the SAR values per mass of total metal ions (see Fig. 6B). The SAR was evaluated from the initial slope of the fit to the heating curves amounting to 6.7 ± 0.1 W g^{-1} for pure MFt, 4.8 ± 0.2 W g^{-1} for pure Zn7, and 25.7 ± 0.5 W g^{-1} for Co7. The low inductive heating response and small SAR values are indeed expected for the MNPs of this diameter.[54,81] SAR values are also low in comparison with the data reported for larger MNPs in the literature[82–85] and our measurements using the same setup,[66] typically amounting to ~100 W g^{-1}. However, the heating rate of the Co7 sample is the maximal value typically achieved for these types of magnetic cores measured under similar conditions[60] and is promising to promote or even initiate heat sensitive cellular processes in the AMF. Moreover, the changes observed for different core doping and different frequency settings highlight that the inductive heating response is dependent on the experimental design for which here optimised AMF excitation settings and core compositions are found. Co7 MFts could hence only act as mild heat mediators when the nanoparticles are accumulated to high local concentrations (*e.g.*, 35 μM), resulting in the surrounding buffer solution heated by 2–3 degrees per minute.

Finally, it should be noted that all measurements were performed using external field parameters which fall below the physiological tolerance threshold.[86] Such settings are important when biological measurements are envisaged, where physiologically serviceable power losses are required.

MFt spatial manipulation

Since cell signalling processes were shown to rely on (i) the spatiotemporal regulation of molecular distribution[14,15] or (ii) the application of mechanical forces,[16,18] we here provide examples of how synthesised MFts are useful in this biological context. In particular, we show how MFts can be redistributed and accumulated in different intracellular compartments. On the one hand, this may be exploited for: (i) the coupling of MFts to signalling proteins and their active spatial redistribution to understand cell signalling processes and on the other hand, (ii) localised MFt accumulations may exert gentle forces to trigger mechanosensitive processes.

To explore the suitability of MFts to respond to an applied magnetic field gradient, we first redistributed the MFts under idealised conditions, *i.e.*, using droplets of MFts in a glycerol/water (25 : 75 V/V) mixture on PDMS-coated glass coverslips. A home-made magnetic tip consisting of spring steel wire connected to neodymium magnets was moved close to the droplet (see Fig. 7 and Video S1†). The magnetic tip generated magnetic gradients on the order of 10^3–10^4 T m^{-1}. To determine such magnetic flux density gradients over small scales (~μm), several assays have been developed. These include (i) The MNP attraction in solution using the Stokes equation[17,31] or (ii) the optical magnetometry based on nitrogen vacancy colour centres in diamond to map the 3D magnetic field of micromagnets.[87] Together with the magnetic moment reported in the previous section, MFts should hence encounter forces in the femto-Newton regime. This is too weak to produce clear ballistic MNP trajectories toward the magnetic tip, and instead the MNPs show a biased diffusion resulting from the superposition of Brownian motion with a magnetic drift. When the

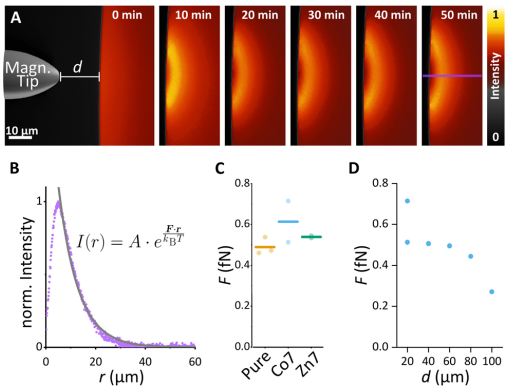

Fig. 7 Droplet assay with differently doped magnetoferritin. (A) Exemplary assay with pure MFt. The magnetic tip was introduced at 0 min at a distance of 20 μm and left at the designated position for 50 min. (B) In the steady state, a line scan over 1 μm (purple line in A) was used to determine the force F affecting MFt using the displayed fit function. (C) Forces determined using droplet assay for all doping conditions. (D) Force–distance dependence for different distances d between the droplet and the magnetic tip using the Co7 MFt sample.

View Article Online
Nanoscale Paper

magnetic tip was positioned at a particular distance d from the surface of the droplet, MFts were attracted towards the tip and formed a sharp gradient from the edge towards the centre of the droplet up to the distance where the attractive magnetic potential was exceeded by the thermal Brownian motion (see Fig. 7B). At the steady state, the MNP distribution followed a Boltzmann distribution and was fitted with an approximate relationship to determine the applied force $\boldsymbol{F}$:

$$I(\boldsymbol{r}) = A \cdot \exp\left(\frac{\boldsymbol{F} \cdot \boldsymbol{r}}{k_B T}\right).$$

where I is the intensity distribution along the purple line in Fig. 7A, A is the amplitude, k_B is the Boltzmann constant, T is the temperature, and $\boldsymbol{r}$ is the radial distance from the tip. Here, it was assumed that the droplet size is sufficiently small to have a constant magnetic force $\boldsymbol{F}$ across the droplet diameter, albeit the magnetic force $\boldsymbol{F}$ decreases as $1/r^2$ for a parabolic tip.[88,89] Fig. 7B shows the steady-state MNP distributions of the pure sample along with the intensity profile fit as an example. Similar distributions were obtained for the MFt with the dopant and were fitted accordingly. The forces are F_{pure} = 0.49 fN, F_{Co7} = 0.61 fN, and F_{Zn7} = 0.54 fN. These data confirm the mentioned theoretical estimate of fN forces generated by the current setup. In contrast to the hyperthermia results, no significant difference in the magnetic response between the different MFts was observed. This is reasonable, given the magnetic moments derived from the Langevin fit to the magnetisation curves vary only by 5% for MFt and Co7. In addition, differences in the magnetic field gradient sensitively depend on the lateral MFt–tip distance, which may vary by a

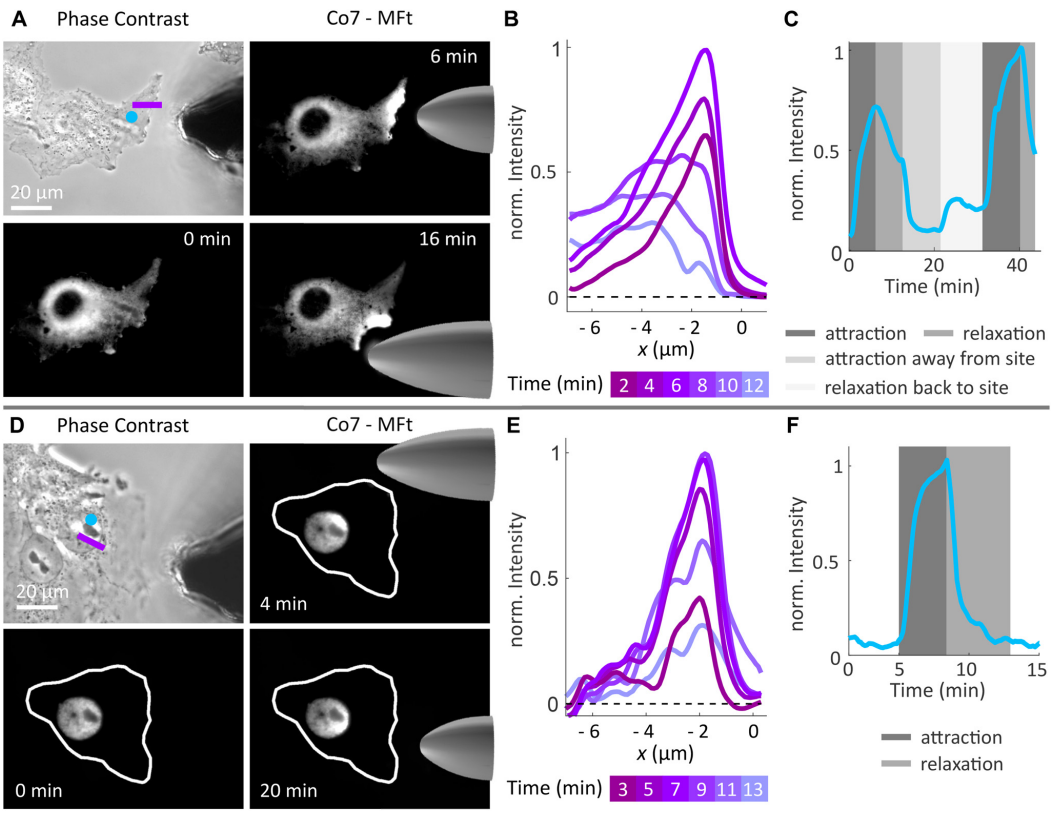

Fig. 8 Spatial manipulation of magnetoferritin in cells. (A) Phase contrast image of Cos7 cells and the micromagnetic tip and fluorescence images of Co7-MFt's spatial redistribution in the cell cytoplasm placing the magnetic tip at different positions. (B) Fluorescence intensity profile along the pink line in (A) during attraction (2–6 min) and relaxation (8–12 min). (C) Average fluorescence intensity within the blue spot in (A) over time. The intensity increases and decreases according to the spatial manipulation mode. (D) Phase contrast image of Cos7 cells and the micromagnetic tip and fluorescence images of Co7-MFt's spatial redistribution in the cell nucleus placing the magnetic tip at different positions. (E) Fluorescence intensity profile along the pink line in (D) during attraction (3–10 min) and relaxation (11–13 min). (F) Average fluorescence intensity within the blue spot in (D) over time. The intensity profile exhibits the characteristic exponential increase and decrease during attraction and relaxation, respectively. In (B) and (E), the background intensity profile was subtracted from the data and spatial averaging was performed over a line with a width of 5 pixels.

View Article Online
Paper Nanoscale

few 100 nm between the samples. In order to probe the force variation with the droplet–tip distance, the steady-state MFt distribution was further analysed, placing the magnetic tip 20 to 100 μm away from the tip. Interestingly, MFt attraction was visible over the whole range up to the 100 μm droplet–tip distance. This is an important prerequisite when magnetic manipulation approaches at a distance, *e.g.*, through a glass cover slip, are envisaged. At the 100 μm distance, a magnetic force of F_{Co7} = 0.27 fN was derived. In summary, the MFt droplet assay confirmed the ability to generate tuneable and reversible MFt profiles. To further demonstrate the suitability of MFts to be spatially redistributed within a subcellular compartment, we microinjected the Co7 MFts into the cell cytoplasm or in the cell nucleus (see Fig. 8 and Videos S2 and S3†). Although microinjection is comparably invasive, with the intracellular pressure or milieu changes regularly leading to cell death after injection, it has several advantages over other transfer methods. Among these advantages are the direct intake of nanoparticles into cells, wherefore it was used in this study to monitor the unrestricted motion of nanoparticles in the cytoplasm. We microinjected MFts into Cos7 cells and consecutively approached the same type of magnetic tip as used for the droplet assay to the cell from different sites. MFts were quickly attracted in the direction of the magnetic tip and formed μm size areas of strong MFt accumulation. A steady state distribution was typically reached after 5 min and the magnetic tip was removed to show the reversible MFt diffusion. When MFts were manipulated in the cell cytoplasm (see Fig. 8A–C), particles were already attracted when the tip was placed about 70 μm away from the cell edge. At short distances from the cell edge (~10 μm), strong MFt accumulations developed. When the magnetic tip was moved to different sites of the cell, the MFts were immediately redistributed. MFts remained mobile and did not form any agglomeration during the field-assisted manipulation. They fully dispersed in the cell cytoplasm after removal of the magnetic tip. MFt manipulation in general did not lead to any microscopic deformations of the cell shape. Yet, in the case of strong MFt accumulation and attraction over several minutes, after tip removal and MFt dispersion, a slight increase in the projected fluorescence intensity at the manipulation site compared to the initial state was observed. This suggested that an increase in the cytoplasmic volume can occur along with a displacement of intracellular structures when high local MFt concentrations are present.

When MFts were manipulated in the cell nucleus (see Fig. 8D–F), particles were reversibly attracted inside the nucleus without observing any intensity change after the manipulation. Interestingly, the attraction was fully reversible and MFts remained inside the nucleus without any detectable escape to the cell cytoplasm.

We further tested the biocompatibility of MFts and found that cells that were incubated with MFt Co7 for 1 h did not show any increased mortality in comparison with buffer controls (see Fig. S5A†). Additionally, the cell death, which occurred only in microinjected cells, was similar between only the microinjected cells and cells after magnetic accumulation of MFts over the course of 6 h (see Fig. S5B†). Additional cell death, which was observed on longer time scales (>6 h), could arise from microinjection late effects, excessive magnetic MFt accumulation, and a change in sterile or imaging conditions (since the sample was not covered during imaging for microinjection and magnetic manipulation purposes), among others. While these long-time effects require further investigation, the Co^{2+}-doped MFt, when brought into contact with the cells alone, suggested a high biocompatibility, in line with previous studies.[9,31]

Thus, provided the MFt transfer to the cellular environment is further improved, the spatial manipulation of MFts can serve as a method to actively redistribute MFt-coupled molecules for cell signalling studies. It may also be used to apply gentle mechanical stimuli to intracellular structures depending on the magnetic field gradient and the magnetic flux density applied.

Conclusion and outlook

We have demonstrated that ferritin-based magnetic nanoparticles (MFts) offer a versatile platform for spatial magnetic manipulation approaches, whereas an inductive heating of the nanoparticles is possible only for optimal alternating magnetic field settings and mineralised cores of high magnetic anisotropy (*e.g.*, Co-doped cores). In particular, we synthesised a bioengineered ferritin-based magnetic nanoparticle (MNP) with mEGFP and PEG coupled to its surface. This enabled tracking of the particle and preventing any unspecific interaction of the particle within a synthetic or cellular environment. Three types of MFts were synthesised with an undoped, 7% Zn- or 7% Co-doped superparamagnetic core with high size homogeneity of the shell and core. Thus, MFts are addressable one particle at a time and allows the transmission of the same magnetic stimulus, an important prerequisite for many bio- and nanotechnological applications.

7% cobalt doping yielded the highest effective magnetic anisotropy and significantly improved the hyperthermic heat performance. Here, inductive heating experiments at 93.75 kHz resulted in a temperature increase of 8 K above a buffer reference within a few minutes. This provided evidence that Co-doped MFts can act as mild heat mediators when optimised magnetic field settings and nanoparticle core properties are used. 7% zinc doping and the pure mineral core resulted in superparamagnetism down to ≤60 K and measurements at different frequencies only brought about a slight heating effect. Our rigorous measurements provide new insights into the recent discussion on whether (or under which conditions) MFts can act as heat mediators.

Next to probing the MFt applicability for magnetic hyperthermia, their suitability for spatial manipulation approaches in a biological context was tested. The performed experiments nicely showed the applicability of our doped MFts in solution and in a cellular context.

View Article Online
Nanoscale Paper

Here, all MFts performed very well and were comparable in terms of their spatial redistribution potential. The MFts were reversibly attracted in droplets or inside cells approaching a magnetic tip (*i.e.*, a magnetic field gradient) and attraction forces were easily modulated by changing the MFt–magnetic tip distance. In agreement with theoretical calculations, the analysis of experimentally obtained MNP distributions revealed that nanoparticles exert mild forces in the fN regime. The MFts could hence be used to couple molecules to the MFt surface (i) to spatially redistribute the molecules to create local signalling hubs, (ii) to switch their (conformational) activity state, or (iii) to exploit the biological mechano-sensitivity in a mild force transduction approach. In conclusion, the Co-doped MFt is an extremely versatile and small functionalised targeting nanosystem, which offers the best magnetic properties for a spatial- or force-mediated manipulation of individual molecules along with some potential for nanotechnological hyperthermia applications.

Author contributions

Conceptualisation: AN, CM, and UW; methodology: AN, CM, DAK, IPN, NT, SS, PH, and UW; investigation: AN, CM, DAK, and UW; visualisation: AN, CM, DAK, and UW; supervision: CM, UW, and MF; writing – original draft: AN, CM, DAK, and UW.

Data availability

The data supporting the manuscript "Semisynthetic ferritin-based nanoparticles with high magnetic anisotropy for spatial magnetic manipulation and inductive heating" (NR-ART-04-2024-001652) have been included as part of the ESI.†

Conflicts of interest

There are no conflicts of interest to declare.

Acknowledgements

CM acknowledges financial support from the Deutsche Forschungsgemeinschaft (DFG, German Research Foundation) through CRC1208 'Identity and Dynamics of Membrane Systems' (A12, Project ID 267205415) and CRC1535 'Microbial Networks' (A09, Project ID 458090666). CM and AN acknowledge financial support *via* the 'Freigeist fellowship' of Volkswagen Foundation. The authors acknowledge the DFG and the State of North Rhine–Westphalia for funding the cryo-TEM (INST 208/749-1 FUGG) hosted by the Centre of Advanced Imaging (CAi, Heinrich-Heine University). The authors thank the group of Prof. Claus Seidel (Physical Chemistry, Heinrich-Heine University) for providing lab space and laboratory equipment, the group of Prof. Lutz Schmitt (Biochemistry, Heinrich-Heine University) for providing the cell disruptor, and the group of Prof. Laura Hartmann (Macromolecular Chemistry, Heinrich-Heine University) for providing the Zetasizer.

References

1 Z. Yuan, B. Wang, Y. Teng, W. Ho, B. Hu, K. O. Boakye-Yiadom, X. Xu and X.-Q. Zhang, *Nanoscale*, 2022, **14**, 6449–6464.
2 I. Inoue, M. Chiba, K. Ito, Y. Okamatsu, Y. Suga, Y. Kitahara, Y. Nakahara, Y. Endo, K. Takahashi, U. Tagami and N. Okamoto, *Nanoscale*, 2021, **13**, 1875–1883.
3 X. Lin, J. Xie, G. Niu, F. Zhang, H. Gao, M. Yang, Q. Quan, M. A. Aronova, G. Zhang, S. Lee, R. Leapman and X. Chen, *Nano Lett.*, 2011, **11**, 814–819.
4 K. Fan, C. Cao, Y. Pan, D. Lu, D. Yang, J. Feng, L. Song, M. Liang and X. Yan, *Nat. Nanotechnol.*, 2012, **7**, 459–464.
5 K. Li, Z. P. Zhang, M. Luo, X. Yu, Y. Han, H. P. Wei, Z. Q. Cui and X. E. Zhang, *Nanoscale*, 2012, **4**, 188–193.
6 C. Massner, F. Sigmund, S. Pettinger, M. Seeger, C. Hartmann, N. P. Ivleva, R. Niessner, H. Fuchs, M. H. de Angelis, A. Stelzl, N. L. Koonakampully, H. Rolbieski, U. Wiedwald, M. Spasova, W. Wurst, V. Ntziachristos, M. Winklhofer and G. G. Westmeyer, *Adv. Funct. Mater.*, 2018, **28**, 1706793.
7 H. J. Kang, Y. J. Kang, Y. M. Lee, H. H. Shin, S. J. Chung and S. Kang, *Biomaterials*, 2012, **33**, 5423–5430.
8 Z. Wang, Y. Dai, Z. Wang, O. Jacobson, F. Zhang, B. C. Yung, P. Zhang, H. Gao, G. Niu, G. Liu and X. Chen, *Nanoscale*, 2018, **10**, 1135–1144.
9 E. Fantechi, C. Innocenti, M. Zanardelli, M. Fittipaldi, E. Falvo, M. Carbo, V. Shullani, L. Di Cesare Mannelli, C. Ghelardini, A. M. Ferretti, A. Ponti, C. Sangregorio and P. Ceci, *ACS Nano*, 2014, **8**, 4705–4719.
10 R. Chen, G. Romero, M. G. Christiansen, A. Mohr and P. Anikeeva, *Science*, 2015, **347**, 1477–1480.
11 K. Ohara, T. Moriwaki, K. Nakazawa, T. Sakamoto, K. Nii, M. Abe and Y. Ichiyanagi, *AIP Adv.*, 2023, **13**, 025238.
12 F. Etoc, D. Lisse, Y. Bellaiche, J. Piehler, M. Coppey and M. Dahan, *Nat. Nanotechnol.*, 2013, **8**, 193–198.
13 F. Etoc, C. Vicario, D. Lisse, J. M. Siaugue, J. Piehler, M. Coppey and M. Dahan, *Nano Lett.*, 2015, **15**, 3487–3494.
14 M. Aubry, W. A. Wang, Y. Guyodo, E. Delacou, J. M. Guigner, O. Espeli, A. Lebreton, F. Guyot and Z. Gueroui, *ACS Synth. Biol.*, 2020, **9**, 3030–3041.
15 Y. Shi, L. Huang, H. Dong, M. Yang, W. Ding, X. Zhou, T. Lu, Z. Liu, X. Zhou, M. Wang, B. Zeng, Y. Sun, S. Zhong, B. Wang, W. Wang, C. Yin, X. Wang and Q. Wu, *Cell Res.*, 2024, **34**, 193–213.
16 D. Seo, K. M. Southard, J. W. Kim, H. J. Lee, J. Farlow, J. U. Lee, D. B. Litt, T. Haas, A. P. Alivisatos, J. Cheon, Z. J. Gartner and Y. W. Jun, *Cell*, 2016, **165**, 1507–1518.
17 D. Lißе, C. Monzel, C. Vicario, J. Manzi, I. Maurin, M. Coppey, J. Piehler and M. Dahan, *Adv. Mater.*, 2017, **29**, 1–7.

18 C. Monzel, C. Vicario, J. Piehler, M. Coppey and M. Dahan, *Chem. Sci.*, 2017, **8**, 7330–7338.
19 A. S. Garanina, M. V. Efremova, A. E. Machulkin, E. V. Lyubin, N. S. Vorobyeva, O. A. Zhironkina, O. S. Strelkova, I. I. Kireev, I. B. Alieva, R. E. Uzbekov, V. N. Agafonov, I. V. Shchetinin, A. A. Fedyanin, A. S. Erofeev, P. V. Gorelkin, Y. E. Korchev, A. G. Savchenko and M. A. Abakumov, *Magnetochemistry*, 2022, **8**, 185.
20 A. K. Gupta and M. Gupta, *Biomaterials*, 2005, **26**, 3995–4021.
21 Y. Zhu, Y. Zhu, T. Cao, X. Liu, X. Liu, Y. Yan, Y. Shi and J. C. Wang, *Med. Rev.*, 2023, **3**, 49–74.
22 D. He and J. Marles-Wright, *Nat. Biotechnol.*, 2015, **32**, 651–657.
23 M. Kumar, J. Markiewicz-Mizera, J. D. Janna Olmos, P. Wilk, P. Grudnik, A. P. Biela, M. Jemioła-Rzemińska, A. Górecki, S. Chakraborti and J. G. Heddle, *Nanoscale*, 2021, **13**, 11932–11942.
24 Y. Jin, J. He, K. Fan and X. Yan, *Nanoscale*, 2019, **11**, 12449–12459.
25 A. Mohanty, A. Parida, R. K. Raut and R. K. Behera, *ACS Bio Med Chem Au*, 2022, **2**, 258–281.
26 A. N. Gabashvili, S. S. Vodopyanov, N. S. Chmelyuk, V. A. Sarkisova, K. A. Fedotov, M. V. Efremova and M. A. Abakumov, *Int. J. Mol. Sci.*, 2021, **22**, 12275.
27 M. Meister, *eLife*, 2016, **5**, 1–14.
28 H. C. Davis, S. Kang, J. H. Lee, T. H. Shin, H. Putterman, J. Cheon and M. G. Shapiro, *Biophys. J.*, 2020, **118**, 1502–1510.
29 Y. Zhang and B. P. Orner, *Int. J. Mol. Sci.*, 2011, **12**, 5406–5421.
30 P. M. Harrison and P. Arosio, *Biochim. Biophys. Acta, Bioenerg.*, 1996, **1275**, 161–203.
31 I. P. Novoselova, A. Neusch, J. S. Brand, M. Otten, M. R. Safari, N. Bartels, M. Karg, M. Farle, U. Wiedwald and C. Monzel, *Nanomaterials*, 2021, **11**, 1–20.
32 E. Falvo, E. Tremante, R. Fraioli, C. Leonetti, C. Zamparelli, A. Boffi, V. Morea, P. Ceci and P. Giacomini, *Nanoscale*, 2013, **5**, 12278–12285.
33 D. Liße, C. P. Richter, C. Drees, O. Birkholz, C. You, E. Rampazzo and J. Piehler, *Nano Lett.*, 2014, **14**, 2189–2195.
34 X. Li, L. Qiu, P. Zhu, X. Tao, T. Imanaka, J. Zhao, Y. Huang, Y. Tu and X. Cao, *Small*, 2012, **8**, 2505–2514.
35 F. Raudzus, H. Schöneborn, S. Neumann, E. Secret, A. Michel, J. Fresnais, O. Brylski, C. Ménager, J. M. Siaugue and R. Heumann, *Sci. Rep.*, 2020, **10**, 22452.
36 M. Le Jeune, E. Secret, M. Trichet, A. Michel, D. Ravault, F. Illien, J.-M. Siaugue, S. Sagan, F. Burlina and C. Ménager, *ACS Appl. Mater. Interfaces*, 2022, **14**, 15021–15034.
37 N. K. Lee, S. Cho and I. S. Kim, *Exp. Mol. Med.*, 2022, **54**, 1652–1657.
38 N. Aronovitz, M. Neeman and R. Zarivach, in *Iron Oxides*, ed. D. Faivre, John Wiley & Sons, Ltd, Hoboken, 2016, pp. 117–142.
39 E. C. Theil, *Adv. Enzymol. Relat. Areas Mol. Biol.*, 1990, **63**, 421–449.
40 A. García-Prieto, J. Alonso, D. Muñoz, L. Marcano, A. Abad Díaz de Cerio, R. Fernández de Luis, I. Orue, O. Mathon, A. Muela and M. L. Fdez-Gubieda, *Nanoscale*, 2016, **8**, 1088–1099.
41 M. A. Kostiainen, P. Ceci, M. Fornara, P. Hiekkataipale, O. Kasyutich, R. J. M. Nolte, J. J. L. M. Cornelissen, R. D. Desautels and J. Van Lierop, *ACS Nano*, 2011, **5**, 6394–6402.
42 M. A. Kostiainen, P. Hiekkataipale, A. Laiho, V. Lemieux, J. Seitsonen, J. Ruokolainen and P. Ceci, *Nat. Nanotechnol.*, 2013, **8**, 52–56.
43 S. Gider, D. D. Awschalom, T. Douglas, S. Mann and M. Chaparala, *Science*, 1995, **268**, 77–80.
44 Q. A. Pankhurst, S. Betteridge, D. P. E. Dickson, T. Douglas, S. Mann and R. B. Frankel, *Hyperfine Interact.*, 1994, **91**, 847–851.
45 M. Allen, D. Willits, M. Young and T. Douglas, *Inorg. Chem.*, 2003, **42**, 6300–6305.
46 D. A. Resnick, K. Gilmore, Y. U. Idzerda, M. T. Klem, M. Allen, T. Douglas, E. Arenholz and M. Young, *J. Appl. Phys.*, 2006, **99**, 2006–2008.
47 P. Mackle, J. M. Charnock, C. D. Garner, F. C. Meldrum and S. Mann, *J. Am. Chem. Soc.*, 1993, **115**, 8471–8472.
48 B. Warne, O. I. Kasyutich, E. L. Mayes, J. A. L. Wiggins and K. K. W. Wong, *IEEE Trans. Magn.*, 2000, **36**, 3009–3011.
49 T. Ueno, M. Suzuki, T. Goto, T. Matsumoto, K. Nagayama and Y. Watanabe, *Angew. Chem., Int. Ed.*, 2004, **43**, 2527–2530.
50 R. M. Kramer, C. Li, D. C. Carter, M. O. Stone and R. R. Naik, *J. Am. Chem. Soc.*, 2004, **126**, 13282–13286.
51 K. K. W. Wong and S. Mann, *Adv. Mater.*, 1996, **8**, 928–932.
52 I. Yamashita, J. Hayashi and M. Hara, *Chem. Lett.*, 2004, **33**, 1158–1159.
53 K. Iwahori, K. Yoshizawa, M. Muraoka and I. Yamashita, *Inorg. Chem.*, 2005, **44**, 6393–6400.
54 J. P. Fortin, C. Wilhelm, J. Servais, C. Ménager, J. C. Bacri and F. Gazeau, *J. Am. Chem. Soc.*, 2007, **129**, 2628–2635.
55 M. Gonzales-Weimuller, M. Zeisberger and K. M. Krishnan, *J. Magn. Magn. Mater.*, 2009, **321**, 1947–1950.
56 L. Lartigue, C. Innocenti, T. Kalaivani, A. Awwad, M. D. M. Sanchez Duque, Y. Guari, J. Larionova, C. Gueírin, J. L. G. Montero, V. Barragan-Montero, P. Arosio, A. Lascialfari, D. Gatteschi and C. Sangregorio, *J. Am. Chem. Soc.*, 2011, **133**, 10459–10472.
57 M. V. Efremova, Y. A. Nalench, E. Myrovali, A. S. Garanina, I. S. Grebennikov, P. K. Gifer, M. A. Abakumov, M. Spasova, M. Angelakeris, A. G. Savchenko, M. Farle, N. L. Klyachko, A. G. Majouga and U. Wiedwald, *Beilstein J. Nanotechnol.*, 2018, **9**, 2684–2699.
58 M. Comes Franchini, G. Baldi, D. Bonacchi, D. Gentili, G. Giudetti, A. Lascialfari, M. Corti, P. Marmorato, J. Ponti, E. Micotti, U. Guerrini, L. Sironi, P. Gelosa, C. Ravagli and A. Ricci, *Small*, 2010, **6**, 366–370.

59 E. Skoropata, R. D. Desautels, E. Falvo, P. Ceci, O. Kasyutich, J. W. Freeland and J. Van Lierop, *Phys. Rev. B: Condens. Matter Mater. Phys.*, 2014, **90**, 174424.
60 R. Das, N. P. Kim, S. B. Attanayake, M.-H. Phan and H. Srikanth, *Appl. Sci.*, 2021, **11**, 930.
61 S. Singhal, T. Namgyal, S. Bansal and K. Chandra, *J. Electromagn. Anal. Appl.*, 2010, **2**, 376–381.
62 D. S. Mathew and R. S. Juang, *Chem. Eng. J.*, 2007, **129**, 51–65.
63 M. G. Christiansen, N. Mirkhani, W. Hornslien and S. Schuerle, *J. Appl. Phys.*, 2022, **132**, 174304.
64 S. Chakrabarti, S. K. Mandal and S. Chaudhuri, *Nanotechnology*, 2005, **16**, 506–511.
65 M. T. Klem, D. A. Resnick, K. Gilmore, M. Young, Y. U. Idzerda and T. Douglas, *J. Am. Chem. Soc.*, 2007, **129**, 197–201.
66 D. A. Kuckla, J.-S. Brand, B. Czech, A. Asharion, J. V. Jüttner, I. P. Novoselova, A. Neusch, P. Hagemann, M. Getzlaff and C. Monzel, *J. Phys. D: Appl. Phys.*, 2023, **56**, 505002.
67 A. L. Thangawng, R. S. Ruoff, M. A. Swartz and M. R. Glucksberg, *Biomed. Microdevices*, 2007, **9**, 587–595.
68 J. Schindelin, I. Arganda-Carreras, E. Frise, V. Kaynig, M. Longair, T. Pietzsch, S. Preibisch, C. Rueden, S. Saalfeld, B. Schmid, J. Y. Tinevez, D. J. White, V. Hartenstein, K. Eliceiri, P. Tomancak and A. Cardona, *Nat. Methods*, 2012, **9**, 676–682.
69 M. A. Hink, R. A. Griep, J. W. Borst, A. Van Hoek, M. H. M. Eppink, A. Schots and A. J. W. G. Visser, *J. Biol. Chem.*, 2000, **275**, 17556–17560.
70 F. Etoc, E. Balloul, C. Vicario, D. Normanno, D. Lißе, A. Sittner, J. Piehler, M. Dahan and M. Coppey, *Nat. Mater.*, 2018, **17**, 740–746.
71 J. I. Langford and A. J. C. Wilson, *J. Appl. Crystallogr.*, 1978, **11**, 102–113.
72 K. Zeth, E. Hoiczyk and M. Okuda, *Trends Biochem. Sci.*, 2016, **41**, 190–203.
73 V. A. Drits, B. A. Sakharov, A. L. Salyn and A. Manceau, *Clay Miner.*, 1993, **28**, 185–207.
74 E. Jansen, A. Kyek, W. Schäfer and U. Schwertmann, *Appl. Phys. A: Mater. Sci. Process.*, 2002, **74**, 1004–1006.
75 W. Kim, C. Y. Suh, S. W. Cho, K. M. Roh, H. Kwon, K. Song and I. J. Shon, *Talanta*, 2012, **94**, 348–352.
76 Y. A. Nalench, I. V. Shchetinin, A. S. Skorikov, P. S. Mogilnikov, M. Farle, A. G. Savchenko, A. G. Majouga, M. A. Abakumov and U. Wiedwald, *J. Mater. Chem. B*, 2020, **8**, 3886–3895.
77 P. Saha, R. Rakshit, M. Alam and K. Mandal, *Phys. Rev. Appl.*, 2019, **11**, 024059.
78 S. Liébana-Viñas, K. Simeonidis, U. Wiedwald, Z.-A. Li, Z. Ma, E. Myrovali, A. Makridis, D. Sakellari, G. Vourlias, M. Spasova, M. Farle and M. Angelakeris, *RSC Adv.*, 2016, **6**, 72918–72925.
79 L. Néel, *Ann. Geophys. (C. N. R. S.)*, 1949, **5**, 99–136.
80 Q. A. Pankhurst, J. Connolly, S. K. Jones and J. Dobson, *J. Phys. D: Appl. Phys.*, 2003, **36**, R167–R181.
81 S. Purushotham and R. V. Ramanujan, *J. Appl. Phys.*, 2010, **107**, 114701.
82 A. Lascialfari, M. Filibian, C. Sangregorio and P. Carretta, *La Riv. del Nuovo Cim.*, 2013, **36**, 211–271.
83 P. Guardia, R. Di Corato, L. Lartigue, C. Wilhelm, A. Espinosa, M. Garcia-Hernandez, F. Gazeau, L. Manna and T. Pellegrino, *ACS Nano*, 2012, **6**, 3080–3091.
84 J.-H. Lee, J. Jang, J. Choi, S. H. Moon, S. Noh, J. Kim, J.-G. Kim, I.-S. Kim, K. I. Park and J. Cheon, *Nat. Nanotechnol.*, 2011, **6**, 418–422.
85 H. Gavilán, K. Simeonidis, E. Myrovali, E. Mazarío, O. Chubykalo-Fesenko, R. Chantrell, L. Balcells, M. Angelakeris, M. P. Morales and D. Serantes, *Nanoscale*, 2021, **13**, 15631–15646.
86 R. Hergt and S. Dutz, *J. Magn. Magn. Mater.*, 2007, **311**, 187–192.
87 L. Toraille, K. Aïzel, É. Balloul, C. Vicario, C. Monzel, M. Coppey, E. Secret, J. M. Siaugue, J. Sampaio, S. Rohart, N. Vernier, L. Bonnemay, T. Debuisschert, L. Rondin, J. F. Roch and M. Dahan, *Nano Lett.*, 2018, **18**, 7635–7641.
88 T. Häberle, F. Haering, H. Pfeifer, L. Han, B. Achinuq, U. Wiedwald, U. Herr and B. Koslowski, *New J. Phys.*, 2012, **14**, 043044.
89 A. H. B. De Vries, B. E. Krenn, R. Van Driel and J. S. Kanger, *Biophys. J.*, 2005, **88**, 2137–2144.
90 M. D. Hanwell, D. E. Curtis, D. C. Lonie, T. Vandermeersch, E. Zurek and G. R. Hutchison, *J. Cheminf.*, 2012, **4**, 17.

Supplementary Information

Semisynthetic Ferritin-based Nanoparticles with High Magnetic Anisotropy for Spatial Magnetic Manipulation and Inductive Heating

Andreas Neusch[a], Ulf Wiedwald[b], Iuliia P. Novoselova[a,c], Daniel A. Kuckla[a], Nikolaos Tetos[b], Sarah Sadik[a,d], Philipp Hagemann[a], Michael Farle[b] and Cornelia Monzel[a,*]

Table of Content

[a] *Experimental Medical Physics, Heinrich-Heine University Düsseldorf, 40225 Düsseldorf, Germany.*
[b] *Faculty of Physics and Center for Nanointegration (CENIDE), University of Duisburg-Essen, 47057 Duisburg, Germany*
[c] *Present address: Institute of Human Genetics, University Hospital Düsseldorf, Heinrich-Heine-University Düsseldorf, 40225 Düsseldorf, Germany*
[d] *Present address: Cell Biology and Cancer, UMR 144 CNRS, Institute Curie, 75248 Paris cedex 05, France.*
** Corresponding author (Cornelia.Monzel@hhu.de)*

Supplementary Figures

DNA sequence:

ATGGTGAGCAAGGGCGAGGAGCTGTTCACCGGGGTGGTGCCCATCCTGGTCGAGCTGGACGGCGACGTAAA
CGGCCACAAGTTCAGCGTGTCCGGCGAGGGCGAGGGCGATGCCACCTACGGCAAGCTGACCCTGAAGTTCAT
CTGCACCACCGGCAAGCTGCCCGTGCCCTGGCCCACCCTCGTGACCACCCTGACCTACGGCGTGCAGTGCTTCA
GCCGCTACCCCGACCACATGAAGCAGCACGACTTCTTCAAGTCCGCCATGCCCGAAGGCTACGTCCAGGAGCG
CACCATCTTCTTCAAGGACGACGGCAACTACAAGACCCGCGCCGAGGTGAAGTTCGAGGGCGACACCCTGGT
GAACCGCATCGAGCTGAAGGGCATCGACTTCAAGGAGGACGGCAACATCCTGGGGCACAAGCTGGAGTACAA
CTACAACAGCCACAACGTCTATATCATGGCCGACAAGCAGAAGAACGGCATCAAGGTGAACTTCAAGATCCGC
CACAACATCGAGGACGGCAGCGTGCAGCTCGCCGACCACTACCAGCAGAACACCCCCATCGGCGACGGCCCC
GTGCTGCTGCCCGACAACCACTACCTGAGCACCCAGTCCAAGCTGAGCAAAGACCCCAACGAGAAGCGCGATC
ACATGGTCCTGCTGGAGTTCGTGACCGCCGCCGGGATCACTCTCGGCATGGACGAGCTGTACAAG–
GGATCCGGTGCAGAATTC–
ATGACGACCGCGTCCACCTCGCAGGTGCGCCAGAACTACCACCAGGACTCAGAGGCCGCCATCAACCGCCAGA
TCAACCTGGAGCTCTACGCCTCCTACGTTTACCTGTCCATGTCTTACTACTTTGACCGCGATGATGTGGCTTTGA
AGAACTTTGCCAAATACTTTCTTCACCAATCTCATGAGGAGAGGGAACATGCTGAGAAACTGATGAAGCTGCA
GAACCAACGAGGTGGCCGAATCTTCCTTCAGGATATCAAGAAACCAGACTGTGATGACTGGGAGAGCGGGCT
GAATGCAATGGAGTGTGCATTACATTTGGAAAAAAATGTGAATCAGTCACTACTGGAACTGCACAAACTGGCC
ACTGACAAAAATGACCCCCATTTGTGTGACTTCATTGAGACACATTACCTGAATGAGCAGGTGAAAGCCATCAA
AGAATTGGGTGACCACGTGACCAACTTGCGCAAGATGGGAGCGCCCGAATCTGGCTTGGCGGAATATCTCTTT
GACAAGCACACCCTGGGAGACAGTGATAATGAAAGCTAG

Amino acid sequence:

MVSKGEELFTGVVPILVELDGDVNGHKFSVSGEGEGDATYGKLTLKFICTTGKLPVPWPTLVTTLTYGVQCFSRYPD
HMKQHDFFKSAMPEGYVQERTIFFKDDGNYKTRAEVKFEGDTLVNRIELKGIDFKEDGNILGHKLEYNYNSHNVYI
MADKQKNGIKVNFKIRHNIEDGSVQLADHYQQNTPIGDGPVLLPDNHYLSTQSKLSKDPNEKRDHMVLLEFVTAA
GITLGMDELYK–GSGAEF–
MTTASTSQVRQNYHQDSEAAINRQINLELYASYVYLSMSYYFDRDDVALKNFAKYFLHQSHEEREHAEKLMKLQN
QRGGRIFLQDIKKPDCDDWESGLNAMECALHLEKNVNQSLLELHKLATDKNDPHLCDFIETHYLNEQVKAIKELGD
HVTNLRKMGAPESGLAEYLFDKHTLGDSDNES*

Figure S1 – Sequence of mEGFP–Linker–HCF.

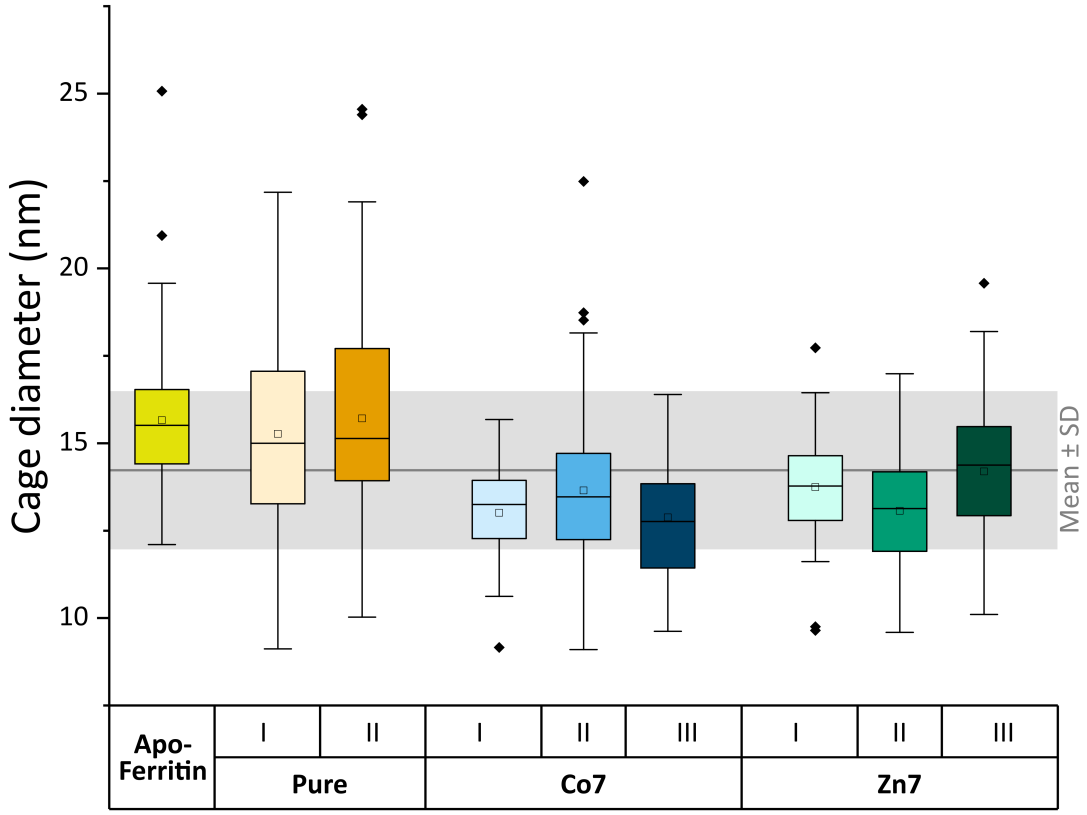

Figure S2 – Sizes of Ferritin cages.
Box plots show diameter of cages of empty Apo-Ferritin and doped Magnetoferritin of different synthesis runs (I, II, III). Mean values are shown as blank boxes, median values as horizontal lines (each N ≥ 41; for all cages: mean ± SD = 14.2 ± 2.3 nm; for all MFt cages: mean ± SD = 13.9 ± 2.2 nm).

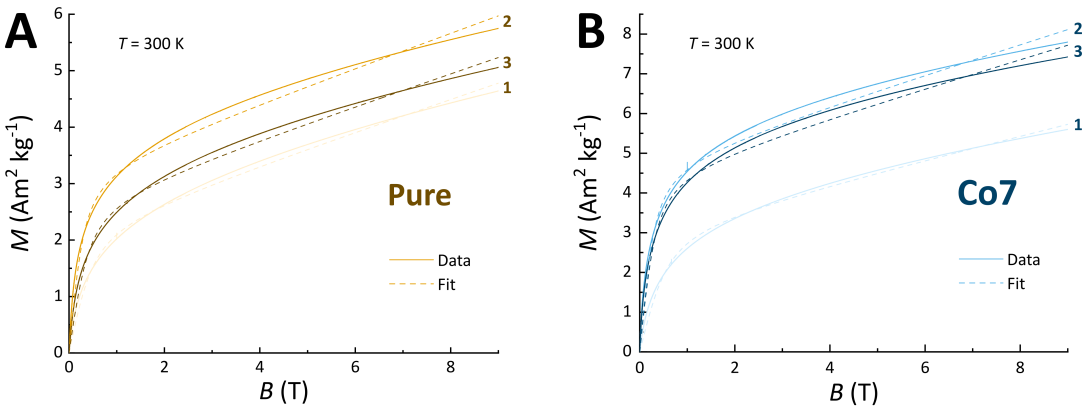

Figure S3 - Langevin Fits.
Measured magnetisation and Langevin fits of pure MFt and Co7 samples. Here, we use the Langevin function and an additional linear slope accounts for add-on contributions of salts, organics and possible antiferromagnetic contributions in the samples.

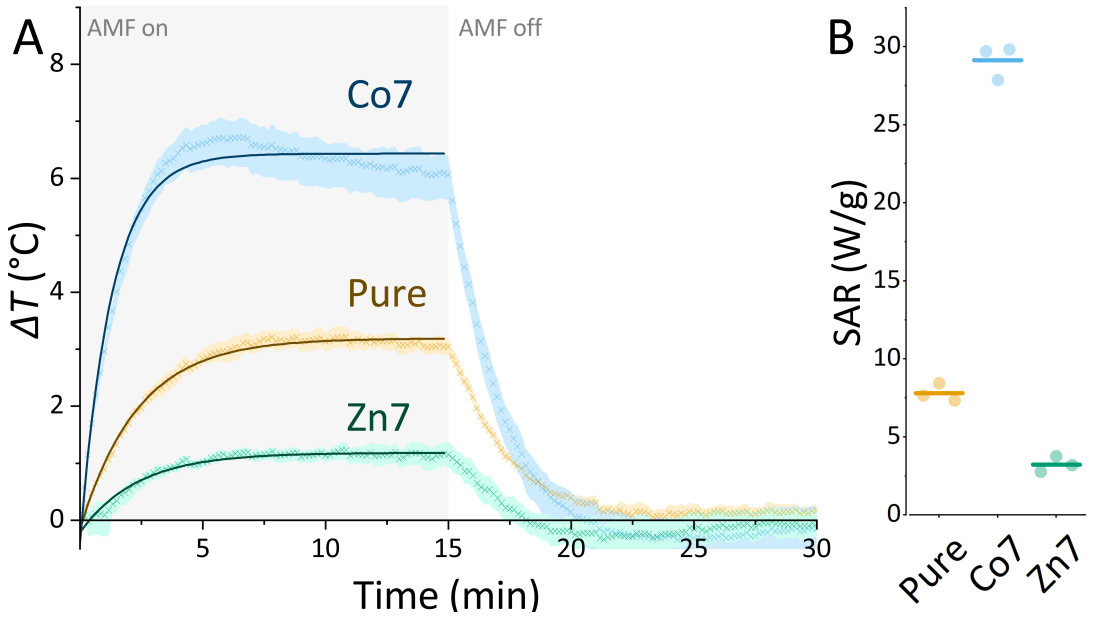

Figure S4 – Hyperthermia measurement.
(A) Temperature kinetics of Pure, Co7, and Zn7 MFt sample (each 35 µM) during exposure to the alternating magnetic field (45 mT, 104.5 kHz). Each curve is an average of three runs. The absolute temperature change ΔT refers to the temperature increase above the temperature of pure buffer solution. All MFt and buffer solution samples were measured in an identical manner. (B) Specific Absorption Rate (W/g) of each run (coloured dot) and average value (coloured line).

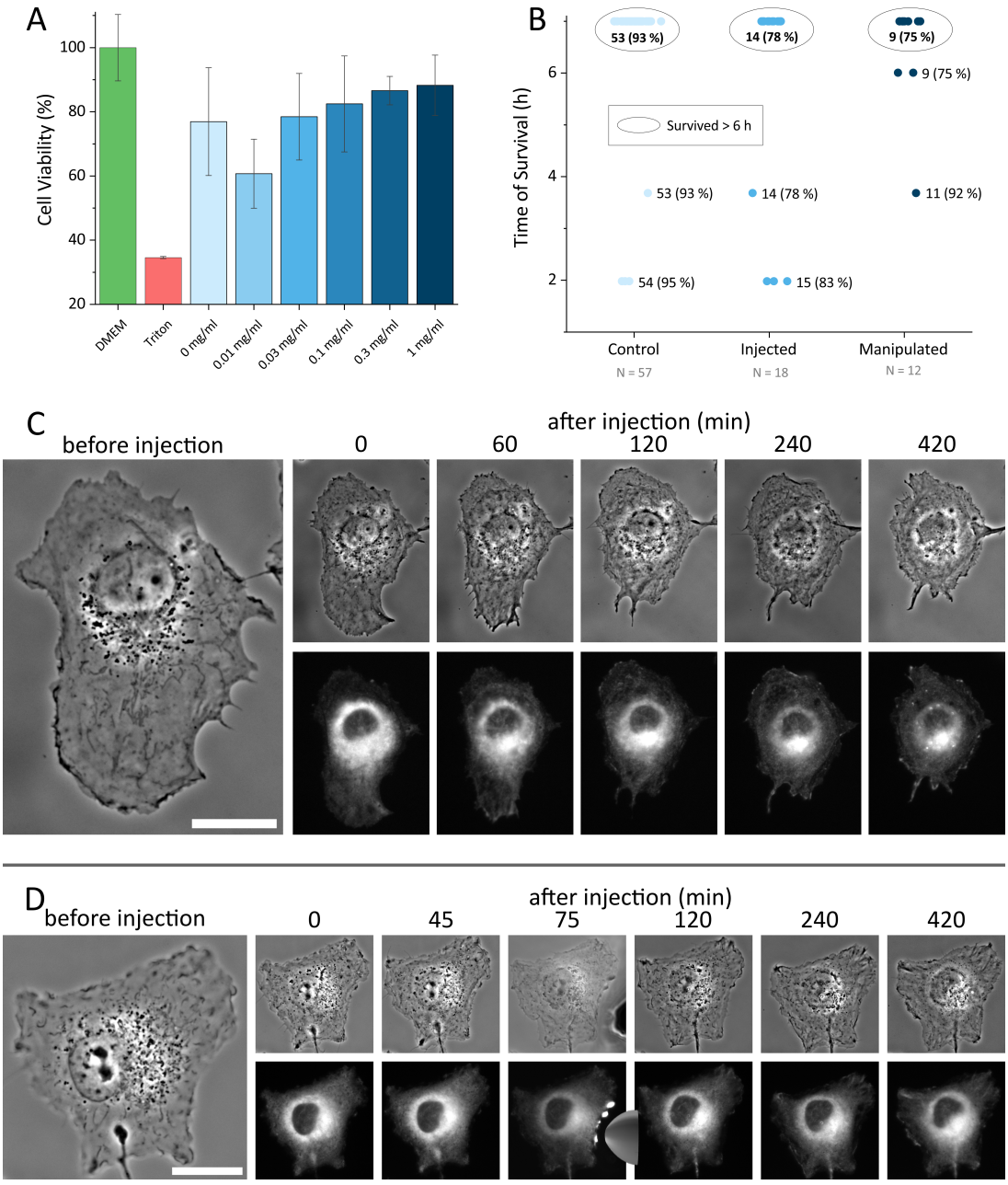

Figure S5 – Cell Viability Assays.
Biocompatibility of MFt Co7 tested in Cos7 cells. (A) CellTiter Blue assay. Cells were incubated with cell medium (DMEM) as positive control, 0.1 % Triton as negative control and several concentrations of MFt Co7 in HEPES-1 buffer (0.01 to 1 mg/ml) and with the same volume of HEPES-1 (0 mg/ml). (B) Cos7 cells were only observed ('control'), microinjected with MFt-Co7 at t = 0 h ('injected') or microinjected and magnetically manipulated for 15 min ('manipulated'). For the three conditions, 93 %, 78 %, and 75 % respectively of cells survived more than 6 h (360 min) after the beginning of the experiment/after injection (indicated by the black circle). (C) and (D) are exemplary images of Cos7 cells being (C) microinjected with MFt Co7 and observed for 420 min and (D) microinjected with MFt Co7, exposed to a magnetic stimulus after 60 min for 15 min and observed for up to 420 min. Images are taken in phase contrast (top row) and fluorescence for mEGFP (bottom row), scale bars are 20 µm.

Supplementary Tables

Table S1 – Properties of doped Magnetoferritins.
(D_H: hydrodynamic diameter, PdI: polydispersity index, both obtained from DLS measurements, ζ-Potential obtained from ELS measurements.)

Sample	Run	D_H (nm)	PdI	ζ-Potential (mV)
Pure	1	36.6 ± 1.9	0.16 ± 0.01	-5.6 ± 0.2
	2	36.8 ± 1.9	0.17 ± 0.01	-5.4 ± 0.5
	3	36.6 ± 2.2	0.16 ± 0.01	-4.4 ± 0.5
Co7	1	46.5 ± 2.5	0.16 ± 0.01	-4.7 ± 0.9
	2	45.1 ± 3.0	0.17 ± 0.01	-5.1 ± 1.6
	3	42.4 ± 3.4	0.19 ± 0.01	-4.3 ± 0.5
Zn7	1	49.9 ± 5.3	0.18 ± 0.01	-4.5 ± 0.7
	2	44.9 ± 3.1	0.17 ± 0.01	-5.1 ± 0.9
	3	35.5 ± 2.6	0.17 ± 0.01	-4.8 ± 0.8

Supplementary Videos

Video S1 – Droplet Assay with Pure MFt.
A droplet of undoped MFt was placed on a coverslip coated with PDMS. A magnetic tip consisting of a neodymium magnet with spring steel tip as described in Novoselova et al.[1] was placed at a distance of 20 µm to the edge of the droplet and left there for up to 1 h. The attraction of MFt towards the tip was recorded via the movement of mEGFP.

Video S2 – Spatial Manipulation of MFt Co7 inside a Cell.
The magnetic tip used in Video S1 is approached to a cell in which MFt Co7 was microinjected. The MFt is reversibly attracted by the magnetic field gradient emerging from the tip. The tip is placed at various positions around the cell and the particles are attracted by the tip to different sites. Particles diffuse away after tip removal within a few minutes.

Video S3 - Spatial Manipulation of MFt Co7 inside a Nucleus.
The magnetic tip used in Video S1 is approached to a cell exhibiting MFt Co7 in the cell nucleus. The MFt is reversibly attracted by the magnetic field gradient emerging from the tip. The tip is successively placed at three different positions around the cell and particles are attracted by the tip and diffuse away after tip removal within a few minutes.

1 I. P. Novoselova, A. Neusch, J. S. Brand, M. Otten, M. R. Safari, N. Bartels, M. Karg, M. Farle, U. Wiedwald and C. Monzel, *Nanomaterials*, 2021, **11**, 1–20.

Chapter V

Conclusion and Outlook

This work was settled at the interface between biology and physics, aiming to develop a toolkit for investigating cellular signalling pathways via magnetogenetics. To this end, the human iron storage protein ferritin was utilised and bioengineered in order to create a potent and versatile MNP for magnetogenetical applications.
Chapter III addressed the biological aspects of this work. In *Publication I*, we produced semisynthetic MFt NPs and compared them to commercially available magnetic multi-core NPs called Synomag®. While both MNPs were shown to possess basic properties that make them suitable for magnetogenetic applications – monodispersity, biocompatibility, fluorescence, superparamagnetism –, we could observe that MFt was more readily taken up by cells during incubation. Initially, we attributed this increased uptake to MFt's reduced size and higher ζ potential. However, it is more likely that intrinsic TfR1 – a natural ferritin receptor – internalised MFt (as described in Section II.2.1), while to our knowledge, no such pathway exists for artificial Synomag®. We could show that ferritin uptake was even enhanced in *Publication II* by overexpressing TfR1 prior to incubation. The increased presence of TfR1 on the cell led to a significant accumulation of ferritin at the cell border and its subsequent internalisation after localised incubation via microshower.
It was possible to spatially redistribute MFt inside cells after internalisation via both incubation and injection. With the help of a static magnetic gradient field emitted by a magnetic tip, it was possible to create localised MFt gradients within several minutes. Attracted MFt redistributed within minutes in the cytosol after removal of the magnetic tip. In contrast to MFt, artificial Synomag® NPs displayed significantly lower mobility, and, hence, slower accumulation and dampened redis-

tribution. This demonstrated the superior properties of MFt over artificial MNPs in intracellular studies.

MFt's performance was further tested after the introduction of cobalt-doping in *Publication IV*. Here, we could accumulate MFt both in the cytosol as well as in the cell's nucleus effectively. Hence, doping had no effect on MFt's mobility. As a next step, this technique might be used to mimic local protein concentration gradients and investigate concentration thresholds that trigger cellular signalling by targeting MFt to internal molecules and membrane-bound receptors.

However, the targeting routes we used up to this point only allowed us to focus on TfR1, while other interesting receptors stayed out of our reach. Thus, we aimed at expanding ferritin's target versatility in *Publication II*. To this end, we created a hybrid ferritin cage that combined established fluorescent subunits with newly designed subunits equipped with a minimal antibody binding domain of Protein A (see Section II.3.2.3). We showed the presence of two distinct subunits in our ferritin cages by SDS-PAGE and estimated the distribution of the subunits spectroscopically to be approximately 1 to 3 (fluorescent subunit to Protein A subunit).

To estimate the number of fluorescent subunits on our ferritin NP more precisely, *confocal photobleaching step analysis* (cPBSA)[53] might serve as an orthogonal quantification approach. Here, single ferritin cages are excited by a confocal laser while emission from the GFP subunits is detected. Bleaching events of single fluorophores due to photodamage will cause the emitted intensity to decay step by step. The number of the detected bleaching steps can then be related to the initial number of GFP subunits on the NP. However, obtaining quantitative data on the ferritin NP has been – and remained – challenging due to their biological complexity and the required sub-micrometre precision.

Nevertheless, the presence of Protein A on ferritin's surface opened the possibility of easily functionalising ferritin with IgG antibodies. We demonstrated the binding properties of ferritin to various subtypes of antibodies and determined the K_D value to be $\sim$3 nM, roughly one magnitude below previously reported K_D values for Protein A (see *Publication II*). The strong binding between ferritin and antibody allowed us to specifically target the death receptor CD95 with ferritin via an αCD95 antibody. Incubation with this construct induced cluster formation and, subsequently, apoptosis. As we demonstrated that ferritin-mediated accumulation is sufficient to induce apoptosis, the next experimental step would be to utilise antibody-labeled

MFt and a matching magnetic field to gain insights into mechanisms and thresholds that are necessary for CD95 to induce apoptosis.
While this dissertation mainly focused on characterising and manipulating single MNPs and, thus, their interaction with single receptors, the expansion of ferritin's versatility might lead to further applications on larger scales. The forces transmitted by single ferritins might be enough to manipulate single receptors, but they are insufficient for manipulating heavier structures. Therefore, it could be beneficial to couple multiple MFts to one target to apply the combined force of an MFt ensemble. With this approach, not only organelles but whole cells could be manipulated, for example, to trap circulating tumour cells from the blood of cancer patients.

Apart from the biological modification of ferritin, Chapter IV concentrated on the magnetic properties of MFt's core. With *Publication III*, we established a setup for heating MNPs using magnetic hyperthermia. To this end, we tackled the challenge of generating and sustaining AMFs ($\sim$100 kHz) with sufficient field amplitudes ($\sim$50 mT). Previously presented setups often failed to maintain these fields for longer periods due to overheating system components. However, by utilising an elaborate cooling system, we could sustain AMFs in our setup for up to 20 min.
With this setup at hand, we produced several variants of MFt in *Publication IV*. Adding cobalt and zinc during the core synthesis gave rise to MFt constructs doped with 7 % of cobalt or zinc, respectively. The magnetic properties of the iron oxide core changed drastically by adding dopant metals, as the introduced atoms altered the core's crystal structure and *e.g.* increased magnetic anisotropy. With this doping procedure, we were able to tune blocking temperature T_B, coercivity H_C, and specific absorption rates (SAR) during magnetic hyperthermia without affecting morphological or biological properties.
By probing the MFt samples in an *in vitro* droplet assay, we could quantify forces acting on single ferritin cages. Approaching our self-built magnetic tip, we were able to pull on MFt with $\sim$0.6 fN. Attraction was possible over distances of at least 100 µm, where the attractive force decrease to $\sim$0.3 fN. It is, hence, possible to fine-tune the forces acting on single MNPs by adjusting the distance between the MNP and magnetic tip. An effect on the effective force transduction by the presence of dopants in MFt's core was not observed.
However, most promisingly, cobalt doped MFt exhibited much higher T_B ($\sim$100 K

above undoped MFt) and a significant opening of the hysteresis loop at 5 K, representing the increased magnetic anisotropy of the crystal. This strongly indicated the construct's applicability as a heat mediator in magnetic hyperthermia measurements. Accordingly, cobalt-doped MFt outperformed the other MFt constructs when exposed to an AMF (93.75 kHz and 45 mT), raising sample temperatures by up to 8 K above buffer controls. Although we could show that under ideal conditions, heating rates of MFt can be significantly increased by doping, actual SAR values (up to $25\,\mathrm{W\,g^{-1}}$) fall short of Synomag® MNPs with magnetic multicores (up to $170\,\mathrm{W\,g^{-1}}$). Nevertheless, heat dissipation of our modified MFt is far superior to natural ferritin and might, therefore, be used to activate heat-sensitive ion channels. Applying doped MFt could, for example, help clarify the mechanisms behind the activation of TRPV1 via magnetic hyperthermia, which has been under discussion recently (see Section II.3.3.3 and II.3.4.3).

In final analysis, this work investigated the capabilities of engineered human ferritin as a magnetic nanoagent. Such nanoagents are a prerequisite for controlling cellular signalling pathways through magnetogenetical approaches. At the same time, exploring these pathways counts as one of the most important goals for both medical and biological research. Here, I demonstrated that – with the proper modifications – ferritin can be specifically directed to a selected target and serve as a potent mediator of both heat as well as forces to induce motion and formation of local concentration gradients. With these properties, it becomes possible to mimic pathway conditions that prevent or trigger certain diseases. Ultimately, elucidating and understanding the related signalling pathways would go miles towards treatments of a myriad of conditions that are, to this day, considered to be incurable.

List of Figures

Protein Data Bank Entries

For the creation of the depicted proteins, structures from the *Research Collaboratory for Structural Bioinformatics Protein Data Bank* (RCSB PDB) were used. Structures were downloaded and printed under the CC0 1.0 Universal (CC0 1.0) Public Domain Dedication license. Illustrations were created with Avogadro (version 1.2.0),[180] ChimeraX (version 1.8),[181] and blender (version 4.2.0, Blender Foundation, Amsterdam, Netherlands).

1IGY Antibody IgG1
Figure II.3.5 and II.3.6

2FFX Human Light Chain Ferritin
Figure II.3.8

4EUL Monomeric Enhanced Green Fluorescent Protein
Figure II.3.3 and II.3.15

5U4Y B domain of Protein A
Figure II.3.6

7LR0 Ion channel TRPV1
Figure II.3.10

8EYX Membrane Receptor (modified structure of Insulin Receptor)
Figure II.2.1 and II.3.10

FTH1 Human Heavy Chain Ferritin
Figure II.3.4, II.3.8, II.3.9, II.3.15, and in all footers

Abbreviations

Ab Antibody

AC Alternating current

AMF Alternating magnetic field

APC Allophycocyanin, a fluorphore

BSA Bovine serum albumine

CD Cluster of differentiation

CD71 Cluster of differentiation 71, see TfR1

CD95 Cluster of differentiation 95

CD95L Ligand of cluster of differentiation 95

Cos7 Fibroblast-like cell line from monkey kidney tissue

cPBSA Confocal photobleaching step analysis

CRD Cysteine-rich domain

CTB CellTiter-blue® assay

DC Direct current

DD Death domain of cluster of differentiation 95

DLS Dynamic light scattering

DLVO Derjaguin-Landau-Verwey-Overbeek (theory)

DNA Deoxyribonucleic acid

DoL Degree of labeling

DR4 Death receptor 4

DREADD Designer receptors exclusively activated by designer drugs

EDTA Ethylenediaminetetraacetic acid

EGFP Enhanced green fluorescent protein

ELS Electrophoretic light scattering

Fab Fragment antigen binding

FBS Fetal bovine serum

Fc Fragment crystallisable

Ft Human ferritin

GFP Green fluorescent protein

HC Heavy chain of an antibody

HCF Heavy chain ferritin

HeLa Immortalised cell line from Henrietta Lacks, a cervical cancer patient

IgG Immunoglobulin G

kDa Kilodalton

LC Light chain of an antibody

LCF Light chain ferritin

MDa Megadalton

mEGFP Monomeric enhanced green fluorescent protein

MFt Magnetoferritin

MNP Magnetic nanoparticle

MPN Magnetoplasmonic nanoparticle

MRI Magnetic resonance imaging

NP Nanoparticle

PAGE Polyacrylamide gel electrophoresis

PBS Phosphate-buffered saline

PDB Protein data bank

PEG Polyethylene glycol

protA Minimal functional binding domain of Protein A from *S. aureus*

RASSL Receptor activated solely by a synthetic ligand

RCSB Research collaboratory for structural bioinformatics

RF Radio frequency

RNA Ribonucleic acid

ROS Reactive oxygen species

SAR Specific absorption rate

SDS Sodium dodecyl sulfate

SI Supporting information

sMNP Small magnetic nanoparticles

SpA Protein A from *Staphylococcus aureus*

SPR Surface plasmon resonance

SQUID Superconducting quantum interference devices

TEA Triethanolamine

TEM Transmission electron microscopy

Tf Transferrin

TfR Family of transferrin receptors

TfR1 Transferrin receptor 1

TNF-R Tumour necrosis factor receptor

TRPM8 Transient receptor potential cation channel subfamily melastatin 8

TRPV1 Transient receptor potential cation channel subfamily V 1

TRPV4 Transient receptor potential cation channel subfamily V 4

VSM Vibrating sample magnetometer

Bibliography

[1] Antonio del Sol et al. "Diseases as network perturbations". In: *Current Opinion in Biotechnology* 21.4 (2010), pp. 566–571. DOI: 10.1016/j.copbio.2010.07.010 (cit. on pp. 1, 40).

[2] Jörg Haus. *Optische Mikroskopie: Funktionsweise und Kontrastierverfahren*. 1st ed. Weinheim, Germany: Wiley-VCH Verlag GmbH & Co. KGaA, 2014 (cit. on pp. 1, 30).

[3] Edward S. Boyden et al. "Millisecond-timescale, genetically targeted optical control of neural activity". In: *Nature Neuroscience* 8.9 (2005), pp. 1263–1268. DOI: 10.1038/nn1525 (cit. on pp. 2, 41).

[4] Antoine R Adamantidis et al. "Neural substrates of awakening probed with optogenetic control of hypocretin neurons". In: *Nature* 450.7168 (2007), pp. 420–424. DOI: 10.1038/nature06310 (cit. on pp. 2, 41).

[5] Étienne du Trémolet de Lacheisserie, Gignoux Damien, and Schlenker Michel, eds. *Magnetism*. New York: Springer, 2002. DOI: 10.1007/978-0-387-23062-7 (cit. on pp. 7, 8, 11, 13, 15, 17).

[6] David Halliday, Robert Resnick, and Jearl Walker. *Fundamentals of Physics*. 10. New York: Wiley & Sons, 2014, p. 1293 (cit. on pp. 8, 13, 17).

[7] Abdollah Hajalilou, Mahmoud Tavakoli, and Elahe Parvini. *Magnetic Nanoparticles*. Wiley, 2022, pp. 679–698. DOI: 10.1002/9783527840762 (cit. on pp. 8, 11, 13–15, 19, 21).

[8] Mark J. Wenzel and Gerd Steinle-Neumann. "Nonequivalence of the octahedral sites of cubic Fe_3O_4 magnetite". In: *Physical Review B* 75.21 (2007), p. 214430. DOI: 10.1103/PhysRevB.75.214430 (cit. on p. 8).

[9] Sergey P. Gubin, ed. *Magnetic Nanoparticles*. Wiley, 2009. DOI: 10.1002/9783527627561 (cit. on pp. 8, 21).

[10] Claude Fermon and Marcel Van de Voorde, eds. *Nanomagnetism: Applications and Perspectives*. Weinheim: Wiley, 2017. DOI: 10.1002/9783527698509 (cit. on pp. 10, 11, 13, 19).

[11] Q. A. Pankhurst et al. "Applications of magnetic nanoparticles in biomedicine". In: *Journal of Physics D: Applied Physics* 36.13 (2003), R167–R181. DOI: 10.1088/0022-3727/36/13/201 (cit. on p. 10).

[12] Carlo A. Gonano, Riccardo E. Zich, and Marco Mussetta. "Definition for polarization P and magnetization M fully consistent with Maxwell's Equations". In: *Progress In Electromagnetics Research B* 64.1 (2015), pp. 83–101. DOI: 10.2528/PIERB15100606 (cit. on p. 10).

[13] Abdollah Hajalilou et al. *Field Responsive Fluids as Smart Materials*. Engineering Materials. Singapore: Springer Singapore, 2016. DOI: 10.1007/978-981-10-2495-5 (cit. on pp. 11–13, 15, 18).

[14] Richard A. Flinn and Paul K. Trojan. *Engineering Materials and Their Applications*. 4th. Wiley-VCH, 1994, p. 1056 (cit. on pp. 14, 17).

[15] Lyle Patrick. "Antiferromagnetism of Manganese". In: *Physical Review* 93.3 (1954), pp. 370–370. DOI: 10.1103/PhysRev.93.370 (cit. on p. 15).

[16] Klaus Lüders. *Relativistische Physik - von der Elektrizität zur Optik*. Ed. by Gebhard Oppen. De Gruyter, 2015. DOI: 10.1515/9783110226706 (cit. on p. 15).

[17] James M. Byrne et al. "Biosynthesis of zinc substituted magnetite nanoparticles with enhanced magnetic properties". In: *Advanced Functional Materials* 24.17 (2014), pp. 2518–2529. DOI: 10.1002/adfm.201303230 (cit. on p. 16).

[18] Elvira Fantechi et al. "A smart platform for hyperthermia application in cancer treatment: Cobalt-doped ferrite nanoparticles mineralized in human ferritin cages". In: *ACS Nano* 8.5 (2014), pp. 4705–4719. DOI: 10.1021/nn500454n (cit. on pp. 16, 43).

[19] Mathias Getzlaff. *Fundamentals of Magnetism*. Berlin, Heidelberg: Springer Berlin Heidelberg, 2008. DOI: 10.1007/978-3-540-31152-2 (cit. on p. 18).

[20] An Hui Lu, E. L. Salabas, and Ferdi Schüth. "Magnetic nanoparticles: Synthesis, protection, functionalization, and application". In: *Angewandte Chemie - International Edition* 46.8 (2007), pp. 1222–1244. DOI: 10.1002/anie.200602866 (cit. on pp. 18, 20, 21).

[21] R.E. Rosensweig. "Heating magnetic fluid with alternating magnetic field". In: *Journal of Magnetism and Magnetic Materials* 252 (2002), pp. 370–374. DOI: 10.1016/S0304-8853(02)00706-0 (cit. on p. 22).

[22] S. Purushotham and R. V. Ramanujan. "Modeling the performance of magnetic nanoparticles in multimodal cancer therapy". In: *Journal of Applied Physics* 107.11 (2010), p. 114701. DOI: 10.1063/1.3432757 (cit. on p. 22).

[23] Venkatesha Narayanaswamy et al. "Role of Magnetite Nanoparticles Size and Concentration on Hyperthermia under Various Field Frequencies and Strengths". In: *Molecules* 26.4 (2021), p. 796. DOI: 10.3390/molecules26040796 (cit. on p. 22).

[24] Shuren Wang and Yanglong Hou. "New Types of Magnetic Nanoparticles for Stimuli-Responsive Theranostic Nanoplatforms". In: (2023). DOI: 10.1002/advs.202305459 (cit. on p. 22).

[25] Panagiotis Ziogas et al. "Novel Magnetic Nanohybrids: From Iron Oxide to Iron Carbide Nanoparticles Grown on Nanodiamonds". In: *Magnetochemistry* 6.4 (2020), p. 73. DOI: 10.3390/magnetochemistry6040073 (cit. on p. 22).

[26] Youngjun Ahn et al. "Progress and prospects in two-dimensional magnetism of van der Waals materials". In: *Progress in Quantum Electronics* 93.1 (2024), p. 100498. DOI: 10.1016/j.pquantelec.2024.100498. arXiv: 2401.13781 (cit. on p. 22).

[27] Bingyu Zhang et al. "2D Magnetic heterostructures: spintronics and quantum future". In: *npj Spintronics* 2.1 (2024), p. 6. DOI: 10.1038/s44306-024-00011-w (cit. on p. 22).

[28] M Gibertini et al. "Magnetic 2D materials and heterostructures". In: *Nature Nanotechnology* 14.5 (2019), pp. 408–419. DOI: 10.1038/s41565-019-0438-6 (cit. on p. 22).

[29] Swapneel Amit Pathak and Riccardo Hertel. "Geometrically Constrained Skyrmions". In: *Magnetochemistry* 7.2 (2021), p. 26. DOI: 10.3390/magnetochemistry7020026 (cit. on p. 22).

[30] X Z Yu et al. "Real-space observation of a two-dimensional skyrmion crystal". In: *Nature* 465.7300 (2010), pp. 901–904. DOI: 10.1038/nature09124 (cit. on p. 23).

[31] G.Steven Martin. "Cell signaling and cancer". In: *Cancer Cell* 4.3 (2003), pp. 167–174. DOI: 10.1016/S1535-6108(03)00216-2 (cit. on p. 23).

[32] Alfredo Ulloa-Aguirre, Teresa Zariñán, and Eduardo Jardón-Valadez. "Misfolded G Protein-Coupled Receptors and Endocrine Disease. Molecular Mechanisms and Therapeutic Prospects". In: *International Journal of Molecular Sciences* 22.22 (2021), p. 12329. DOI: 10.3390/ijms222212329 (cit. on p. 23).

[33] Kun Ping Lu. "Pinning down cell signaling, cancer and Alzheimer's disease". In: *Trends in Biochemical Sciences* 29.4 (2004), pp. 200–209. DOI: 10.1016/j.tibs.2004.02.002 (cit. on p. 23).

[34] K. Scheuer et al. "Cortical NMDA Receptor Properties and Membrane Fluidity Are Altered in Alzheimer's Disease". In: *Dementia and Geriatric Cognitive Disorders* 7.4 (1996), pp. 210–214. DOI: 10.1159/000106881 (cit. on p. 23).

[35] Tito Calì, Denis Ottolini, and Marisa Brini. "Calcium signaling in Parkinson's disease". In: *Cell and Tissue Research* 357.2 (2014), pp. 439–454. DOI: 10.1007/s00441-014-1866-0 (cit. on p. 23).

[36] Krishna A. Adeshara, Arundhati G. Diwan, and Rashmi S. Tupe. "Diabetes and Complications: Cellular Signaling Pathways, Current Understanding and Targeted Therapies". In: *Current Drug Targets* 17.11 (2016), pp. 1309–1328. DOI: 10.2174/1389450117666151209124007 (cit. on p. 23).

[37] Simon C. Andrews, Andrea K. Robinson, and Francisco Rodríguez-Quiñones. "Bacterial iron homeostasis". In: *FEMS Microbiology Reviews* 27.2-3 (2003), pp. 215–237. DOI: 10.1016/S0168-6445(03)00055-X (cit. on p. 23).

[38] Elena Gammella et al. "The transferrin receptor: The cellular iron gate". In: *Metallomics* 9.10 (2017), pp. 1367–1375. DOI: 10.1039/c7mt00143f (cit. on pp. 23, 24).

[39] Michael Schieber and Navdeep S. Chandel. "ROS Function in Redox Signaling and Oxidative Stress". In: *Current Biology* 24.10 (2014), R453–R462. DOI: 10.1016/j.cub.2014.03.034. arXiv: NIHMS150003 (cit. on p. 23).

[40] Dimitrios Galaris, Alexandra Barbouti, and Kostas Pantopoulos. "Iron homeostasis and oxidative stress: An intimate relationship". In: *Biochimica et Biophysica Acta (BBA) - Molecular Cell Research* 1866.12 (2019), p. 118535. DOI: 10.1016/j.bbamcr.2019.118535 (cit. on p. 23).

[41] Martin Merkofer et al. "Fenton Chemistry and Iron Chelation under Physiologically Relevant Conditions: Electrochemistry and Kinetics". In: *Chemical Research in Toxicology* 19.10 (2006), pp. 1263–1269. DOI: 10.1021/tx060101w (cit. on p. 23).

[42] Elizabeth C. Theil. "Ferritin protein nanocages – the story". In: *Nanotechnology Perceptions* 8.1 (2012), pp. 7–16. DOI: 10.4024/N03TH12A.ntp.08.01 (cit. on p. 23).

[43] Tracy R. Daniels et al. "The transferrin receptor and the targeted delivery of therapeutic agents against cancer". In: *Biochimica et Biophysica Acta - General Subjects* 1820.3 (2012), pp. 291–317. DOI: 10.1016/j.bbagen.2011.07.016 (cit. on p. 24).

[44] Tracy R. Daniels et al. "The transferrin receptor part I: Biology and targeting with cytotoxic antibodies for the treatment of cancer". In: *Clinical Immunology* 121.2 (2006), pp. 144–158. DOI: 10.1016/j.clim.2006.06.010 (cit. on p. 24).

[45] Pierre V Candelaria et al. "Antibodies Targeting the Transferrin Receptor 1 (TfR1) as Direct Anti-cancer Agents". In: *Frontiers in Immunology* 12 (2021), p. 607692. DOI: 10.3389/fimmu.2021.607692 (cit. on p. 24).

[46] Ahmed Essaghir and Jean-Baptiste Demoulin. "A Minimal Connected Network of Transcription Factors Regulated in Human Tumors and Its Application to the Quest for Universal Cancer Biomarkers". In: *PLoS ONE* 7.6 (2012). Ed. by Paolo Provero, e39666. DOI: 10.1371/journal.pone.0039666 (cit. on p. 24).

[47] Li Li et al. “Binding and uptake of H-ferritin are mediated by human transferrin receptor-1”. In: *Proceedings of the National Academy of Sciences of the United States of America* 107.8 (2010), pp. 3505–3510. DOI: 10.1073/pnas.0913192107 (cit. on p. 24).

[48] Joseph P. Kolb et al. “Programmed Cell Death and Inflammation: Winter Is Coming”. In: *Trends in Immunology* 38.10 (2017), pp. 705–718. DOI: 10.1016/j.it.2017.06.009 (cit. on p. 24).

[49] Peter H. Krammer. “CD95’s deadly mission in the immune system”. In: *Nature* 407.6805 (2000), pp. 789–795. DOI: 10.1038/35037728 (cit. on pp. 24, 26).

[50] Bruce Alberts et al. *Molekularbiologie der Zelle*. Weinheim, Germany: Wiley-VCH Verlag GmbH & Co. KGaA, 2017. DOI: 10.1002/9783527698448 (cit. on p. 25).

[51] Xuebo Xu, Yueyang Lai, and Zi-Chun Hua. “Apoptosis and apoptotic body: disease message and therapeutic target potentials”. In: *Bioscience Reports* 39.1 (2019), p. 20180992. DOI: 10.1042/BSR20180992 (cit. on p. 25).

[52] J Lopez and S W G Tait. “Mitochondrial apoptosis: killing cancer using the enemy within”. In: *British Journal of Cancer* 112.6 (2015), pp. 957–962. DOI: 10.1038/bjc.2015.85 (cit. on p. 25).

[53] Nina Bartels et al. “Advanced multiparametric image spectroscopy and super-resolution microscopy reveal a minimal model of CD95 signal initiation”. In: *Science Advances* 10.35 (2024), eadn3238. DOI: 10.1126/sciadv.adn3238 (cit. on pp. 26, 170).

[54] Masato Tanaka et al. “Expression of the functional soluble form of human fas ligand in activated lymphocytes.” In: *The EMBO Journal* 14.6 (1995), pp. 1129–1135. DOI: 10.1002/j.1460-2075.1995.tb07096.x (cit. on p. 26).

[55] Fiona L Scott et al. “The Fas–FADD death domain complex structure unravels signalling by receptor clustering”. In: *Nature* 457.7232 (2009), pp. 1019–1022. DOI: 10.1038/nature07606 (cit. on p. 26).

[56] Éva S Vanamee, Gábor Lippner, and Denise L Faustman. “Signal Amplification in Highly Ordered Networks Is Driven by Geometry”. In: *Cells* 11.2 (2022), p. 272. DOI: 10.3390/cells11020272 (cit. on p. 26).

[57] Éva S Vanamee and Denise L Faustman. "Structural principles of tumor necrosis factor superfamily signaling". In: *Science Signaling* 11.511 (2018), p. 4910. DOI: 10.1126/scisignal.aao4910 (cit. on p. 26).

[58] Richard P. Feynman. "There's Plenty of Room at the Bottom: An Invitation to Enter a New Field of Physics". In: *Engineering and Science* 23.5 (1960), pp. 22–36. DOI: 10.1201/9781315217178-6 (cit. on pp. 26, 30).

[59] Nadeem Joudeh and Dirk Linke. "Nanoparticle classification, physicochemical properties, characterization, and applications: a comprehensive review for biologists". In: *Journal of Nanobiotechnology* 20.1 (2022), pp. 1–29. DOI: 10.1186/s12951-022-01477-8 (cit. on p. 26).

[60] Raghuraj Singh Chouhan et al. "Emerging tri-s-triazine-based graphitic carbon nitride: A potential signal-transducing nanostructured material for sensor applications". In: *Nano Select* 2.4 (2021), pp. 712–743. DOI: 10.1002/nano.202000228 (cit. on p. 26).

[61] Muhammad Aqeel Ashraf et al. "Effects of Size and Aggregation/Agglomeration of Nanoparticles on the Interfacial/Interphase Properties and Tensile Strength of Polymer Nanocomposites". In: *Nanoscale Research Letters* 13 (2018). DOI: 10.1186/s11671-018-2624-0 (cit. on p. 27).

[62] Günter Jakob Lauth and Jürgen Kowalczyk. *Einführung in die Physik und Chemie der Grenzflächen und Kolloide*. Berlin, Heidelberg: Springer Berlin Heidelberg, 2016, pp. 409–419. DOI: 10.1007/978-3-662-47018-3 (cit. on p. 27).

[63] Claire Chassagne. *Introduction to Colloid Science*. TU Delft OPEN Publishing, 2021, p. 6. DOI: 10.34641/MG.16 (cit. on p. 29).

[64] Ajeet Kumar and Chandra Kumar Dixit. "Methods for characterization of nanoparticles". In: *Advances in Nanomedicine for the Delivery of Therapeutic Nucleic Acids* (2017), pp. 44–58. DOI: 10.1016/B978-0-08-100557-6.00003-1 (cit. on p. 29).

[65] Víctor Agmo Hernández. "An overview of surface forces and the DLVO theory". In: *ChemTexts* 9.4 (2023), p. 10. DOI: 10.1007/s40828-023-00182-9 (cit. on p. 30).

[66] Francesco M Veronese and Gianfranco Pasut. "PEGylation, successful approach to drug delivery". In: *Drug Discovery Today* 10.21 (2005), pp. 1451–1458. DOI: 10.1016/S1359-6446(05)03575-0 (cit. on p. 30).

[67] Alok Dhawan et al. *Nanobiotechnology*. Ed. by Alok Dhawan et al. Boca Raton : Taylor & Francis, 2018.: CRC Press, 2018, p. 513. DOI: 10.1201/9781351031585 (cit. on p. 30).

[68] Osamu Shimomura, Frank H Johnson, and Yo Saiga. "Extraction, Purification and Properties of Aequorin, a Bioluminescent Protein from the Luminous Hydromedusan, *Aequorea*". In: *Journal of Cellular and Comparative Physiology* 59.3 (1962), pp. 223–239. DOI: 10.1002/jcp.1030590302 (cit. on p. 31).

[69] Douglas C. Prasher et al. "Primary structure of the *Aequorea victoria* green-fluorescent protein". In: *Gene* 111.2 (1992), pp. 229–233. DOI: 10.1016/0378-1119(92)90691-H (cit. on p. 31).

[70] John F Morrow et al. "Replication and Transcription of Eukaryotic DNA in *Escherichia coli*". In: *Proceedings of the National Academy of Sciences* 71.5 (1974), pp. 1743–1747. DOI: 10.1073/pnas.71.5.1743 (cit. on p. 31).

[71] S James Remington. "Green fluorescent protein: A perspective". In: *Protein Science* 20.9 (2011), pp. 1509–1519. DOI: 10.1002/pro.684 (cit. on pp. 31, 32).

[72] William W. Ward et al. "Spectrophotometric Identity of the Energy Transfer Chromophores in *Renilla* and *Aequorea* Green-Fluorescent Proteins". In: *Photochemistry and Photobiology* 31.6 (1980), pp. 611–615. DOI: 10.1111/j.1751-1097.1980.tb03755.x (cit. on p. 32).

[73] Wiesława Widłak, ed. *Molecular Biology*. Vol. 8248. Lecture Notes in Computer Science. Berlin, Heidelberg: Springer Berlin Heidelberg, 2013. DOI: 10.1007/978-3-642-45361-8 (cit. on p. 32).

[74] T.-T. Yang, Linzhao Cheng, and Steven R Kain. "Optimized Codon Usage and Chromophore Mutations Provide Enhanced Sensitivity with the Green Fluorescent Protein". In: *Nucleic Acids Research* 24.22 (1996), pp. 4592–4593. DOI: 10.1093/nar/24.22.4592 (cit. on p. 33).

[75] Roger Heim, D C Prasher, and Roger Y Tsien. "Wavelength mutations and posttranslational autoxidation of green fluorescent protein." In: *Proceedings of the National Academy of Sciences* 91.26 (1994), pp. 12501–12504. DOI: 10.1073/pnas.91.26.12501 (cit. on p. 33).

[76] Jürgen Haas, Eun-Chung Park, and Brian Seed. "Codon usage limitation in the expression of HIV-1 envelope glycoprotein". In: *Current Biology* 6.3 (1996), pp. 315–324. DOI: 10.1016/S0960-9822(02)00482-7 (cit. on p. 33).

[77] David A. Zacharias et al. "Partitioning of Lipid-Modified Monomeric GFPs into Membrane Microdomains of Live Cells". In: *Science* 296.5569 (2002), pp. 913–916. DOI: 10.1126/science.1068539 (cit. on p. 33).

[78] Marc Zimmer. "GFP: from jellyfish to the Nobel prize and beyond". In: *Chemical Society Reviews* 38.10 (2009), p. 2823. DOI: 10.1039/b904023d (cit. on p. 33).

[79] Y A Labas et al. "Diversity and evolution of the green fluorescent protein family". In: *Proceedings of the National Academy of Sciences* 99.7 (2002), pp. 4256–4261. DOI: 10.1073/pnas.062552299 (cit. on p. 33).

[80] Nathan C Shaner et al. "Improved monomeric red, orange and yellow fluorescent proteins derived from *Discosoma* sp. red fluorescent protein". In: *Nature Biotechnology* 22.12 (2004), pp. 1567–1572. DOI: 10.1038/nbt1037 (cit. on p. 33).

[81] Umberto Oreste, Alessia Ametrano, and Maria Rosaria Coscia. "On Origin and Evolution of the Antibody Molecule". In: *Biology* 10.2 (2021), p. 140. DOI: 10.3390/biology10020140 (cit. on p. 33).

[82] Kenneth Murphy and Casey Weaver. *Janeway Immunologie*. Vol. 10. 2. Berlin, Heidelberg: Springer Berlin Heidelberg, 2018, p. 140. DOI: 10.1007/978-3-662-56004-4 (cit. on p. 34).

[83] Stefan Dübel et al. *Rekombinante Antikörper*. Berlin, Heidelberg: Springer Berlin Heidelberg, 2019. DOI: 10.1007/978-3-662-50276-1 (cit. on pp. 34–36).

[84] S.C. Kuo and D.A. Lauffenburger. "Relationship between receptor ligand binding affinity and adhesion strength". In: *Biophysical Journal* 65.5 (1993), pp. 2191–2200. DOI: 10.1016/S0006-3495(93)81277-3 (cit. on p. 34).

[85] Alex Bear et al. “The immune evasion roles of *Staphylococcus aureus* protein A and impact on vaccine development”. In: *Frontiers in Cellular and Infection Microbiology* 13 (2023). DOI: 10.3389/fcimb.2023.1242702 (cit. on p. 36).

[86] Sophia Hober, Karin Nord, and Martin Linhult. “Protein A chromatography for antibody purification”. In: *Journal of Chromatography B* 848.1 (2007), pp. 40–47. DOI: 10.1016/j.jchromb.2006.09.030 (cit. on p. 36).

[87] Marc Graille et al. “Crystal structure of a Staphylococcus aureus protein A domain complexed with the Fab fragment of a human IgM antibody: Structural basis for recognition of B-cell receptors and superantigen activity”. In: *Proceedings of the National Academy of Sciences* 97.10 (2000), pp. 5399–5404. DOI: 10.1073/pnas.97.10.5399 (cit. on p. 36).

[88] David P. Clark and Nanette J. Pazdernik. *Molekulare Biotechnologie*. Vol. 7. 2. Heidelberg: Spektrum Akademischer Verlag, 2009. DOI: 10.1007/978-3-8274-2189-0 (cit. on p. 37).

[89] Fabiana Falugi et al. “Role of Protein A in the Evasion of Host Adaptive Immune Responses by *Staphylococcus aureus*”. In: *mBio* 4.5 (2013). Ed. by Michael S. Gilmore. DOI: 10.1128/mBio.00575-13 (cit. on p. 37).

[90] Tomas Moks et al. “Staphylococcal protein A consists of five IgG-binding domains”. In: *European Journal of Biochemistry* 156.3 (1986), pp. 637–643. DOI: 10.1111/j.1432-1033.1986.tb09625.x (cit. on p. 37).

[91] Björn Nilsson et al. “A synthetic IgG-binding domain based on staphylococcal protein A”. In: *Protein Engineering, Design and Selection* 1.2 (1987), pp. 107–113. DOI: 10.1093/protein/1.2.107 (cit. on p. 37).

[92] Andrew C. Braisted and James A. Wells. “Minimizing a binding domain from protein A”. In: *Proceedings of the National Academy of Sciences of the United States of America* 93.12 (1996), pp. 5688–5692. DOI: 10.1073/pnas.93.12.5688 (cit. on p. 37).

[93] Lena Cedergren et al. “Mutational analysis of the interaction between staphylococcal protein A and human IgG 1”. In: *”Protein Engineering, Design and Selection”* 6.4 (1993), pp. 441–448. DOI: 10.1093/protein/6.4.441 (cit. on p. 38).

[94] Mikail D. Levasseur et al. “Cell-Specific Delivery Using an Engineered Protein Nanocage”. In: *ACS Chemical Biology* 16.5 (2021), pp. 838–843. DOI: 10.1021/acschembio.1c00007 (cit. on p. 38).

[95] Abhinav Mohanty et al. “Ferritin: A Promising Nanoreactor and Nanocarrier for Bionanotechnology”. In: *ACS Bio and Med Chem Au* 2.3 (2022), pp. 258–281. DOI: 10.1021/acsbiomedchemau.2c00003 (cit. on pp. 38, 39, 49, 50).

[96] Abhinav Mohanty et al. “Iron Mineralizing Bacterioferritin A from *Mycobacterium tuberculosis* Exhibits Unique Catalase-Dps-like Dual Activities”. In: *Inorganic Chemistry* 58.8 (2019), pp. 4741–4752. DOI: 10.1021/acs.inorgchem.8b02758 (cit. on p. 38).

[97] Elizabeth C. Theil, Rabindra K. Behera, and Takehiko Tosha. “Ferritins for chemistry and for life”. In: *Coordination Chemistry Reviews* 257.2 (2013), pp. 579–586. DOI: 10.1016/j.ccr.2012.05.013 (cit. on p. 38).

[98] Günther Jutz et al. “Ferritin: A versatile building block for bionanotechnology”. In: *Chemical Reviews* 115.4 (2015), pp. 1653–1701. DOI: 10.1021/cr400011b (cit. on pp. 38, 39).

[99] David M. Lawson et al. “Solving the structure of human H ferritin by genetically engineering intermolecular crystal contacts”. In: *Nature* 349.6309 (1991), pp. 541–544. DOI: 10.1038/349541a0 (cit. on p. 39).

[100] Vanessa J. Wade et al. “Influence of site-directed modifications on the formation of iron cores in ferritin”. In: *Journal of Molecular Biology* 221.4 (1991), pp. 1443–1452. DOI: 10.1016/0022-2836(91)90944-2 (cit. on p. 39).

[101] A. Treffry et al. “Defining the roles of the threefold channels in iron uptake, iron oxidation and iron-core formation in ferritin: a study aided by site-directed mutagenesis”. In: *Biochemical Journal* 296.3 (1993), pp. 721–728. DOI: 10.1042/bj2960721 (cit. on p. 39).

[102] Rabindra K Behera et al. “Fe^{2+} substrate transport through ferritin protein cage ion channels influences enzyme activity and biomineralization”. In: *JBIC Journal of Biological Inorganic Chemistry* 20.6 (2015), pp. 957–969. DOI: 10.1007/s00775-015-1279-x (cit. on p. 39).

[103] V. A. Drits et al. “Structural Model for Ferrihydrite”. In: *Clay Minerals* 28.2 (1993), pp. 185–207. DOI: 10.1180/claymin.1993.028.2.02 (cit. on p. 39).

[104] F. Marc Michel et al. “The Structure of Ferrihydrite, a Nanocrystalline Material”. In: *Science* 316.5832 (2007), pp. 1726–1729. DOI: 10.1126/science.1142525. arXiv: science.1142525 [10.1126] (cit. on p. 39).

[105] A. García-Prieto et al. “On the mineral core of ferritin-like proteins: structural and magnetic characterization”. In: *Nanoscale* 8.2 (2016), pp. 1088–1099. DOI: 10.1039/C5NR04446D (cit. on p. 39).

[106] Jianxuan Zhang, Ning Zheng, and Pengbo Zhou. “Exploring the functional complexity of cellular proteins by protein knockout”. In: *Proceedings of the National Academy of Sciences* 100.24 (2003), pp. 14127–14132. DOI: 10.1073/pnas.2233012100 (cit. on p. 40).

[107] Gregory Prelich. “Gene Overexpression: Uses, Mechanisms, and Interpretation”. In: *Genetics* 190.3 (2012), pp. 841–854. DOI: 10.1534/genetics.111.136911 (cit. on p. 40).

[108] Bryan L. Roth. “DREADDs for Neuroscientists”. In: *Neuron* 89.4 (2016), pp. 683–694. DOI: 10.1016/j.neuron.2016.01.040 (cit. on p. 41).

[109] Blaine N Armbruster et al. “Evolving the lock to fit the key to create a family of G protein-coupled receptors potently activated by an inert ligand”. In: *Proceedings of the National Academy of Sciences* 104.12 (2007), pp. 5163–5168. DOI: 10.1073/pnas.0700293104 (cit. on p. 41).

[110] Karl Deisseroth. “Optogenetics”. In: *Nature Methods* 8.1 (2011), pp. 26–29. DOI: 10.1038/nmeth.f.324 (cit. on p. 41).

[111] Ofer Yizhar et al. “Optogenetics in Neural Systems”. In: *Neuron* 71.1 (2011), pp. 9–34. DOI: 10.1016/j.neuron.2011.06.004 (cit. on p. 41).

[112] Marc Clement, Gwenaelle Daniel, and Mario Trelles. “Optimising the design of a broad-band light source for the treatment of skin”. In: *Journal of Cosmetic and Laser Therapy* 7.3-4 (2005), pp. 177–189. DOI: 10.1080/14764170500344575 (cit. on p. 41).

[113] Anastasiia A. Latypova et al. “Magnetogenetics as a promising tool for controlling cellular signaling pathways”. In: *Journal of Nanobiotechnology* 22.1 (2024), p. 327. DOI: 10.1186/s12951-024-02616-z (cit. on p. 41).

[114] Jung-uk Lee et al. “Non-contact long-range magnetic stimulation of mechanosensitive ion channels in freely moving animals”. In: *Nature Materials* 20.7 (2021), pp. 1029–1036. DOI: 10.1038/s41563-020-00896-y (cit. on pp. 42, 43).

[115] Fred Etoc et al. “Magnetogenetic Control of Protein Gradients Inside Living Cells with High Spatial and Temporal Resolution”. In: *Nano Letters* 15.5 (2015), pp. 3487–3494. DOI: 10.1021/acs.nanolett.5b00851 (cit. on pp. 42, 47).

[116] Domenik Liße et al. “Engineered Ferritin for Magnetogenetic Manipulation of Proteins and Organelles Inside Living Cells”. In: *Advanced Materials* 29.42 (2017), pp. 1–7. DOI: 10.1002/adma.201700189 (cit. on pp. 42, 43, 50, 56).

[117] Greta Jarockyte et al. “Accumulation and Toxicity of Superparamagnetic Iron Oxide Nanoparticles in Cells and Experimental Animals”. In: *International Journal of Molecular Sciences* 17.8 (2016), p. 1193. DOI: 10.3390/ijms17081193 (cit. on p. 42).

[118] Alexey V. Yaremenko et al. “Influence of magnetic nanoparticle biotransformation on contrasting efficiency and iron metabolism”. In: *Journal of Nanobiotechnology* 20.1 (2022), p. 535. DOI: 10.1186/s12951-022-01742-w (cit. on p. 42).

[119] Aziz B. Mirkasymov et al. “Macrophage blockade using nature-inspired ferrihydrite for enhanced nanoparticle delivery to tumor”. In: *International Journal of Pharmaceutics* 621.March (2022), p. 121795. DOI: 10.1016/j.ijpharm.2022.121795 (cit. on p. 42).

[120] Hendrik Schöneborn et al. “Novel Tools towards Magnetic Guidance of Neurite Growth: (I) Guidance of Magnetic Nanoparticles into Neurite Extensions of Induced Human Neurons and *In Vitro* Functionalization with RAS Regulating Proteins”. In: *Journal of Functional Biomaterials* 10.3 (2019), p. 32. DOI: 10.3390/jfb10030032 (cit. on pp. 43, 44).

[121] F. Etoc et al. “Subcellular control of Rac-GTPase signalling by magnetogenetic manipulation inside living cells”. In: *Nature Nanotechnology* 8.3 (2013), pp. 193–198. DOI: 10.1038/nnano.2013.23 (cit. on pp. 43, 44, 47).

[122] D. A. Resnick et al. "Magnetic properties of Co_3O_4 nanoparticles mineralized in *Listeria innocua* Dps". In: *Journal of Applied Physics* 99.8 (2006), pp. 2006–2008. DOI: 10.1063/1.2163839 (cit. on p. 43).

[123] Fiona C. Meldrum, Brigid R. Heywood, and Stephen Mann. "Magnetoferritin: *in vitro* synthesis of a novel magnetic protein". In: *Science* 257.5069 (1992), pp. 522–523. DOI: 10.1126/science.1636086 (cit. on pp. 43, 50, 51).

[124] Cornelia Monzel et al. "Magnetic control of cellular processes using biofunctional nanoparticles". In: *Chemical Science* 8.11 (2017), pp. 7330–7338. DOI: 10.1039/c7sc01462g (cit. on p. 43).

[125] Andreas Neusch et al. "Semisynthetic ferritin-based nanoparticles with high magnetic anisotropy for spatial magnetic manipulation and inductive heating". In: *Nanoscale* 16.32 (2024), pp. 15113–15127. DOI: 10.1039/D4NR01652A (cit. on p. 43).

[126] Gabriela Romero et al. "Modulating cell signalling *in vivo* with magnetic nanotransducers". In: *Nature Reviews Methods Primers* 2.1 (2022), p. 92. DOI: 10.1038/s43586-022-00170-2 (cit. on p. 43).

[127] Solenne Fleutot et al. "Spacing-dependent dipolar interactions in dendronized magnetic iron oxide nanoparticle 2D arrays and powders". In: *Nanoscale* 5.4 (2013), p. 1507. DOI: 10.1039/c2nr32117c (cit. on p. 44).

[128] Mahendran Subramanian et al. "Remote manipulation of magnetic nanoparticles using magnetic field gradient to promote cancer cell death". In: *Applied Physics A* 125.4 (2019), p. 226. DOI: 10.1007/s00339-019-2510-3 (cit. on p. 44).

[129] Steven Hughes et al. "Selective activation of mechanosensitive ion channels using magnetic particles". In: *Journal of The Royal Society Interface* 5.25 (2008), pp. 855–863. DOI: 10.1098/rsif.2007.1274 (cit. on pp. 44, 45).

[130] Amanda J. Patel, Michel Lazdunski, and Eric Honoré. "Lipid and mechanogated 2P domain K^+ channels". In: *Current Opinion in Cell Biology* 13.4 (2001), pp. 422–428. DOI: 10.1016/S0955-0674(00)00231-3 (cit. on p. 44).

[131] Mi Hyeon Cho et al. "A magnetic switch for the control of cell death signalling in *in vitro* and *in vivo* systems". In: *Nature Materials* 11.12 (2012), pp. 1038–1043. DOI: 10.1038/nmat3430 (cit. on pp. 45, 46).

[132] Michael Rotherham and Alicia J. El Haj. "Remote Activation of the Wnt/β-Catenin Signalling Pathway Using Functionalised Magnetic Particles". In: *PLOS ONE* 10.3 (2015). Ed. by Shao-Jun Tang, e0121761. DOI: 10.1371/journal.pone.0121761 (cit. on p. 46).

[133] Michael Rotherham et al. "Remote regulation of magnetic particle targeted Wnt signaling for bone tissue engineering". In: *Nanomedicine: Nanotechnology, Biology and Medicine* 14.1 (2018), pp. 173–184. DOI: 10.1016/j.nano.2017.09.008 (cit. on p. 46).

[134] Andy Tay and Dino Di Carlo. "Magnetic Nanoparticle-Based Mechanical Stimulation for Restoration of Mechano-Sensitive Ion Channel Equilibrium in Neural Networks". In: *Nano Letters* 17.2 (2017), pp. 886–892. DOI: 10.1021/acs.nanolett.6b04200 (cit. on p. 47).

[135] Daeha Seo et al. "A Mechanogenetic Toolkit for Interrogating Cell Signaling in Space and Time". In: *Cell* 165.6 (2016), pp. 1507–1518. DOI: 10.1016/j.cell.2016.04.045 (cit. on pp. 47, 48).

[136] Craig D. Buckley et al. "The minimal cadherin-catenin complex binds to actin filaments under force". In: *Science* 346.6209 (2014). DOI: 10.1126/science.1254211 (cit. on p. 48).

[137] Raphael Kopan and Ma Xenia G. Ilagan. "The Canonical Notch Signaling Pathway: Unfolding the Activation Mechanism". In: *Cell* 137.2 (2009), pp. 216–233. DOI: 10.1016/j.cell.2009.03.045 (cit. on p. 48).

[138] Heng Huang et al. "Remote control of ion channels and neurons through magnetic-field heating of nanoparticles". In: *Nature Nanotechnology* 5.8 (2010), pp. 602–606. DOI: 10.1038/nnano.2010.125 (cit. on pp. 48, 49, 54).

[139] Michael J Caterina et al. "The capsaicin receptor: a heat-activated ion channel in the pain pathway". In: *Nature* 389.6653 (1997), pp. 816–824. DOI: 10.1038/39807 (cit. on p. 48).

[140] Makoto Tominaga et al. "The Cloned Capsaicin Receptor Integrates Multiple Pain-Producing Stimuli". In: *Neuron* 21.3 (1998), pp. 531–543. DOI: 10.1016/S0896-6273(00)80564-4 (cit. on p. 48).

[141] Dekel Rosenfeld et al. "Transgene-free remote magnetothermal regulation of adrenal hormones". In: *Science Advances* 6.15 (2020), pp. 1–11. DOI: 10.1126/sciadv.aaz3734 (cit. on pp. 48, 49).

[142] Scott A Kinlein, Christopher D Wilson, and Ilia N Karatsoreos. "Dysregulated hypothalamic-pituitary-adrenal axis function contributes to altered endocrine and neurobehavioral responses to acute stress". In: *Frontiers in Psychiatry* 6 (2015). DOI: 10.3389/fpsyt.2015.00031 (cit. on p. 49).

[143] Jae-Woo Kim et al. "Cobalt oxide hollow nanoparticles derived by bio-templating". In: *Chemical Communications* 32 (2005), p. 4101. DOI: 10.1039/b505097a (cit. on p. 49).

[144] Takehiko Tosha et al. "Moving Metal Ions through Ferritin-Protein Nanocages from Three-Fold Pores to Catalytic Sites". In: *Journal of the American Chemical Society* 132.41 (2010), pp. 14562–14569. DOI: 10.1021/ja105583d (cit. on p. 49).

[145] Kenji Iwahori et al. "Fabrication of ZnSe Nanoparticles in the Apoferritin Cavity by Designing a Slow Chemical Reaction System". In: *Inorganic Chemistry* 44.18 (2005), pp. 6393–6400. DOI: 10.1021/ic0502426 (cit. on p. 49).

[146] Basudev Maity, Kenta Fujita, and Takafumi Ueno. "Use of the confined spaces of apo-ferritin and virus capsids as nanoreactors for catalytic reactions". In: *Current Opinion in Chemical Biology* 25 (2015), pp. 88–97. DOI: 10.1016/j.cbpa.2014.12.026 (cit. on p. 49).

[147] Simonetta Stefanini et al. "Thermal Stability of Horse Spleen Apoferritin and Human Recombinant H Apoferritin". In: *Archives of Biochemistry and Biophysics* 325.1 (1996), pp. 58–64. DOI: 10.1006/abbi.1996.0007 (cit. on p. 50).

[148] Maria C. Linder et al. "Dissociation of ferritins". In: *Archives of Biochemistry and Biophysics* 269.2 (1989), pp. 485–496. DOI: 10.1016/0003-9861(89)90132-X (cit. on p. 50).

[149] Bruce M Moskowitz et al. "Determination of the preexponential frequency factor for superparamagnetic maghemite particles in magnetoferritin". In: *Journal of Geophysical Research: Solid Earth* 102.B10 (1997), pp. 22671–22680. DOI: 10.1029/97JB01698 (cit. on pp. 50, 51).

[150] Togar Saragi et al. "Blocking temperature of magnetite nanoparticles Fe_3O_4 encapsulated silicon dioxide SiO_2". In: *Key Engineering Materials* 855.1 (2020), pp. 172–176. DOI: 10.4028/www.scientific.net/KEM.855.172 (cit. on p. 51).

[151] Kim K W Wong et al. "Biomimetic Synthesis and Characterization of Magnetic Proteins (Magnetoferritin)". In: *Chemistry of Materials* 10.1 (1998), pp. 279–285. DOI: 10.1021/cm970421o (cit. on p. 51).

[152] Krishan Kumar. "Iron Assay and Size Exclusion High Performance Liquid Chromatography of Ferritin and Magnetoferritin". In: *Journal of Liquid Chromatography & Related Technologies* 20.20 (1997), pp. 3351–3364. DOI: 10.1080/10826079708005836 (cit. on p. 51).

[153] Fabio E. Furcas et al. "Solubility and speciation of iron in cementitious systems". In: *Cement and Concrete Research* 151.October (2022), p. 106620. DOI: 10.1016/j.cemconres.2021.106620 (cit. on p. 51).

[154] Masaki Uchida et al. "Targeting of cancer cells with ferrimagnetic ferritin cage nanoparticles". In: *Journal of the American Chemical Society* 128.51 (2006), pp. 16626–16633. DOI: 10.1021/ja0655690 (cit. on p. 51).

[155] M Gerl and R Jaenicke. "Mechanism of the self-assembly of apoferritin from horse spleen". In: *European Biophysics Journal* 15.2 (1987), pp. 103–109. DOI: 10.1007/BF00257503 (cit. on p. 52).

[156] B. Webb et al. "Molecular Entrapment of Small Molecules within the Interior of Horse Spleen Ferritin". In: *Archives of Biochemistry and Biophysics* 309.1 (1994), pp. 178–183. DOI: 10.1006/abbi.1994.1100 (cit. on p. 52).

[157] Mihee Kim et al. "pH-dependent structures of ferritin and apoferritin in solution: Disassembly and reassembly". In: *Biomacromolecules* 12.5 (2011), pp. 1629–1640. DOI: 10.1021/bm200026v (cit. on p. 52).

[158] Minmin Liang et al. "H-ferritin–nanocaged doxorubicin nanoparticles specifically target and kill tumors with a single-dose injection". In: *Proceedings of the National Academy of Sciences* 111.41 (2014), pp. 14900–14905. DOI: 10.1073/pnas.1407808111 (cit. on p. 52).

[159] Yuanjun Zhu et al. "Ferritin-based nanomedicine for disease treatment". In: *Medical Review* 3.1 (2023), pp. 49–74. DOI: 10.1515/mr-2023-0001 (cit. on p. 52).

[160] Luca Conti et al. “Ferritin nanocomposites for the selective delivery of photosensitizing ruthenium-polypyridyl compounds to cancer cells”. In: *Inorganic Chemistry Frontiers* 9.6 (2022), pp. 1070–1081. DOI: 10.1039/D1QI01268A (cit. on p. 52).

[161] Nicola Pontillo et al. “Cisplatin encapsulation within a ferritin nanocage: a high-resolution crystallographic study”. In: *Chemical Communications* 52.22 (2016), pp. 4136–4139. DOI: 10.1039/C5CC10365G (cit. on p. 52).

[162] Dan Fu et al. “Self-assembling nanoparticle engineered from the ferritinophagy complex as a rabies virus vaccine candidate”. In: *Nature Communications* 15.1 (2024), p. 8601. DOI: 10.1038/s41467-024-52908-z (cit. on p. 52).

[163] Yongli Zhang et al. “Development of T follicular helper cell-independent nanoparticle vaccines for SARS-CoV-2 or HIV-1 by targeting ICOSL”. In: *npj Vaccines* 9.1 (2024), p. 176. DOI: 10.1038/s41541-024-00971-4 (cit. on p. 52).

[164] Wei Zheng et al. “Recombinant ferritin-based nanoparticles as neoantigen carriers significantly inhibit tumor growth and metastasis”. In: *Journal of Nanobiotechnology* 22.1 (2024), p. 562. DOI: 10.1186/s12951-024-02837-2 (cit. on p. 52).

[165] Xiao Yin et al. “Simultaneous determination of two phosphorylated p53 proteins in SCC-7 cells by an ICP-MS immunoassay using apoferritin-templated europium(III) and lutetium(III) phosphate nanoparticles as labels”. In: *Microchimica Acta* 186.7 (2019), p. 424. DOI: 10.1007/s00604-019-3540-4 (cit. on p. 53).

[166] Fatemeh Nasrollahi et al. “Incorporation of Graphene Quantum Dots, Iron, and Doxorubicin in/on Ferritin Nanocages for Bimodal Imaging and Drug Delivery”. In: *Advanced Therapeutics* 3.3 (2020). DOI: 10.1002/adtp.201900183 (cit. on p. 53).

[167] Silvio Aime, Luca Frullano, and Simonetta Geninatti Crich. “Compartmentalization of a Gadolinium Complex in the Apoferritin Cavity: A Route To Obtain High Relaxivity Contrast Agents for Magnetic Resonance Imaging”. In: *Angewandte Chemie International Edition* 41.6 (2002), pp. 1017–1019. DOI: https://doi.org/10.1002/1521-3773(20020315)41:6⟨1017::AID-ANIE1017⟩3.0.CO;2-P (cit. on p. 53).

[168] Yao Cai et al. “Positive magnetic resonance angiography using ultrafine ferritin-based iron oxide nanoparticles”. In: *Nanoscale* 11.6 (2019), pp. 2644–2654. DOI: 10.1039/C8NR06812G (cit. on p. 53).

[169] S Kanbak-Aksu et al. “Ferritin-supported palladium nanoclusters: selective catalysts for aerobic oxidations in water”. In: *Chemical Communications* 48.46 (2012), p. 5745. DOI: 10.1039/c2cc31401k (cit. on p. 53).

[170] Takafumi Ueno et al. “Size-Selective Olefin Hydrogenation by a Pd Nanocluster Provided in an Apo-Ferritin Cage”. In: *Angewandte Chemie International Edition* 43.19 (2004), pp. 2527–2530. DOI: 10.1002/anie.200353436 (cit. on p. 53).

[171] N Matsukawa et al. “Hexagonal Close-Packed Array Formed by Selective Adsorption onto Hexagonal Patterns”. In: *Langmuir* 25.6 (2009), pp. 3327–3330. DOI: 10.1021/la8032012 (cit. on p. 53).

[172] Michael A Wheeler et al. “Genetically targeted magnetic control of the nervous system”. In: *Nature Neuroscience* 19.5 (2016), pp. 756–761. DOI: 10.1038/nn.4265 (cit. on pp. 53, 54).

[173] Stephen Loukin et al. “Wild-type and Brachyolmia-causing Mutant TRPV4 Channels Respond Directly to Stretch Force”. In: *Journal of Biological Chemistry* 285.35 (2010), pp. 27176–27181. DOI: 10.1074/jbc.M110.143370 (cit. on p. 53).

[174] Sarah A. Stanley et al. “Remote regulation of glucose homeostasis in mice using genetically encoded nanoparticles”. In: *Nature Medicine* 21.1 (2015), pp. 92–98. DOI: 10.1038/nm.3730 (cit. on p. 54).

[175] Markus Meister. “Physical limits to magnetogenetics”. In: *eLife* 5 (2016), pp. 1–14. DOI: 10.7554/eLife.17210. arXiv: 1604.01359 (cit. on p. 54).

[176] Hunter C. Davis et al. “Nanoscale Heat Transfer from Magnetic Nanoparticles and Ferritin in an Alternating Magnetic Field”. In: *Biophysical Journal* 118.6 (2020), pp. 1502–1510. DOI: 10.1016/j.bpj.2020.01.028 (cit. on p. 55).

[177] Mladen Barbic. “Possible magneto-mechanical and magneto-thermal mechanisms of ion channel activation in magnetogenetics”. In: *eLife* 8 (2019), pp. 1–18. DOI: 10.7554/eLife.45807 (cit. on p. 55).

[178] Matthew I. Brier et al. “Uncovering a possible role of reactive oxygen species in magnetogenetics”. In: *Scientific Reports* 10.1 (2020), p. 13096. DOI: 10.1038/s41598-020-70067-1 (cit. on p. 55).

[179] Guillaume Duret et al. “Magnetic Entropy as a Proposed Gating Mechanism for Magnetogenetic Ion Channels”. In: *Biophysical Journal* 116.3 (2019), pp. 454–468. DOI: 10.1016/j.bpj.2019.01.003 (cit. on pp. 55, 56).

[180] Marcus D Hanwell et al. “Avogadro: an advanced semantic chemical editor, visualization, and analysis platform”. In: *Journal of Cheminformatics* 4.1 (2012), p. 17. DOI: 10.1186/1758-2946-4-17 (cit. on p. 174).

[181] Eric F. Pettersen et al. “UCSF ChimeraX: Structure visualization for researchers, educators, and developers”. In: *Protein Science* 30.1 (2021), pp. 70–82. DOI: 10.1002/pro.3943 (cit. on p. 174).

Corrigenda

This thesis is a revised version of the original document submitted on 7$^{\text{th}}$ November 2024. Changes to the content made during the revision are listed in this chapter. If applicable, changes are highlighted in bold.
Additionally, corrections to spelling, punctuation, formatting, and minor grammatical errors were made, but are not listed here.

Location	**Original**	**Revision**
Excursion 1, Page 9	'...undefined exemplary material **at a predefined**.'	'...undefined exemplary material.'
Page 14	'...anti-parallel to each other (**Section II.1.2.2**)'	'...each other (**Figure II.1.4**)'.
Page 15	'...randomly oriented state ($T > T_{\text{N}}$) [...] ordered state ($T < T_{\text{N}}$).'	'...randomly oriented state (**for** $T > T_{\text{N}}$) [...] ordered state (**for** $T < T_{\text{N}}$).'
Figure II.1.8, Page 18	—	Added 0 at the labelling of the y-axis
Page 21	'Generally, τ_0 has a value between 10^{-9} and $10^{-8}\,\mathbf{s}$.'	'...between 10^{-9} and $10^{-8}\,\mathbf{s}^{-1}$.'
Excursion 5, Page 32	'Depending on the last **atom** of the exposed...'	'...on the last **atoms**...'

Location	**Original**	**Revision**
Page 34	'...two identical *heavy chains* (HC, ∼**25** kDa)...'	'...(HC, ∼**50** kDa)'...
Page 43	'The force $\mathbf{F}_m$ exerted on the particle will be...'	'The force $\vec{\mathbf{F}}_m$...'
Equation II.3.6, Page 43	'$\mathbf{F}_{\mathrm{m}} = (\vec{m} \cdot \nabla)\vec{B}$'	'$\vec{\mathbf{F}}_{\mathrm{m}} = ...$'
Page 43	—	Rearranged order of paragraphs to match the order of Figure II.3.10
Figure II.3.10, Page 45	—	Rearranged order of A, B, and C
Page 172	'Here, **we** demonstrated that...'	'Here, **I** demonstrated that...'

Danksagungen

Das Beste kommt bekanntlich zum Schluss, daher widme ich dieses Kapitel meinem Dank gegenüber allen Menschen, die mich in den letzten Jahren sowohl wissenschaftlich als auch persönlich auf dieser Reise begleitet und bereichert haben.

Zuallererst bedanke ich mich bei meiner Doktormutter, Prof. Dr. Cornelia Monzel — Vielen Dank für die Möglichkeit, meine Doktorarbeit in deiner Arbeitsgruppe zu machen. Vielen Dank für die Freiheiten, die du mir in meinen Überlegungen und Ansätzen gelassen hast und gleichzeitig vielen Dank für deine Ratschläge, Unterstützung und deine Positivität, wenn es mal nicht so lief wie erhofft!

Mein Dank gilt außerdem Dr. Iuliia Novoselova, die mich in den ersten beiden Jahren in der alltäglichen Arbeit betreut hat. Iuliia, vielen Dank für dein offenes Ohr, deine Hilfestellungen und die Möglichkeit mit dir ein Büro/Restaurant zu teilen!

Vielmals bedanke ich mich bei Prof. Dr. Philip Kollmannsberger für die Bereitschaft und Übernahme des Zweitgutachtens dieser Dissertation!

Eine Arbeit in solchem Umfang wäre ohne helfende Hände nicht denkbar. Deswegen bedanke ich mich bei allen Studenten, die mich mit ihrer Zeit und ihrem Tatendrang unterstützt haben. Allen voran bedanke ich mich bei Christina, Liesa und Sarah für eure Mithilfe an diesem Projekt!

Genauso wäre meine Arbeit allerdings auch nicht möglich gewesen ohne die Unterstützung außerhalb meiner Arbeitsgruppe. Unseren Kooperationspartnern aus Duisburg, Nikolaos Tetos, Prof. Dr. Michael Farle und Prof. Dr. Ulf Wiedwald sende ich außerordentlichen Dank für die magnetische Charakterisierung unserer Nanopartikel und die hilfreichen Diskussionen über Magnetismus.

Da wissenschaftlicher Fortschritt immer eine gemeinsame Anstrengungen ist, bedanke ich mich bei allen Arbeitsgruppen der Heinrich-Heine Universität, die mir und uns mit Ausrüstung und Expertise zur Seite standen. Ich hebe hier auch noch einmal explizit alle Unterstützer hervor und bedanke mich bei...

...dem Institut für Molekulare Physikalische Chemie unter Prof. Dr. Claus Seidel für die Überlassung von Räumlichkeiten, Geräten und Ratschlägen!

...dem Institut für Synthetische Membransysteme unter Prof. Dr. Alexej Kedrov für die bereitwillige Zurverfügungstellung allerlei Equipments! Danke an Max Busch für die Einführung in die SPR!

...dem Institut für Computational Pharmaceutical Chemistry unter Prof. Dr. Holger Gohlke für die vielen kleinen unterstützenden Gesten im Laboralltag!

...dem Institut für Kolloide und Nanooptik unter Prof. Dr. Matthias Karg und insbesondere Dr. Marius Otten und Jonas Schmitz für die Unterstützung am TEM!

...dem Institut Biochemie I unter Prof. Dr. Lutz Schmitt für die Überlassung der Geräte zur Proteinaufreinigung!

...dem Institut für Makromolekulare Chemie unter Prof. Dr. Laura Hartmann für den Zetasizer!

Mein besonderer Dank gilt meinen Mitstreitern des Instituts für Experimentelle Medizinische Physik. Vielen Dank, Dr. Nina und Dr. Daniel, für eure herzliche Aufnahme in die Arbeitsgruppe und eure tatkräftige Hilfe über all die Jahre! Thank you, Xiaoyue, for sharing all ups and downs during our PhD time! Danke Dr. Philipp, Luisa, Jan und Soner für euer Engagement und eure Hilfsbereitschaft! Danke Christiane und Siegrun für eure Unterstützung während der gesamten Zeit!

Ich bedanke mich ganz besonders bei all meinen Freunden, die über Deutschland und die Welt verstreut sind und die mir immer mit einem offenen Ohr und einem Lachen zur Seite standen. Fühlt euch gedrückt!

Von Herzen danke ich meiner Familie, meinem Vater Gebhard, meiner Schwester Ina und Thomas, für den Zusammenhalt, den ich in allen noch so schweren Zeiten erfahren durfte. Ich danke euch für eure bedingungslose Unterstützung und euer Verständnis, auch in Zeiten, in denen die Uni mal wieder viel Zeit eingenommen hat!

In Erinnerung an meine Mutter Gabriele und meine Großmutter Helene, danke ich euch beiden dafür, dass ihr mir den Weg bereitet habt, der mich hierher geführt hat! Ich werde euch immer in meinem Herzen tragen.

As described previously, kommt das Beste zum Schluss. Liebe Alexandra, ich danke dir dafür, dass du mir in den tiefsten Tiefen zur Seite stehst, die höchsten Höhen mit mir teilst und dabei immer an mich glaubst. Danke für dein Vertrauen und dafür, dass du mein Fundament bist. Ich freue mich auf unsere gemeinsame Ruhe nach dem Sturm!

Macht's gut, und danke für den Fisch!